UNIVERSITÀ DI SIENA 1240

Department of Physical Sciences, Earth and Environment

PhD in Experimental Physics

XXXV Cycle

Coordinator: Prof. Riccardo Paoletti

Fast photodetectors and their role in measuring star diameters with the MAGIC intensity interferometer

Disciplinary Scientific Sector: FIS/01

A thesis submitted in partial fulfillment of the requirements for the degree of Doctor of Philosophy

PhD Student
Carolin Waltraud Wunderlich
University of Siena
Via Roma 56

Carolin Waltraud Wunderlich

Signed 11/05/2023

Signature

Supervisor
Dr. Daniel Guberman
University of Barcelona

Signature

Co-Supervisor
Prof. Dr. Riccardo Paoletti
University of Siena

Signature

Acknowledgements

I would like to express my sincere gratitude to my tutor Professor Riccardo Paoletti for giving me the possibility to complete my PhD studies in his group at the University of Siena. His advice allowed me to grow as a scientist and his continuous support and patience encouraged me in the time of my academic research. I would like to extend my sincere thanks to my supervisor Dr. Daniel Guberman for all his help, tremendous support and encouragement, and for sharing his invaluable knowledge about SiPMs. Your advice on both research as well as on my career has been priceless.
Additionally, I would like to thank all the members of the MAGIC intensity interferometry group. Their immense knowledge and plentiful experience were the basis to develop a deeper understanding of the field. I want to express special thanks to the other analyzers. Our weekly discussions helped me a lot to shape my analysis methods. I also want to thank the MAGIC interferometry members in Madrid that gave me the possibility to visit them and work together in person.
Words cannot express how grateful I am to my family and my loved one: You always supported me, loved me and encouraged me with never-ending patience even in the hardest times. Finally, I would like to express my gratitude to my friends in Italy. You helped me to orientate myself in a foreign country, practice the beautiful Italian language and discover the wonderful Tuscany. I would also like to thank all my friends from Germany who visited me and stayed in contact with me during the difficult time of the pandemic.

List of Acronyms

AC	Alternating Current
ADC	Application Delivery Controllers
AMC	Active Mirror Control
AOI	Angle of Incidence
AP	Afterpulsing
APD	Avalanche Photo Diode
ARM	Advanced RISC Machines
ASIC	Application-Specific Integrated Circuit
CPU	Central Processing Unit
CT	Crosstalk
CTA	Cherenkov Telescope Array
CTAO	Cherenkov Telescope Array Observatory
DC	Direct Current
DCR	Dark Count Rate
DeCT	Delayed Crosstalk
ExtCT	External Optical Crosstalk
FACT	First G-APD Cherenkov Telescope
FFI	Flat Field Irradiation
FFT	Fast-Fourier-Transform
FIR	Finite Impulse Response
FOV	Field Of View
FPGA	Field Programmable Gate Arrays
FWHM	Full Width Half Maximum
GM-APD	Geiger-mode Avalanche Photodiodes
GPU	Graphic Processing Unit
GUI	Graphical User Interface
HV	High Voltage
IACT	Imaging Atmospheric Cherenkov Telescope
INFN	Istituto Nationale di Fisica Nucleare
LASiP	Large-Area SiPM Pixel
LB	Long Baseline
LRF	Light Response Function
LST	Large-Sized Telescopes
MAGIC	Major Atmospheric Gamma Imaging Cherenkov

MAGIC-SII	MAGIC Stellar Intensity Interferometer
MC	Monte-Carlo
MLE	Maximum Likelihood Estimation
MST	Medium-Sized Telescopes
NSB	Night Sky Background
NUV	Near Ultra Violet
NIR	Near Infrared
pCT	Prompt Crosstalk
PDE	Photon Detection Efficiency
PDF	Posterior Distribution Function
PET	Positron Emission Tomography
PMT	PhotoMultiplier Tube
PST	Polystyrene
PVT	Polyvinyltoluene
OAP	Optically induced afterpulsing
ORM	Observatoro del Roque de los Muchachos
QE	Quantum efficiency
RDMA	Remote-Direct-Memory Access
RMS	Root Mean Square
SB	Short Baseline
SCAPP	Spectrum CUDA Access for Parallel Processing
SiPM	Silicon Photomultiplier
SNR	Signal-to-Noise Ratio
SOC	Systems On a Chip
SPAD	Single Photon Avalanche Diodes
SPECT	Single Photon Emission Computed Tomography
SPTR	Single Photon Time Resolution
SST	Small-Sized Telescopes
TE	Trapping efficiency
TIR	Total Internal Reflection
TTD	Transit Time Difference
TTS	Transit Time Spread
UV	Ultra Violet
VCSEL	Vertical Cavity Surface Emitting Lasers
VHE	Very High Energy
WLS	Wavelength Shifter
ZBC	Zero-baseline correlation

Contents

Abstract

A few years ago MAGIC Stellar Intensity Interferometer (MAGIC-SII) was implemented by applying adjustments to the existing MAGIC IACT array. One of the key parts of the instrument are the photodetectors. Improved photodetector properties as a higher PDE or a better SPTR could increase the sensitivity of the interferometer. This could be achieved, for instance, if the PMTs were replaced by SiPMs thanks to their excellent SPTR. Probably the main drawback of SiPMs is their limited area. I worked on two approaches that aimed at overcoming this limitation: LASiP and Photo-Trap. The first one sums the current of several SiPMs into a single output. We built and characterized a LASiP prototype that used an ASIC called MUSIC to sum the output of 8 SiPMs of 6 mm × 6 mm. I explored the feasibility of using LASiPs in SPECT, which is an application in which one needs to cover a large area (50 × 40 cm^2) with a limited amount of readout channels (typically ~ 100). I showed that it was possible to reconstruct simple images with an energy resolution of ~ 11.6 % and an intrinsic spatial resolution of ~ 2 mm (comparable to standard SPECT cameras). Using SiPMs would allow reducing by at least 50 % the volume of a SPECT camera which would result in a compact and lighter camera. A few LASiPs are also present in one of the MAGIC cameras. These pixels could be a good starting point for testing the feasibility of using SiPMs in intensity interferometry.
Photo-Trap provides a different solution to build large SiPM pixels, combining a WLS plastic and a dichroic filter with a commercial SiPM. We built four prototypes using WLS plastics of 20 × 20 mm^2 or 40 × 40 mm^2 and SiPMs of 3 × 3 mm^2 or 3 × 12 mm^2. One of those prototypes is, as far as I know, the largest existing SiPM pixel with single-phe resolution at room temperature. One of the main advantages of Photo-Trap is that it is easily scalable to larger sizes. The prototypes achieved a trapping efficiency of ~ 10 – 50% (which corresponds to a peak PDE of ~ 5 – 25%) with a time resolution of ~ 2 – 5 ns (FWHM).
My main contribution to the MAGIC-SII was the development of the analysis chain which was used to analyze the data of multiple calibration campaigns. The calibration results of the MAGIC-SII showed that the current MAGIC-SII is a working and reliable instrument. MAGIC-SII has so far measured the diameter of over 25 stars. The diameters of several of them were measured for the first time by MAGIC-SII, at least in its wavelength band (412-438 nm). Since some of them are variable stars, they appear as interesting targets to study their oblateness and might be candidates for asteroseismology studies. Observations of these types of targets may contribute to improving our knowledge of stellar structure and evolution.

Introduction

Nowadays there are many scientific and industrial projects that require fast photodetectors with the ability to resolve single photons and a time resolution of at least a few ns. Examples of such applications can be found for instance in medical imaging, astrophysics and astroparticle physics. Photodetectors can indeed provide a connection between two fields that at a first glance may appear completely different like medical imaging and astrophysics. A connection that allows for a continuous flow of know-how between these two fields. A connection that will be also present in the next chapters.

This thesis aims at exploiting the main capabilities of photodetectors, providing some solutions to overcome their limitations and exploring some of their applications. In particular, the focus is set on the role they play in intensity interferometry. This thesis describes a series of hardware and software modifications that allowed to turn the MAGIC telescopes, originally designed for gamma-ray astronomy, into a powerful instrument for measuring star diameters. I will describe how this implementation took place and present the first results of the MAGIC intensity interferometer (MAGIC-SII). In this context, I will also discuss the challenges and benefits that new developments in photodetection may bring in this field. In particular, I will discuss the possibility of replacing the traditional photomultiplier tubes (PMTs) by silicon photomultipliers (SiPMs).

In the year 1963 the Narrabri Stellar Intensity Interferometer started its operation [85]. The telescope was working in the optical range and measured in the following years the diameter of the 32 brightest stars in the Southern Hemisphere. Despite this success, intensity interferometry has nearly not undergone any development due to its requirement of large photon collectors and photodetectors with high sensitivity and time response [6]. The requirements may now be fulfilled with the development of Imaging Atmospheric Cherenkov Telescopes, that feature large light collectors and fast photodetectors, which are typically PMTs.
Currently, PMTs are the standard light sensor in Imaging Atmospheric Cherenkov Telescopes [113], but there are plans to build new telescopes or upgrade existing ones using SiPMs. SiPMs have typically a higher photon-detection efficiency and a better time resolution. Additionally, they are operated at low bias voltage and their cost is going down. SiPMs have indeed the potential to increase the sensitivity of an intensity interferometer.
One main obstacle of using SiPMs in telescopes like MAGIC is their limited area. To cover a large camera with SiPMs one would need to increase significantly the number of readout channels, increasing its cost and complexity. In this thesis two approaches

to build large SiPM pixels are presented. The first concept is Large-Area SiPM Pixel (LASiP) where the individual channels of several SiPMs are summed into a single output. The second approach is Photo-Trap, a SiPM coupled to a wavelength-shifter plastic combined with a 1-dimensional dichroic filter.
Coming back to the connection discussed before, with our LASiP I will discuss how a technology developed for high-energy astrophysics could be used to build pixels for an application in medical physics like Single Photon Emission Computed Tomography (SPECT).

Chapter 1 briefly introduces PMTs and SiPMs. In Chapter 2 I explain the theory of intensity interferometry and how Imaging Atmospheric Cherenkov Telescopes can be used as intensity interferometers. In this chapter also the MAGIC telescopes are briefly introduced. Chapter 3 describes the complete signal path and the basic analysis chain of MAGIC-SII. In Chapter 4 I present two approaches to build large SiPM pixels (LASiP and Photo-Trap), I show the results of the characterization of LASiP and Photo-Trap prototypes and discuss possible applications. Finally, Chapter 5 is devoted to the achievements of the MAGIC-SII: I present the results of the calibration of the instrument and a catalog of star diameters measured by the MAGIC-SII. For many stars this represents the first diameter measurement in the blue visible light band.
Finally, and as a result of this flow of research between astrophysics and medical imaging, Appendix A and B are devoted to SPECT. In Appendix A I describe the evaluation of a proof-of-concept micro-camera we built to study the feasibility of using LASiPs in SPECT. Appendix B hosts the work I did, based on simulations, to extend the results of the micro-camera into a large, full-body SPECT camera.

1. Fast Photodetectors

Many experiments and applications require fast photodetectors (time resolution of a few ns or less) with an intrinsic gain ($\sim 10^6$) that allows to resolve single photons. For many years, this task was mostly left to Photomultiplier tubes (PMTs). It is currently the standard photodetector in ground-based Gamma-Ray Telescopes [14, 17, 91] and neutrino experiments [40] in the field of high-energy astrophysics. In addition, PMTs are widely applied in medical imaging, for example in Positron Emission Tomography (PET) [42] or in Single Photon Emission Computed Tomography (SPECT) [105].
Silicon photomultipliers (SiPMs) underwent developments that allowed to improve their performance and challenge the dominant position of PMTs in many applications [151]. Examples can be found in high energy astrophysics [19, 132], particle physics [103, 25, 37, 156, 158] and in medical imaging [29, 100].
This chapter introduces the main characteristics of PMTs and SiPMs and compares their advantages and drawbacks.

1.1. Photomultiplier Tubes

At the end of the 19th century, two important discoveries were made: in 1887 the photoelectric effect was found by Heinrich Hertz [89]. Two years later, Julius Elster and Hans Geitel observed the photoelectric effect of visible light hitting sodium-potassium [95]. This was the starting point for the development of compound photoemissive surfaces (photocathodes) [96]. The second important discovery were secondary emissive surfaces. The first report of such a surface was done by Luis W. Austin and H. Starke in 1902 [21]. In 1935, finally, a photocathode was combined with a secondary emissive surface for electron multiplication by Harley Iams and Bernard Salzberg [93]. This was the first reported photomultiplier tube (PMT).

1.1.1. Working principle

A PMT consists of a photocathode, a system of dynodes and an anode as shown in Figure 1.1. The photocathode is made of a photosensitive material and is the one that absorbs the photons and releases electrons. The dynodes are bent electrodes and act as electron multipliers, generating secondary electrons. Between the cathode and the dynodes an electric field is applied. There exist different dynode configurations which impact the efficiency, timing and compactness of a PMT. An optical and electrical focusing system with a focusing electrode leads the electrons from the cathode to the first dynode. All the PMT components are placed inside a glass tube filled with vacuum [96, 101].
Incoming light goes through the faceplate and impinges on the photocathode. In the photocathode the photons are absorbed and electrons in the valence band are excited. The electrons move to the surface of the photocathode by diffusion and if they have enough energy they are emitted into the vacuum. Electrons in the photocathode are released as a result of the photoelectric effect. For it to take place, the energy of the

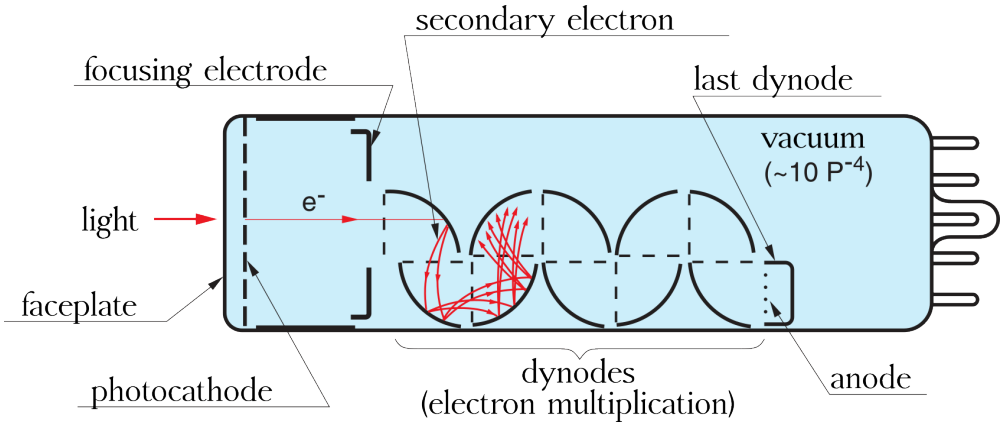

Figure 1.1.: Sketch of the structure of a PMT: it consists of a photocathode, a system of dynodes and an anode. The dynode configuration shown here is the linear-focused type. Adapted from [96]

incident photon $h\nu$ needs to be larger than the work function Ψ, the energy difference between the Fermi level and the vacuum level barrier.

$$E = h\nu - \Psi \qquad > 0 \tag{1.1}$$

h is the Plank's constant, ν the frequency of the photon and E the kinetic energy of the emitted phe. In Figure 1.2 a scheme of the photoelectric effect and the conditions for its occurrence are shown [101].
Not every incident photon fulfilling the condition for the photoelectric effect leads indeed to the emission of an electron from the photocathode. This will be determined by the quantum efficiency $\eta(\nu)$, the ratio between the number of impinging photons N_λ and emitted electrons N_e,

$$\eta(\nu) = \frac{N_e}{N_\lambda} = (1 - R)\frac{P_\nu}{k} \cdot \left(\frac{1}{1 + 1/kL}\right) \cdot P_s. \tag{1.2}$$

R is the reflection coefficient and k is the full absorption coefficient of the photons of the photocathode (both are wavelength dependent).
P_ν is the probability that an electron is excited over the vacuum barrier level by photon absorption. L is the mean escape length of an excited electron and P_s is the probability that an excited electron at the surface of the photocathode is emitted into the vacuum. Thus, the quantum efficiency depends on the wavelength of the incident light and the photocathode material. The dominant factors of the material are here L which can be improved by using a photocathode material with fewer impurities and P_s which depends on the gap between the conduction band and the valence band of the semiconductor [96]. Quantum efficiencies up to ~ 40% are possible, for example for

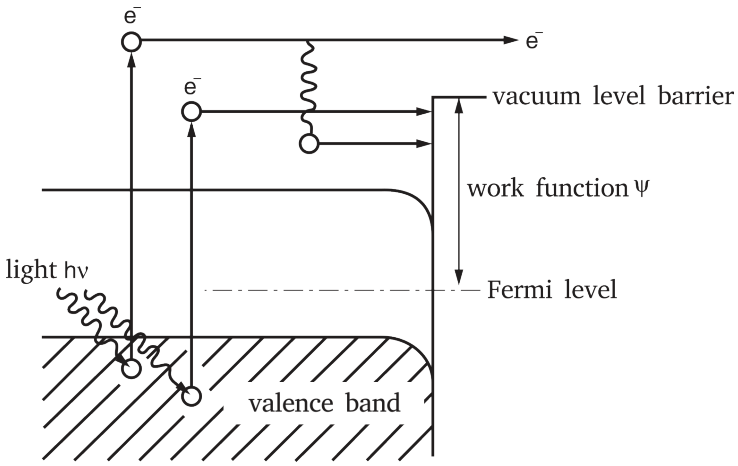

Figure 1.2.: If the energy of an incident photon is higher than the work function Ψ, the condition for the photoelectric effect is fulfilled. The photon is absorbed and an electron is excited and emitted. Adapted from [96].

a Hamamatsu ultra bialkali photocathode and with a borosilicate faceplate (see [96] for typical spectral response characteristics of PMTs with different photocathode and faceplate materials). For PMTS with a multialkali photocathode the peak quantum efficiency is typically lower (~ 25-30 % at 260 nm) [96].

The emitted phes are accelerated by the applied electric field and focused on the first dynode. The position and characteristics of the first dynode and the electric field are designed to maximize the collection efficiency. The collection efficiency is the ratio between electrons emitted from the photocathode and electrons reaching the effective area of the first dynode. It is typically between 60 to 90 percent [96], although higher values have been reported [113].
Dynodes are electrodes made of nickel, stainless steel, or copper-beryllium alloy, coated with secondary emissive materials such as alkali antimonide (Sb), beryllium oxide (BeO) and magnesium (Mg0) [96, 101]. If an electron impinges on the dynode material and is absorbed, a larger number of secondary electrons is emitted (electron multiplication). The primary phe is multiplied in all stages of the dynode system (up to 19 stages [96]). There are different designs of PMTs. In Figure 1.3 two types of PMTs can be seen that differ in the position of the faceplate: the side-on type and the head-on type. Also the photocathode material and the material of the faceplate can be different, as well as the number of dynodes and the structure of the dynode system. The dynodes can be, for example, arranged as linear-focused (see Figure 1.1) as well as circular-cage or a metal-channel type (see Figure 1.4). The linear focused type features a good time resolution and excellent pulse linearity and is used in head-on PMTs. The circular-cage type is compact and fast and is used in side-on PMTs. The metal-channel type provides excellent timing properties and is less sensitive to magnetic fields than other types [96].

All secondary electrons are collected in the anode. The total charge at the anode is proportional to the number of electrons that were emitted from the photocathode,

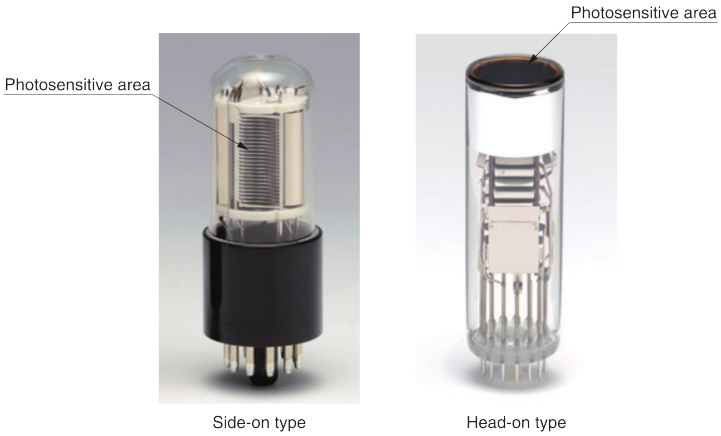

Figure 1.3.: Different types of PMT that differ in the position of the entrance window. Image by [96]

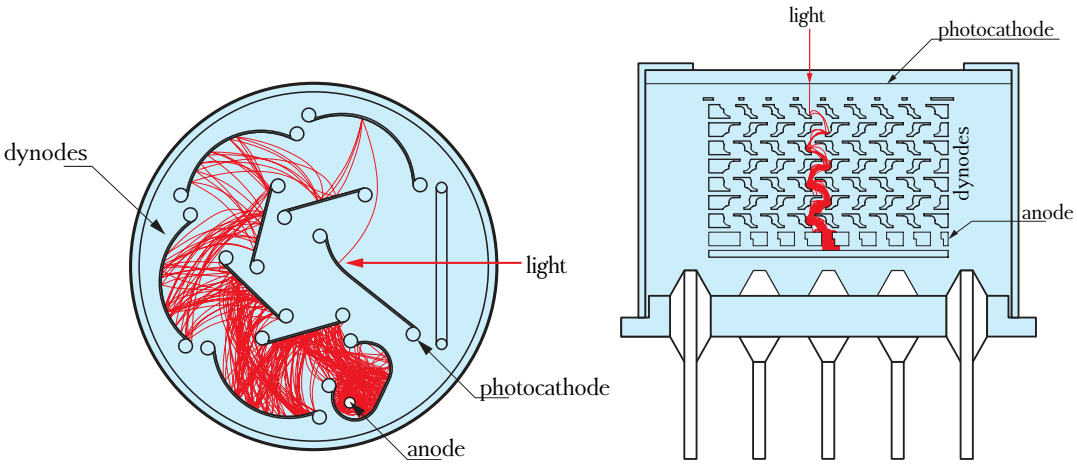

Figure 1.4.: **Left**: PMT with circular-cage dynode structure. Image adapted from [96]. **Right**: PMT with metal channel dynode structure. Image adapted from [96].

which in turn is proportional to the number of incident photons. The gain G of a PMT is the number of secondary electrons collected at the anode. A PMT can reach a gain of up to 10^7 [35]. The gain depends on the mean number of emitted secondary electrons per absorbed primary electron δ, also called the secondary emission factor, and the number of dynodes n.

$$G = \delta^n \tag{1.3}$$

Working with a PMT

For the operation of a PMT a high-voltage supply (usually between 500 to 2000 V) is needed to have a sufficient electric field for the acceleration of the phe and the electron multiplication. Due to the high gain of a PMT, the voltage supply needs to be very stable because even small variations in the bias voltage could change the amplification and hence the output significantly. In addition, a voltage-divider circuit is required that supplies each dynode with an appropriate voltage as shown in Figure 1.5. The voltage divider circuit creates a potential "ladder" [101] from the cathode to the anode to trigger the acceleration and multiplication of the phes. Besides the high voltage several things need to be taken into account when working with PMTs: they should not be exposed to intense light for a longer time. Otherwise, the PMT performance degrades due to accelerated aging of the anode, which means that the anode loses gain as it is hit by more electrons. Furthermore, PMTs are sensitive to magnetic fields since the shape of the electron trajectory is essential for the collection efficiency and therefore for the detection probability.

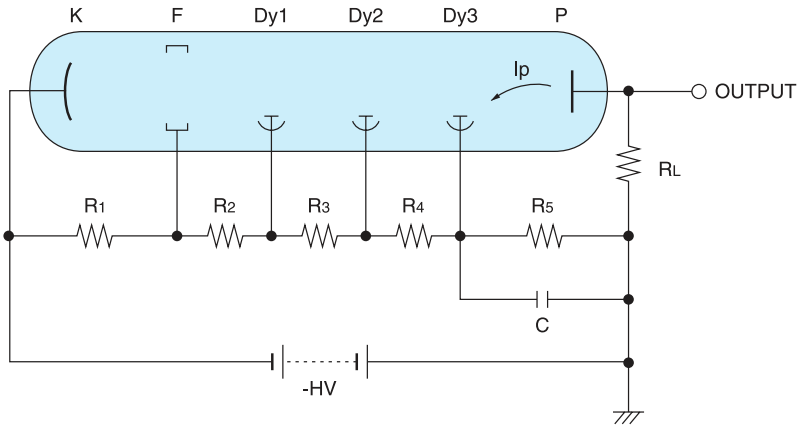

Figure 1.5.: PMT with voltage divider circuit. The applied high voltage is divided between the photocathode (K), the dynodes Dy1, Dy2 and Dy3 and the anode P. Image from [96].

1.1.2. Materials and characteristic parameters

The majority of photocathodes consist of a compound semiconductor. This material is made of alkali metals that have a small work function and high quantum efficiency of 10 to 30 % [101]. In the valence band of the photocathode the electrons are approximately free and can be excited by a photon. Since the semiconductor is arranged in a tight lattice, the electrons would lose only a small amount of energy in possible collisions with lattice atoms. That increases the chances for a free electron to reach the surface [101]. Photocathodes are highly sensitive down to the ultraviolet wavelength range. The main limitation at shorter wavelengths is the transmission of the material of the faceplate. Examples of window materials are silica glass, sapphire or MgF_2 crystal. At long wavelengths the limit is determined by the photocathode material: when the energy of the incident light is smaller than the work function of the photocathode material, the light cannot be detected anymore.
In general, the temperature has a rather small effect on the performance of PMTs (compared to SiPMs as will be shown in the next section). The gain has a small dependence on the temperature (~ -0.25 %/°C as reported [110]). The secondary emission factor of the dynode system instead does not depend directly on the temperature [101].

Photodetection efficiency

The photodetection efficiency (PDE) indicates the percentage of impinging photons that are detected by the PMT. This parameter depends on the quantum efficiency ν, the probability that the photoelectric effect takes place, and on the collection efficiency κ that an accelerated phe reaches the first dynode.

$$\text{PDE} = \nu \cdot \kappa \tag{1.4}$$

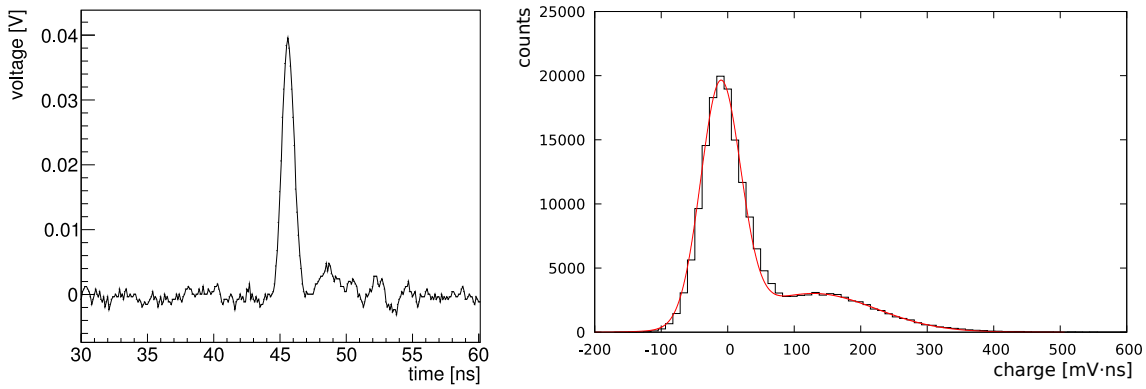

Figure 1.6.: **Left**: a waveform with a pulse of a PMT used in the MAGIC telescope. **Right**: charge distribution of the Hamamatsu PMT R8520-406 with a pedestal around zero and a wider distribution corresponding to the single-phe events.

PMT signal and timing

The signal of a PMT has a fast rise time and a slightly slower decay time. In the left panel of Figure 1.6 an example of a PMT pulse is shown from a PMT of the camera of the MAGIC telescopes. The charge distribution for single-phe events can be obtained by exposing the PMT with a very-week photon flux (~ 1 detection every 100 events). In the right panel of Figure 1.6 an example of the charge distribution can be seen. It features a prominent noise pedestal around zero and a wider distribution corresponding to the single-phe events. The charge/amplitude generated by a single-phe event has a large spread due to the statistical nature of the electron multiplication [101].
The timing performance of a PMT is influenced by fluctuations in the transit time of electrons traveling in the PMT. The transit time difference (TTD) stems from differences in the path length for different electrons. Electrons that are emitted in the center of the photocathode have a smaller distance to travel than an electron emitted in the edge [113]. The transit time spread (TTS) are variations of the transit time due to the different energies and the direction of the emitted electrons [101]. In addition, the statistical nature of the photoelectric effect and the secondary emission process have an impact on the timing jitter of a PMT [101].

Linearity and uniformity

A PMT is linear if the current is entirely collected by each dynode, i.e., if the output current is strictly proportional to the initial current of the photocathode. The linearity of a PMT depends on the voltage steps for the voltage divider circuit and the dynode configuration [101].
The uniformity of a PMT is the fluctuation of the output current with respect to the incident light position in which the incident light hits the photocathode. Non-uniformities are typically larger at longer wavelengths, nearer to the energy limit for the photoelectric effect [96].

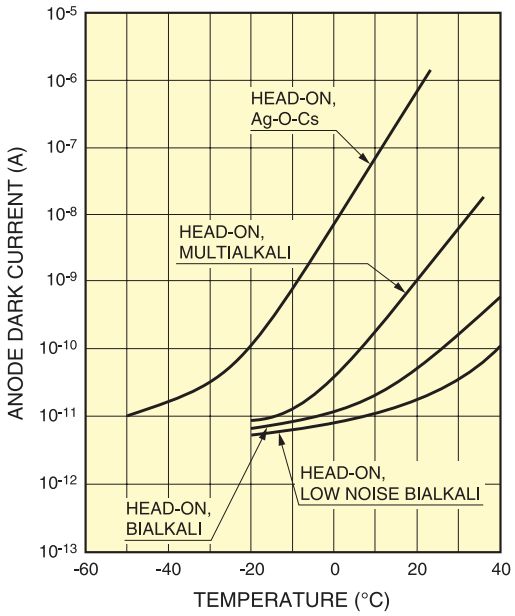

Figure 1.7.: Dark current of PMTs with different photocathode material and design as a function of the temperature [96].

1.1.3. PMT noise

The main source of noise in a PMT are the dark current, afterpulsing and shot noise.

Dark current

Even if no light enters the faceplate, a small current is present in the PMT, called dark current. Causes of dark current are for example the thermionic emission of electrons from the photocathode or the dynode surface. This means that due to the low work function of the photocathode material electrons are emitted at room temperature without a trigger from outside. The rate of the thermionic emission is affected by the temperature.
Other causes of dark current are the leakage current between the anode and the dynodes, radioactive contamination, ionization and light phenomena [101]. With a rising supply voltage the dark current increases.

Afterpulsing

Afterpulses are pulses with small amplitudes that are observed directly after normal signal pulses. It can be distinguished between two types of afterpulses: (1) Pulses that have only a short delay to the previous signal (ns to tens of ns). The majority of them are generated by the elastic scattering of electrons on the first dynode. (2) Pulses that have a longer delay of hundreds of ns to μs. Those longer afterpulses are generated by positive ions caused by the ionization of residual gases in the PMT. The ions move to the photocathode and generate new phes. Since some materials of the

faceplate are permeable for small atom gas, this has to be taken into consideration when handling a PMT in a gas environment. A high-vacuum level typically helps to reduce the afterpulsing probability.

Statistical noise

Fluctuations in the PMT output have also a statistical component, the so-called shot noise [101]. Shot noise are fluctuations in the output current due to the stochastic nature of the generation of phes. The charge is quantized and as a consequence, the current in PMT has discrete values. The standard deviation of the average number of electrons in a given time interval is, following Poisson statistics, its square root. The effect of the shot noise underlies this relation and represents a minimal noise limit in a PMT [146, 111].

1.2. Silicon Photomultiplier

The silicon photomultiplier (SiPM) is a solid-state photodetector with a high amplification of $10^5 - 10^6$ [149] and fast timing of tens of picoseconds [9]. It is a compact detector that does not require high-voltage operation and is insensitive to magnetic fields. In addition, it is a robust device that does not undergo any significant aging when exposed to bright light. A SiPM consists of an array of Geiger-mode avalanche photodiodes (GM-APDs), also called single photon avalanche diodes (SPADs) [139].

A GM-APD is usually composed of a reversed biased n^+/p junction with a lowly-doped layer π. In this notation the + superscript tags a region of high doping. Around the n^+/p junction a high electric field is formed (see the left panel of Figure 1.8). When a photon is absorbed, an electron-hole pair is generated. The electron drifts to the zone with a high electric field, the hole to the region with a low field. Due to the electric field the drifting electron can generate secondary electron-hole pairs which are then again separated. The secondary electrons create more electron-hole pairs at the n^+/p junction. Hence a multiplication of the original phe occurs and an avalanche of secondary particles is produced [139]. The avalanche-triggering probability of a GM-APD P_T is the probability that a charge carrier (electron or hole) triggers an avalanche. The probability for the holes to trigger an avalanche is smaller than for electrons [128].
In contrast to an Avalanche Photo Diode (APD) which features a linear multiplication, a GM-APD is specifically designed to work with a bias voltage (U_{bias}) above the avalanche breakdown voltage (U_{bd}). In this so-called Geiger mode the electric field is sufficiently high to start an avalanche from a single electron-hole pair. The avalanche works as a strong internal amplification. In this regime, the amount of secondary

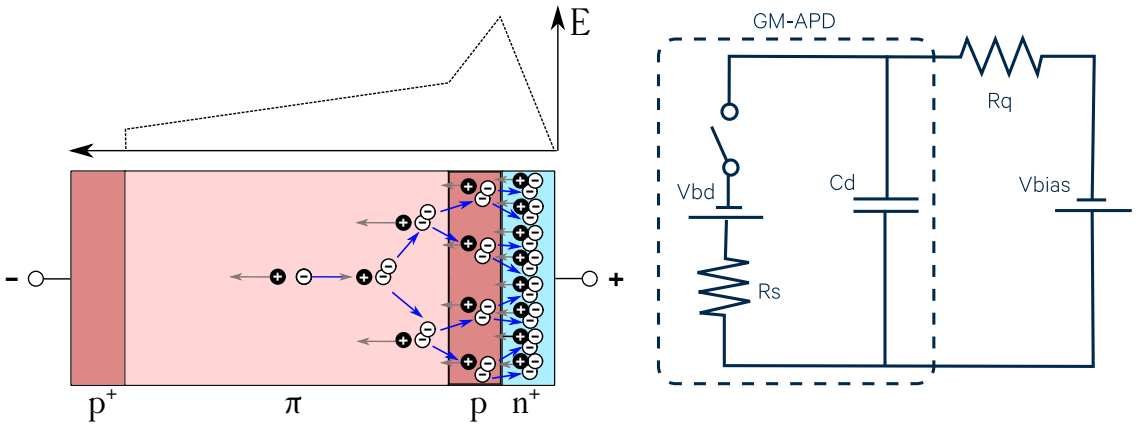

Figure 1.8.: **Left**: doping structure of a GM-APD with a scheme showing the corresponding electric field. First, the electron-hole pair is separated and the electron is accelerated. Then secondary electron-hole pairs are created and an avalanche is triggered. Adapted from [139]. **Right**: equivalent circuit of a GM-APD with quenching resistor R_Q. Image from [57].

electrons in an avalanche is independent of the number of absorbed photons. Already a single electron-hole pair is enough to produce a self-sustaining avalanche, thus a macroscopic charge. Therefore a GM-APD is sensitive to single photons.
In the right panel of Figure 1.8 the equivalent circuit of a SiPM is shown. The GM-APD can be modeled by a junction capacitance at the operation voltage C_d, the space-charge resistance of the avalanche region R_s, a voltage supply at U_{bd} and a switch. External to the GM-APD is the $U_{\mathrm{bias}}(> U_{\mathrm{bd}})$ and a series quenching resistor R_q. In the case of a steady state, the switch in the circuit is open, C_d is charged and no current flows. When an electron-hole pair is moving through the high-field region, it can start an avalanche. If an avalanche is triggered, the switch closes. C_d discharges from the U_{bias} to U_{bd} through R_s. During the avalanche, the internal current I_{int} in the diode decreases exponentially while the external current I_{ext} is increasing rapidly to a macroscopic level [139].

$$I_{\mathrm{int}} \sim \exp((U_{\mathrm{bias}} - U_{\mathrm{bd}})/R_s) \qquad I_{\mathrm{ext}} \sim C_d R_s \tag{1.5}$$

The leading edge of the fast-rising I_{ext} pulse marks the arrival time of a detected photon [9]. The avalanche is a self-sustaining process and would theoretically spread all over the region with a high electric field. When the external current through the quenching resistor R_q is high enough that U_{bias} drops below U_{bd}, the condition for a further creation of secondary electron-hole pairs is not longer fulfilled. The avalanche is suffocated with a quenching probability P_Q. Due to the quenching resistor the diffusion of secondary particles is limited to a few micrometers around the starting point [97]. After the avalanche is quenched, the switch opens again and the U_{bias} is restored. $I_{int} = 0$ and I_{ext} decreases exponentially The neutral status of the diode is recovered and hence a new photon can be detected [139, 35].
The GM-APDs of a SiPM are connected in parallel and each of them is equipped with a quenching resistor, as can be seen in the left panel of Figure 1.9. In this context, the GM-APDs are called microcells. A SiPM consists of hundreds or thousands of

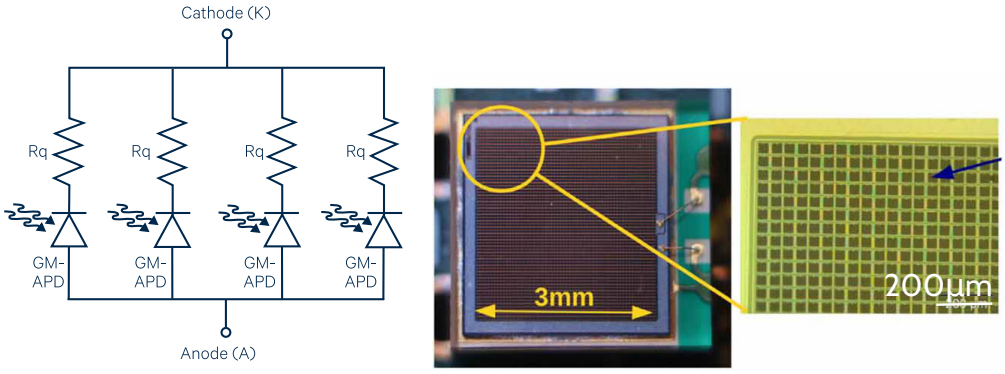

Figure 1.9.: **Left**: parallel connected GM-APDs with quenching resistor. A SiPM is an array of GM-APDs. Image from [57]. **Right**: zoom to the individual GM-APDs of the SiPM HPK S10931-3050P. Image from [100].

microcells [9] (see right panel of Figure 1.9). A microcell typically has a square shape and the microcell pitch goes from 10 μm [7] to 100 μm [166]. Commercially available SiPMs have usually sizes not larger than 6 × 6 mm^2. The main limitation for building larger SiPMs is their capacitance, which increases considerably with size [71, 148].

1.2.1. Pulse shape

In Figure 1.10 and in Figure 1.11 typical SiPM pulses are shown. They feature a fast rising edge (from 30 ps [144] to a few hundred ps [35]) and an exponential decay of ~ 1-100 of ns [144]. The rising edge is determined by the drift time of electron-hole pairs during an avalanche [144]. The decay or recovery time τ_{decay} is defined by the recharge time of the microcells. It can be estimated as [108]

$$\tau_{\text{decay}} = R_q(C_d + C_q) + NR_L\frac{C_dC_q}{C_d + C_q}. \tag{1.6}$$

C_d is the junction capacitance of the inner depletion layer and C_q is the stray capacitance associated with the quenching resistor of the microcell. R_L is the load resistor or rather the input impedance of the readout amplifier and N is the number of microcells in the SiPM. C_d is proportional to the size of the microcells, i.e. the capacitance of a SiPM is proportional to its sensitive detector area. A larger capacitance results in a larger recovery time of the SiPM.

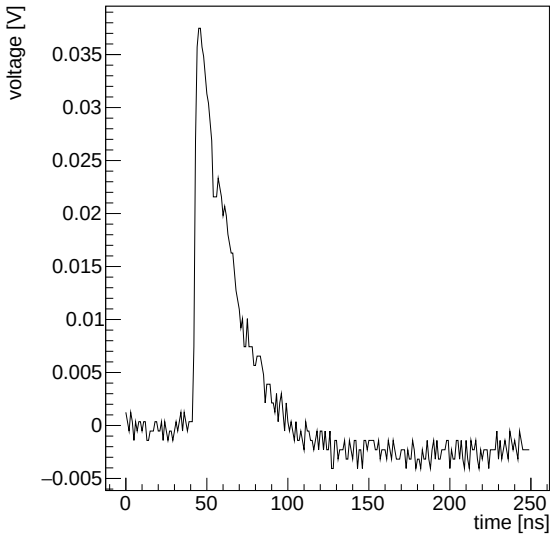

Figure 1.10.: Measurement from the laboratory of MICROFJ-30035-TSV SiPM from Onsemi with the Advatech preamplifier AMP-0611 (×10-×20 gain, ~0.7 ns rise time) at room temperature and U_{over}=5.4 V. 2 phe pulse with characteristic fast rise time and long decay time.

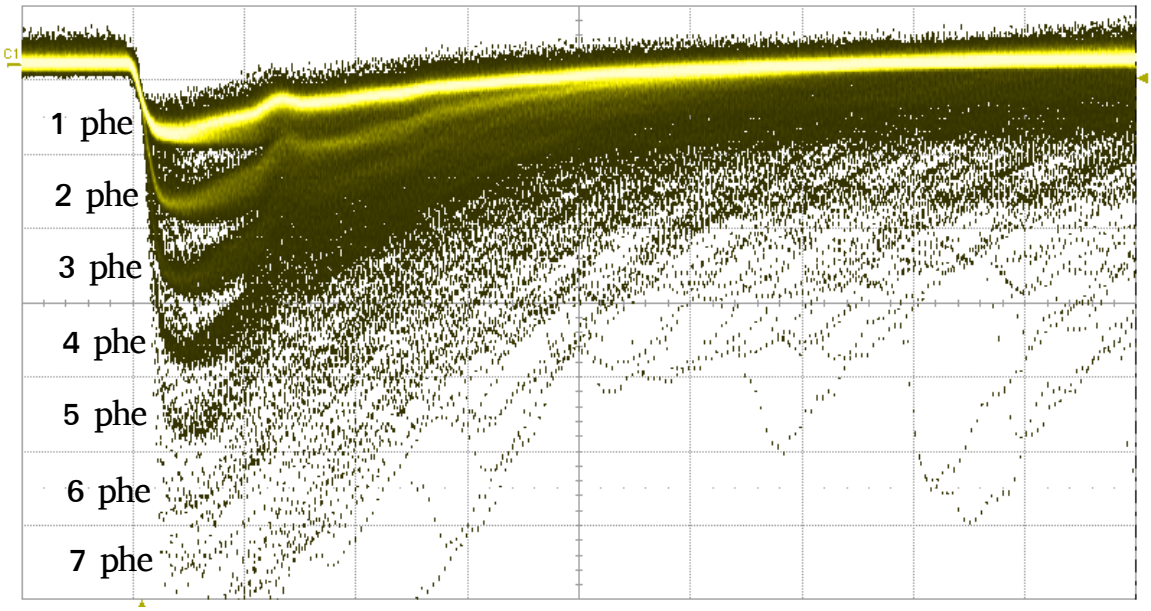

Figure 1.11.: SiPM pulses on oscilloscope of the MICROFJ-30035-TSV SiPM from Onsemi with the Advatech preamplifier AMP-0611 (×10-×20 gain, ~0.7 ns rise time) at room temperature with U_{over}=5.4 V.

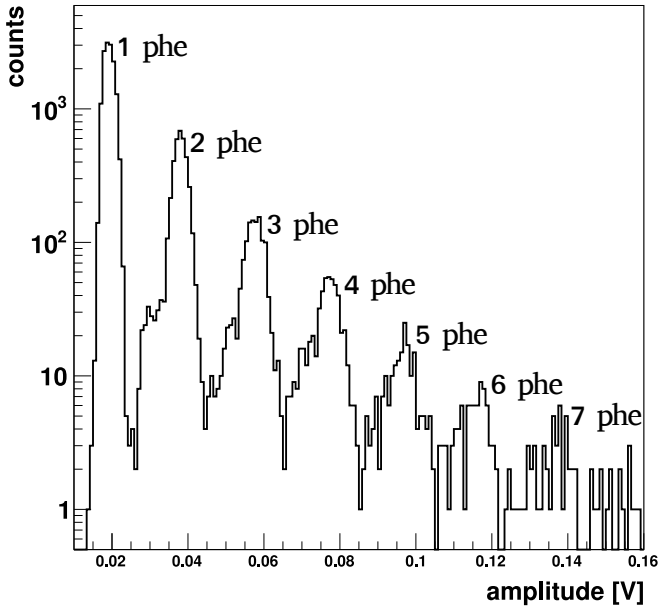

Figure 1.12.: Measurement from the laboratory of MICROFJ-30035-TSV SiPM from Onsemi with the Advatech preamplifier AMP-0611 (×10-×20 gain, ~0.7 ns rise time) at room temperature and U_{over}=5.4 V. Spectrum with clear quantization of the pulse amplitudes.

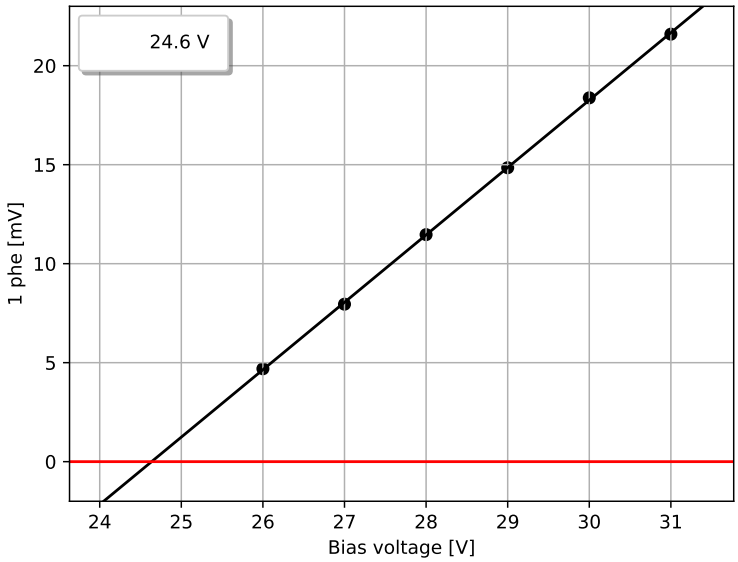

Figure 1.13.: Amplitude of the 1 phe pulse as a function of U_{bias} of a MICROFJ-30035-TSV SiPM from Onsemi with the Advatech preamplifier AMP-0611 (×10-×20 gain, ~0.7 ns rise time) at room temperature, measured in the laboratory. The intersection point of U_{bias} and zero amplitude corresponds to the U_{bd}.

The amplitude of the SiPM pulse is proportional to the number of fired microcells (see Figure 1.11) which would be proportional to the number of detected photons if the photons hit different SiPM cells and if we could neglect noise (see Section 1.2.3). In that case, SiPMs would be able to count the number of impinging photons [139]. In Figure 1.12 a histogram of the pulse amplitude is shown. The measurement was performed with the MICROFJ-30035-TSV SiPM from Onsemi at room temperature with U_{over}=5.4 V and with the Advatech preamplifier AMP-0611 (×10-×20 gain, ~0.7 ns rise time). The histogram demonstrates that the amplitude of the SiPM signal is quantized and SiPMs are sensitive to single photons.

1.2.2. Overvoltage, Gain and PDE

SiPMs operate above U_{bd}. In Figure 1.13 a laboratory measurement of the amplitude of the 1 phe pulse of the MICROFJ-30035-TSV SiPM from Onsemi as a function of U_{bias} at room temperature is presented. The amplitude is proportional to U_{bias}. The intersection point of the curve and zero amplitude corresponds to U_{bd}. The overvoltage can be defined as the difference between U_{bias} and U_{bd} [131]:

$$U_{\text{over}} = U_{\text{bias}} - U_{\text{bd}} \tag{1.7}$$

The gain G of a SiPM is the ratio between the charge of an electron and the output charge of a single-phe event [144], i.e. the number of electron-hole pairs generated in an avalanche. Typical values for G are $\sim 10^6$ and hence are comparable to the gain of most PMTs [139, 35]. The relation between G, the microcell capacitance and U_{bias} is described by

$$G = \frac{C_d \cdot U_{\text{bias}}}{e}, \tag{1.8}$$

with e the elementary charge. G is proportional to U_{bias} because the number of secondary particles generated in an avalanche depends linearly on the strength of the electric field.
An important characterization parameter of a SiPM is its PDE. It is the probability that an incident photon creates a primary electron-hole pair in the active part of the microcell and triggers an avalanche, i.e gives an output pulse. The PDE is a function of the wavelength of the incident light and U_{over} (see Figure 1.14) [139]:

$$\text{PDE}(U_{\text{over}}; \lambda) = \text{QE}(\lambda) \times P_T(U_{\text{over}}, \lambda) \times \text{FF}. \tag{1.9}$$

QE is the quantum efficiency. It depends on the probability of a photon to cross the antireflective coating (ARC) at the entrance of the microcell and the probability of the photon to create an electron-hole pair that reaches the high-field region of the diode [139]. P_T is the avalanche triggering probability and FF is the SiPM cell fill factor. The fill factor is the ratio between the active area to the total area of the microcell. The inactive regions of a microcell are occupied by the quenching resistor,

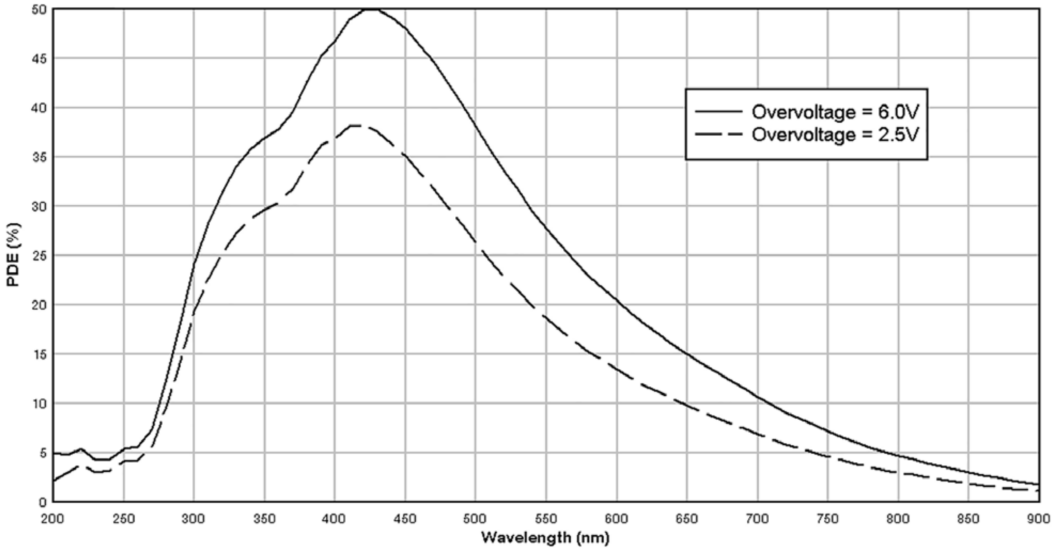

Figure 1.14.: PDE for MICROFJ-30035-TSV SiPM from Onsemi for U_{over}=2.5 V and 6.0 V. According to the manufacturer [147].

the guard ring which increases the electric field at the borders of the diode and the isolation structure that separates the microcells in the SiPM electrically and optically. Such an isolation structure can be for example a p-stop, a narrow p-layer between the microcells or a trench isolation using a surrounding dielectric layer [139].

1.2.3. SiPM noise

Uncorrelated noise

Uncorrelated noise originates from electron-hole pairs that are not created by an absorbed photon but due to thermal generation or by tunneling in the depleted region [119]. This noise can be compared to the dark current of a PMT. The electron of an uncorrelated noise event is accelerated and triggers an avalanche. The resulting signal cannot be distinguished from the one generated by a photon. These events are called dark counts. The occurrence of these events is typically known as the dark count rate (DCR). The generation, collection and triggering of dark counts are independent of each other. Therefore the number of dark counts in a fixed time interval follows a Poisson distribution. The probability density function of the arrival time between two dark counts f(t) is described by

$$f(t) = \chi \exp(-\chi t). \tag{1.10}$$

Here the DCR is expressed with χ. Dark counts are the main source of noise in SiPMs [119]. The DCR increases with U_{over} since the probability to trigger an avalanche is higher in presence of a stronger electric field. In addition, the DCR increases with the SiPM size.

Correlated noise

Correlated noise instead is an avalanche event that was triggered by a previous avalanche. Examples of correlated noise are optical crosstalk and afterpulsing [139].
In an avalanche process, a large number of electrons and holes is passing across the depleted region. During this drift, photons are emitted isotropically by hot carriers moving through the high-field region. These photons can be absorbed in a neighboring microcell and generate an electron-hole pair that triggers another avalanche. This effect is called optical crosstalk (CT).

An important parameter regarding CT is the time between the primary event and the triggered CT event. If this time is short (in orders of tens of ps [139]), we talk about prompt CT (pCT). An example of the path of a pCT event is shown in the left panel of Figure 1.15. In this scenario, the CT photon is absorbed in the active part of the neighboring microcell. With a standard electronic readout it is not possible to distinguish between both events (the primary and the CT event) and it would be

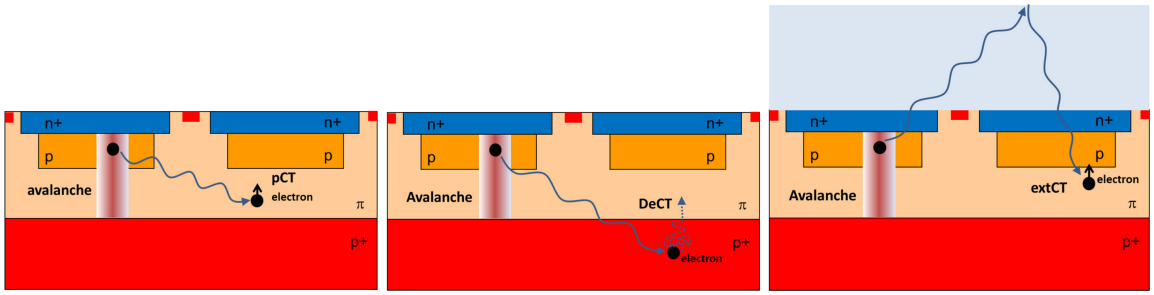

Figure 1.15.: Sketch of different types of crosstalk. Image from [139]: **Left**: prompt Crosstalk (pCT). A CT photon moves to the neighboring cell is absorbed and an avalanche is triggered. **Center**: delayed Crosstalk (DeCT). A CT photon moves to the inactive part of a neighboring cell and generates an electron-hole pair. The electron travels due to diffusion to the active part. **Right**: external Crosstalk (ExtCT). A CT photon leaves the microcell on the front and is reflected back to a neighboring cell. There it is detected.

observed as two microcells that fired at the same time. An effective method to reduce pCT is the introduction of deep trenches around each GM-APD to separate it from neighboring microcells [119].
Figure 1.16 shows the curve of the DCR as a function of the trigger threshold of the pulse amplitude. The measurement was done in a dark box with the MICROFJ-30035-TSV SiPM from Onsemi. We can assume that no light was impinging the SiPM and the observed pulses stem from thermal electron-hole-pairs. The resulting curve has a step-like shape due to the quantized pulse amplitude of the SiPM. The first step of the curve corresponds to 1 phe events, the next step to 2 phe events. These events consist mainly of a dark count that triggered a CT event in the neighboring cell.

CT photons can also be absorbed in the undepleted part of a neighboring GM-APD. It generates an electron-hole-pair that can reach the depleted region due to diffusion. After entering the depleted region, the electron moves to the high-field part and can trigger an avalanche. This effect is called Delayed Crosstalk (DeCT) and a possible path for a DeCT event is demonstrated in the center panel of Figure 1.15: a CT photon moves to the inactive part of a neighboring cell and generates an electron. The electron travels due to diffusion to the active part of the cell. The time interval between the primary event and the DeCT event is typically long enough so that both signals can be distinguished.

Another way to trigger an avalanche for CT photons is External Optical Crosstalk (ExtCT), shown in the right panel of Figure 1.15: a CT photon leaves the microcell on the front and is reflected back to a neighboring cell due to a change of the refractive index in the material (for example at the Anti-reflective coating of the GM-APD entrance window). In the neighboring cell it can be absorbed, generate an electron-hole

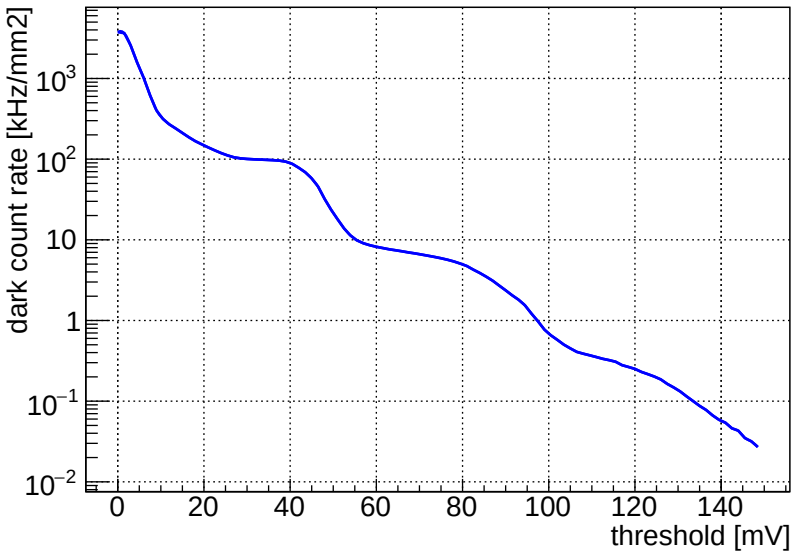

Figure 1.16.: Dark Count Rate of the MICROFJ-30035-TSV SiPM from Onsemi at room temperature with U_{over}=3.3 V. The measurement from the laboratory.

pair and trigger an avalanche.

During an avalanche many electron-hole pairs are generated in the high-field region of the diode. Some of them can be captured by trapping centers caused by defects in the high-field region. When they are re-emitted after some time, they can trigger an avalanche. This process is called afterpulsing (AP). To reduce this type of noise one has to reduce impurities or defects in the silicon lattice (and thus the number of trapping centers).
Similar to DeCT there is a phenomenon called optically induced afterpulsing (OAP). Here the electron-hole pair is trapped outside the high-field region but can reach the active part of the microcell due to diffusion and trigger an avalanche.

1.2.4. Temperature dependence

Most SiPM parameters show a temperature dependence. The breakdown voltage increases with temperature [133]. As a consequence, parameters depending on U_{over} as the gain, the PDE and the CT would become smaller for higher temperatures if U_{bias} stays constant (see Figure 1.17). If the U_{bias} is adjusted, the temperature dependence of e.g. the gain is eliminated [137].

However, the DCR depends on the temperature T despite a constant U_{over} [139]:

$$\text{DCR}(T) \sim \exp -\frac{E_a}{kT} \tag{1.11}$$

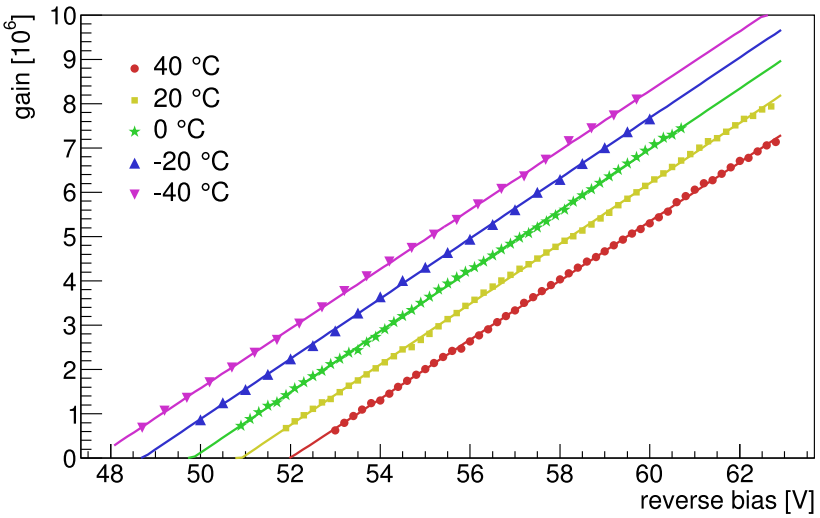

Figure 1.17.: Temperature dependence of Hamamatsu S13360-3050CS SiPM gain as a function of U_{bias}. Plot from [133].

E_a is here the activation energy of the generation process of the noise event. Since dark counts are the main source of noise, a cooling mechanism can reduce the noise significantly.

1.2.5. Single photon time resolution

The timing performance of a SiPM is typically characterized by the single photon time resolution (SPTR) which can be defined as the full width at half maximum (FWHM) of the arrival time distribution of 1 phe pulses. In Figure 1.18 the SPTR is shown for several SiPMs with different sizes and microcell pitches. The SPTR decreases with increasing U_{bias} before it saturates and is typically higher in SiPMs with larger microcells [74].

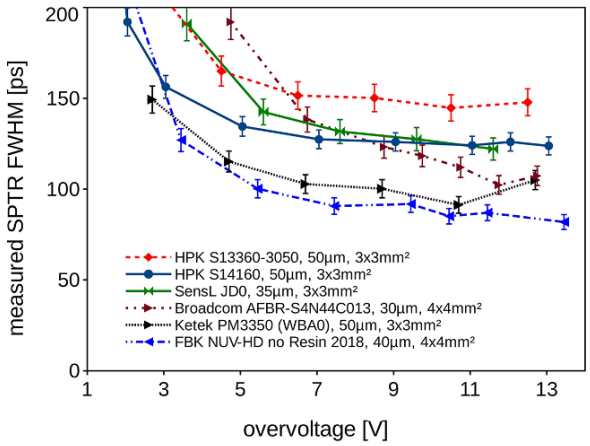

Figure 1.18.: SPTR of SiPMs with different sizes and microcell pitch as a function of U_{over}. Plot from [74].

1.3. PMTs vs. SiPMs

Compared to PMTs SiPM feature several advantages. They provide a higher PDE and are insensitive to magnetic fields. In addition, SiPMs do not show significant aging when exposed to bright light and their operation does not require high voltage. However, the use of SiPMs is limited because of their small size and the higher noise compared to PMTs due to DCR and optical crosstalk.

Table 1.1 compares typical parameters of PMTs and SiPMs. Since SiPMs require a much lower operational voltage, their associated power consumption is typically lower [149]. Whereas most of the PMTs feature a PDE of 25% to 35% [96], SiPMs can reach 60% [144]. Traditionally, PMTs tended to be more sensitive at lower wavelengths (UV to blue) [96] while SiPMs achieved their highest PDE at green and red wavelengths. This however changed in the last years, in particular thanks to the developments performed for reading the near-UV (NUV) to blue light emitted by Cherenkov radiators and scintillators [8]. The use of LIDAR systems in the automotive industry motivated also the development of SiPMs sensitive to near-infrared (NIR) light [8].
Both photodetectors provide a high gain, PMTs up to 10^7 [96] and SiPMs up to

	PMT	SiPM
required U_{bias}	500 V-2000V [101]	20-60 V [144]
PDE	$<$ 40 % at 350 nm [96]	~ 25-60 % (visible light) [144]
spectral range	~ 150-900 nm [96]	~ 300-900 nm [147, 56]
SPTR	650-7000 ps [96]	100 to a few hundred ps [74]
gain	up to 10^7 [96]	up to 10^6 [149]
temperature sensitivity	low	medium
dark current at 25 °C	$<$ 1 μA [96]	~ 2-10 μA [31, 130, 147] [a]
sensitive to ambient light	yes	no
sensitivity to magnetic fields	yes	no
single phe resolution	good	excellent
compactness	no	yes
pixel area	130 mm^2 - 130 cm^2 [96]	$<$ 36 mm^2 [71]

[a] ~ 2 μA for U_{over}=6.0 V for 3 × 3 mm^2 30035 J-Series SiPM from ON Semiconductor [147].

Table 1.1.: Comparison of PMT and SiPM propertiesproperties. Table adapted from [35].

10^6 [149]. The PMT gain shows a low temperature dependence of ~ -0.25 %/°C [1] [110]. The SiPM gain instead can change by ~ -1 %/°C (estimated from Figure 1.17 [133]). In addition, the temperature has a strong impact on the SiPM DCR (see Section 1.2.4). PMTs are damaged when exposed to bright light. The PMT PDE is lower in the presence of a magnetic field because the collection efficiency is reduced.
The multiplication of phes in a PMT happens step-wise by secondary emission of the dynodes. A small fluctuation of the secondary emission factor of the first dynode has a significant impact on the total gain. The excess noise factor indicates how much the single-phe resolution is reduced by fluctuations of the gain. PMTs have a high excess noise factor. SiPMs, instead, have a small excess noise factor because the charge amplification mechanism in Geiger mode does not show large avalanche fluctuations [149].

1.3.1. Limited area of SiPMs

Probably the main limitation of SiPMs is their small sensitive area. While PMTs can be produced with diameters of several centimeters, commercial SiPMs are hardly available in sizes larger than 6 × 6 mm^2. This size limitation of SiPMs is a strong drawback in experiments in which the incoming light is spread over a large area. In these applications the use of SiPMs would demand a significant increase in the number of readout channels, increasing the cost and complexity of the system.
To construct a larger SiPM, essentially a larger number of GM-APD (see Section 1.2) needs to be connected in parallel. The capacitance of a SiPM is the sum of the capacitance of each GM-APD. Thus, the SiPM capacitance increases significantly with the sensitive detector area. An increasing capacitance reduces the speed of the pixel response. This is particularly critical in applications in which fast timing and close to single-phe resolution are required. The idea of building a large SiPM pixel by directly connecting several SiPMs in parallel is problematic: the number of parallel connected GM-APDs would be much larger, causing an extreme increase in the total pixel capacitance [62]. In addition, also the DCR increases with the size.

This size limitation constrains the use of SiPMs in many applications that would benefit from their advantages like high PDE or fast time resolution. One of them, which will be introduced in the next chapter, is intensity interferometry.

[1] Hamamatsu R7400U PMT

2. Intensity Interferometery

2.1. Amplitude Interferometry

Nowadays amplitude interferometry is a widely used technique to study astronomical targets with high angular resolution [125]. A basic amplitude interferometer consists of two light collectors (telescopes) A and B, at positions $\vec{r_1}$ and $\vec{r_2}$, that detect light from a point source P1 (see 2.1). d is here the baseline, the distance between $\vec{r_1}$ and $\vec{r_2}$, and d_1 is the path difference of the photons detected by A and B. The angular resolution of the interferometer $\Delta\Theta$ can be expressed as

$$\Delta\Theta = \frac{\lambda}{2d}\text{rad}, \tag{2.1}$$

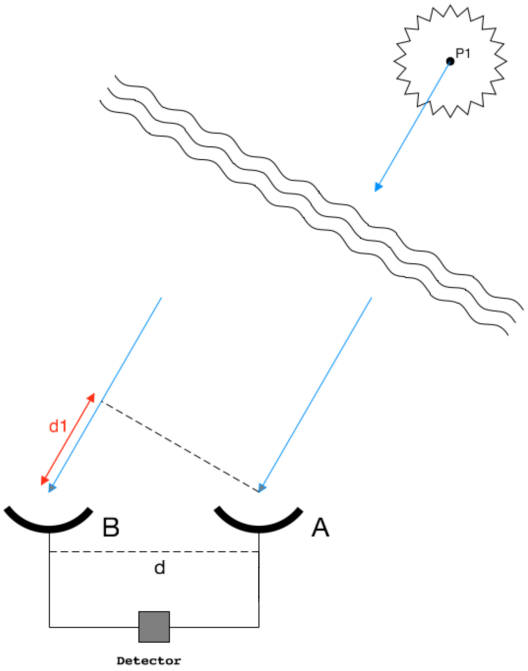

Figure 2.1.: Working principle of an amplitude interferometer. Two collectors A and B at positions $\vec{r_1}$ and $\vec{r_2}$ detect the photons of a point source P1. The distance between $\vec{r_1}$ and $\vec{r_2}$ is the baseline d. The path difference of light detected by A and B is d_1. Scheme from [58].

with λ the wavelength of the incoming light [115]. The light of each light collector has to be transmitted to a correlator using precise optics to preserve the coherence of the light.

A typical amplitude interferometer exploits the first order correlation function $g^{(1)}$, the correlation between electromagnetic fields at two different locations $\vec{r}_1$, $\vec{r}_2$ and two different times t_1, t_2. The first order correlation function is defined as

$$g^{(1)}(\vec{r}_1, t_1, \vec{r}_2, t_2) = \frac{\langle E^*(\vec{r}_1, t_1) E(\vec{r}_2, t_2)\rangle}{\left[\langle |E(\vec{r}_1, t_1)|^2\rangle \langle |E(\vec{r}_2, t_2)|^2\rangle\right]^{1/2}}, \tag{2.2}$$

for a time average that is long compared to the period of the oscillation of the electric field E [58]. For coherent light $|g^{(1)}| = 1$ and for incoherent light $|g^{(1)}| = 0$. An important parameter of interferometry observations is the spatial visibility function V_M which corresponds to the fringe contrast of an interference pattern in a Michelson interferometer [58]:

$$V_M = |g^{(1)}(\vec{r}_1, t_1, \vec{r}_2, t_2)|. \tag{2.3}$$

Amplitude interferometry of astronomical targets takes advantage of the first-order spatial coherence of light (condition $\vec{r}_1 \neq \vec{r}_2$ and $t_1 = t_2$), the 'statistical average of single point sources' ([58], p. 1720). According to the Van Cittert-Zernike theorem, the complex spatial visibility function V (equivalent to the normalized correlation function) is proportional to the Fourier transform $\mathcal{F}$ of the angular distribution of the sky brightness I [49, 87],

$$V(u, v) = \iint I(l, m) \exp(-2\pi i(ul + vm) dl\, dm = \mathcal{F}(I(l, m)). \tag{2.4}$$

The (u,v)-plane is perpendicular to the observation line and (l,m) is the position of the source in the (u,v)-plane.

It is clear from Equation 2.1 that for smaller wavelengths, for example in the optical domain, large baselines are needed to achieve a good angular resolution. In addition, good weather conditions are required because atmospheric turbulences can alter the incoming plane light wave. For very long baselines (few hundred meters) optical interferometry is still challenging [143].
In spite of these drawbacks, amplitude interferometry is still the most popular astronomical interferometry technique for visible light. A different technique, intensity interferometry needs less accuracy in optics and has therefore a huge potential for inferometry in the optical domain, especially at longer baselines.

2.2. Intensity Interferometry

The intensity interferometry technique was developed by Hanbury Brown and Richard Twiss in the 1950s. It was initially proposed for radio astronomy [80] and later also in the optical band [85]. Several experiments were performed to demonstrate the feasibility of this technique in the optical domain. In 1955 they performed laboratory experiments to measure the correlation of the light of an artificial star made of a high-pressure mercury arc focused to a pinhole. The fact that the arrival time of photons between two coherent beams of light was correlated was a prove for the so called Hanbury-Brown-Twiss effect [82]. This effect is also called *photon bunching* and states that photons from a thermal source which are detected at the level of single particles, arrive in bunches, i.e. there is a correlation in their arrival time [150].

2.2.1. Working principle of an Intensity Interferometer

In Figure 2.2 the principle of an intensity interferometer is illustrated: P_1 and P_2 are two points in a star emitting radiation. Their emission is independent from each other and from any other point on the surface of the star and can be represented as the superposition of sinusoidal components. The amplitude and the phase of each component is random compared to the other components. The light is detected by telescopes A and B and then goes through an interference filter. For simplicity we assume a superposition of only two components. One component reaches telescope A from P_1 and the other one reaches telescope B from P_2 [58, 85].

$$C_1 = E_1 \sin(\omega_1 t + \theta_1) \tag{2.5}$$
$$C_2 = E_2 \sin(\omega_2 t + \theta_2) \tag{2.6}$$

The output current of each telescope is proportional to the intensity of the light. Assuming linear polarisation, the intensity of the light can be written as

$$I_A = K_A[E_1 \sin(\omega_1 t + \theta_1) + E_2 \sin(\omega_2 t + \theta_2)]^2 \tag{2.7}$$
$$I_B = K_B[E_1 \sin(\omega_1 (t + d_1/c) + \theta_1) + E_2 \sin(\omega_2 (t + d_2/c) + \theta_2)]^2. \tag{2.8}$$

K_A and K_B are constants of the detector and d_1 and d_2 are the path differences of the incoming light. If Equation 2.7 and 1.8 are expanded, only the last term is of interest (the other terms are rejected by the interference filter in the interferometer).

$$I_A = K_A E_1 E_2 \cos[(\omega_1 - \omega_2)t + (\theta_1 - \theta_2)] \tag{2.9}$$
$$I_A = K_B E_1 E_2 \cos[(\omega_1 - \omega_2)t + (\theta_1 - \theta_2) + (\omega_1 d_1 - \omega_2 d_2)/c)] \tag{2.10}$$

The two components are correlated because they have the same beat frequency, which is defined as the difference in frequency between to interfering waves $(\omega_1 - \omega_2)$ [136].

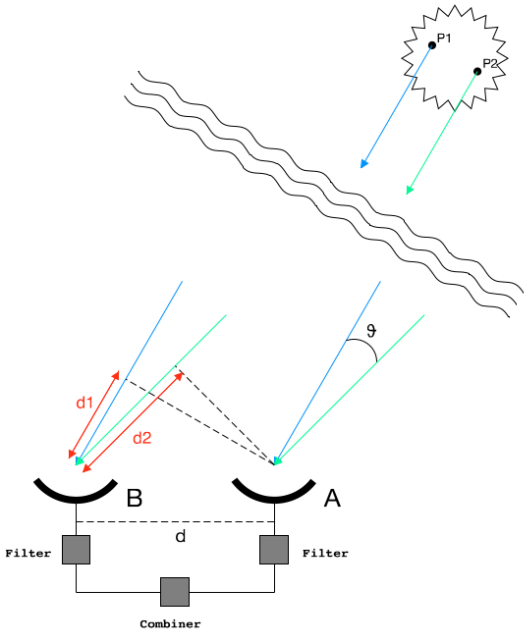

Figure 2.2.: Working principle of an intensity interferometer. Two light collectors A and B at positions $\vec{r_1}$ and $\vec{r_2}$ with interference filters measure the light of the point sources P1 and P2. The distance between $\vec{r_1}$ and $\vec{r_2}$ is the baseline d. d_1 and d_2 are the path differences of the incoming light. Scheme from [58].

$(\omega_1 d_1 - \omega_2 d_2)/c$ is the difference of the relative phases of the Fourier components. If we assume $\omega_1 \approx \omega_2$, the contrast $c(d)$ (the product of I_A and I_B) for a given baseline d is:

$$c(d) = K_A K_B E_1^2 E_2^2 \cos\Big[\frac{\omega}{c}(d_1 - d_2)\Big]. \tag{2.11}$$

θ is the angular distance of the points P_1 and P_2 on the surface of the star. Because θ is small ($\sin(\theta) \approx \theta$) and the baseline is $d = d_1 - d_2$, Equation 2.11 can be re-written as

$$c(d) = K_A K_B E_1^2 E_2^2 \cos[2\pi d\theta/\lambda], \tag{2.12}$$

where λ is the wavelength of the light. If Equation 2.12 is integrated over all pairs of point sources on a star, the result is

$$\frac{c(d)}{c(0)} = \frac{\langle \Delta I_1 \Delta I_2 \rangle}{\langle I_1 \rangle \langle I_2 \rangle} = |V(d)|^2. \tag{2.13}$$

The correlation is proportional to the square of the modulus of the complex degree of coherence of the light of two detectors, i.e. to the square of the visibility function V. $\Delta i_1(t)$ and $\Delta i_2(t)$ are the fluctuations of the currents of the telescopes [85]. The

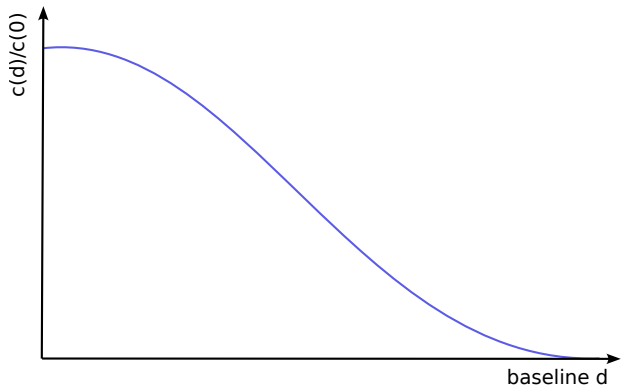

Figure 2.3.: $c(d)/c(0)$ as a function of the baseline d.

contrast $c(0)$ at d=0, also called zero-baseline correlation (ZBC), is used for calibrating the setup and should be constant.

We assume that a star can be described by a circular disk with an uniform surface brightness and a diameter θ. Under this assumption V can be described with a Bessel function of first order J_1 [85]:

$$|V| = 2\frac{J_1(\pi d\theta/\lambda)}{\pi d\theta/\lambda} \tag{2.14}$$

As can be seen in Figure 2.3, $c(d)/c(0)$ decreases as the baseline increases. The curve can be fitted using the visibility function in Equation 2.14, from which it is possible to estimate the star diameter. The first zero of the visibility function in Equation 2.14 is given by

$$d = 1.22\lambda/\theta. \tag{2.15}$$

In contrast to amplitude interferometry, the phase of light does not needed to be preserved with a two-telescope-based intensity interferometer since the square of the modulus of the complex part of the coherence is considered. Due to this property, an intensity interferometer requires much less precision from the optics than an amplitude interferometer. The path difference needs to be small compared to the highest beat frequency of the light. If the frequency is restricted to 100 MHz, a precision of 30 cm on the path difference would be sufficient. Since path differences due to atmospheric turbulences are usually much smaller than the beat frequency of the light, intensity interferometry is less sensitive to atmospheric conditions [85].

2.2.2. Theory of Intensity Interferometry

In contrast to amplitude interferometry, intensity interferometry assess the 'statistical average of the correlation between pairs of point sources' ([58], p. 1720). Each pair

of point sources is independent. An intensity interferometer does not measure the interference of light from a classical point of view, but the correlation of electrical fluctuations (i.e. intensity fluctuations). The term intensity *interferometry* can be a bit misleading [49]. The main component of these intensity fluctuations is classical shot noise which does not feature any correlation between two detectors. Besides, there is another component, the wave noise, which is defined as the beating between the Fourier components of the detected light. The wave noise between two telescopes is correlated as long as the light is coherent [99]. The correlation is a function of the phase difference between low frequency beats in both detectors and not of the phase difference between two light waves as in amplitude interferometry. If two light collectors (telescopes) are sufficiently close to each other and measure simultaneously intensity fluctuations from a star, a correlation in the signal of both light collectors can be observed. If the telescopes move apart, the strength of this correlation decreases. The correlation signal is a measurement of the second-order spatial coherence and contains information about the spatial properties of a star [49]. Intensity interferometry is hence a technique that exploits the second order correlation function $g^{(2)}$

$$g^{(2)}(\tau) = \frac{\langle E^*(t)E^*(t+\tau)E(t)E(t+\tau)\rangle}{\langle E^*(t)E(t)\rangle}, \tag{2.16}$$

with τ the time delay originating from the different path lengths of the position $\vec{r_1}$ and $\vec{r_2}$ of the two telescopes to the place where the signal is collected.
The intensity I measured by a telescope is the amplitude of the electric field E times its complex conjugate.

$$\langle I(t)\rangle = \langle E(t)E^*(t)\rangle \tag{2.17}$$

For non-coherent light (i.e. a thermal light source like a star), the cross terms cancel, because the relative phases are random [58], and Equation 2.16 can be written as

$$g^{(2)}(\tau) = \frac{\langle E^*(t)E(t)E^*(t+\tau)E(t+\tau)\rangle}{\bar{I}^2} = \frac{\langle \bar{I}(t)\bar{I}(t+\tau)\rangle}{\bar{I}^2} \tag{2.18}$$

Following [102], $g^{(2)}$ can be re-written as a function of $g^{(1)}$ for N independent radiative atoms (i.e. a randomly polarised light source) and for a detector with an electronic bandwidth Δf that is much smaller than the optical bandwidth $\Delta\nu$ [6]:

$$g^{(2)}(\tau) = 1 + \frac{\Delta f}{\Delta\nu}|g^{(1)}(\tau)|^2 \qquad \text{for } n \gg 1 \tag{2.19}$$

Using Equation 2.3 we can define the normalised contrast c as a function of the complex visibility V, the Fourier transform of the source brightness distribution [85].

$$c = g^{(2)} - 1 = \frac{\Delta f}{\Delta\nu}|V|^2 \tag{2.20}$$

2.2.3. Narrabri Stellar Telescope

In the winter of 1955/1956 a first prototype of an optical intensity interferometer was tested with the objective of measuring the angular diameter of Sirius. They managed to measure a diameter of (6.8 ± 0.5) milliarcseconds (~ 6.3 milliarcseconds were expected from theoretical predictions) [81]. After these successful tests the first optical intensity interferometer was built: the Narrabri Stellar Telescope, in Narrabri, Australia. In 1965 the interferometer started its main operation. It consisted of two light collectors mounted on trucks that could move on a railway track of a diameter of 188 m (see the left panel of Figure 2.4). Baselines between 10 to 188 m were possible. The trucks were connected via cable to the main building to transport the signal. When no observation was taking place, the trucks and the light collectors could be stored in a garage. The light collectors had the shape of a 12-sided polygon with a diameter

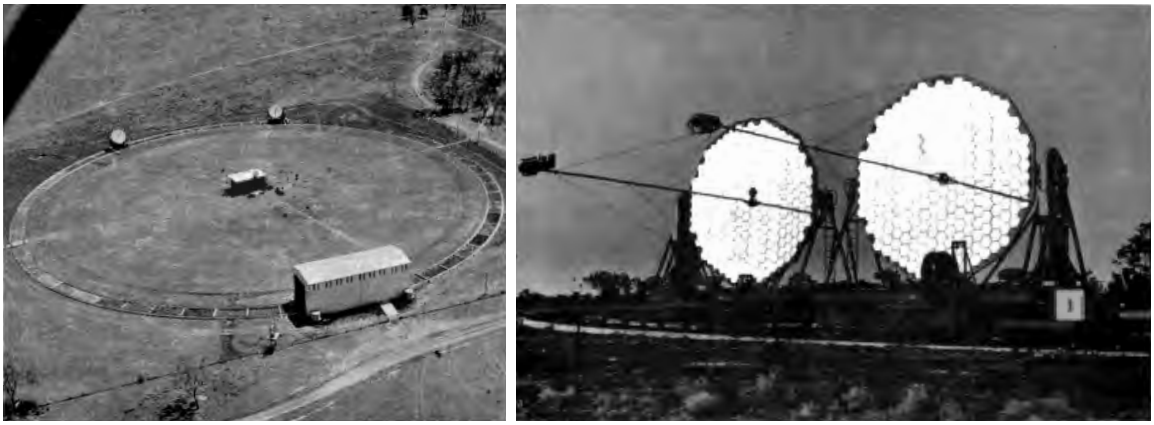

Figure 2.4.: **Left**: top-view of the Narrabri Stellar Telescope with railway track. **Right**: light collectors of the Narrabri Stellar Telescope. Pictures from [85]

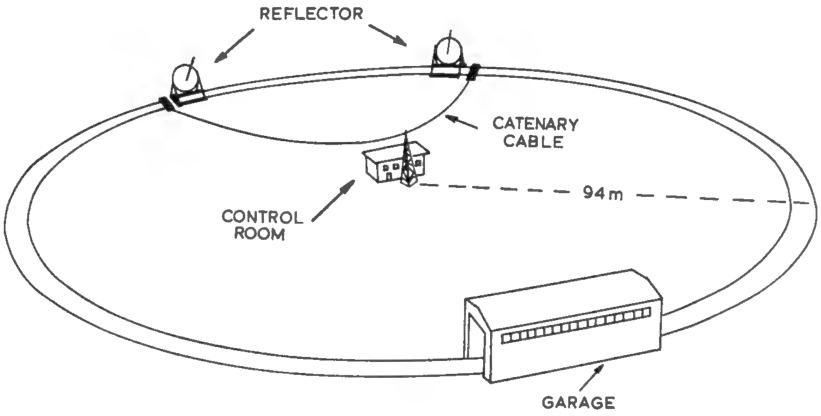

Figure 2.5.: Scheme showing the experimental setup of the Narrabri Stellar Telescope. The light collectors could be moved on a railway track and parked in a garage. The signal was transported to a control room. Scheme from [85].

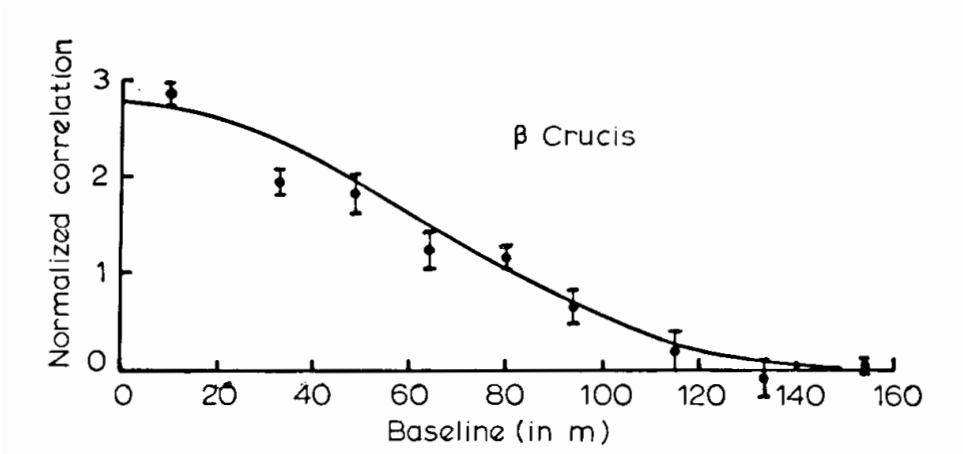

Figure 2.6.: Visibility plot of β Crucis measured with the Narrabri Stellar Telescope in 1965. Plot from [83]

of ~ 6.5 m (reflecting area ~ 30 m^2). Each collector consisted of 252 hexagonal glass mirrors and had a focal length of 11 m (see the right panel of Figure 2.4). The light was reflected from the collector surface and collimated at the focus of each telescope. Then it passed through an interference filter with a central wavelength of 443 nm. The light was measured with PMTs with a PDE of ~ 25% at 440 nm. The effective bandwidth was of 60 MHz. The signals were transported to a control room (see Figure 2.5) where the correlation was performed. The interferometer was able to measure successfully the diameter of 32 stars with an apparent magnitude < +2.5 mas [85]. They also performed new measurements of the diameter of Sirius, which was found to be of (5.60 ± 0.15) milliarcseconds [84]. Figure 2.6 shows the measured visibility (normalized correlation) as a function of the baseline for the star β Crucis (1965) [83].

Notwithstanding the success of the Narrabri Stellar Telescope and that there were plans for a future larger interferometer, the technique was abandoned. The main limitation was the low sensitivity of intensity interferometry, coming from the fact that it is a second-order effect [58]. At the same time, amplitude interferometry kept gaining popularity due to the progress in optics and photodetection [99].
Even if intensity interferometry was not longer used in optical astronomy for decades, the principle of measuring the correlation of intensity fluctuations was applied in other fields like in high-energy particle physics [24].

2.3. Cherenkov Telescopes as Intensity Interferometers

The Narrabri Stellar Telescope was not only used as an interferometer, but also to search for very high energy gamma-rays of energy > 300 Gev [68] in 1970s, the early days of ground-based gamma-ray astronomy. The measurements exploited the Imaging Atmospheric Cherenkov Technique. When a gamma-ray enters the atmosphere, it interacts with atmospheric molecules and produces an avalanche of secondary electrons and positrons, forming an electromagnetic shower (see Figure 2.7). The secondary particles move with a velocity faster than the speed of light in the atmosphere, causing the radiation of Cherenkov light. The Cherenkov light is emitted in a cone around the radiating secondary particle, in an altitude of around 10-20 km above sea level. It is spread in a large circle on the ground (typical diameter ~ 250 m). The arriving signal is usually weak, typical Cherenkov light flashes have a density of a few up to several hundred photons per square-meter on nanosecond time scales [52]. Therefore huge light collectors are required to detect the Cherenkov light, and very fast and sensitive photodetectors, that are able to detect single photons with high efficiency [13, 106]. These telescopes are called Imaging Atmospheric Cherenkov Telescopes (IACTs).

The most sensitive IACT arrays that are operative today are VERITAS [91], HESS [14] and MAGIC [17]. Even if initially conceived for observing (indirectly) gamma rays, some of the characteristics of IACTs can potentially turn them into powerful instruments for optical intensity interferometry. The main advantage of the mentionend IACT

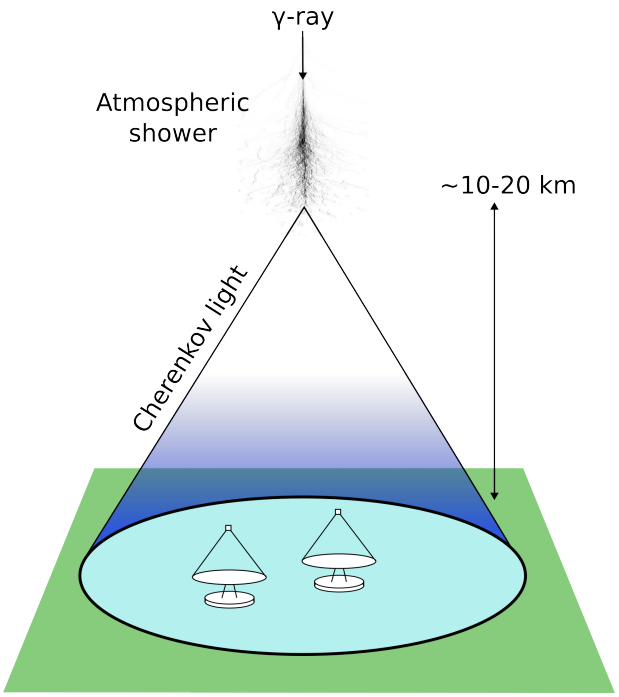

Figure 2.7.: Scheme of Cherenkov light cone observed with the MAGIC telescopes. Image of gamma-ray from [27].

arrays is their large light collection area (> 100 m^2) [99]. They feature fast acquisition chains (~ 1 ns) and for IACT arrays with more than two telescopes it is possible to take measurements at several baselines simultaneously [43, 99]. Intensity interferometry observations with IACTs can be performed during the nights around Full Moon, when the demand for observation time of standard gamma-ray sources is much lower [15]. In the following subsections the implementation of an intensity interferometer with an IACT array is discussed in detail.

2.3.1. Noise limitations

The light of a star detected with an interferometer is affected by the night sky background (NSB). The main contributors to the NSB (in a clear moonless night) are zodiacal light and airglow, an emission from atoms and molecules at high altitudes due to the excitation by UV-radiation [26]. The NSB degrades the sensitivity, since it essentially introduces more uncorrelated photons. The NSB determines a limit to the magnitude of stars that could be measured theoretically with the available receiver optics. The starlight needs to be brighter than NSB for a successful detection. For a typical point-spread function of 0.05° (~ 6×10^{-7} sr) as it is provided by VERITAS, HESS or MAGIC, the dimmest star that could be measured is of 9.6 magnitude [99]. The limit in magnitude decreases significantly under moonlight. This needs to be considered since interferometry observations would usually take place around Full Moon.

2.3.2. Baselines

The Narrabri Stellar Telescope featured moveable telescopes with which it was possible to track a star at a fixed baseline during the whole night. IACT arrays however consist of telescopes at fixed positions. Programmable delays have to be introduced to keep the signals in time. The effective baseline of the telescopes changes during the night as a consequence of the Earth rotation. This can be useful, as it means that the same source can be observed over a continuous range of baselines during the same night. The distance between telescopes in an IACT array is optimized to detect the large Cherenkov light pool of an air shower. Thus, it is very hard to study the correlation at baselines close to zero [99].

2.3.3. Optical design of Cherenkov Telescope Reflectors

IACTs are designed optimize the angular resolution for Cherenkov light detection over the widest possible field of view (FOV), i.e. the ratio of the focal length to the aperture is between unity and 2 [34]. To reduce the image quality degradation away from the optical axis, in the Davies-Cotton design the primary reflector forms a spherical structure which is centred on the focal point [47, 49]. The Davies-Cotton design is used by HESS and VERITAS and provides smaller aberrations away from the optical axis compared to the parabolic design used by MAGIC. However, reflectors

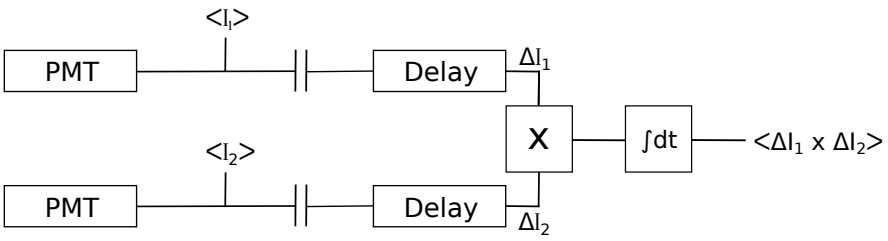

Figure 2.8.: Scheme of the photodetection and readout of an IACT with two light collectors as intensity interferometer. The PMTs in the camera measure the intensity fluctuations of the star light ΔI_1 and ΔI_2. The signal is transported with a time delay to the correlator which multiplies ΔI_1 and ΔI_2 and integrates the product over time. In addition, the DC component $\langle I_1 \rangle$ and $\langle I_2 \rangle$ of the signal needs to be measured. Adapted from [99].

with the Davies-Cotton design exhibit a broadening of the arrival time distribution which acts like a filter removing the fastest intensity fluctuations [49]. This leads to a bandwidth limitation. In case of a 12 m telescope with aperture close to unity, the limitation is 100 MHz [99]. As a consequence it is not possible to reach a much higher sensitivity, i.e. a better time resolution compared to the Narrabri Stellar Telescope (which had a bandwidth of 60 MHz). The parabolic reflector of MAGIC instead does not produce such time dispersion. Hence it is in principal possible to operate with at higher bandwidths [99].

2.3.4. Photodetection

VERITAS, HESS and MAGIC are equipped with a camera of PMTs capable of detecting faint Cherenkov light pulses. In principle for intensity interferometry only one pixel per telescope is required. The starlight is focused by the reflector to a single pixel. To prevent any damage by bright starlight, the photon flux needs to be reduced with an interference filter in front of the PMT. This can be done because the signal-to-noise ratio in intensity interferometry is independent of the optical passband [49]. The reduced photon flux in a narrow spectral segment is compensated by an increase in the temporal coherence. In Figure 2.8 a scheme of the photodetection and the readout of an IACT with two light collectors as intensity interferometer is shown. The PMTs in the pixels measure the intensity fluctuations ΔI_1 and ΔI_2 of the star light, i.e. they are coupled to the Alternating Current (AC coupled).
Since the time of the Narrabri Stellar Telescope there have been significant advances in photodetection. Modern PMTs provide higher bandwidth and quantum efficiency. There are even PMTs with a peak quantum efficiency of ~ 50 % [99], which is twice the quantum efficiency of the PMTs used in the Narrabri Stellar Telescopes [99].

2.3.5. Cable Bandwidth and correlator

The analog signal needs to be transported to a central location with a time delay to correct for the fixed position of the light collectors (see Figure 2.8). The analog signal transmission bandwidth can limit the sensitivity of the instrument. A possible solution is to use analog optical fiber transmission, which has already been implemented in MAGIC for the gamma-ray observations. This way it is possible to achieve a larger dynamic range without compromising the sensitivity of the instrument.
In the correlator the signals ΔI_1 and ΔI_2 are multiplied. The product is integrated over time and divided by the Direct Current (DC) components $\langle I_1 \rangle$ and $\langle I_2 \rangle$. The result is the square of the visibility function, a measurement of the degree of coherence of the light detected by the PMTs (see Equation 2.13). At the time of the Narrabri Stellar Telescopes an analog correlator multiplied the photocurrent from the PMTs. Nowadays Field Programmable Gate Arrays (FPGA) allow to program electronic units in high-speed correlators with a time resolution of a few ns or better [49].

2.4. The MAGIC telescopes as an Intensity Interferometer

MAGIC (Major Atmospheric Gamma-ray Imaging Cherenkov) is a system of two IACTs located at the Roque de los Muchachos Observatory (Observatoro del Roque de los Muchachos, ORM) in the Canary Island of La Palma, Spain [17] at an altitude of ~ 2200 m above sea level. A picture of MAGIC can be seen in Figure 2.9. MAGIC uses the Imaging Atmospheric Cherenkov Technique to detect gamma rays. MAGIC observes very high energy (VHE) gamma-ray sources (> 50 GeV) like supernova remnants, pulsars or active galactic nuclei. The telescopes are also employed for dark matter searches and observing transient events like gamma-ray bursts.

The first telescope, MAGIC-I, started its operation in 2004 and the second telescope, MAGIC-II, five years later in 2009. Besides a few technical differences, the telescopes are almost identical. The position of MAGIC-I and MAGIC-II with respect to the control building is shown in Figure 2.10. The distance between the two telescopes is ~ 86 m.
The structure of the telescopes, made of reinforced carbon fiber tubes, contains the drive system that moves the reflector and the camera. Sources can be tracked with an accuracy of 0.02° [70]. The telescopes feature a 17 m diameter parabolic reflector with a total reflective mirror surface of ~ 236 m^2 per telescope. Due to the parabolic shape of the reflector, the time spread of synchronous light signals is insignificant with

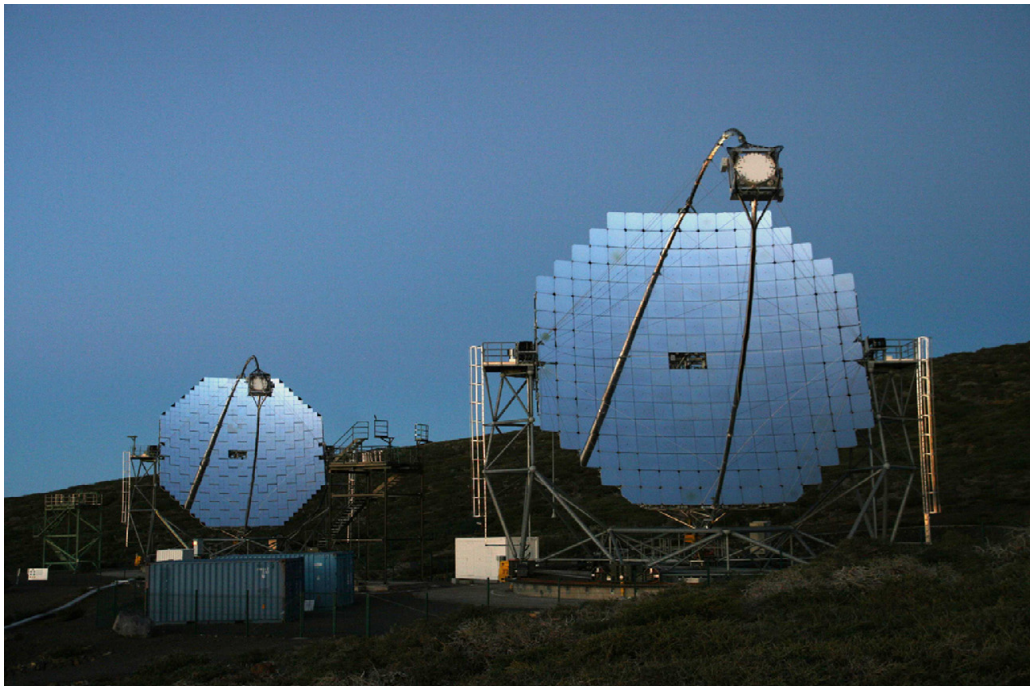

Figure 2.9.: The MAGIC telescopes on La Palma. Image from [17].

respect to the time spread of Cherenkov pulses, which is of 1-2 ns [16]. Each telescope is equipped with a 3.5° diameter camera with PMTs as individual pixels. The camera can be deployed with a spectralon target, also called *T-Point lid*, a diffuse plate that is used during the calibration of the focusing system. In this procedure a bright star is focused and projected on the deployed T-Point lid of the camera. The PMT signals are calibrated with a calibration box, a system using a passively Q-switched Nd:YAG laser that is mounted in the middle of the reflector dish. The calibration box produces very short light pulses (calibration pulses) which are shed on the camera of the telescopes. The calibration pulses have a FWHM of ~ 1 ns [17]. The resulting PMT pulses have an average width of ~ 2.5 ns [161].
The electric pulses from the PMT output are converted to optical signals with the use of vertical cavity surface emitting laser diodes (VCSELS) and are transported via optical fibers to the control building where the readout, trigger and data acquisition system are located (see Figure 2.10). The optical signals arrive in the receiver board and are split into a trigger branch and a readout branch. When the trigger conditions are fulfilled, the signal of each pixel is recorded and stored [16]. The images obtained from both telescopes are cleaned and then parametrized. After processing the images it is possible to estimate the energy and the incident direction of the gamma-ray that started the shower [13, 106, 70]. Details about the MAGIC data taking and analysis are found in [16].
MAGIC achieves its best performance under dark conditions, in the absence of moonlight or twilight. When the Moon is present the energy threshold increases. Besides, if the moonlight level is relatively strong, it may damage the PMTs. As a result, MAGIC standard observations are typically stopped in the 3-5 nights around Full Moon. The Full Moon break is the ideal time to use MAGIC for intensity interferometry without interfering with its gamma-ray observations.

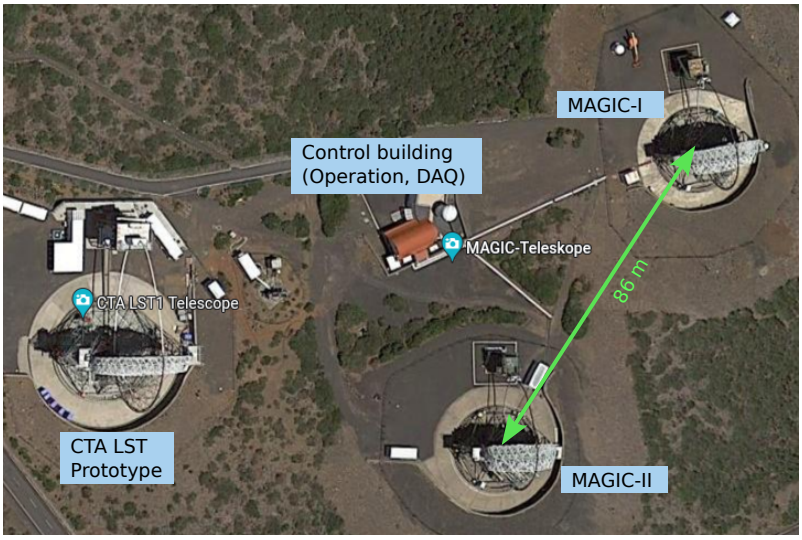

Figure 2.10.: Arrangement of MAGIC telescopes compared to control building. Close to MAGIC a prototype of the Cherenkov Telescope Array (CTA) is tested.

As explained in Section 2.3, Cherenkov telescopes as MAGIC fulfill the requirements to be used as an intensity interferometer. In 2019 the MAGIC Stellar Intensity Interferometer (MAGIC-SII) was installed by applying several minor modifications to the existing telescopes. Spatial correlations in two telescopes of three different stars were detected (see [6] for details). In 2020 and 2021 the interferometer design was updated. MAGIC-SII started its main operations in July 2021. Unfortunately a vulcano eruption in La Palma inhibited any datataking from September 2021 until the end of December 2021. The interferometer resumed its operations in January 2022.
Currently MAGIC is roughly 10 times more sensitive than the Narrabri Stellar Telescope [6]. The MAGIC Stellar Intensity Interferometer was implemented in such a way that allows to easily switch between standard and intensity interferometry observations.

2.4.1. Correlation measurements with MAGIC-SII

This section describes how the correlation of starlight can be measured with MAGIC. Since the PMTs in MAGIC are *AC* coupled, only fast variations of the signal are measured. Frequencies below 10 kHz are attenuated by the amplifier of the photodetector. Because the *DC* value of $\langle I_1 \rangle$ and $\langle I_2 \rangle$ is not known (*AC* value of $\langle I_i \rangle$=0), it is not possible to establish the absolute value of $g^{(2)}$ or c in Equation 2.20.
However, in an interferometer we are actually not interested on the absolute value of c but on how the relative quantity $c(d)/c(0)$ changes with the baseline d (see Equation 2.13) so that we can fit the resulting curve to extract the angular diameter θ with Equation 2.14. This can be achieved without knowing $\langle I_i \rangle$ by means of the Pearsons's correlation coefficient p [6, 135]:

$$p(\tau) = \frac{\langle (I_1(t) - \langle I_1 \rangle)(I_2(t+\tau) - \langle I_2 \rangle) \rangle}{\sqrt{\langle (I_1(t) - \langle I_1 \rangle)^2 \rangle} \sqrt{\langle (I_2(t) - \langle I_2 \rangle)^2 \rangle}}. \tag{2.21}$$

τ is here the time delay. The actual measurement of the interferometer are fast variations of the intensity $\Delta I_i = I_i(t) - \langle I_i \rangle$. If the fluctuations of I_1 and I_2 can be described by a Poisson distribution, then

$$\langle I_i \rangle \approx \langle (I_i(t) - \langle I_i \rangle)^2 \rangle. \tag{2.22}$$

Hence the Pearson's correlation coefficient can be used as an estimate of $g^{(2)}$.
If the PMT gain is assumed to be constant, the standard deviation $\sqrt{\langle (I_i(t) - \langle I_i \rangle)^2 \rangle}$ is proportional to the anode current *DC* (DC_1 for MAGIC-I and DC_2 for MAGIC-II):

$$\sqrt{\langle (I_i(t) - \langle I_i \rangle)^2 \rangle} \propto \sqrt{DC_i} \tag{2.23}$$

The contrast c of Equation 2.13 can be written as function of the DC and ρ:

$$c(\tau, t) = K \frac{\rho(\tau, t)}{\sqrt{DC_1(t) DC_2(t)}} \tag{2.24}$$

with K a constant and ρ the numerator of p in Equation 2.21.

$$\rho(\tau, t) = \langle (I_1(t) - \langle I_1 \rangle)(I_2(t+\tau) - \langle I_2 \rangle) \rangle \tag{2.25}$$

2.4.2. Observational targets of the MAGIC interferometer

The MAGIC-SII is able to detect B=3 mag stars in 4.5 minutes. Around 170 possible targets with this magnitude can be found in the sky. Stars with B=4 mag can be detected in 28 minutes. In this case there are ~ 500 possible targets.
Most observations of the MAGIC-SII aim at measuring the diameters of stars, in particular those that have not been measured before. Knowing the diameters of some of them may allow to improve our understanding of stellar structure and their evolution.

2.4.2.1. Asteroseismology targets

The majority of physical process that affect the stellar structure and evolution take place in the interior of a star, for example the production of nuclear energy that occurs in the core of a star [86]. The starlight however is emitted from the surface, whereas the stellar interior is not observable. Variable stars however represent a possibility to gain insight in the physics going on in stellar interiors.
Asteroseismology is a technique to study stellar oscillation modes of variable stars. Thereby new information about macroscopic aspects of the stellar structure and evolution can be obtained, such as mixing at the border of convective cores, rotation and angular momentum transport in stellar interiors. Also microscopic aspects can be studied, for instance, opacities and the equation of state of stellar material.
β Cephei stars are pulsating stars that show oscillation modes of various nature (pressure and gravity modes). The oscillation modes can be studied with asteroseismology to probe the stellar interior. β Cephei stars can act as a laboratory for the theory of stellar structure and evolution which plays a key role in chemical composition and evolution of the Universe. Since the structure of β Cephei stars is similar to that of more massive objects of which no pulsations are available, they act as a crucial link to transpose the constraints from the seismology of low-mass stars (in particular solar-like oscillators) to the higher-mass regime [45].
θ Oph is a candidate target of MAGIC-SII for asteroseismology [167]. Its diameter is not known, but is possible to estimate it with basic stellar parameters, although with a large uncertainty [168]. The resulting diameter can be used together with asteroseimic data from BRITE, [170] to derive information about the interior of the star, in particular its metallicity. This is done by studying models of the stellar interior and of the predicted frequencies as a function of stellar parameters compared to seismology frequencies and the stellar diameter [168].

2.4.2.2. Fast rotators

Equation 2.14 assumes that a given star has a uniform disk shape. However, from the width of the OB spectral lines it was measured that the velocity of some stars is close to their critical velocity, i.e. the effective gravity in their equatorial regions is very small [49]. Such extreme rotation distorts the shape of the stellar photosphere and produces a detectable elongation perpendicular to the rotation axis [60]. Studying the shape of such *fast rotators* represents an unique opportunity to measure their oblateness (R_b/R_a -1) and to improve the understanding of stellar structure and evolution (see [164] for details). Fast rotator candidate targets of MAGIC-SII are η Cen, γ Cas, α Cep [172], ζ Oph and η UMa. In Table 2.1 their oblateness is listed [164].

star	**oblateness**
η UMa	0.05
η Cen	0.16
γ Cas	0.12
ζ Oph	0.20
α Cep	0.21

Table 2.1.: List of fast rotator candidate stars with oblateness (R_b/R_a -1) [164].

2.4.2.3. Binary systems

A binary system consists of two stars bound to each other by gravitation [160]. ι Ori is a quadruple binary system (i.e. consisting of four stars). The two central components (B ~ 2.6 mag) form a spectroscopic binary of orbital period of 29 days and a mean separation of 1.5 mas [134]. The combination of the expected angular diameters of the individual stars, the difference in fluxes and the accessible baselines and coordinates in the UV plane make this system an ideal binary system candidate to be studied with the MAGIC-SII. In principle, MAGIC-SII could even be sensitive to tidal distortions of the system during the periastron in which the two stars are the closest.

2.4.2.4. Be supergiant

Be-stars are a stellar class of rapid rotators with dense equatorial gas discs. Over timescales of months or years their discs can evolve, develop and disappear. In Be-stars the Balmer lines, in particular H_α, exhibit emission or incipient emission (Be-phenomenon, details in [22]). A possible target of MAGIC-SII is the Be supergiant and binary system 3 Pup, which is the brightest star that shows the Be-phenomenon [112]. The orbital parameters and the properties of the H_α line profile of this star suggest that the circumstellar gaseous disc in 3 Pup is predominantly circumbinary and that it is contaminated by the stellar wind from the supergiant primary [112]. Observing the continuum of 3 Pup with MAGIC-SII and the H_α line with CHARA [36], the stellar

and wind/disc components could possibly be discriminated which would allow to track the orbital/secular variability of the latter. SII measurements and quasi-simultaneous optical spectroscopy could improve the understanding of the structure and dynamics of this type of binary [88, 109].

3. Signal path and data analysis of MAGIC-SII

In this chapter, we will follow the complete signal path of the incoming starlight through the MAGIC-SII setup and the subsequent data analysis until the diameter of a star is extracted. I actively participated in the development of the MAGIC-SII and one of my main tasks was to take part in the development of the analysis chain.

Figure 3.1 shows the structure of the signal path and the analysis chain of MAGIC-SII. The incoming starlight is collected by the reflector and focused on a camera pixel (1). The light passes through an interference filter (2). The light is detected by a PMT (3). The signal output of the PMT is transported via optical fibers to the digitizer and the correlator (4). Several corrections are applied to the correlation data to compensate for gain differences, the impact of the NSB and the time delay (5). The correlation data is binned to baseline and the amplitude of the correlation signal is extracted (6). The amplitude of the correlation signal is plotted as a function of the baseline and fitted with Equation 2.14. For the uniform disk model, the fit parameters are the diameter of the star and a normalization factor (the zero baseline correlation) (7). In the following sections, steps 1-7 are explained in detail.

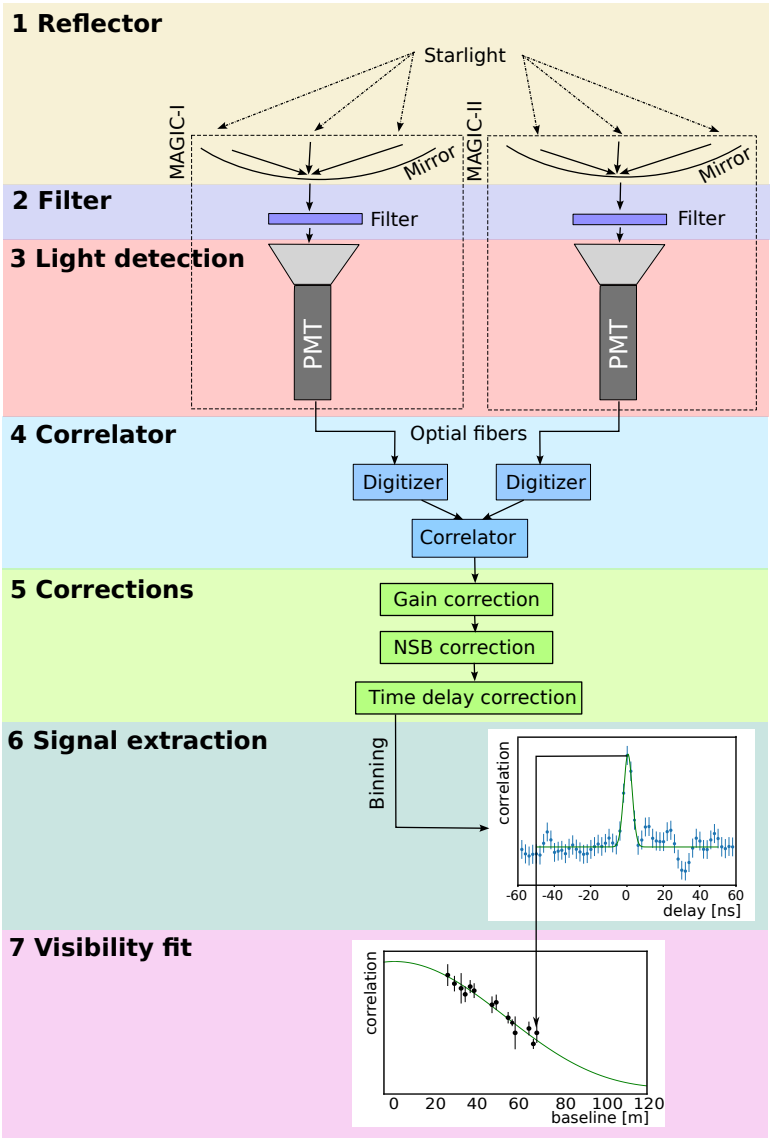

Figure 3.1.: Scheme of the structure of the signal path and the analysis chain of MAGIC-SII: the incoming starlight is collected by the reflector and focused to a camera pixel (1). The light passes through an interference filter (2). The light is detected by a PMT (3). The signal output of the PMT is transported via optical fibers to the digitizer and the correlator (4). Several corrections are applied to the correlation data to compensate for gain differences, the impact of the NSB and the time delay (5). The correlation data is binned in baseline and the amplitude of the correlation signal is extracted (6). The amplitude of the correlation signal is plotted as a function of the baseline and fitted with Equation 2.14. For the uniform disk model, the fit parameters are the diameter of the star and a normalization factor (the zero baseline correlation) (7).

3.1. Reflector and Active Mirror Control

The reflector has a parabolic shape to guarantee a minimal time spread at the focal plane. The focal length is 17 m. The reflector consists of 250 mirror panels of about 1 m^2 area each. Behind each mirror panel two actuators are installed that allow moving the mirror. With the so-called Active Mirror Control (AMC) [28] the reflector can be adjusted in a few seconds while tracking a source. The AMC usually adjusts the position of the mirrors every 20 minutes. The light is normally focused in such a way that around 70 % of the light of a point source is collected in one pixel.
During gamma-ray observations the mirrors are focused at ~ 10 km since this is the typical distance to the extensive atmospheric showers, but stars need to be focused to infinity. The AMC allows easily switching the mirror configuration optimized for gamma-ray observations to the one optimized for intensity interferometry.
The AMC software has been modified in order to focus the entire reflector or arbitrary groups of mirror panels on an arbitrary point in the camera (with a circle of ~ 1 deg radius). Configuration files define which mirror panels are focussed on which camera pixel. Three main settings are implemented for intensity interferometry observations [43]:

- **Full-mirror mode:** The entire reflector is focused on one pixel that is located at 0.8 deg from the camera center. Baselines between ~ 17 - 86 m can be achieved.
- **Chessboard mode:** The mirror panels are divided into two groups, arranged like the black and the white squares in a chessboard. One group is focused on one pixel, the other group to a second pixel. In the left panel of Figure 3.2 a scheme of the reflector in Chessboard mode can be seen. The correlation in

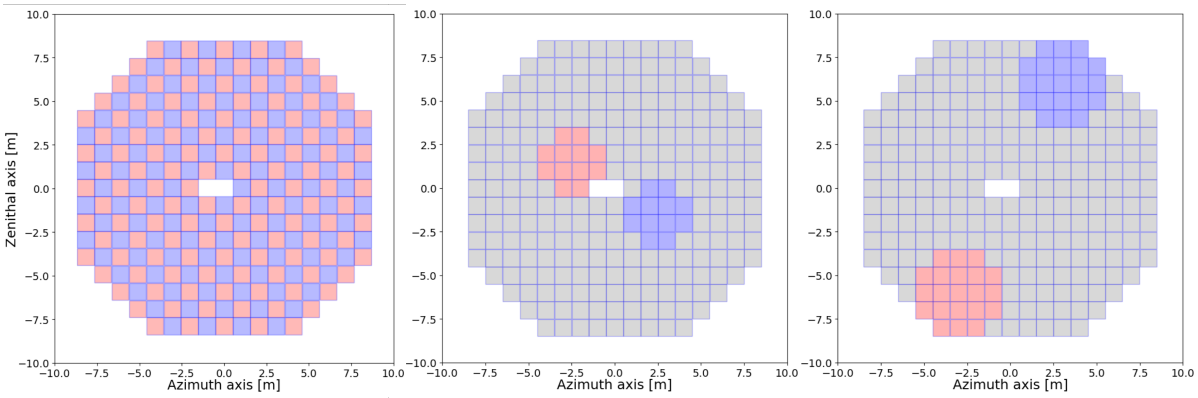

Figure 3.2.: Scheme of the reflector adjusted with AMC in Chessboard or Submirror mode. The red-colored mirror panels are focussed on one pixel, the blue-colored mirror panels are on a second pixel. The remaining panels are not used during the observation and are focused elsewhere. Reflector in Chessboard mode (**left**). Submirrors with an area of 12 m^2 (**center**). Submirrors with an area of 21 m^2 (**right**). Image credits: Juan Cortina [43].

Chessboard mode corresponds to a baseline of ~ 1.17 m. The Chessboard mode allows studying the correlation for baselines close to zero.

- **Submirror mode:** Two roundish-shaped groups of 12-21 panels are focussed on a pixel each. This was inspired by the I3T concept [66] which proposes to focus the single mirror panels of the reflector to a detector and thereby record the photon fluxes from each mirror panel independently as well as their pairwise or triple correlation. The submirror mode in MAGIC allows measuring the correlation for very small baselines (< 17 m). In Figure 3.2 a scheme of the reflector in submirror mode can be seen. It shows two submirror configurations with a 12 m^2 area (center panel) or a 21 m^2 area (right panel). The red-colored mirror panels are focussed on one pixel and the blue-colored mirror panels to another pixel.

The AMC is controlled with an interferometry graphical user interface (GUI). In this GUI the configuration of the mirror panels can be selected and the data-taking can be easily started and stopped.

3.2. Optical filters

In the front of the pixels dedicated to interferometry observations a filter is mounted to lower the *DC* of the PMTs sufficiently to prevent any damage during bright Moon observations or when pointing to bright stars. A filter spectral response with a sharp cutoff in the spectrum reduces the effective optical bandwidth Δf (see Equation 2.20) and can improve the sensitivity of the measurement even if the signal-to-noise ratio of the correlation of the telescope signals is insensitive to Δf [43]. Besides, since the correlation is wavelength dependent a filter would be useful to reject the contribution from other wavelengths.
A filter holder keeps the filter at a distance of 20 mm from the pixels. This holder is fixed on an existing mechanical structure that holds the T-Point lid. The structure and the filter holder can be controlled remotely. MAGIC-SII observations are performed while the T-Point lid is deployed. The filter holder can hold up to six filters (see Figure 3.3). Each filter is positioned in front of a PMT.
In MAGIC-SII a single-band bandpass filter Semrock FF01-425/26-50 of 50 mm diameter and 5 mm thickness is used (see [94]). Its transmission band for incident parallel light goes from 412 nm to 438 nm (average transmission $> 90\%$) with a center wavelength of 425 nm and a FWHM of 25 nm with sharp edges. The transmission curve shape is affected by the setup because the MAGIC reflectors have a small f/D. With the *MyLight* modeling online tool provided by Semrock the effective spectral transmission curve in a cone of half-angle 26.5° was calculated. Figure 3.4 shows the obtained transmission curve of the filter as a function of the wavelength [43].

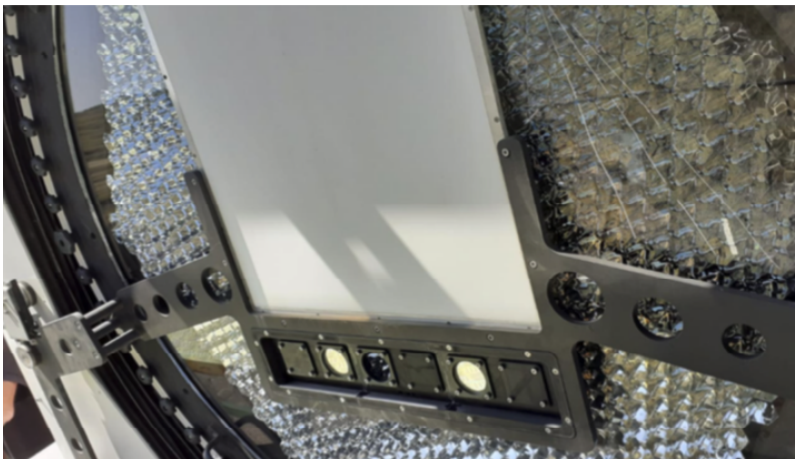

Figure 3.3.: Filter holder with room for up to six filters, fixed to the holder of the spectralon target. Two filters were installed (white circles) when the image was taken. One of the holes was left open and the three other ones were closed with a plastic cap. Behind the spectralon target, the Winston cones of the camera pixels are visible. Image credits: Juan Cortina.

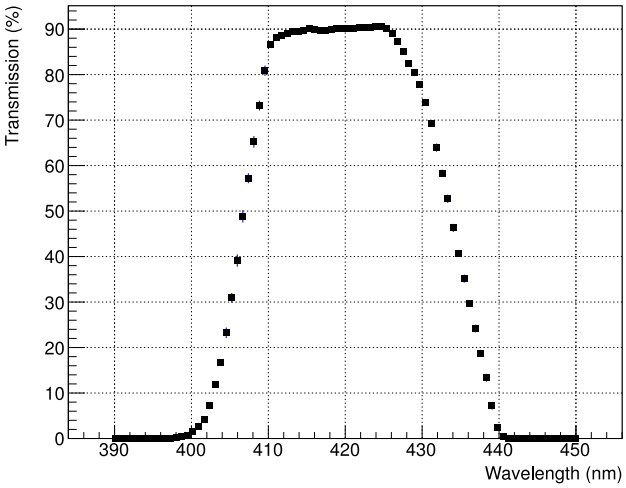

Figure 3.4.: Transmisson curve of Semrock FF01 -425/26-50 for light collected by the MAGIC reflector. The transmission was calculated using the MyLight modeling online tool provided by Semrock [94]. Image credits: Juan Cortina.

3.3. Light detection

Each telescope is equipped with a PMT camera with 1039 pixels. The PMTs are the Hamamatsu R10480 with a hemispherical photocathode, 6 dynodes and a 25.4 mm diameter. To achieve shorter pulses and a large dynamic range, a PMT with a relatively small number of dynodes was chosen. PMTs are operated at a relatively low gain of 10^4 to allow observations under the moonlight. The gain of the MAGIC-I PMTs is distributed from 1.5×10^4 to 9.0×10^4 with a mean gain of 4.5×10^4. In MAGIC-II the gain goes from 1.0×10^4 to 6.0×10^4 with a mean gain of 3.0×10^4 (at a mean bias voltage of 850 V). The differences in the gain of the PMTs are compensated by using different high voltages (HV) [43, 17].

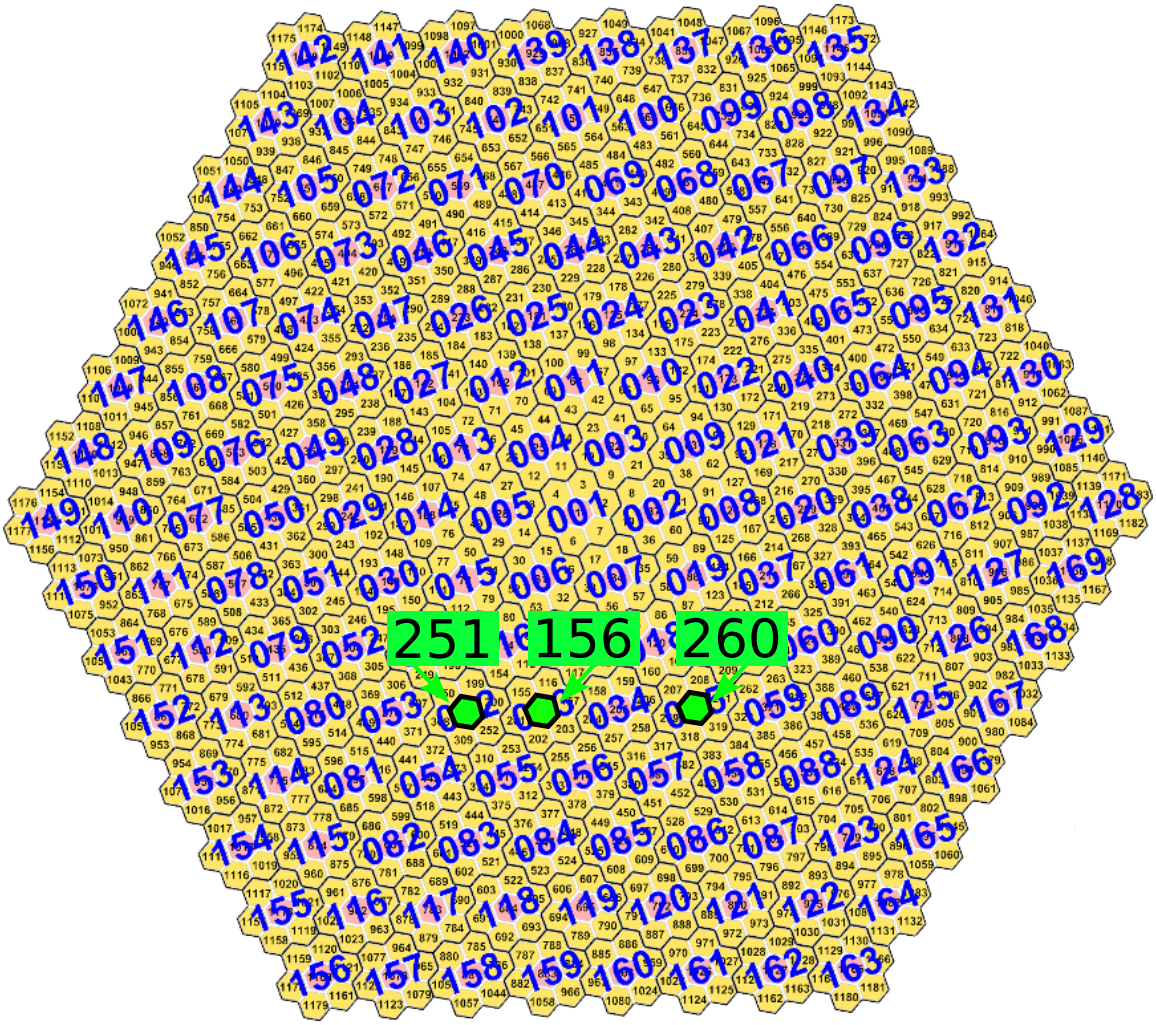

Figure 3.5.: Position of interferometry pixels number 156, 251 and 260 in one of the MAGIC cameras. The small black numbers indicate the pixel number and the larger blue numbers are the pixel cluster number.

pixel	HV MAGIC-I [V]	HV MAGIC-II [V]
156	700	700
251	1050	1090
260	850	1025

Table 3.1.: Special HV settings for pixel 156, 251 and 260 for interferometry data-taking. The remaining pixels have HV=0 during intensity interferometry observations.

Each pixel consists of a PMT and a hexagonal Winston cone. The distance between the PMT centers is 30 mm. This corresponds to a pixel FOV of 0.1°. A low-power Cockroft-Walton DC-DC converter provides the PMT bias voltages (up to 1250 V peak voltage). The electrical signal is amplified (AC coupled, ~ 25 dB amplification). The average full-width half maximum (FWHM) of the PMT pulse is 2.5 ns. The signal is transported via optical fibers using vertical cavity surface emitting lasers (VCSELs) to a control building. The fibers have a length of ~ 162 m. At the readout end of the fiber, the 850 nm multimode optical signal is converted to an electrical signal.
An electrical signal can be produced with a pulse injection circuit. This allows to inject pulses after the PMT output and just before the preamplifier for testing [54]. The shape of the injected pulses is similar to that produced by the MAGIC PMTs, with a typical FWHM of ~ 2.6 ns [17]. The amplitude of the injected pulses can be adjusted from tens of phes to saturation of the detector. The time jitter of the pulses is of the order of 1 ns [6, 43, 17]. Figure 3.6 compares an injected and a calibration pulse (see Section 2.4).

Only three PMTs per telescope are normally used during intensity interferometry observations. Their position in the camera is shown in Figure 3.5. Two of them (numbers 251 and 260) are used to collect the starlight and are connected to the correlator. These pixels are disconnected from the VHE gamma-ray data acquisition.

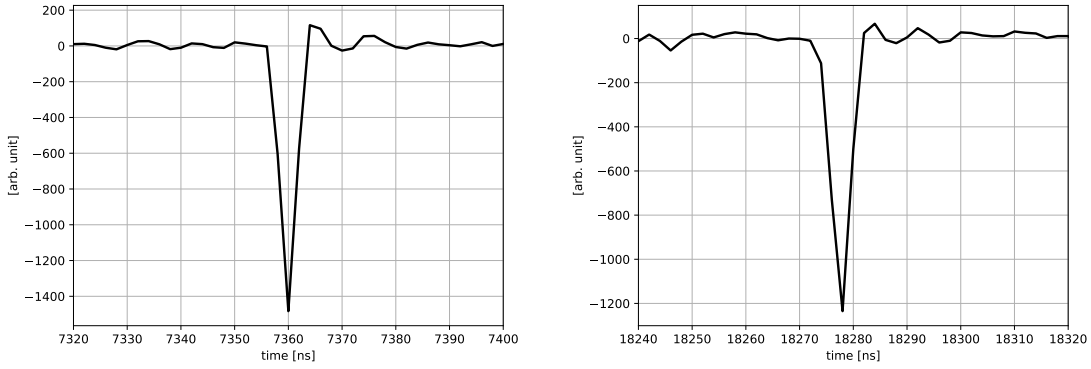

Figure 3.6.: Example of an injected pulse (**left**) and calibration pulse (**right**). The pulses were acquired with the MAGIC-SII readout, the sampling rate was 500 MSps.

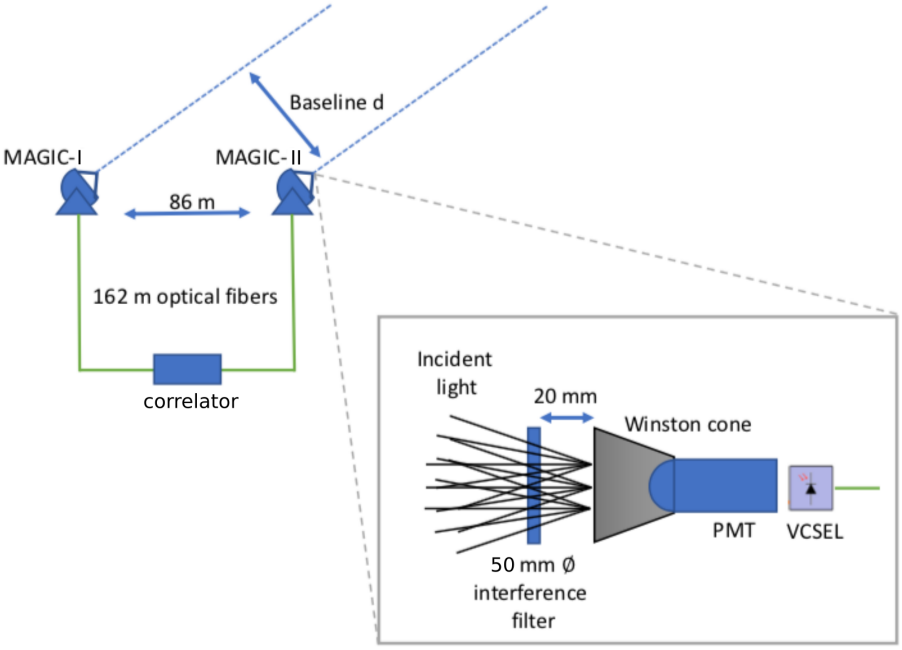

Figure 3.7.: Scheme of the MAGIC-SII. The incoming light with a baseline d is focussed by the reflectors of MAGIC-I and II to a camera pixel. The incident light goes through the interference filter and the Winston cone and is detected by the PMT. The signal is transmitted via optical fibers to the correlator. Adapted from [6].

Instead, they are connected to fiber delays of different lengths terminated with a GaAs photodiode from IMM Photonics which is located in an electromagnetically shielded enclosure. The signal of the photodetector is amplified with a Femto HSA-Y-2-40 amplifier with 40 dB and 2 GHz bandwidth. The amplifier has a lower frequency cutoff of 10 kHz. Afterward, the signal is digitized and correlated (see Section 3.4). Another pixel (number 156) is used to measure the NSB to correct the correlation signal for moonlight (see Section 3.5.2).
During intensity interferometry observations, the HV of all camera pixels is zero except for pixels 156, 251 and 260. The HV values of those pixels are listed in Table 3.1.

Figure 3.7 shows the path that the signal follows, from the light collection until the PMT pulses are transferred to the correlator. The incoming light with a baseline d is focussed by the reflectors to a camera pixel. The incident light goes through the interference filter and the Winston cone and is detected by the PMT. The signal is transmitted via optical fibers to the correlator.

3.4. Correlator

The correlator is located in a control building together with the readout and trigger electronics for VHE observations. The hardware and the software of the correlator have been designed to process the data in real-time by means of a parallel structure of state-of-the-art Graphic Processing Units (GPUs) and two fast digitizer boards M4i.4450-x8 PCI 2.0 by Spectrum [61] (see Figure 3.8).

Each digitizer has two channels and provides a simultaneous sampling rate of 500 MS/s with a resolution of 14 bits per sample. The digitizers support remote-direct-memory access (RDMA). RDMA is a technology that allows direct data transfer between the memory of two machines (in this case: between the digitizer and the GPU). The data can be directly transferred between memory buffers of different machines without intermediate copies. The throughput is improved and latency is lower between RDMA systems. This results in a faster data transfer [48].
The digitizer board clocks are synchronized using a Star-hub module which is implemented into the carrier card on the correlator chassis. The correlator is installed in a computing server with commercial hardware: two processors (20 cores in total), SSDs

Telescope	pixel	channel
MAGIC-II	251	A
MAGIC-II	260	B
MAGIC-I	251	C
MAGIC-I	260	D

Table 3.2.: Designation of the pixels and channels.

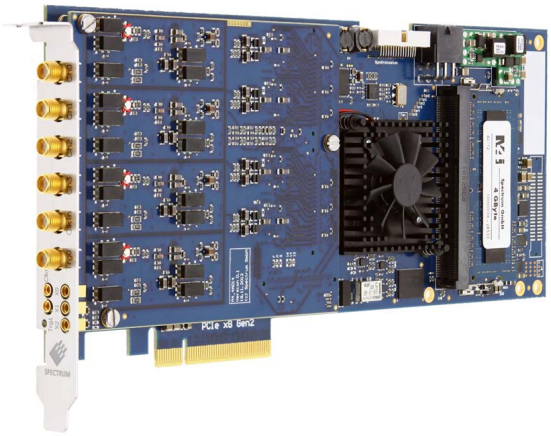

Figure 3.8.: Digitizer board M4i.4450-x8 PCI 2.0 by Spectrum [61] with two channels with a sampling rate of 500 MS/s and with a resolution of 14 bits per sample.

for fast access and HDDs for long-term storage and testing, together with a Nvidia Tesla V100 GPU. As GPU the PCIe 3.0 x16 model with 5120 cores, 32 GB HBM2 RAM and 14 TFLOPs of single-precision performance was selected [43].
The correlator software calculates the correlation as a function of the delay between pairs of channels using the convolution theorem in Fourier space with the Fast-Fourier-Transform (FFT). The program is written in CUDA C including the Nvidia FFT library for the convolution computation and the Spectrum CUDA Access for Parallel Processing (SCAPP) SDK for direct data transfer between the digitizer and the GPU in streaming mode. The calculations use double precision. With the correlator software the data from two digitizers can be processed in real-time at 4 GB/s. MAGIC-SII has four readout channels (two channels per digitizer of each telescope). Table 3.2 shows the correspondence between the digitizer channels and the pixels in the MAGIC telescopes. In total six correlations are calculated: $A–B, A–C, A–D, B–C, B–D, C–D$.

The correlator software runs in three stages [43]:

- The initialization section adjusts several parameters of the digitizer and the GPU, for example, the number of channels, acquisition rates, input paths and ranges, RDMA and execution time. In addition, it initializes the data structure in the CPU and the GPU and it creates, next to the main thread, a second thread to write the resulting correlation in a storage file. Due to a double buffer scheme, both threads can proceed in parallel.

- In the main thread a data processing loop runs continuously for the preset duration of data taking as long as no error occurs or the loop is interrupted by the operator. In the loop, the digitizer data is read interlaced in frames of 0.5 ms. For channels A, B, C and D and n frames, the data is read as $(A_1, B_1, C_1, D_1, A_2, B_2, C_2, D_2, ..., A_n, B_n, C_n, D_n)$. The data is reordered as $(A_1, A_2, ..., A_n; B_1, B_2, ..., B_n; C_1, C_2, ..., C_n; D_1, D_2, ...D_n)$. Then the correlation for each channel pair ch_i-ch_j $(A-B, A-C, A-D, B-C, B-D, C-D)$ is calculated.

- Every second the writer thread turns active (buffer full) to save the convolution result and any obtained statistics to disk. At the same moment, the output buffer is swapped. Then the writer thread turns inactive again and a new cycle starts.

3.4.1. Computation of the correlation

The main computation time of the correlator software is due to the calculation of the numerator of Pearson's correlation coefficient ρ in Equation 2.21. A single data run consists of N non-overlapping time frames. Each time frame consists of a fixed number of samples S. For discrete time steps $i = 1, ..., S$ the signals for MAGIC-I and MAGIC-II are given by $I_1(i)$ and $I_2(i)$. With Equation 2.21 ρ is estimated for each time frame. The final estimate of ρ for the entire data run is obtained by averaging the results of the single time frames [6]:

$$\rho(\tau) = \frac{1}{N}\sum_{j=1}^{N}\rho_j(\tau). \tag{3.1}$$

ρ_j is the numerator of Pearson's correlation coefficient for the time frame j. The uncertainty of $\rho(\tau)$ is estimated with [6]:

$$\sigma(\rho(\tau)) = \frac{\Delta(\rho_j(\tau))}{\sqrt{N}}, \tag{3.2}$$

where $\Delta(\rho_j(\tau))$ is the root mean square (RMS) of a set of $N\rho$ estimates. In Equation 3.1 the averaging of Equation 2.21 is trivial except for the cross term $\langle I_1(t)I_2(t+\tau)\rangle$. For the condition of non-overlapping windows, it is calculated as [6]:

$$\langle I_1(t)I_2(t+\tau)\rangle = \frac{\sum_{i=1}^{S} I_1(t_i)I_2(t_i+\tau)W(t_i+\tau)}{\sum_{i=1}^{S} W(t_i+\tau)} \tag{3.3}$$

$W(t)$, the 'windowing function', is introduced to secure that the computation of ρ is independent for each time frame. It is set to 1 if t is within the time frame, otherwise, it is set to 0.
The direct computation of the numerator of Equation 3.3 is very time-consuming. This problem can be by-passed by applying the Convolution Theorem for discrete Fourier Transforms [129]: for two periodic discrete functions f and g with a period P

$$\frac{1}{P}\sum_{i=1}^{P} f(i)g(i+j) = \mathcal{F}^{-1}(\mathcal{F}(f)\mathcal{F}^{*}(g)). \tag{3.4}$$

$\mathcal{F}(f)$ is the discrete Fourier's transform of the function f, $\mathcal{F}^{*}(g)$ the complex conjugate of the discrete Fourier's transform of the function g and $\mathcal{F}^{-1}$ denotes the inverse discrete Fourier's transform. The discrete Fourier's transform can be calculated efficiently with a Fast Fourier Transform (FFT) algorithm.
Equation 3.3 has to be adapted to exploit the Theorem of Equation 3.4: two periodic functions $I_{P,1}(i)$ and $I_{P,2}(i)$ of period $2S$ are defined. They are equal to $I_1(i)$ and $I_2(i)$ respectively for $(i \mod 2S) \leq S$ and they are 0 for $(i \mod 2S) > S$. Hence τ is limited to $|\tau| < S-1$. With this modification Equation 3.3 can be written as [6]:

$$\langle I_1(t)I_2(t+\tau)\rangle = \frac{S}{S-|\tau|}\mathcal{F}^{-1}(\mathcal{F}(I_{P,1})\mathcal{F}^{*}(I_{P,2})) \tag{3.5}$$

With Equation 3.5 the cross term of ρ_i in Equation 3.1 can be calculated.

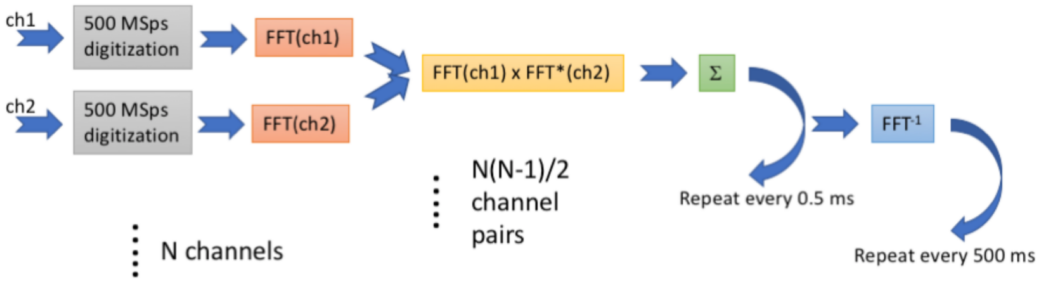

Figure 3.9.: Scheme of the operation mode of the correlator for N channels. The output of ch_1, ... ch_N is digitized at 500 MSps and their FFT is calculated for times frames of 0.5 ms. Then an array with $\mathrm{FFT}(\mathrm{ch}_i) \times \mathrm{FFT}^*(\mathrm{ch}_j)$ is calculated with $i = 1, ...N$ and $j = 1, ...N$ for $N(N-1)/2$ channel pairs. The resulting product is summed up for 1000 iterations. Finally the FFT^{-1} of this sum is calculated. Image credits: Juan Cortina.

Figure 3.9 shows how the correlation is calculated for N channels. The output of ch_1, ... ch_N is digitized at 500 MSps and their FFT is calculated for times frames of 0.5 ms. Then an array with $\mathrm{FFT}(\mathrm{ch}_i) \times \mathrm{FFT}^*(\mathrm{ch}_j)$ is calculated with $i = 1, ...N$ and $j = 1, ...N$ for $N(N-1)/2$ channel pairs. The resulting product is summed over 1000 iterations. Afterwards the FFT^{-1} of this sum is calculated. The last step is repeated every 500 ms. The computation is done in this way to save computing power.

During the data taking, every 5 minutes the data is processed as a subrun. After computing the correlation, the subrun is saved by the correlator software as a binary file. In this file data frames with the correlation ρ as a function of the time delay of all six channel pairs and the autocorrelation of each individual channel are stored. In addition, the start time of the data frames and the standard deviation of the correlation of each channel is saved. The online analysis produces preliminary images of the correlation signal to control the strength of the signal during the observation of a star.

3.5. Data correction

The correlator outputs data frames with the numerator ρ of the Pearson's correlation coefficient (see 2.21). To obtain the contrast c, ρ needs to be divided by DC_1 and DC_2 (see Equation 2.24). DC_1 and DC_2 depend on the star and the observation conditions. The DC should always be kept below 45 μA to prevent damaging the PMTs. This is important, especially for very bright stars. The DCs of the PMTs are routinely stored every second during observations. At this stage, they are read to obtain the contrast c/K (see Equation 2.24) and to correct the data for differences in the gains of the PMTs and for the impact of the NSB. This allows the combination of data on longer time scales like from different nights or even months.

3.5.1. Gain correction

Equation 2.24 assumed that the gain of the PMTs was constant. However, this is rarely the case. Even if PMTs HVs have been adjusted to minimize the difference in gain, a perfect flat fielding is almost impossible to achieve. Then a gain correction needs to be applied to obtain the correct contrast c:

$$c(\tau, t) = K \frac{\rho(\tau, t)}{\sqrt{DC_1(t) G_1(t) DC_2(t) G_2(t)}} \tag{3.6}$$

G_1 and G_2 are the gain correction factors. They are calculated using a set of dedicated measurements of the DC at different HV for all interferometry pixels which is shown in

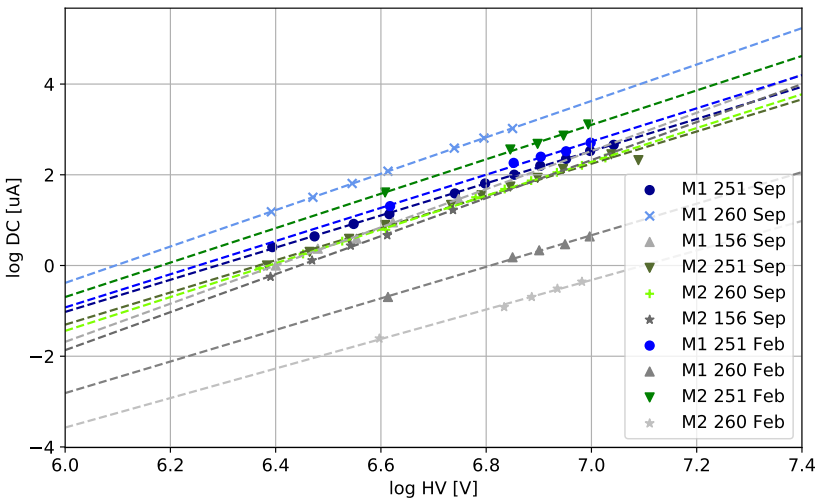

Figure 3.10.: Calibration measurement of each interferometry pixel in MAGIC-I and MAGIC-II to calculate the expected DC for a given HV. The measurement was performed in February 2021 and in September 2021. The slope of the fit function is consistent between the two campaigns.

Figure 3.10. The measurements were fitted linearly on a logarithmic scale. The resulting fit functions give the expected DC value for a given HV value. The expected DC is calculated for the actual HV as $DC_{\mathrm{exp,act}}$ and for a reference HV (see reference HV values in Table 3.1) as $DC_{\mathrm{exp,ref}}$. The gain correction factor G is the ratio $DC_{\mathrm{exp,ref}}/DC_{\mathrm{exp,act}}$. Gain calibration measurements were taken in February 2021 and September 2021. The slope of the fit functions of the February 2021 measurement is consistent with the September 2021 measurement. Hence the relation between HV and DC is stable in time. From January to April 2021 pixel 251 in MAGIC-I and MAGIC-II was used to collect starlight, pixel 260 served for background measurements.

3.5.2. Night Sky Background Correction

The measured DC is the result of mainly two contributions: light coming from the star that is being observed and from the NSB [85]. Since most interferometry observations with MAGIC are performed around the Full Moon, diffuse Moonlight has a strong impact on the DC. During the measurements with the first MAGIC interferometer in 2019, the DC generated by Moonlight and NSB was around ~ 15 % of the DC of the star [6].
Pixel 156 is used to measure the DC produced by the NSB (DC_{NSB}). To determine the DCs produced by starlight, the DC_{NSB} needs to be subtracted from the DC of pixel 259 and pixel 260. Since the PMTs in the camera do not have the same gain also the DC of 156 has to be scaled. A calibration measurement was performed with the pixels 156, 251 and 260 to extract a conversion factor. After this correction, the DC_{NSB} can be used in Equation 3.6 to calculate the normalized contrast:

$$c(\tau,t) = K \cdot \frac{\rho(\tau,t)\sqrt{\frac{DC_1(t)DC_2(t)}{(DC_1(t)-DC_{\mathrm{NSB},1}(t))\cdot(DC_2(t)-DC_{\mathrm{NSB},2}(t))}}}{\sqrt{(DC_1(t)-DC_{\mathrm{NSB},1}(t))\cdot(DC_2(t)-DC_{\mathrm{NSB},2}(t))}} \tag{3.7}$$

The DC in Equation 3.7 is gain corrected, i.e. $DC = DC_{raw} \cdot G$ with G the gain correction factor and DC_{raw} the measured DC. Equation 3.7 is the final expression for the NSB-corrected contrast that is used in the analysis.

3.5.3. Time delay correction

The contrast of a channel pair ch_i-ch_j is calculated as a function of the time delay τ between those two channels. The time delay between two channels is the result of the different path lengths of the incoming starlight due to the position of the star in the sky with respect to the light collectors associated with those channels. This delay changes during the night with the Earth's rotation. In addition, there is a constant hardware delay of ch_i and ch_j because of the path length of the signal transmission to the correlator. The hardware delay depends on the temperature and the HV of the channel. To compensate for the total time delay of ch_i and ch_j, a time delay correction is applied to the data. In a time delay corrected data sample a correlation signal is

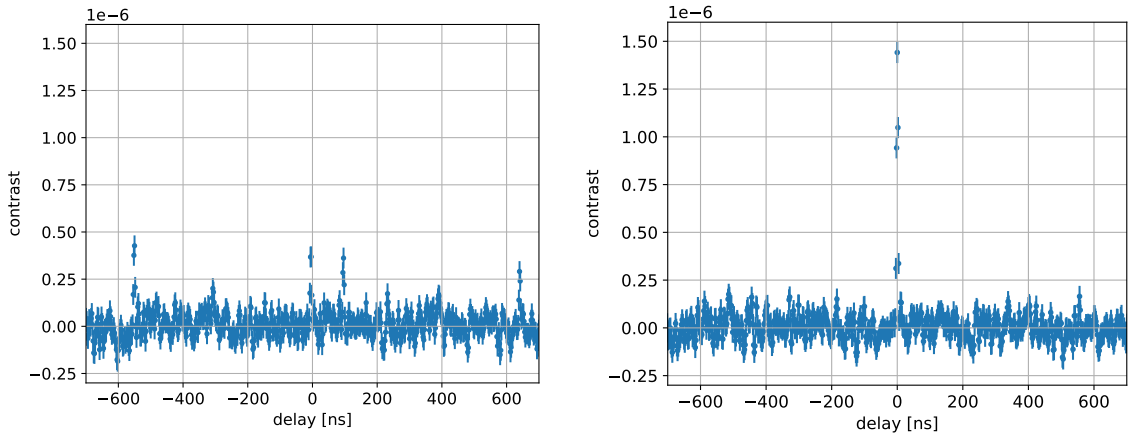

Figure 3.11.: Correlation data of ϵ CMa measured in Chessboard mode: the contrast as a function of the time delay of the four channel pairs $A-C, A-D, B-C, B-D$. The correlation data was time delay corrected with a fixed hardware delay for all channel pairs (**left**) or with an individual hardware delay (**right**). In the last case, the signal of all channel pairs falls at delay=0.

expected at delay=0 ns when a star was successfully detected.

In the left panel of Figure 3.11 the contrast as a function of the delay of the four channel pairs $A-C, A-D, B-C, B-D$ is shown. The data was measured in Chessboard mode of the star ϵ CMa. The data were corrected for the time delay introduced by the position of the star, but a fixed hardware delay for all channel pairs was assumed. The correlation signal of the channel pairs is not located at delay=0 ns but at different delays. Therefore it is not possible to combine the correlation signal of the four channel pairs into a single signal. The example in the left panel of Figure 3.11 demonstrates why a correct time delay correction is important for the analysis of the correlation signal. In the right panel of Figure 3.11 the contrast data of every channel pair was corrected with an individual hardware delay. Now the correlation signals of all channel pairs are located at delay=0 ns. The combined correlation signal of all channel pairs is much larger compared to the individual correlation signal of each channel pair in the left panel of Figure 3.11. In Figure 3.12 the position of correlation signals of the four channel pairs $A-C, A-D, B-C, B-D$ after a correct time delay correction is shown. The correlation signals are from different correlation data samples. The weighted mean of the signal position is close to delay=0 ns as expected.

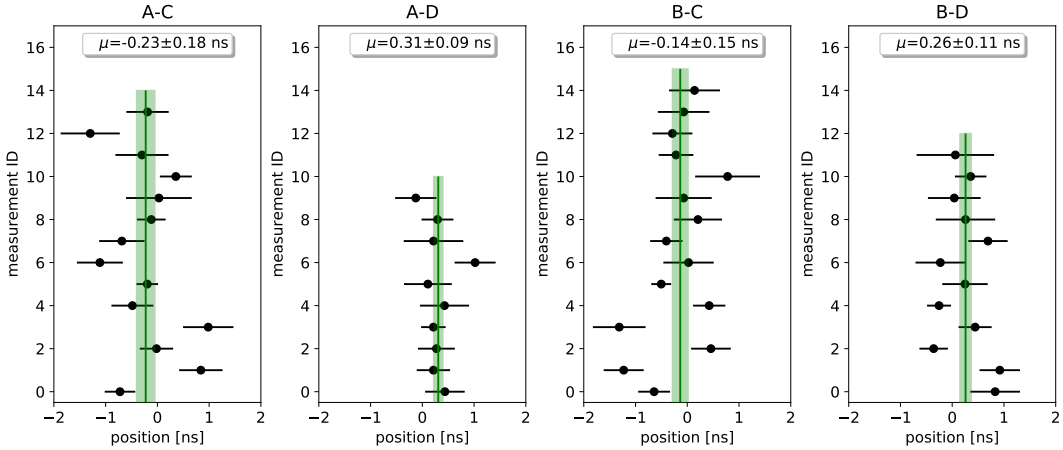

Figure 3.12.: Distribution of the position of correlation signals of the four channel pairs $A-C, A-D, B-C, B-D$ after a correct time delay correction. The correlation signals are from data samples of different stars and time points. The weighted mean of the signal position is close to delay=0 ns.

3.6. Signal extraction

After the time delay correction, the correlation data is binned in baseline bins of fixed length. The binning is selected depending on the strength of the correlation signal. For bright stars with strong correlation signals, I used a 2.5 m baseline binning. I used a larger binning for weaker signals.
I tried different methods to extract the correlation signal:

- **Maximum point:** This method uses the maximum of the correlation signal as an indicator of the strength of the correlation signal.
- **Gaussian:** A Gaussian was fitted to the signal. The indicator of the signal strength was the amplitude of the Gaussian.
- **Gaussian (mean fixed):** A Gaussian with a fixed mean was fitted to the signal. The amplitude of the Gaussian was the indicator of the signal strength. The mean was fixed to delay=0 where the signal is expected.
- **Pulse model:** The shape of the correlation signal from calibration pulses was interpolated (details in Chapter 5.1). The resulting template of the signal shape is fitted to the correlation signal from a star. The amplitude of the fit is used as an indicator of the signal strength.
- **Area:** A Gaussian was fitted to the signal and its area was calculated. In this case, the area was used to evaluate the signal strength instead of the amplitude. The reason to use the area as an indicator is that it takes into account both the amplitude and the width of the correlation signal.

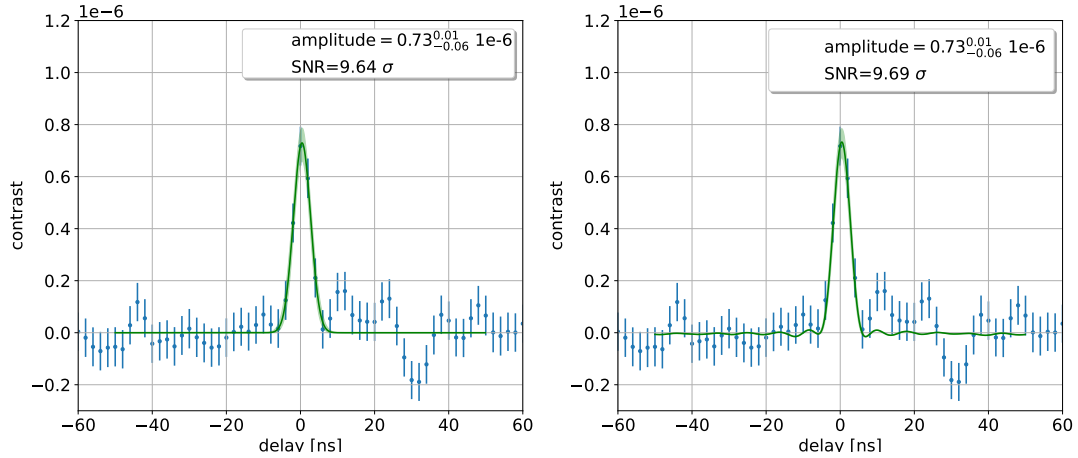

Figure 3.13.: 5 minutes of correlation data for ϵ CMa taken in Full-mirror mode for $A-C$. The signal was extracted with a Gaussian fit (**left**) and with a fit of the pulse model (**right**).

extraction method	signal amplitude	SNR [σ]
Maximum point	0.72 ± 0.08	9.48
Gaussian	0.73 ± 0.06	9.61
Gaussian (fixed mean)	0.72 ± 0.06	9.50
Pulse model	0.73 ± 0.05	9.65

Table 3.3.: Comparison of different signal extraction methods on the $A - C$ data sample of the star ϵ CMa measured in Full-mirror mode.

In Figure 3.13 two examples of the signal extraction are shown of 5 minutes of time delay corrected correlation data recorded in Full-mirror mode of the $A - C$ channel while the telescopes were focused on the star ϵ CMa. In the left panel, the signal amplitude was extracted with a Gaussian fit, and in the right panel with a fit of the pulse model to the data. The signal-to-noise ratio (SNR) was calculated as the ratio of the signal amplitude to the RMS of the data in a background region defined by

$$\text{delay} = \begin{cases} -140 \text{ ns} < x < -40 \text{ ns} \\ 40 \text{ ns} < x < 140 \text{ ns} \end{cases} \tag{3.8}$$

In Table 3.3 different signal extraction methods which use the signal amplitude as an indicator for the signal strength are compared for the data sample in Figure 3.13. The extracted signal amplitude was very similar for different extraction methods.
The width of the signal varied slightly between different data samples. I studied the signal width in detail, results are presented in Section 5.2.1. Different signal extraction methods may lead to different results for signals with a larger signal width or smaller SNR. The impact of the signal extraction method on the calculation of the angular diameter is discussed in Section 5.3.

3.7. Visibility fit

Most observations of the MAGIC interferometer were performed aiming at measuring the angular diameter θ of a star. After extracting the signal for each baseline bin, the obtained contrast as a function of the baseline $c(d)$ is fitted with Equation 2.14. From *visibility fit* two important results are extracted: the uniform disk diameter θ and the zero baseline correlation $c(0)$. The last one should be a constant of the instrument.
I performed the visibility fits using different methods. I used the `python` *emcee* package [59] and a baseline-weighted fit that was introduced by Tarek Hassan which I implemented in my analysis as well.
To fit a model with the *emcee* package, a Likelihood function of the fit problem is defined. The values that maximize the Likelihood function are the Likelihood estimates of the fit parameters. Additionally, a prior function is defined, that encodes the previous knowledge about the expected range of the fit parameters. With the prior function the Likelihood function is modified and a Log-probability function is defined. The Likelihood estimates of the fit parameters act as initial values for the *walkers*. The walkers of a fit parameter is a set of variables that are Gaussian distributed around the Likelihood estimate. In each step of the following Markov chain Monte Carlo the Log-probability function is evaluated for the given variables of the walkers. The walkers explore the full posterior distribution function (PDF) of each fit parameter to find the best set of variables describing the data. At the end of predefined number of Markov

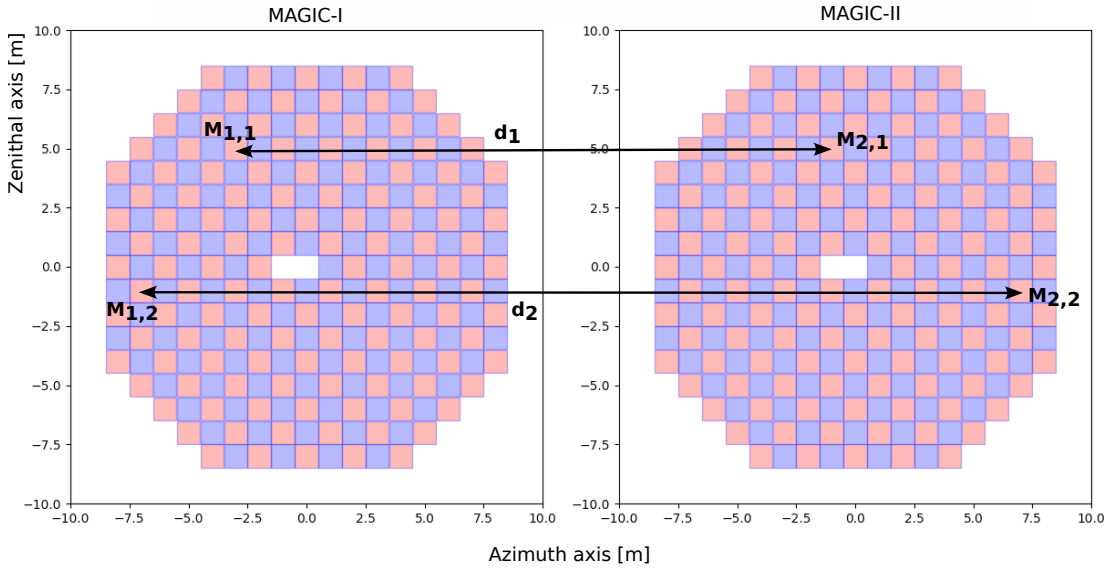

Figure 3.14.: Illustration of baselines in Chessboard mode: it is assumed that the correlation data consists of the correlation of starlight that falls on different points on the mirror surface of MAGIC-I (for example $M_{1,1}$ and $M_{1,2}$) and MAGIC-II (for example $M_{2,1}$ and $M_{2,2}$). The correlation data have different baselines, for example d_1 and d_2.

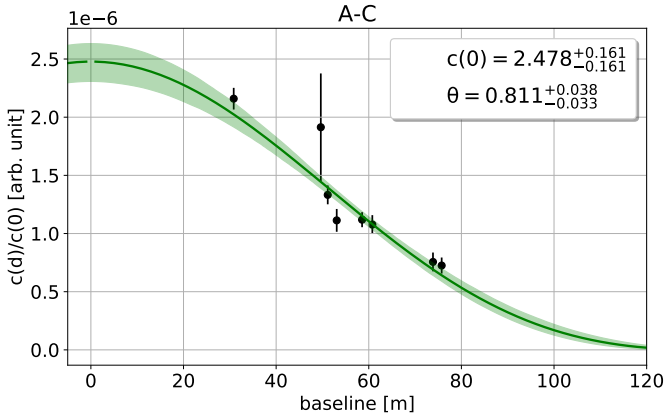

Figure 3.15.: Contrast as a function of the baseline of correlation data taken in Full-mirror mode of the star ϵ CMa for $A-C$. A visibility fit was performed using the baseline-weighted method.

chain Monte Carlo steps each walker provides an estimate of the fit parameters. The complete fit result is the mean of the estimates of the fit parameters for each walker. More details about fitting a model with emcee are found in [59].
The baseline weighted fit method aims to take the mirror size into account. It was based on the assumption that if the starlight detected by a pixel in MAGIC-I and by another one in MAGIC-II is correlated, the correlated data consists actually of the correlation of different points of the mirror surface of MAGIC-I and MAGIC-II. The data has not *one* baseline but actually *a range* of possible baselines for a given distance between two light collectors with a given mirror size (see Figure 3.14). The range of possible baselines could be obtained by simulating 1000 random points $M(x_i, y_i)$ on the mirror surfaces that focus starlight on the pixels that are associated with the input channels. In Figure 3.14 the red mirror panels in MAGIC-I focus the light on one pixel and the red mirror panels in MAGIC-II on another pixel. Between different points on the mirror surface (here $M_{1,1}, M_{1,2}, M_{2,1}, M_{2,2}$) two baselines d_1 and d_2 can be defined. The baselines between simulated points $M_1(x_i, y_i)$ in MAGIC-I and $M_2(x_i, y_i)$ in MAGIC-II are calculated. The resulting set of baselines $d_1, ...d_{1000}$ describes the true distribution of baselines of the correlation data. A residual function is defined that evaluates the difference of the model in Equation 2.14 to the data for each baseline in the set of baselines of a baseline bin. The fit was performed by minimizing the residual function.

In Figure 3.15 an example of a visibility fit is shown. The contrast measurement (amplitude/area of the correlation signal) as a function of the baseline of correlation data taken in Full-mirror mode of the star ϵ CMa for $A-C$ is plotted. The visibility fit here was performed using the baseline-weighted method. The baseline coordinates of the data points in Figure 3.15 are the mean values of the baseline sets of each baseline bin that were simulated to consider the size of the involved light collectors.

4. Large SiPM Pixels

Chapter 1 described the main characteristics of SiPMs and showed how they can offer several advantages with respect to traditional PMTs. In principle, SiPMs have the potential to outperform PMTs and replace them in several applications, for example in IACTs as MAGIC. Also, intensity interferometry could benefit from the use of SiPMs: the sensitivity of an intensity interferometer would increase with a higher PDE and a better SPTR of the involved photodetectors. In addition, the robustness of SiPMs to intense light is advantageous when observing bright stars. Their higher sensitivity to red visible light would enable also new observational targets. While PMTs can be produced with diameters of several centimeters, commercial SiPMs are usually not available in sizes larger than 6 $\times$ 6 mm^2 (see Section 1.3.1 for details). If commercial SiPMs would be employed in a large camera as in MAGIC, the amount of readout channels would significantly increase, as well as the cost and complexity of the system.

Several solutions to build large SiPM pixels while keeping the capacitance at a reasonable level have been developed in high-energy astrophysics ([71, 77, 107, 120, 142]). Inspired by these approaches, two concepts for large pixels made of SiPMs were proposed and studied at the INFN in Pisa: the Large-Area SiPM Pixel (LASiP) and the Photo-Trap pixel. I took part in the construction and characterization of these pixels. In the following, I will introduce the basic concept of both approaches, discuss potential applications and present the results of their characterization.

4.1. LASiP

4.1.1. The LASiP concept

The capacitance of a sensor can be reduced by re-partitioning the sensor area into n small ones, each with an independent readout chain [38]. If the output signal of the parallel readout chains is summed, the signal from the original sensor is recovered. The capacitance however is reduced by a factor n and the noise increases only by $\sqrt{n}$ if series noise is dominating in the detector (details in [53]). This approach can be applied to build a large sensor from n smaller ones. This approach has been successfully realized in Very High Energy (VHE) astrophysics [77, 107, 142] and enables to cover a camera with fewer readout channels made of SiPM pixels without dramatically increasing the capacitance. In addition, it provides flexibility to build pixels with different geometries. The analog current of several SiPMs can be summed into a single output also using a custom-designed Application-Specific Integrated Circuit (ASIC) as shown in Figure 4.1. This ASIC should provide low noise, high bandwidth and large dynamic range [38]. In our group we applied this concept to develop a Large-Area SiPM Pixel (LASiP) targeting applications involving gamma cameras based on scintillators (see Section 4.1.4). In our LASiP the sum was performed using the MUSIC, a multipurpose ASIC that was originally designed for high-energy astrophysics experiments. The MUSIC could sum up to 8 SiPMs using a current switch consisting of common base transistors and an operational transconductance amplifier (see [62] for details).

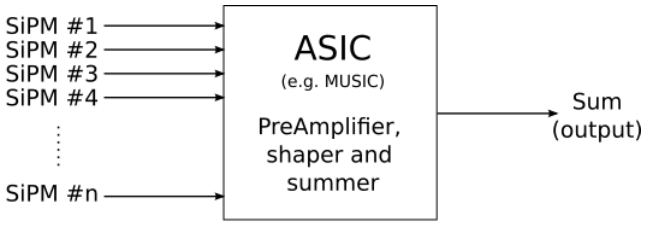

Figure 4.1.: The ASIC sums the input of n SiPMs in a single output.

4.1.2. The LASiP prototype

Our group developed a LASiP prototype that summed the currents of 8 FBK NUV-HD3 SiPMs of 6 × 6 mm^2 (pixel area ~ 2.9 cm^2). The prototype combined technology that was already available: the prototype consisted of one SCT matrix and one eMUSIC MiniBoard. The SCT matrix was developed to equip the Schwarzschild-Couder medium-size Telescope which was proposed for the Cherenkov Telescope Array [10]. A single matrix held 16 FBK NUV-HD3 SiPMs of 6 × 6 mm^2 with a ~ 0.5 mm gap between neighboring SiPMs as can be seen in the left panel of Figure 4.2. The SiPMs had a peak PDE of ~ 60 % at ~ 350 nm and a DCR of ~ 0.13 MHz/mm^2 at 20°C when operated at ~ 33 V [10]. The MUSIC could be programmed from the computer using the eMUSIC Miniboard [1], an evaluation board that could be connected to up to 8

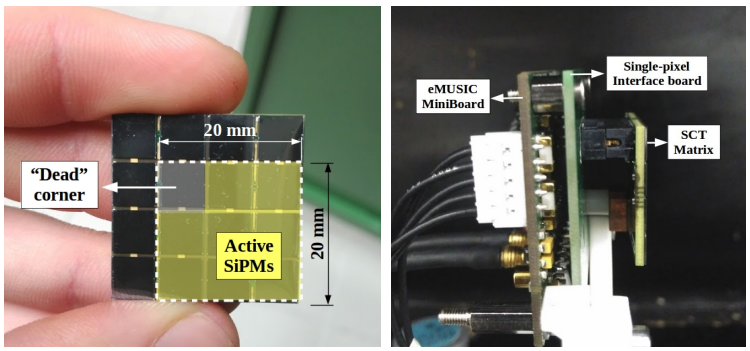

Figure 4.2.: Components of the LASiP Prototype: SCT Matrix with 16 SiPMs. Only the 8 yellow marked SiPMs are summed and part of the prototype pixel (**left**). Side view on LASiP (**right**): a custom-made interface board connects the SCT matrix to the eMUSIC Miniboard.

SiPMs (see the right panel in Figure 4.2). The eMUSIC Miniboard allowed us to easily exploit the functionalities of the MUSIC. Some of them that were particularly relevant in our case [72]:

- Performing the sum of up to 8 SiPM
- Enabling/disabling individual channels
- Setting an individual bias voltage offset for each SiPM. This is particularly useful to equalize the gain of the different channels.
- Apply a filter with pole-zero cancellation to shape the pulse. The pole-zero is configurable to optimize the amplitude, width and decay time of the pulses depending on the application and the SiPM employed. This is useful for instance to maximize the SNR for a better identification of the single-phe peak.

Since with the eMUSIC Miniboard we could sum up to 8 channels, we could only use 8 of the 16 SiPMs of the SCT Matrix. With this limitation, we built a square pixel of 20 mm × 20 mm with a dead corner, as shown in the left panel of Figure 4.2.

4.1.3. Performance of the LASiP prototype

The basic concept of LASiP would theoretically allow building pixels of any size by summing several SiPMs. The main limitation to increase the number of SiPMs that are summed is the degradation of the SNR. In a LASiP not only the signal, but also the noise is summed. Besides, as described in Section 4.1.1, the capacitance of a LASiP increases with its size (even if not at the same rate as if we were just building an equally large SiPM by adding more microcells in parallel). This degrades the timing performance and the single-phe resolution of the pixel.
To examine the single-phe resolution of our LASiP prototype, we placed it inside a

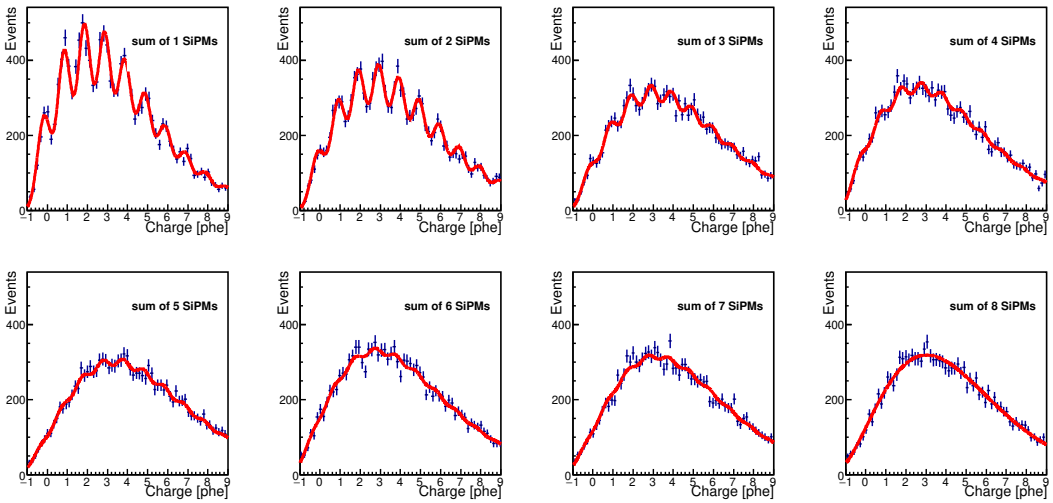

Figure 4.3.: Development of the single-phe spectrum with an increasing number of summed SiPMs. The fit was performed with Equation 4.1.

dark box where it could be illuminated by a ~ 0.5 ns pulses of ~ 380 nm generated by a PicoQuant PDL 800-B LED driver. The measurements were first performed for every single SiPM that built the LASiP, i.e. without performing the sum.
The gain of each SiPM may be slightly different. This difference may come for instance from the manufacturing process of the SiPMs but also from the readout electronics. It can be compensated by adjusting U_{over} of the individual SiPMs. When we operated our prototypes we applied a common bias voltage to all SiPMs. The gain equalization could be achieved by using the MUSIC functionality that allowed to adjust the individual offset voltages. To monitor the gain difference, the spectrum of each SiPM was fitted with Equation 2 of [71]

$$f(x) \sim P(0|\mu)G(x - x_0, 0, \sigma_0) + \sum_{n=1}^{N} \sum_{m=1}^{n} p_{n,m}(p_{XT})P(m|\mu)G(x - x_0, n, \sigma_t), \tag{4.1}$$

a multi-peak function that includes optical crosstalk and is regularly used to describe SiPM charge spectra. $P(m|\mu)$ is the Poisson probability of having m fired cells given a mean number of photons μ. $G(x, n, \sigma)$ is a Gaussian function with expected value n and variance σ^2. The probability of the optical crosstalk p_{XT} is modeled by a binomial function $p_{n,m}$ (see Equation 1 in [71]). x_0 is the position of the pedestal peak in the spectrum and x is measured in phe. The width of the n-th peak is given by $\sigma_t = \sqrt{\sigma_0^2 + n\sigma_1^2}$ with σ_0 the pedestal noise and σ_1 corresponding to SiPM cell-to-cell gain fluctuations. The smaller $\sigma_t(n)$, the better the SiPM resolution of the n-th peak.

The LASiP measurement described above was repeated changing the number of summed SiPMs from 1 to 8. The LED intensity was regulated to keep the mean flux at a level of a few phes to simplify the identification of single-phe pulses. The obtained charge

spectrum was fitted with Equation 4.1. In Figure 4.3 the obtained spectra are shown for the measurements of the light of a pulsed LED with a single LASiP while changing the number of summed SiPMs. The single-phe resolution decreases as the number of summed SiPMs increases. All spectra could be fitted with Equation 4.1 except the last spectrum for 8 summed SiPMs where it was impossible to identify peaks. In the remaining seven cases we obtained constant fit parameters $p_{XT} \sim 25\%$ and $\sigma_1 \sim 0.07$ phe. The parameter σ_0 increased with the square root of the number of summed SiPM $\sqrt{N_{SiPM}}$ as shown in Figure 4.4. The fit function $\sigma_0 = p_0 + p_1\sqrt{N_{SiPM}}$ was used to estimate σ_0 for the case of 8 SiPMs as ~ 0.53 phe.

4.1.4. Application of LASiPs in SPECT

The LASiP prototype was developed with the goal of testing the feasibility of using large SiPM pixels in single-photon emission computed tomography (SPECT). SPECT is a nuclear imaging technique that employs a single gamma-ray tracer. It is highly efficient in diagnosing diseases such as Alzheimer's [163] and Parkinson's [153]. A standard clinical SPECT camera has one or more gamma camera heads. A typical gamma camera for SPECT consists of a lead collimator followed by a large scintillating crystal ($\sim 50 \times 40 \times 1$ cm^3) [20] and an array of 50-100 PMTs (4-8 cm diameter). The camera is shielded by a thick layer of lead, making it heavy (it can weigh a few hundred kilograms) and bulky. A gantry with two cameras can have a weight of more than 2000 kilograms.
Reducing the size and weight of SPECT scanners would have many advantages: a lighter and more compact scanner would be safer to operate and allow more flexibility for the physician and the patient. In addition, such a scanner could be installed in smaller rooms and would therefore fit easier into smaller hospitals [72]. In the last

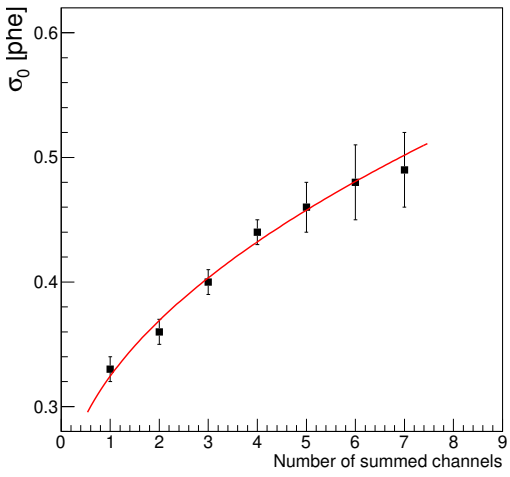

Figure 4.4.: σ_0 obtained from a fit of the spectra in Figure 4.3 as a function of the number of summed LASiP channels, i.e. SiPMs. It was fitted with $\sigma_0 = p_0 + p_1\sqrt{N_{SiPM}}$

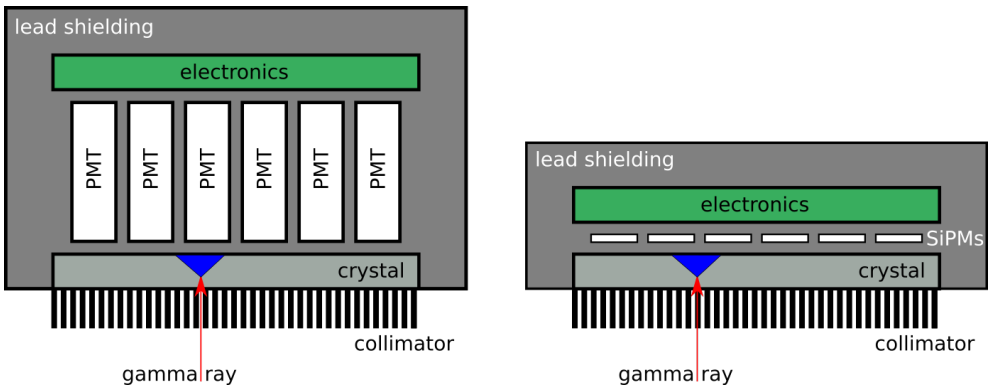

Figure 4.5.: The main components of a gamma camera are a lead collimator, a scintillator crystal and an array of PMTs (**left**). Replacing PMTs with SiPMs would allow reducing the volume of the camera and thus the amount of lead needed for the shielding (**right**).

years, the use of direct conversion detectors based on Cadmium Telluride (CdT) and Cadmium-Zinc-Telluride (CZT) gained popularity. Compared to standard systems, they provide an improvement in energy and spatial resolution and are lighter and more compact. However, the increasing camera price with size limits the use of this technology for full-body SPECT [12]. Most CZT-SPECT scanners which were developed in the last decade are relatively small instruments with the purpose to image specific organs (for example [123]).
A cost-effective way to develop compact and light full-body SPECT cameras would be to replace the PMTs of a SPECT camera with SiPMs. A typical PMT in a SPECT camera is ~ 15 cm long (without electronics). About 50 % of the camera volume is occupied by the PMTs. The thickness of a SiPM is negligible in comparison. A SPECT camera using SiPMs would require less shielding material which would reduce the weight of the camera significantly (see Figure 4.5). Moreover, the insensibility of SiPMs to magnetic fields is interesting for combining SPECT and Magnetic Resonance Imaging [92]. The main obstacle to use SiPMs in a full-body SPECT camera is their small sensitive area. One would need a few thousand channels to fill a camera with the largest commercially-available SiPMs of 6×6 mm^2. This would increase dramatically the cost and complexity of the system and is one of the main reasons why nearly all research about SiPMs in SPECT has been limited to small cameras [92, 32, 140].

Our group proposed the LASiP concept as a solution to use SiPMs in full-body SPECT cameras. In order to test the feasibility of using LASiPs in a SPECT camera we built a proof-of-concept micro-camera that consisted of 4 LASiPs. Further information about the structure of the micro-camera and the results of its characterization are presented in Appendix A.

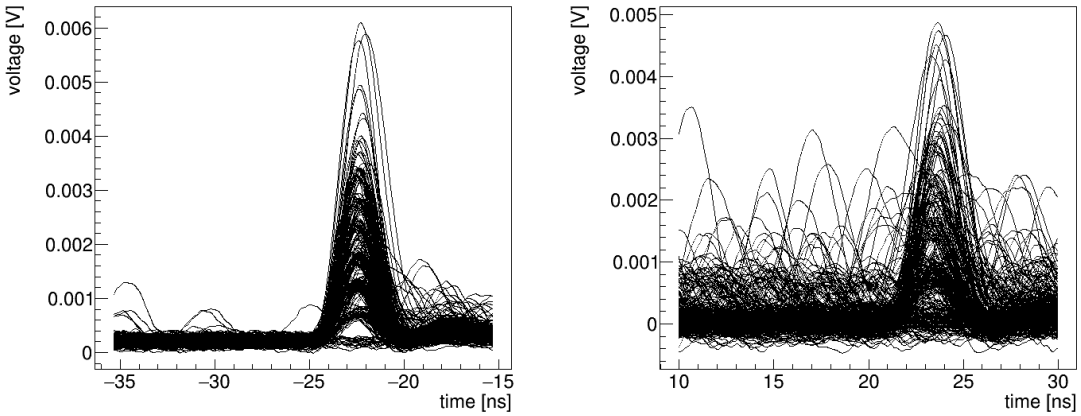

Figure 4.6.: Pulses from single S13360-6075VS MPPC from Hamamatsu (**left**) and summed output of the SiPM detector module equipped with nine S13360-6075VS MPPC from Hamamatsu (**right**).

4.1.5. Application of LASiP in MAGIC

The most sensitive IACT arrays as VERITAS [91], HESS [14] and MAGIC [17] use PMTs as photodetectors. Only about 18 % of the available observation time corresponds to a dark sky, i.e. a night sky with no Moon or twilight [77]. Observations under moonlight and twilight are sometimes possible if the HV of the PMTs is reduced or if optical filters that block background light are employed [15]. Also, the MAGIC interferometer uses special Moon filters in order to prevent damaging the PMTs under bright moonlight (see Section 3.5.2). In contrast to PMTs SiPMs are robust devices that do not undergo any significant aging when exposed to bright light [138]. In addition, SiPMs provide usually a higher PDE and a better time resolution. Especially NUV-SiPMs have the potential to improve the performance of IACT arrays compared to standard PMTs [10]. Time resolution and PDE are also relevant for the performance of IACT arrays when employed as intensity interferometers (see Chapter 2.3).
SiPMs have successfully been implemented in the First G-APD Cherenkov Telescope (FACT) which proved that they are suitable to detect Cherenkov light of extended air showers [34]. However, the pixel size in the FACT telescope is small. The solution implemented in FACT is not feasible for large IACTs as MAGIC . A modular SiPM detector cluster was developed for the camera of MAGIC-I with the same dimension as the PMT modules in MAGIC (see details in [76], [77] and [78]). The goal of the SiPM detector module was not to compete with the PMT modules but to test the feasibility of large SiPM-based pixels in IACTs. The second generation pixel [77] was equipped with nine SiPMs (either S13360-6075VS MPPC from Hamamatsu [79] or MicroFJ-60035-TSV from SensL [147]). The individual SiPM signals are summed into a single output (as in the LASiP concept). The sum is performed by using discrete transistor common base circuits with low input impedance and high output impedance

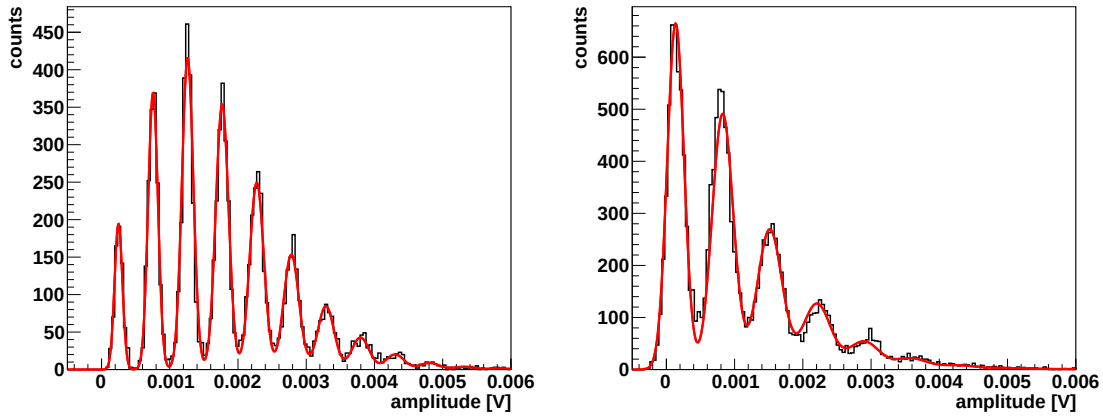

Figure 4.7.: Single photo-electron spectrum of a single S13360-6075VS MPPC from Hamamatsu (**left**) and summed output of SiPM detector module equipped with nine S13360-6075VS MPPC from Hamamatsu (**right**).

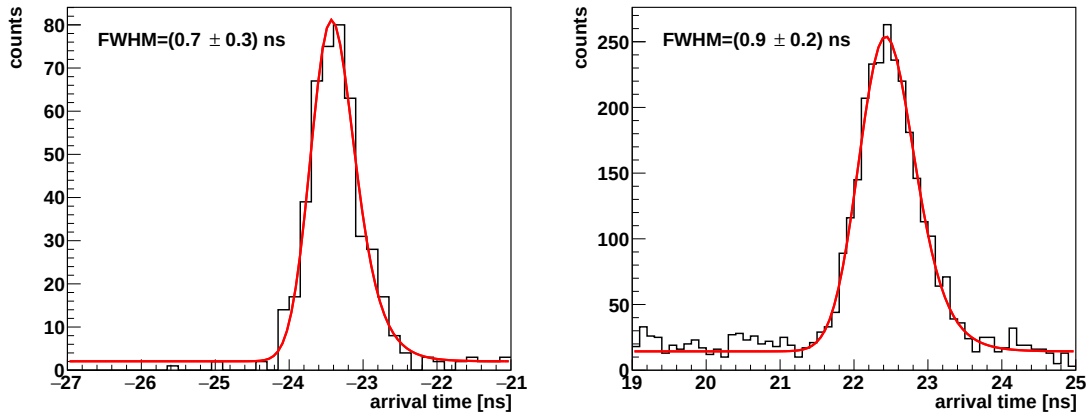

Figure 4.8.: Arrival time distribution of a single S13360-6075VS MPPC from Hamamatsu (**left**) and summed output of SiPM detector module equipped with nine S13360-6075VS MPPC from Hamamatsu (**right**).

to preserve the fast signal shape. Details of the circuit design can be found in [55].

I received from Alexander Hahn data files with 10k pulses of a single S13360-6075VS MPPC and the SiPM detector module equipped with nine S13360-6075VS MPPCs. The pulses were recorded with a Rohde & Schwarz RTO 1044 oscilloscope with a sampling rate of 50 GS/s. The photodetectors (either single SiPM or SiPM detector module) were flashed with a 457 nm PicoQuant sub-nanosecond pulsed LED with a FWHM of 704 ps. The oscilloscope and LED were triggered by an external signal from an Agilent 81110A pulse generator. The LED driver was a PDL 800-D. The LED intensity was adjusted to keep the mean photon number at a level of a few phes.

In the left panel of Figure 4.6 pulses of a single S13360-6075VS MPPC are presented, in the right panel pulses of the sum of nine S13360-6075VS MPPC. The pulses do not have the typical SiPM pulse shape (fast rise time, slow decay time), but were adjusted to have a shape similar to PMT pulses. In Figure 4.7 the single photo-electron spectrum of a S13360-6075VS MPPC (left panel) and of the sum of nine S13360-6075VS MPPC (right panel) are shown. The spectrum was fitted with Equation 2 of [71] (see Section 4.1.3). The spectrum proves that the SiPM detector module provides a very good single photon resolution (see [77]). In Figure 4.8 the arrival time distribution of a single S13360-6075VS MPPC (left panel) and of a SiPM pixel (right) is shown. The arrival time was defined as the time when the rising edge exceeded the 60 % level of the maximum amplitude. The arrival time distribution was fitted with a Gaussian convolved with an exponential (as in [121]). I obtained a SPTR of 0.7 ± 0.3 ns FWHM for a single S13360-6075VS MPPC and 0.9 ± 0.2 ns FWHM for a LASiP that sums nine of them. The errors are relatively large because statistics of the arrival time distribution in 4.8 were rather low due to a limited amount of data available.

In [78] the SNR was calculated for SiPM- and PMT-based pixels as a function of the zenith angle. The SiPM pixels performed slightly better than PMT pixels for low zenith angles, at large zenith angles they even outperformed MAGIC PMTs. In Section 5.6 and 5.7 I am going to discuss the potential of using SiPM pixels in MAGIC intensity interferometry observations.

4.2. Photo-Trap

In the last section, the concept of summing the currents of several SiPMs into a single output to build a large SiPM pixel was introduced. This approach provides a relatively simple solution to increase the area of a SiPM pixel without compromising, for instance, its PDE. Still, it has some limitations. The capacitance of the pixel increases by $\sqrt{N_{SiPM}}$ and also the noise is summed. As a consequence, the SNR is degraded, in particular the single-phe resolution as well as the timing performance. Apart from this, the cost of a pixel and its DCR still increases linearly with the area.

An alternative approach to build large pixels consists in combining SiPMs with passive light collectors that behave as 'traps' for photons [104]. The concept of using solid light concentrators coupled to photodetectors to increase the collection area has been widely used in different fields like particle physics [98] or solar energy [46]. Based on this approach a prototype pixel with a 15 mm diameter that was made by coupling a SiPM to a PMMA disk doped with a wavelength-shifter (WLS) fluor was presented in [71]. In this so-called *Light-Trap* pixel incoming photons are absorbed by the WLS. Then they are re-emitted isotropically and a fraction of them is trapped by total internal reflection (TIR) inside the PMMA disk until they reach the SiPM. The benefit of this approach is that, while keeping the noise, capacitance, SNR and cost of a single SiPM, a Light-Trap pixel can have a sensitive area that is several tens times larger than the area of a classical SiPM. Furthermore, it requires only very simple electronics. The main disadvantage of Light-Trap is its low efficiency because a large fraction of photons either escape or are absorbed without reaching the SiPM. Moreover, the refractive index of the incident medium needs to be significantly lower than the one of WLS plastic (~ 1.5) to accomplish a sufficiently low critical angle for TIR. This limits the application of Light-Trap to setups in which the incident medium is air or vacuum.
In this section the *Photo-Trap* is introduced, a large-area SiPM pixel that combines a 1-D photonic crystal (or dichroic) filter with a Light-Trap. The filter could both enable to increase the efficiency and soften the condition on the refractive index of the incident medium. Photo-Trap also introduces some upgrades like the use of diffuse reflectors and simple, commercial and compact readout electronics. In order to test the concept, we built and characterized four different Photo-Trap prototypes with active areas of 2×2 and 4×4 cm^2.

4.2.1. The Photo-Trap principle

In the left panel of Figure 4.9 the different components of a Photo-Trap pixel are shown. A plastic volume with a refractive index $n \simeq 1.5$ is coupled to a SiPM. The plastic is doped with a WLS that absorbs light in a wavelength range $\Delta\lambda_0$ and re-emits it at longer wavelengths $\Delta\lambda_1$. The sides and the back of the WLS plastic are covered with a reflecting material. The front of the plastic is covered with a dichroic filter with a very high transmittance for $\Delta\lambda_0$ and a very high reflectivity for $\Delta\lambda_1$. There is a very narrow air gap between the WLS plastic, the filter and the reflecting material.

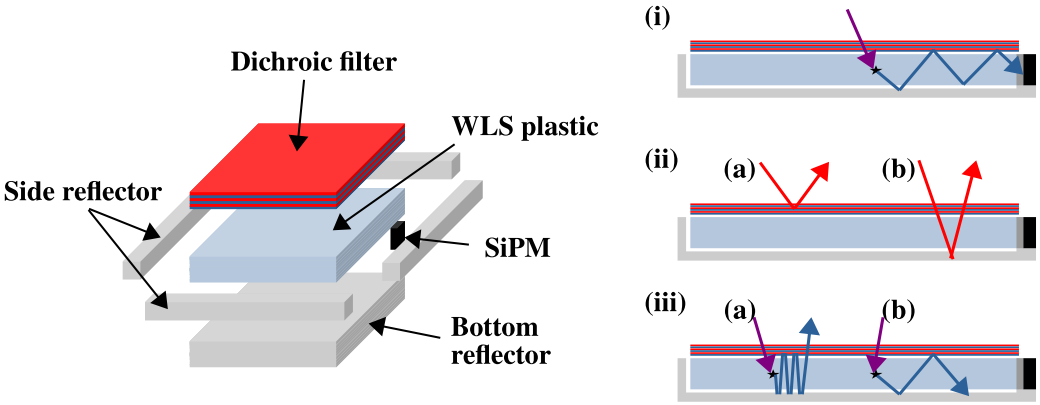

Figure 4.9.: Scheme showing the different components of a Photo-Trap pixel (**left**). Examples of interactions of photons with the pixel (**right**): (i) An incident photon with a wavelength within $\Delta\lambda_0$ is absorbed by the WLS. The re-emitted photon is reflected a few times in WLS and is *detected* by the SiPM. (ii) An incident photon with wavelengths outside $\Delta\lambda_0$ is either *rejected* by the filter (a) or goes through the WLS plastic without being absorbed and escapes through the top (b). (iii) The wavelength-shifted photons could *escape* either through the filter with a probability given by the filter transmittance at $\Delta\lambda_1$ (a) or they could be *absorbed* by a pixel component (like the reflectors) (b).

Photons that hit the front of the pixel can interact in different ways (examples are illustrated in the right panel of Figure 4.9): photons with wavelengths within $\Delta\lambda_0$ pass through the filter, enter the plastic volume and are absorbed by the WLS. A photon with a wavelength within $\Delta\lambda_1$ will be re-emitted with a probability given by the quantum yield of the WLS. The re-emission of wavelength-shifted photons is isotropic. A fraction of these photons is trapped inside the plastic volume due to total internal reflection (TIR) or due to reflections at the filter or the reflecting detector walls. Some photons will reach the SiPM, whereas the rest is either absorbed or escapes the pixel. The concept of Photo-Trap enables a significant increase of the total collection area while keeping the noise, capacitance and power consumption of a single SiPM. Hence, it is possible to build pixels of a few cm^2 with the single-phe resolution, capacitance and DCR of a SiPM of a few mm^2. Besides, a significant cost reduction can be achieved because the WLS plastic and the filter can be mass-produced.
The optical gain G at a given wavelength λ and angle of incidence (AOI) θ is defined as:

$$G(\lambda,\theta) = \frac{S_{\mathrm{WLS}}}{S_{\mathrm{SiPM}}}\,\epsilon(\lambda,\theta). \tag{4.2}$$

S_{WLS} is the area of the WLS plastic and S_{SiPM} the area of the SiPM. The trapping efficiency ϵ of the pixel is defined as:

$$\epsilon(\lambda,\theta) = T_F(\lambda,\theta)\, T_{\mathrm{WLS}}(\lambda,\theta)\, A_{\mathrm{WLS}}(\lambda)\, Y_{\mathrm{WLS}}\, C_{\mathrm{eff}}(\Delta\lambda_1)\, \frac{PDE_{\mathrm{SiPM}}(\Delta\lambda_1)}{PDE_{\mathrm{SiPM}}(\lambda)}. \tag{4.3}$$

T_F is the filter transmittance and T_{WLS} is the Fresnel transmittance at the top surface of the WLS plastic (~ 96 % at normal incidence if the incident medium is air and the refractive index of the WLS plastic $\simeq 1.5$). A_{WLS} is the WLS absorption probability and Y_{WLS} the WLS re-emission (quantum yield) probability. PDE_{SiPM} is the PDE of the SiPM and C_{eff} is the collection efficiency which is the ratio of the wavelength-shifted photons that reach the SiPM compared to the overall number of wavelength-shifted photons. The pixel is essentially blind to all wavelengths outside $\Delta\lambda_0$. It is then possible to achieve sensitivity in a specific wavelength range by properly choosing the filter and the WLS plastic. This could be useful for background rejection in some applications.
Under the condition of an homogeneous flux, $G(\lambda)$ can be obtained as:

$$G(\lambda) = \frac{\mu_{\text{Photo-Trap}}(\lambda)}{\mu_{\mathrm{SiPM}}(\lambda)} \tag{4.4}$$

where $\mu_{\text{Photo-Trap}}$ the mean number of photons detected by Photo-Trap and μ_{SiPM} the mean number of photons detected by a reference SiPM with the same area as the one used to build the pixel. The PDE of Photo-Trap is related to ϵ as:

$$PDE_{\text{Photo-Trap}}(\lambda) = \epsilon(\lambda)\, PDE_{\mathrm{SiPM}}(\Delta\lambda_1) \tag{4.5}$$

4.2.2. Proof-of-concept pixels

Our group built four proof-of-concept pixels. They differ in the size of their WLS plastic and in the area of their SiPM. The main physical characteristics of the four prototypes are summarized in Table 4.1. A picture of Prototype I, with and without filter, is shown in Figure 4.10.
All pixels are equipped with an EJ-286 WLS plastic from Eljen Technology. The WLS absorbs light between 320 nm and 380 nm and re-emits at blue wavelengths

Prototype nr.	$\mathbf{S}_{\mathrm{WLS}}$	$\mathbf{S}_{\mathrm{SiPM}}$
I	20×20 mm^2	3×3 mm^2
II	20×20 mm^2	3×12 mm^2
III	40×40 mm^2	3×3 mm^2
IV	40×40 mm^2	3×12 mm^2

Table 4.1.: Main physical differences of the four Photo-Trap prototypes. S_{WLS} and S_{SiPM} are the areas of the WLS plastic and the SiPM, respectively.

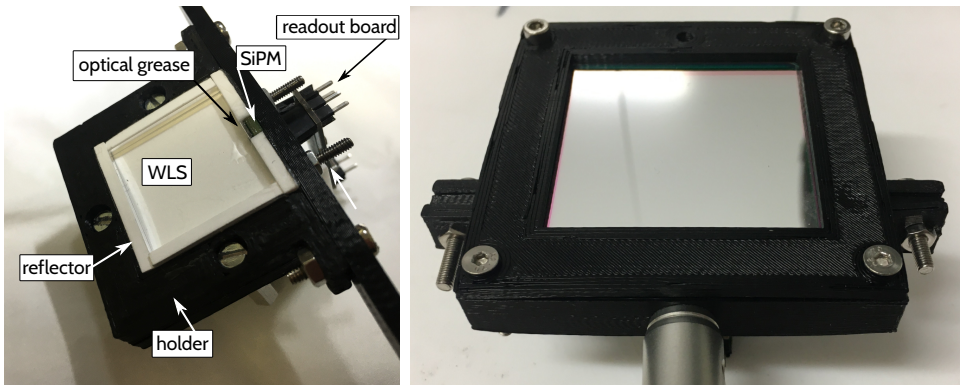

Figure 4.10.: Picture of Prototype I without the filter showing the different pixel components (**left**). Prototype I seen from top with the filter mounted (**right**).

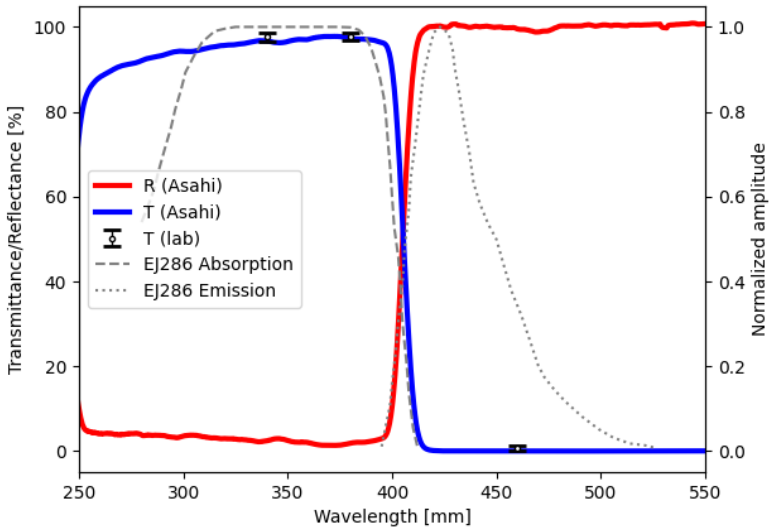

Figure 4.11.: Transmittance (blue solid line) and reflectance (red solid line) at normal incidence of the Asahi ZUV0400 short pass filter, as provided by Asahi Spectra. Black dots show the transmittance measured in the lab at 340, 375 and 460 nm. The plot also shows the absorption (gray dashed line) and re-emission (gray dotted line) spectra of the EJ-286 WLS.

(peaking at ~ 425 nm, see Figure 4.11). The re-emission time can be described by an exponential with a characteristic decay time of ~ 1.2 ns. We ordered plastics with enough concentration of the EJ-286 dopant to absorb > 99 % of 350 nm photons within 1.5 mm. The plastics were cut by Eljen in sizes of $20 \times 20 \times 3$ mm^3 and $40 \times 40 \times 3$ mm^3. The $20 \times 20 \times 3$ mm^3 samples were either of Polyvinyltoluene (PVT) or Polystyrene (PST), and polished with two different techniques: (1) diamond-milled only and (2) additionally to diamond-milled, hand polished using moist polishing compounds of sub-micron particle size, according to the manufacturer. The goal of having these

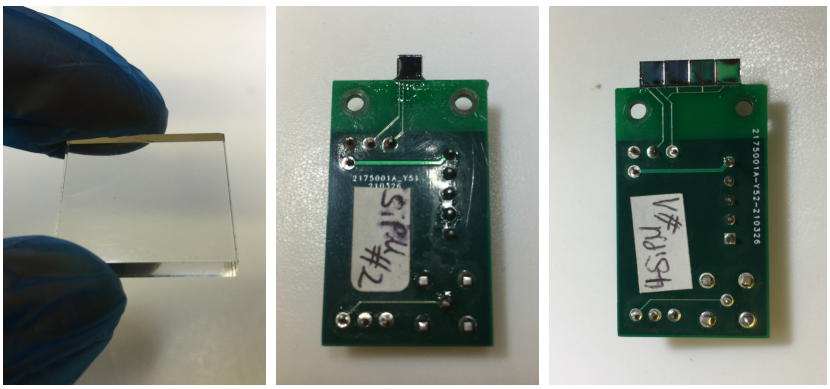

Figure 4.12.: One of the 20 × 20 × 3 mm^3 PVT pieces supplied by Eljen (**left**). The readout board is equipped with a 3 × 3 mm^2 SiPM of ON Semiconductor 30035 J-Series (**center**). Readout board equipped with 3 × 12 mm^2 SiPM built of four 3 × 3 mm^2 SiPMs (**right**).

different samples was to evaluate if the substrate material or the polishing technique had an impact on the pixel performance. The 40 × 40 × 3 mm^3 samples were bought only in PVT and with the second optical polishing technique. In the left panel of Figure 4.12 one of the PVT samples can be seen.
All pixels used a commercial ZUV0400 short-pass interference filter from Asahi Spectra. The filter features a thickness of ~ 1 mm and an area of 50 × 50 mm^2 with a clear aperture of 46 × 46 mm^2. Its cut-off wavelength at normal incidence is 400 nm. The filter transmittance/reflectance curve match very well with the spectral characteristics of the EJ-286 (see Figure 4.11).
The pixels use MICROFJ-30035-TSV SiPMs from Onsemi[1], which have an active area of 3.07 × 3.07 mm^2. We decided to use these SiPMs because of their small chip size (3.16 × 3.16 mm^2) which allowed us to minimize dead space when designing and building the pixel. The MICROFJ-30035-TSV SiPM has a breakdown voltage of ~ 24.6 V at 22°C. I performed all our measurements at an over-voltage of 3.4 V, at which these SiPMs provide a peak PDE of ~ 41 %, according to the manufacturer. At this over-voltage, I measured a DCR of ~ 100 kHz/mm^2 and a crosstalk probability of ~ 13 %, which was consistent with the specifications from the datasheet.
We mounted the SiPMs on a custom-made compact readout board that allowed to switch between two different preamplifiers from Advatech: AMP-0604 (×20 - ×60 gain, ~ 5 ns rise time) and AMP-0611 (×10 - ×20 gain, ~ 0.7 ns rise time). Two readout boards were built: one was designed to host a single SiPM, the other one to hold four of them connected in parallel which corresponds to a single SiPM of ~ 3 × 12 mm^2. In doing so we could achieve a SiPM that had approximately the area of a 6 × 6 mm^2 SiPM but could be coupled to a 3 mm thick WLS plastic. The readout boards can be seen in the center and right panels of Figure 4.12.

[1] www.onsemi.com

The SiPM was attached to the WLS plastic with an optical coupling gel SS-988 from Silicone Solutions. According to the manufacturer, its refractive index is ~ 1.466 and its transmittance > 99.9 % at ~ 420 nm. The pixel components were mounted with 3D-printed plastic holders that I designed and printed. The walls of the holder were covered with a 2 mm thick Optopolymer® film from Berghof Fluoroplastics (~ 98 % diffuse reflectivity above 400 nm) to create reflecting walls.

4.2.3. Characterization methods

I characterized the four Photo-trap prototypes in the laboratory. In addition, the impact of the different pixel components on the performance was studied through simulations.

4.2.3.1. Laboratory measurements

I characterized the four Photo-Trap prototypes in the laboratory using the setup shown in Figures 4.13 and 4.14. I illuminated the prototypes with different PicoQuant PLS-Series pulsed LEDs, peaking at ~ 340 nm and ~ 370 nm (FWHM of ~ 9 nm and ~ 20 nm respectively). The LEDs were driven by a PDL 800-B PicoQuant LED driver and generated pulses with a width of ~ 800 ps. The output signal was recorded either with a CAEN DT5720 digitizer or with a LeCroy SD 3010 oscilloscope depending on the measurement to be performed. The Photo-Trap prototypes were mounted on rotation and translation stages that allowed to rotate the sensor and to move it along the *(x,y)* plane (detector plane), which was orthogonal to the direction of the incident beam.

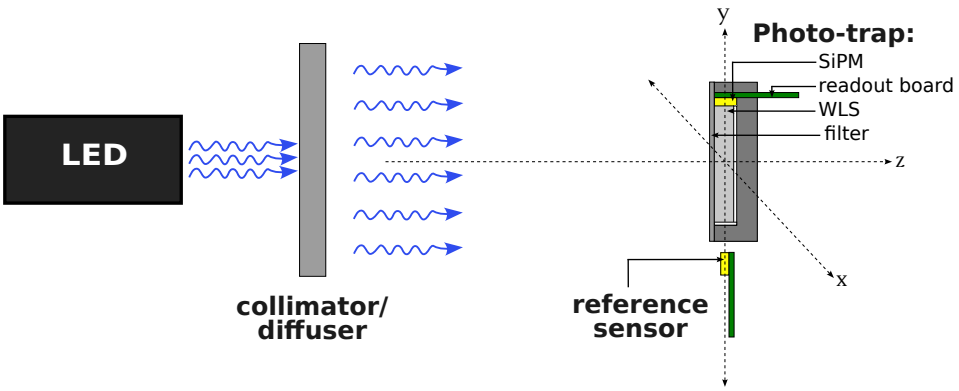

Figure 4.13.: Scheme showing the setup used to characterize the Photo-Trap prototypes. The light of the LED is either collimated or diffused (as shown here), depending on the measurement to be performed. The Photo-Trap prototypes can be moved in the *(x,y)* plane and rotated on the *y* axis. Depending on the measurement to be performed, a reference sensor is mounted in the *(x,y)* plane.

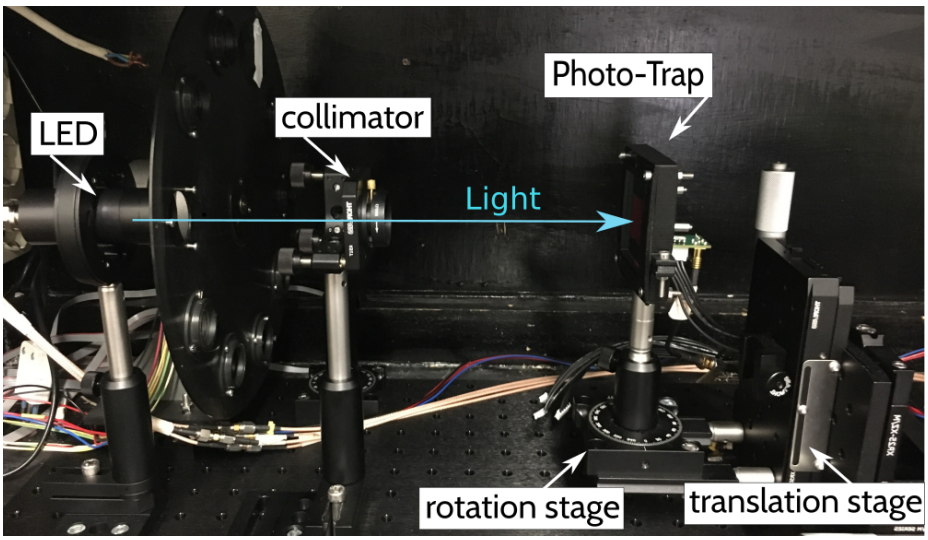

Figure 4.14.: Image from the laboratory showing the setup to characterize the Photo-Trap prototypes. The light of the LED was collimated. The Photo-Trap prototypes can be moved in the *(x,y)* plane using a translation stage and rotated on the y axis with a rotation stage.

Optical gain

The optical gain could be obtained by measuring the ratio of the signal that was collected by the Photo-Trap prototypes to the one that was collected by a reference sensor in the same, spatially homogeneous, incident flux. The reference sensor was a single, 'naked' SiPM, similar to the one that was used to build the prototypes. I flashed the LED at a frequency of 1 kHz. Right after the LED, I placed a Teflon diffuser to guarantee an uniform flux in the area of the prototype and the reference detector. I used an AMP-0604 amplifier in these measurements because it provides a higher gain. I recorded waveforms of 400 ns length with the CAEN DT5720 digitizer at 250 MSps. A single measurement comprised of 50k waveforms is obtained when the LED is ON, followed by additional 50k waveforms when the LED is OFF. Inside a 40 ns window, I extracted the signal as the maximum amplitude. The single-phe spectrum of Prototype III and IV from a measurement when the LED is ON in Figure 4.15 demonstrates the very good single-phe resolution of the Photo-Trap prototypes. As described in [133], the mean number of photons μ collected by a detector can be determined as

$$\mu = ln(N_{\text{led}})/ln(N_{\text{dark}}), \tag{4.6}$$

where N_{led} is the probability of having no detection (i.e. the signal < 0.5 phe) when the LED is ON and N_{dark} when the LED is OFF. The expression is valid under the condition that the number of detected photons and dark counts of each event is Poisson distributed. This method to determine μ is independent of the optical crosstalk and afterpulsing probability of the SiPMs employed. If μ is obtained both for Photo-Trap and for the reference sensor, the optical gain can be calculated using Equation 4.4.

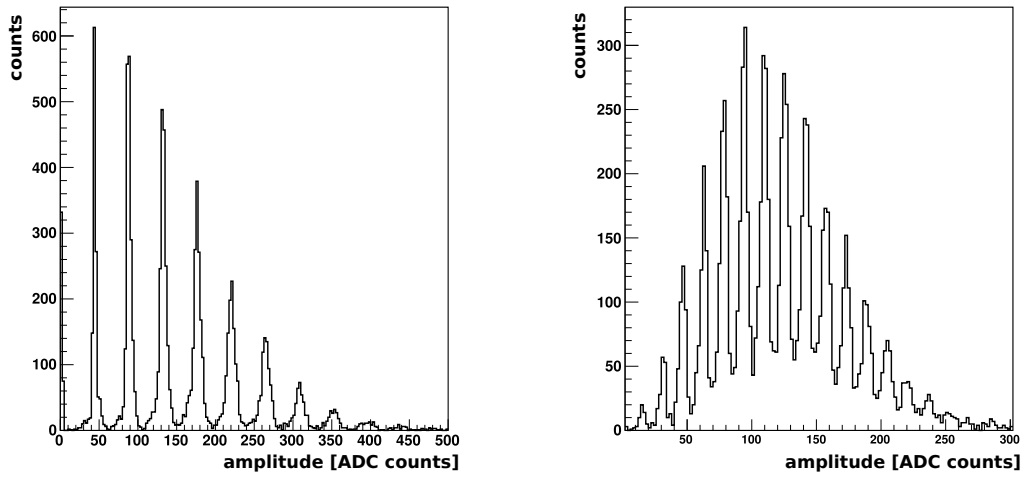

Figure 4.15.: Single-phe spectrum with LED ON of Prototype III (**left**) and Prototype IV (**right**).

To avoid any biasing of the result and to test how reproducible it was, I executed all measurements following this procedure:

1. Cleaning of the WLS plastic and the filter;
2. Mounting of the pixel components;
3. Recording a measurement;
4. Removing all components from the holder (except for reflectors that were stuck to the holder);

To evaluate the impact of the filter and the reflecting walls, I performed measurements with and without the filter and with and without reflecting material for all prototypes.

Position-dependent efficiency

I studied the position dependence of the trapping efficiency of each prototype. For this purpose, I operated the LEDs in continuous mode and placed a collimator, which allowed me to achieve a beam size of ~ 5 mm FWHM in the detector plane. I mounted the Photo-Trap prototype on a translation stage and moved it in the *(x,y)* plane, following a 2D orthogonal grid with a lattice spacing of 2 mm. For each *(x,y)* coordinate pair I measured the output current of the prototype.
The measurement in the *(x,y)* plane served also to find a precise alignment of the setup to focus the beam to the pixel center. For this, I moved the prototype along a 1D line in the *(x,y)*-plane with a line spacing of less than 2 mm. The left panel of Figure 4.16 shows an example of such a measurement for Prototype III in the x-direction through the center of the pixel. The measured current, relative to the current at the pixel

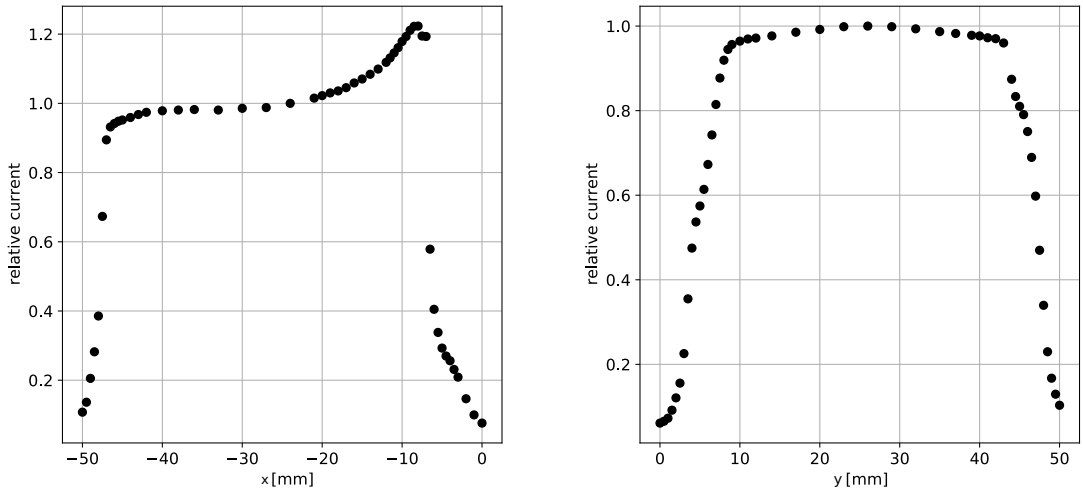

Figure 4.16.: Measured current, relative to the current at the pixel center, of Prototype III: as a function of the x-coordinate of the measurement position (**left**), or as a function of the y-coordinate of the measurement position (**right**).

center, is plotted as a function of the x-coordinate of the measurement position. At the edges of the pixel the relative current drops rapidly. Near the position of the SiPM the current increases. In the right panel of Figure 4.16 the measurement of Prototype III in the y-direction is shown. Here the measured current, relative to the current at the pixel center, is plotted as a function of the y-coordinate of the measurement position.

AOI dependence

The FOV of Photo-Trap is wavelength-dependent because the transmittance of the interference filter depends on the angle of incidence (AOI). I studied this effect by measuring first the filter transmittance at 340 and 370 nm as a function of the AOI. I placed a filter on a rotating stage and a collimator between the filter and the LED as shown in Figure 4.14. The reference sensor detected the light transmitted by the filter. I operated the LEDs in continuous mode. With this setup I recorded and compared the output of the reference sensor with and without the filter for AOIs ranging from 0 to 70°. For a cross-check, I also measured the angular dependence of the trapping efficiency of Prototype I.

Time resolution

I studied the timing properties of the Photo-Trap prototypes by flashing them with LED pulses at a frequency of 1 kHz. With the oscilloscope at 10 GS/s I recorded waveforms of a length of 190 ns. To guarantee a constant photon flux all over the Photo-Trap area, I diffused the light using Teflon. I used for these measurements the AMP-0611 amplifier because it had a faster rise time. Since the goal was to measure

the SPTR of the SiPMs and Photo-Trap prototypes, I only kept those events that corresponded to a single-fired microcell, i.e. waveforms with a maximum amplitude between 0.5 phe and 1.5 phe. I defined the arrival time as the time (relative to the trigger) at which the rising edge of the pulse reached a threshold that was equal to 60 % of the amplitude of an average single-phe pulse. The obtained arrival time distributions of the Photo-Trap prototypes and the reference sensors were compared with those coming from the simulations that are described in Section 4.2.3.2.

4.2.3.2. Simulations

Daniel Guberman simulated the Photo-Trap pixel with Geant4 [11]. The aim was to examine the impact of the different components of Photo-Trap on its performance. In the simulation optical photons move towards a PVT volume with the same absorption and re-emission properties as the Eljen EJ-286 WLS plastic. All photons are tracked until they are either wavelength-shifted and detected by the SiPM or get lost in some way (absorption, escape). The SiPM is assumed to be an ideal sensor with 100 % detection efficiency. The PDE is taken later into account by scaling the output accordingly. The simulation also contains a thin volume of 0.1 mm thickness that optically couples the SiPMs and the PVT. It has the same area as the SiPM and the refractive index and absorption properties of the optical coupling gel SS-988 used in the laboratory. The reflecting material at the sides and bottom of the pixel is described with the *RoughTeflon_LUT* look-up table from the LUT DAVIS model [154]. The filter was simulated as an additional volume with 100 % transmittance below 380 nm and 100 % reflectance above 400 nm at all AOI (assumed the ideal case). The bottom surface of the filter was handled as a dichroic-dielectric boundary. The thickness of the air gap between volumes of the WLS plastic and reflectors and between WLS plastic and filter was an input parameter of the simulation.
The surface roughness of the WLS plastic has a significant impact on the trapping efficiency of Photo-Trap. The roughness depends on the production process of the WLS plastic (cutting and polishing) and on the way in which it is manipulated in the laboratory. The roughness can be understood as local differences in the direction of the normal vector between the real surface and a perfectly flat one. The rougher a surface is, the less ordered will be the photon path. The impact of the roughness could be studied with the simulation by using different models available in Geant4 to describe the interaction of photons in the boundaries of the WLS plastic. The simulation used the *Glisur* model (*polished* and *rough*) and the DAVIS *Polished_LUT* and *Rough_LUT* models. The Glisur model controls the surface finishing with a single polishing parameter that can be adjusted from 0 to 1. It indicates the scattering probability of the photons at the boundaries. A polishing of 1 corresponds to a perfectly polished surface. The DAVIS model is based on look-up tables that define the path of a photon that reaches the boundary. These tables were actually developed for LYSO crystals but were used successfully also for other crystals (see also [72] for details).

4.2.4. Evaluation of performance of the Photo-Trap prototypes

In this section, I present the results of my characterization measurements and of the simulation of the Photo-Trap prototypes.

4.2.4.1. Optical gain and trapping efficiency

In Figure 4.17 the measured optical gain G and trapping efficiency (TE) at 340 nm are shown for each prototype. The results are plotted for different levels of the pixel construction: without reflectors or filter ('WLS only'), after adding the reflectors but before adding the filter ('WLS + Reflectors') and after adding the filter ('Full Pixel'). For Prototype I I also show the results for different plastic materials/polishing techniques. The average values of G and TE are listed in Table 4.2.
The filter represents the main upgrade of Photo-Trap compared to the Light-Trap. It

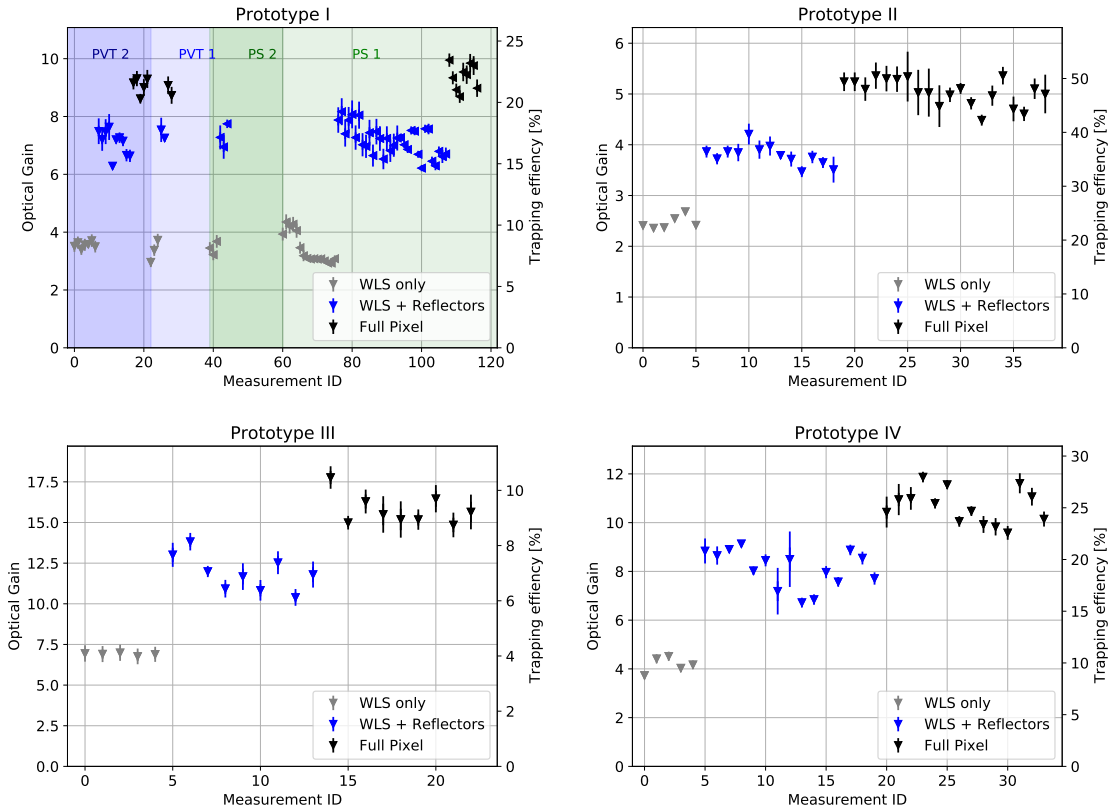

Figure 4.17.: Optical gain and trapping efficiency of all prototypes at different construction 'levels': without reflectors or filter ('WLS only'), after adding the reflectors but before adding the filter ('WLS + Reflectors') and after adding the filter ('Full Pixel'). In the case of Prototype I the results are shown for different WLS substrate materials (PS and PVT) and for polishing techniques 1 and 2 (see Section 4.2.2).

Prototype nr.	$\mathbf{S_{WLS}/S_{SiPM}}$	**G**	**TE [%]**
I	~ 42	9.2 ± 0.4	21.7 ± 1.0
II	~ 10	5.0 ± 0.3	47.5 ± 2.4
III	~ 170	15.8 ± 0.9	9.3 ± 0.6
IV	~ 42	10.7 ± 0.7	25.1 ± 1.7

Table 4.2.: Measured optical gain G and trapping efficiency TE of the Photo-Trap prototypes at 340 nm. S_{WLS} is the area of the WLS and S_{SiPM} the area of the SiPM.

allowed to increase the TE of the prototypes by ~30%. The TE is higher (while G is lower) in prototypes with a lower $S_{\mathrm{WLS}}/S_{\mathrm{SiPM}}$ ratio.
I attribute the spread in the measurements mainly to the pixel construction process. In Figure 4.17 the results of tens of measurement are shown. Not all plastic samples used for the same prototype had exactly the same size, which means that the air gap between WLS plastic and reflectors could be different. Every time I mounted the pixel again for a new measurement (see Section 4.2.3.1) there was a certain chance that something in the pixels changed: the amount of grease used, the alignment of the different components, the size of the reflectors, etc. In particular, I noticed that there was a degradation of the trapping efficiency after several iterations of taking the same WLS plastic in and out. The efficiency increased again when the reflector and/or WLS plastic were replaced with new ones. However, If I left the pixel untouched for a few days and repeated the measurement without taking out any of the pixel components the results were stable (within an error of ~ 3%).
I investigated, in addition, the 'wear and tear' effect by comparing the results obtained with Prototype III using three different WLS pieces. *WLS 1* was a 'new' sample that had no visible scratches on its surface. *WLS 2* was a sample that I used for a long time and was exhibiting some scratches as a result of all the times it had been taken in and out from the pixel. *WLS 3* was a sample that I intentionally scratched using sandpaper. The results are summarized in Table 4.3. The effect of the degradation of the WLS surface can be clearly seen. In the measurements performed without reflector the optical gain was ~ 35 % and ~ 60 %lower in *WLS 2* and *WLS 3*, respectively. The addition of the reflectors helped to recover some of the escaping photons and this degradation turned to be ~ 18 % and ~ 45 % in *WLS 2* and *WLS 3*, respectively. The relative difference became much smaller when the filter is added. In the case of *WLS 2* it even reached the level of *WLS 1*, while the optical gain of *WLS 3* was still ~ 25 % lower.
For Prototype I, Figure 4.17 shows the results for different substrate materials/polishing techniques. Contrary to what I found with the scratches, it would seem that the materials/polishing techniques provided by Eljen did not have any significant effect on the pixel performance (at least not beyond the overall spread). This probably means that the final surface roughness obtained with both polishing techniques in both materials is not different enough to have a strong impact on the performance.

Construction level	WLS 1	WLS 2	WLS 3
WLS only	6.9 ± 0.3	4.6 ± 0.2	2.7 ± 0.1
WLS + Reflector	11.8 ± 0.5	9.7 ± 0.4	5.5 ± 0.2
Full Pixel	15.6 ± 0.6	15.5 ± 0.6	11.7 ± 0.5

Table 4.3.: Measured optical gain G of Photo-Trap Prototype III at 340 nm at different pixel construction levels. The WLS employed was either new (WLS 1) or already in use for a long time showing wear and tear marks (WLS 2). To understand better the impact of scratches on the pixel performance, one WLS was scratched on purpose with sandpaper (WLS 3).

4.2.4.2. Position-dependent efficiency

Figure 4.18 shows the measured position-dependent TE in comparison with the simulated one. The TE here was normalized to the TE at the pixel center. Obviously, I could not achieve the same level of precision with my setup as in the simulations in which one has complete control of the hit position. In the laboratory, I was mainly limited by the light source that provided a non-negligible beam size of a few mm in the detector plane and an asymmetric beam shape. In addition, I could not perfectly control the hit position. My measurements can be seen rather as a support for the results obtained with the simulations. Even if they do not offer many details, they allowed to draw some conclusions:

- TE is mostly flat (within 10 %) over most of the pixel area
- It achieves its maximum close to the SiPM
- It has its minimum close to the corners of the side that contains the SiPM

The results can be interpreted with a purely geometrical approach: when a photon is absorbed and isotropically wavelength-shifted, the probability of directly hitting the SiPM without being affected by a reflection is higher close to the SiPM and lower in the mentioned corners. Figure 4.19 illustrates this effect. For Prototype II, in which the SiPM covers 60 % of the WLS-plastic side, the sensitivity is, indeed, more homogeneous than in the other prototypes, whereas Prototype III shows the opposite scenario.

4.2.4.3. AOI dependence

Figure 4.20 shows the filter transmission and TE of Photo-Trap as a function of the incident angle, relative to the transmission/efficiency at normal incidence. The results are shown both for 340 and 370 nm. At 370 nm the angular response of Photo-Trap is dominated by the filter. The filter transmission and the TE curves are very close to each other. The TE is nearly flat up to ~ 30° and drops to ~ 50 % at ~ 50°. At 340 nm the relative TE of Photo-Trap seems to start dropping before the filter transmission. Probably the main reason for this difference comes from the limitations imposed by

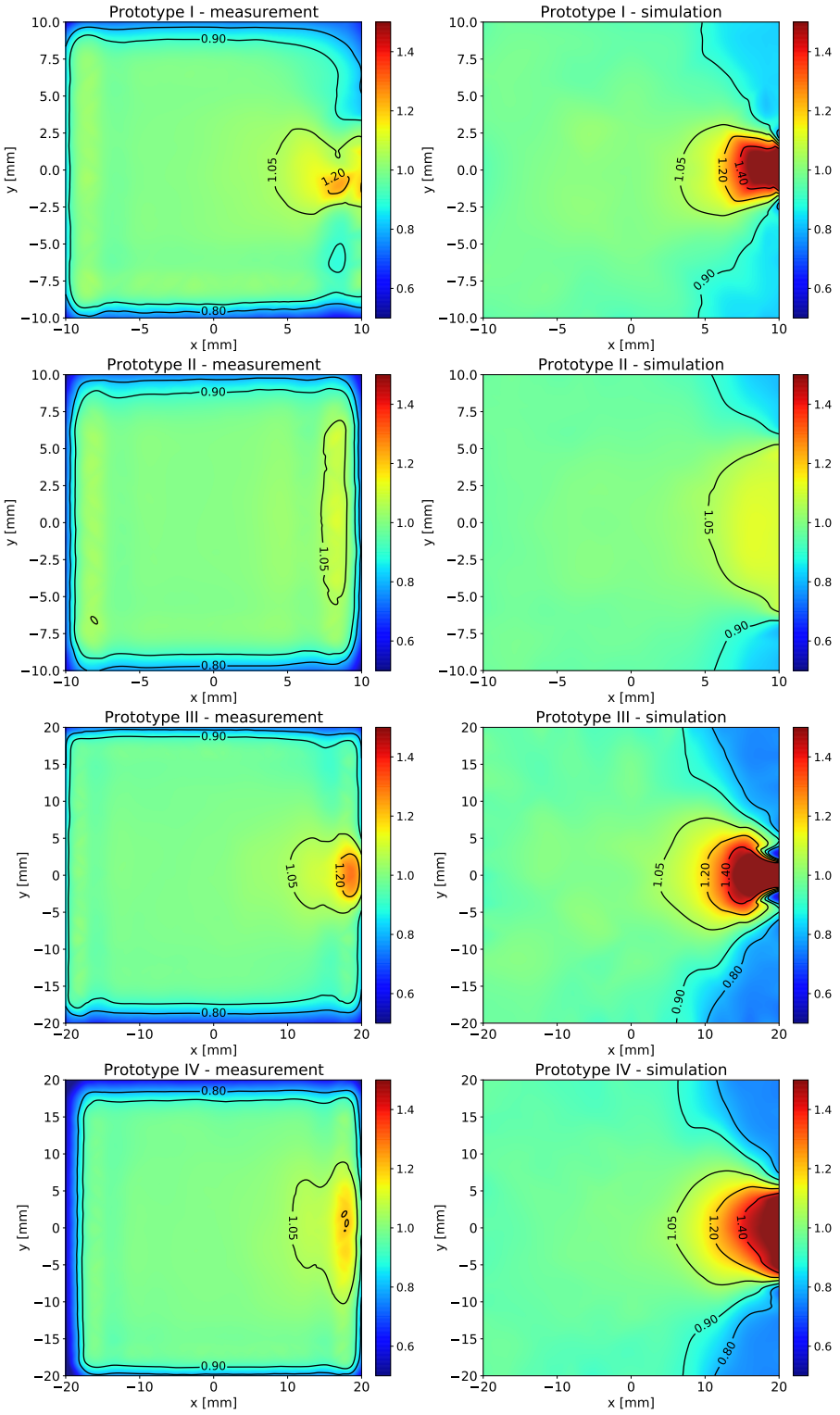

Figure 4.18.: Measured (left) and simulated (right) position-dependent TE for the four prototypes.

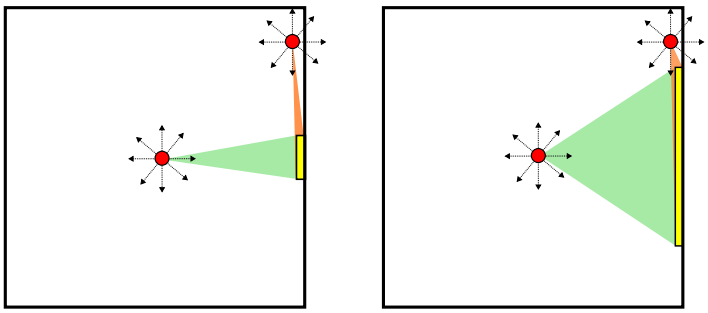

Figure 4.19.: Scheme showing the available solid angle for directly hitting the SiPM after re-emission in different parts of the pixels for Prototype I **(left)** and Prototype II **(right)**. The larger the angle, the higher is the probability of detection for a wavelength-shifted photon.

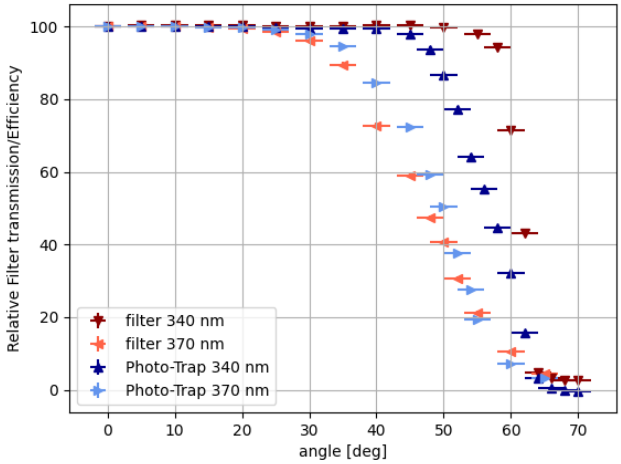

Figure 4.20.: Angular dependence of the Photo-Trap efficiency and of the filter transmission at 340 nm and 370 nm relative to the transmission/efficiency at orthogonal incident light (zero deg).

my measurement setup. At large AOIs my setup was more sensitive to effects that are introduced by a non-negligible beam size: the light may affect a larger part of the Photo-Trap surface, which, as was shown in section 4.2.4.2, has a position-dependent sensitivity. When I measured the filter transmission instead, I only collected light that goes directly into the small area of the SiPM. Furthermore, at large AOIs the Photo-Trap setup is also more sensitive to the alignment.
Besides the limitations imposed by my setup, I expect an additional degradation of the angular response of Photo-Trap at longer AOIs. This degradation is due to Fresnel losses. Close to normal incidence it is expected that ~ 5 % of the light is reflected in a medium with a refractive index of 1.58 like PVT. At 60° this percentage increases to ~ 20 %.

4.2.4.4. Time resolution

Figure 4.21 shows the measured and simulated arrival time distribution of single-phe events for all prototypes. I fitted the distributions associated to the measurements with a Gaussian convolved with an exponential (as in [121]). The resulting values of the SPTR (given as the FWHM of the fits) are listed in Table 4.4, in which the main performance parameters of all prototypes are summarized. I measured a SPTR of ~ 1.3 ns FWHM with the 3 × 3 mm^2 reference SiPM and ~ 2.7 ns FWHM with the 3 × 12 mm^2 reference SiPM. The values are higher than what can be found with state-of-the-art SiPMs and fast-timing electronics since the amplifier in my setup is not optimized for ultra-fast timing applications. In addition, the measured SPTR is also affected by the jitter of the LED diode, which is not optimized for ultra-fast timing studies.
By comparing the SPTR of the prototypes with those of the reference SiPMs it is clear that the contribution of the light source and the SiPM is sub-dominant. This implies that even if the SPTR can be reduced using a faster amplifier we should still expect an SPTR going from ~ 2 to ~ 4 ns in the Photo-Trap pixels. Additionally, the signal recorded by the Photo-Trap pixel is delayed by 1-2 ns compared to the signal of the reference sensor. I consider that both the delay and the additional jitter in the arrival time introduced by Photo-Trap are the result of two effects: the exponential decay time of the WLS and the time that the wavelength-shifted photons spend traveling and bouncing inside the detector before reaching the SiPM, as it was shown in [71].

Among the different Geant4 models tested the LUT Davis 'Rough LUT' model was the one that reproduced better my experimental results of SPTR, as can be seen in Figure 4.21. This is particularly clear in prototypes I and III, where the difference with the other models is more significant. The distributions obtained using the LUT Davis 'Rough LUT' model match reasonably well with the measured arrival time distributions in all prototypes. Since the SiPM response was not included in the simulations, to build the histograms shown in Figure 4.21 we added to the raw arrival time distributions obtained with Geant4 an additional artificial jitter that followed the measured arrival time distributions of the reference sensors.

Prototype nr.	$S_{\mathrm{WLS}}/S_{\mathrm{SiPM}}$	G	TE [%]	SPTR (FWHM) [ns]	DCR [kHz/mm^2]
I	~ 42	9.2 ± 0.4	21.7 ± 1.0	3.2 ± 0.3	2.3
II	~ 10	5.0 ± 0.3	47.5 ± 2.4	4.3 ± 0.3	9.0
III	~ 170	15.8 ± 0.9	9.3 ± 0.6	4.3 ± 0.3	0.7
IV	~ 42	10.7 ± 0.7	25.1 ± 1.7	5.2 ± 0.3	2.3

Table 4.4.: Summary of the main performance parameters of the Photo-Trap prototypes. The DCR of the prototypes was estimated for a DCR of the SiPMs employed of 100 kHz/mm^2.

4.2.4.5. Simulations

In Table 4.5 the measurements of the optical gain are compared with those obtained with the simulations using different models for the surface roughness. The results are presented at different stages of the pixel construction: only the WLS plastic attached to the SiPM without reflectors or filter ('WLS only'), after adding the reflectors but before adding the filter ('WLS + Reflectors') and after adding the filter ('Full Pixel').

The 'WLS only' level was best suited to examine how well the different roughness models describe the interaction of the photons at the surface of the WLS plastic. At

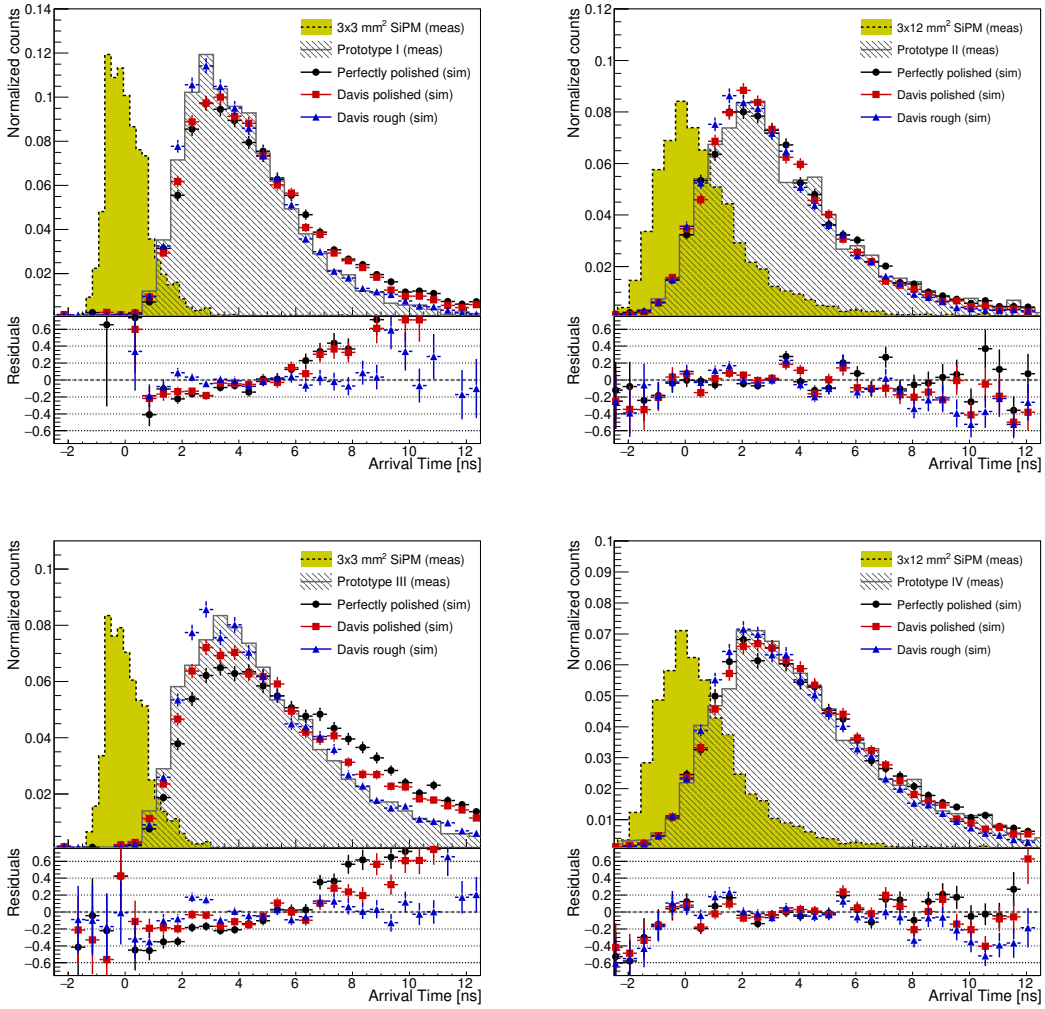

Figure 4.21.: Laboratory measurement of arrival time distribution compared to reference sensors and simulations using different Geant4 models for the surface roughness for Prototype I (**upper left**), Prototype II (**upper right**), Prototype III (**lower left**) and Prototype IV (**lower right**).

this construction stage only a few parameters should affect the optical gain as the WLS response (absorption and re-emission probability), the surface roughness of the plastic piece and the properties of the optical coupling layer (thickness and transmittance). In the simulations we have found that the thickness of the optical coupling layer has a minor impact on the performance. What seems to have a strong impact, and as can be seen in Table 4.5, is the model describing the surface roughness of the WLS plastic. This would suggest that the quality of the surface finishing of the plastic should be a key parameter towards maximizing the efficiency of the pixel. The highest gain was achieved for a perfectly polished surface. This result was much higher than the measured value. Rough models such as Glisur (in this case for a roughness of 0.7) and Davis LUT Rough on the other hand tended to underestimate the overall efficiency. Regarding the optical gain, the Davis Polished LUT model was the one in better agreement with the measurements. In the previous section we showed that the timing performance seemed to be better explained with the Davis Rough LUT model (Figure 4.21). The optimal roughness model for the WLS plastics is probably somewhere in between the Davis Rough LUT and Davis Polished LUT model. Since the Davis models actually were developed for LYSO crystals this is not surprising. Crystals are harder materials and then a higher quality surface finishing can probably be obtained.
At the pixel construction stage ('WLS + Reflectors' level) two additional parameters impact the performance of Photo-Trap: the reflectance of the reflectors and the thickness of the air gap that separates them from the WLS plastic. In [71] was shown that the thicker this air gap, the worse the trapping efficiency. In the simulations an

Nr	Pixel level	Meas.	Pol.	Davis Pol.	Glisur 0.7	Davis Rough
I	WLS only	3.5 ± 0.4	9.2	4.2	1.5	1.4
	WLS + Reflectors	7.2 ± 0.5	14.8	6.4	5.9	2.9
	Full Pixel	9.2 ± 0.4	16.9	7.9–14.8	15.0	11.7
II	WLS only	2.5 ± 0.1	3.1	2.6	1.6	1.5
	WLS + Reflectors	3.8 ± 0.2	5.1	3.6	3.7	2.5
	Full Pixel	5.0 ± 0.3	6.2	4.4–6.3	6.5	6.1
III	WLS only	6.9 ± 0.3	16.6	4.8	2.6	2.1
	WLS + Reflectors	11.9 ± 1.1	33.1	7.9	8.9	3.8
	Full Pixel	15.8 ± 0.9	37.8	11.6–27.6	30.8	22.1
IV	WLS only	4.2 ± 0.3	8.5	4.6	2.7	2.1
	WLS + Reflectors	8.1 ± 0.8	15.0	6.5	7.0	3.4
	Full Pixel	10.7 ± 0.7	18.1	9.6–17.1	18.1	14.8

Table 4.5.: Comparison of the measured optical gain (Meas.) with the values obtained with the simulations using different models to describe the surface roughness of the WLS plastic: perfectly polished (Pol), Davis Polished LUT (Davis Pol.), Glisur with a surface roughness of 0.7 (Glisur 0.7) and Davis LUT Rough (Davis Rough).

air gap of 0.1 mm was included. For this value the Davis Polished LUT model predicts an optical gain that is quite consistent with what was obtained experimentally in most of the pixels, except for Prototype III where it is underestimated.
For a fully assembled pixel two additional parameters have an impact on the pixel efficiency: the filter transmittance and the thickness of the air gap between the filter and the WLS plastic. As indicated in Section 4.2.3.2, The simulation assumed an ideal filter with 100 % reflectance above 400 nm and 100 % transmittance below 380 nm at all AOI. The results are here presented for two different distances between the filter and the WLS plastic: 0.1 and 1 mm. The aim was not a perfect matching with the experiments but an estimation of the maximum optical gain that could be accomplished in an optimized design. As shown in Table 4.5, the distance from the filter to the WLS plastic has a high impact on the trapping efficiency.

4.2.5. Summary and comparison to standard high-gain photosensors

Photo-Trap was introduced as a low-cost, large-area SiPM pixel. In the previous section, I have shown that this approach enables to achieve large pixels with very good SNR. This solution allows increasing the collection area without increasing the capacitance or the DCR. Our group built prototypes with a sensitive area of 4×4 cm^2, which, as far as I know, represent the largest existing SiPM pixels with single-phe resolution at room temperature. The prototypes achieve a trapping efficiency of $\sim 10-50\%$ (which translate into a peak PDE of $\sim 5-25\%$) with a time resolution of $\sim 2-5$ ns (FWHM). The main upgrade of Photo-Trap compared to Light-Trap was the additional dichroic filter. My measurements have demonstrated that this upgrade increased the efficiency of the pixel by ~30%. Simulations of the system suggest that further improvement could be achieved if the distance between the filter and WLS could be controlled and reduced.
Several parameters affect the trapping efficiency of the Photo-Trap pixel. The area ratio $S_{\mathrm{WLS}}/S_{\mathrm{SiPM}}$ has an impact on the achievable gain and hence it should be optimized depending on the application. The simulations suggest that the surface finishing has a strong impact on the WLS plastic as well (see Section 4.2.4.5 and especially Table 4.5). This is particularly clear when we look at the results without reflectors or filter. At this level the surface finishing should be the main responsible for the achieved efficiency. For example, the optical gain obtained with the Davis Polished LUT model is more than twice the one obtained with the Rough one in prototypes I, III and IV without filter and reflectors. In general, the rougher the surface, the more photons escape the WLS plastic. However, the simulations suggest that the addition of an appropriate filter (i.e., very-high transmittance and reflectivity in the wavelengths of interest) would be able to send back to the WLS plastic many of the photons that escaped: the difference between the efficiencies obtained with the different models is much smaller when adding the filter. Hence, by using a proper filter it might be possible to achieve reasonably high efficiency without needing to apply potentially difficult and expensive polishing techniques.
I could not see any impact on the trapping efficiency when studying the results obtained

with several PVT and PS samples polished with the two different techniques by Eljen. Possibly the final roughness level achieved with both techniques on both materials is not different enough to have an impact on the performance. A better surface finishing that results in higher efficiencies might be achieved if using harder plastics like PMMA. Interestingly, I observed a drop in the trapping efficiency when using a sample that ended up with several 'wear and tear' scratches after being manipulated many times in several cycles of measurements. With this 'scratched' sample the measured trapping efficiency was ~ 18% lower at the 'WLS + Reflectors' level. At the 'Full Pixel' level, however, the trapping efficiency was almost not affected by the scratches. As a test, I scratched another sample on purpose using sandpaper. In this sample the trapping efficiency was ~ 25% lower at the 'Full Pixel' level and ~ 50% at the 'WLS + Reflectors' level. This supports the idea that the filter is able to recover a significant fraction of the photons that escape a WLS with a poorly-polished surface.
As can be seen in Section 4.2.4.2, the TE is rather constant over most of the pixel area. Only near the SiPM the TE is higher and in the closest corners it is lower. Probably the efficiency would be more homogeneous if the SiPMs were distributed in more than one side of the pixel. Though, this would rise the complexity of the mechanic and electronic design.
Systems that use a WLS plastic to enlarge the FOV (as Photo-Trap) allow a more compact design than systems based on lenses. The Photo-Trap prototypes feature a relatively large FOV ($> 45°$ at 340 nm, $> 30°$ at 375 nm). The FOV actually depends on the angular dependence of the filter transmittance. For a given application the filter could be selected according to this criteria if required.
The re-emission properties of the WLS and the overall uncertainty of the total path length of a photon restrict the time resolution of Photo-Trap. Possibly the arranging of SiPMs in different parts of the pixel could improve the timing by reducing the average path length.
An industrial manufacturing process of the pixels would not only reduce their cost, but it would probably allow the improvement of the performance as well. It would be easier to control the thickness of the gaps between the WLS plastic, the filter and reflectors as well as the coupling between the SiPM and the WLS. In addition, industrial manufacturing would maybe pave the way to obtain WLS-doped samples of harder materials like PMMA. Companies like Eljen would probably only agree to an order on a larger scale.

The main characteristics of Photo-Trap are compared to those of standard PMTs and SiPMs in Table 4.6. The main limitation of Photo-Trap is its lower PDE, which in some applications might be compensated by increasing the collection area. Its sensitivity band depends on the properties of the filter and the WLS. Since the absorption spectrum of WLS materials typically extend over ~100 nm, the sensitivity band of Photo-Trap is relatively short. This is a disadvantage if we wanted to use Photo-Trap in experiments where the light to be collected has a broad spectrum (like Cherenkov light detection with IACTs). In other cases this narrow sensitivity band could be useful for rejecting background light. The wavelength-sensitivity band could be broadened by

	PMT	**SiPM**	**Photo-Trap**
PDE[a]	~ 35 %	~ 50 %	~ 5 – 25 %
SPTR (FWHM) [ns]	~ 1 – 4 [17, 165]	~ 0.1 – 0.4 [74, 121]	~ 2 – 5
DCR[b] [kHz/mm^2]	-	~ 50	~ 0.3 – 5
High Voltage	Yes	No	No
Sensitive to magnetic fields	Yes	No	No
Ambient light exposure	No	Yes	Yes
Largest Area [cm^2]	~ 10^2	~ 10^{-1}	~ 10^1
Capacitance/mm^2	Low	High	Low
Cost/mm^2	Low-Medium	High	Low

Table 4.6.: Comparison of the main characteristics of Photo-Trap with those of standard high-gain photosensors. [a] Typical values at ~375 nm; [b] at room temperature and assuming a SiPM DCR of 50 kHz/mm^2. For this comparison. we considered the DCR per unit area of PMTs to be negligible.

combining different WLS plastics. A narrower band, in contrast, could be achieved by choosing a different dichroic filter. Moreover, a narrower absorption spectra could be feasible by using quantum dots instead of the traditional wavelength shifters. These quantum dots would have as well the potential to rise the pixel sensitivity since they provide a higher quantum yield. An additional drawback of Photo-Trap is its timing performance which clearly limits its use in ultra-fast-timing applications like Positron Emission Tomography. Having said this I need to point out that the time resolution of the Photo-Trap prototypes (2 – 5 ns FWHM) is comparable to that of the PMTs used for instance in experiments like MAGIC (~ 2 ns FWHM [17]) or IceCube (~ 4 ns FWHM [165]). Because of the limited SPTR Photo-Trap is not suited for intensity interferometry where excellent time resolution is a key factor for a good SNR.
The main advantage of Photo-Trap is that it offers a low-cost solution to build photodetectors of a few cm^2 without several of the limitations related to PMTs (for example high-voltage operation, bulkiness, fragility or sensitivity to magnetic fields). The remarkable thing is that this increase in the pixel size can be achieved without increasing the noise or power consumption. Photo-Trap could be suitable for applications in which the sensitivity increases with the collection area, for example in large Cherenkov detectors like HAWC [18]/SWGO [145]. It could also be interesting for applications where the sensitivity is highly affected by background light or DCR or where compactness, cost and power consumption are critical. A possible application that combines most of these requirements could be optical wireless communication (OWC [75]).

5. Measuring stellar diameters with MAGIC-SII

In this chapter I present the results of my analysis of MAGIC-SII data. This includes the analysis of *raw data* (before passing through the correlator) and the measurement of the diameter of several stars. The data analyzed here was taken between May 2021 and August 2022.

5.1. Study of raw data

The term *raw data* is used to designate data that is measured before the computation of the correlation in the correlator software. It allows studying the individual properties of each channel.

5.1.1. Behaviour of individual channels

Raw data from injected and calibration pulses (see Section 2.4 and 3.3) was used to study the performance of each channel. The goal was to extract the average pulse shape. The position of each pulse was determined by fitting the pulse with a Gaussian. The pulses were shifted according to their extracted position (mean of the Gaussian fit) in order that they are all positioned at time=0 ns. An interpolation was performed on 1000 superimposed pulses using the `Python scipy` package `CubicSpline` to estimate the average pulse shape. A Gaussian was fitted to the average pulse shape.
Figure 5.1 shows superimposed injected pulses recorded by all four channels. The red line marks the interpolated result, and the cyan line is the Gaussian fit to the interpolation data. The average pulse and the Gaussian have very similar shapes. I evaluated the pulse width with the σ of the Gaussian fit and estimated the standard error of the σ using a bootstrap method [169].
Figure 5.2 shows superimposed calibration pulses recorded by all four channels. The red line marks the interpolation result, and the cyan line is the Gaussian fit to the average pulse shape.
In Table 5.1 the σ of the Gaussian fit to the average pulse shape of injected and calibration pulses together with the approximate σ of the input pulses are listed. The σ of injected and calibration pulses cannot be compared directly, because the pulses are produced in different way: calibration pulses are the response of the PMTs to light pulses while injected pulses are electric signals that are injected after the PMTs. The input σ of injected pulses and the σ of the PMT pulses produced by the calibration box

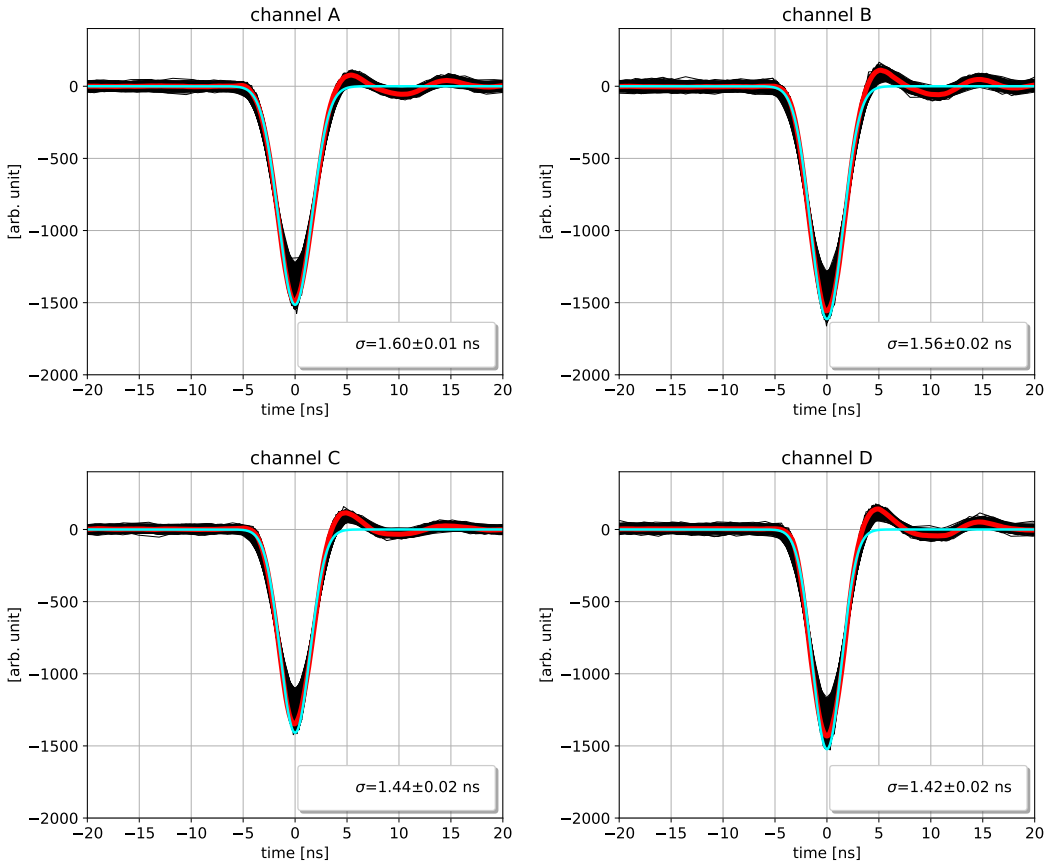

Figure 5.1.: Superimposed injected pulses recorded by all four channels. The pulses were interpolated to extract the average pulse shape (red). A Gaussian was fitted to the interpolation result (cyan).

is ~ 1.1 ns. Table 5.1 shows clearly that the pulses measured with the interferometry setup exhibit a larger pulse width. The pulses seem to be widened by the hardware after the PMT, i.e. the electronics and the digitizer. The widening of the pulses is expected due to the limited bandwidth of the interferometry setup, especially of the digitizer.
In the case of injected pulses, the σ of channel A and B is larger compared to channel C and D. This means, that the bandwidth of the digitizer and the electronics in MAGIC-II is probably smaller than in MAGIC-I. In the case of calibration pulses, channel C and D show wider pulses than channel A and B. Possibly, a faster PMT performance in MAGIC-II compensates for the effect of a reduced bandwidth in the hardware. Since calibration pulses represent the overall signal path (detection in PMT + signal transmission + digitization), it can be concluded that the channels of MAGIC-II provide a better timing performance than the channels of MAGIC-I.

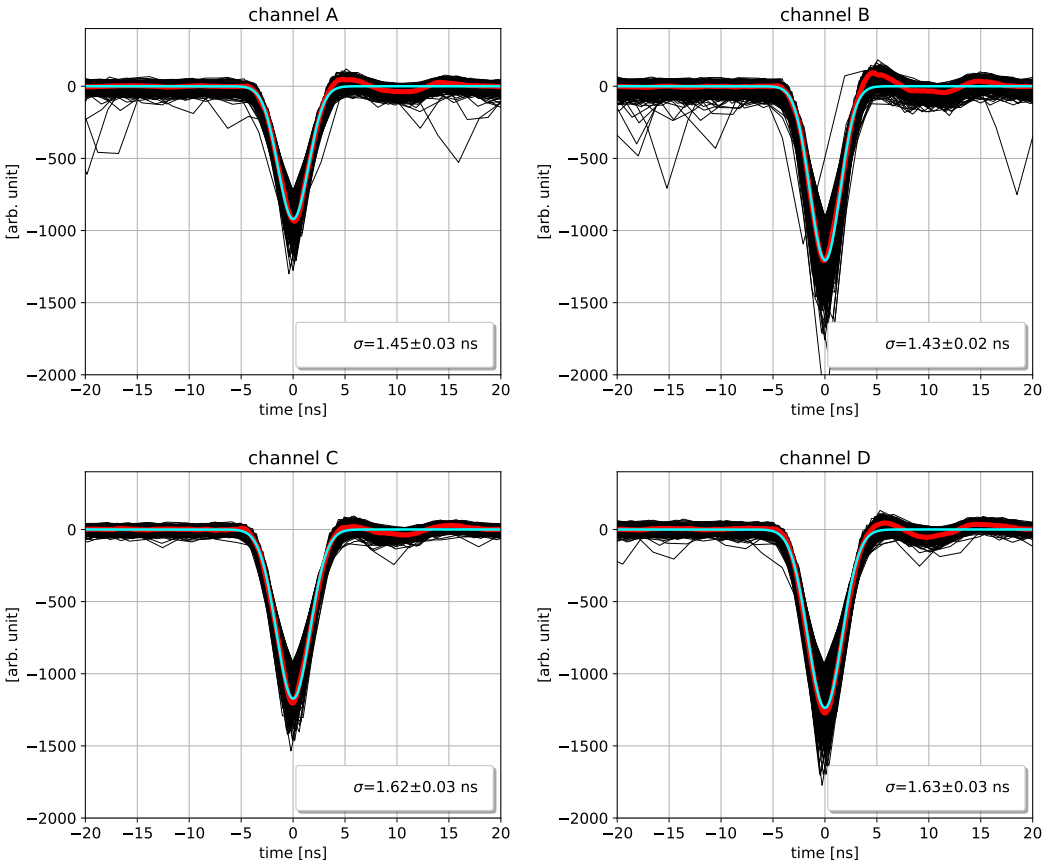

Figure 5.2.: Superimposed calibration pulses recorded by all four channels. The pulses were interpolated to extract the average pulse shape (red). A Gaussian was fitted to the interpolation result (cyan).

channel	input σ [ns]	injected pulses σ [ns]	calibration pulses σ [ns]
A	~ 1.1	1.6 ± 0.02	1.5 ± 0.03
B	~ 1.1	1.6 ± 0.02	1.4 ± 0.03
C	~ 1.1	1.4 ± 0.01	1.6 ± 0.03
D	~ 1.1	1.4 ± 0.02	1.6 ± 0.03

Table 5.1.: σ of the Gaussian fit to the average pulse shape of injected and calibration pulses of all four channels. The input sigma represents the approximate width of both injected and PMT pulses during calibration [17].

5.1.2. Channel correlation

The pulse shape of each channel has an impact on the width of the correlation signal and on its amplitude. The expected correlation signal of each channel pair can be

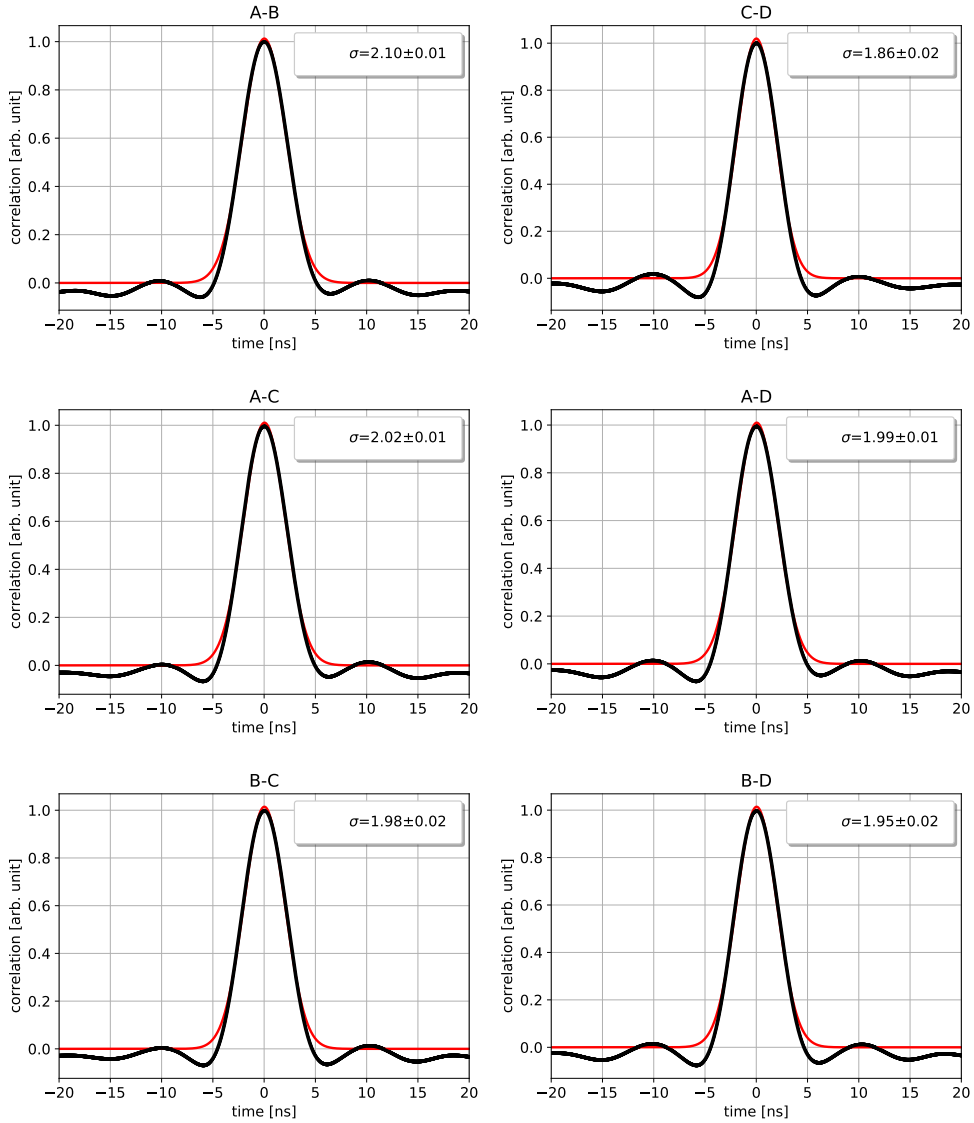

Figure 5.3.: Correlation of the average pulse shape of injected pulses for each channel pair. A Gaussian fit was applied to the correlation data (red line). The pulse width is given as the σ of the Gaussian fit.

studied using the pulse shape that was extracted in Section 5.1.1. The correlation of a channel pair ch_{ij} is estimated as the convolution of the pulse shape of channels i and j. The channel pairs $A-B$ and $C-D$ represent the correlation between channels of the same telescope ($A-B$ in MAGIC II, $C-D$ in MAGIC I). These correlations feature short baselines (<17 m). The channel pairs $A-C, A-D, B-C, B-D$ correspond to the correlation measured in channels from different telescopes and hence they are associated to long baselines ($>$ 17 m). Hereafter short baseline (SB) channel pairs refer to channels

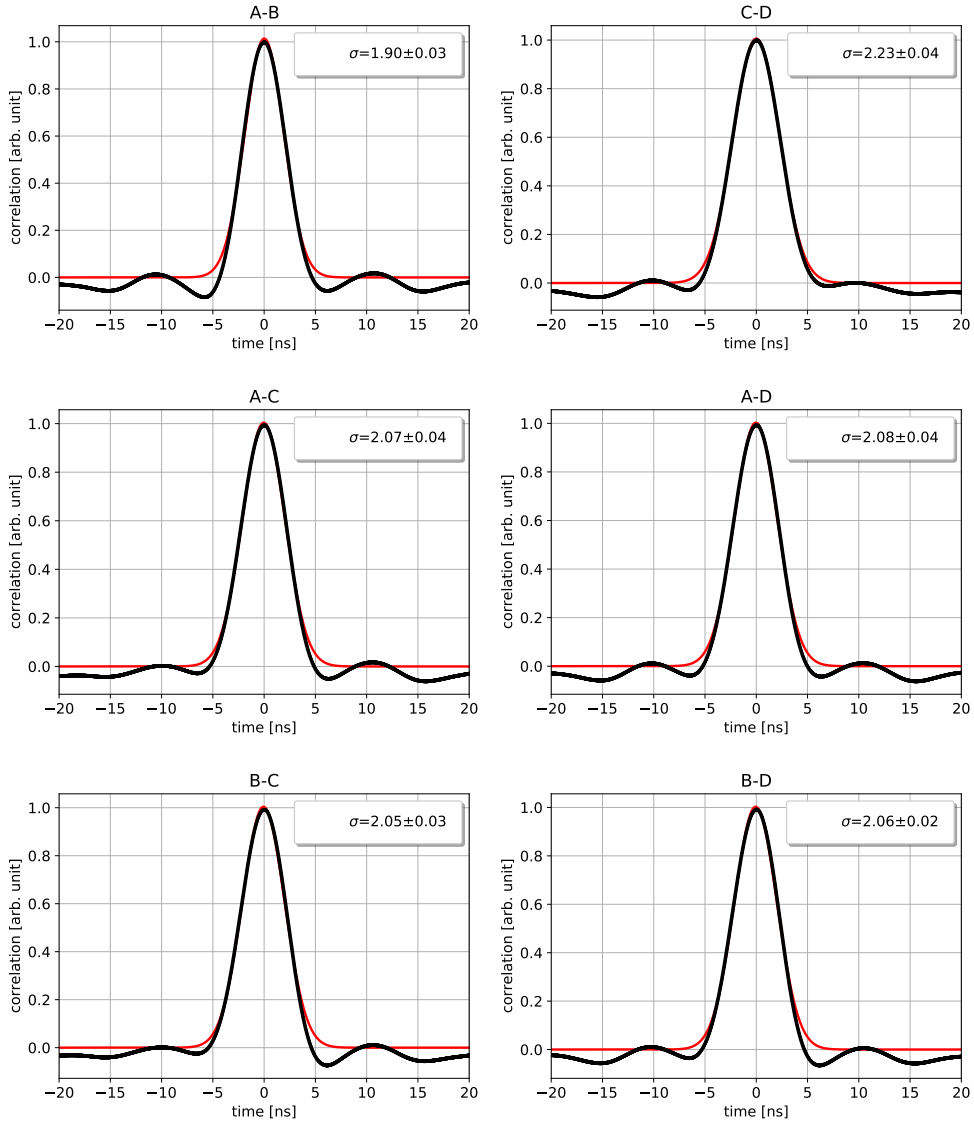

Figure 5.4.: Correlation of the average pulse shape of calibration pulses for each channel pair. A Gaussian fit was applied to the correlation data (red line). The pulse width is given as the σ of the Gaussian fit.

$A-B$ and $C-D$. Long baseline (LB) channel pairs refers to $A-C, A-D, B-C, B-D$. Figure 5.3 shows the correlation of the average pulse shape of injected pulses for all channel pairs and Figure 5.4 the correlation of the average pulse shape of calibration pulses. The correlation data were fitted with a Gaussian (red line). Since the fit matches well the data in the signal region, we can use the σ of the Gaussian fit to evaluate the width of the correlation signal. In Table 5.2 the σ of the correlation signal of each channel pair is listed. The error of σ was estimated with a bootstrap method.

channel pair	injected pulses σ [ns]	calibration pulses σ [ns]
A-B	2.10 ± 0.01	1.90 ± 0.03
C-D	1.86 ± 0.02	2.23 ± 0.04
A-C	2.02 ± 0.01	2.07 ± 0.04
A-D	1.99 ± 0.01	2.08 ± 0.04
B-C	1.98 ± 0.02	2.05 ± 0.03
B-D	1.95 ± 0.02	2.06 ± 0.02

Table 5.2.: σ of Gaussian fit to correlation signal. The signal was obtained by correlating the average pulse shape of different channels for the case of injected pulses and calibration pulses. $A - B$ and $C - D$ are pairs of channels in the same telescope (MAGIC-I (C-D) or MAGIC-II (A-B)). The other four channel pairs are correlations between the channels of both telescopes .

The correlation signals of LB channel pairs have a similar σ both for injected and calibration pulses. In contrast, the signal width of SB channel pairs is different between MAGIC-I and MAGIC-II. All correlation signals have the same amplitude and are centered at delay=0 ns. As discussed in Section 5.1.1, there could be differences in the digitizer and the PMTs response in each telescopes. Whereas a different pulse amplitude of the average pulse shape of the channels does not seem to affect the correlation, the pulse width has a clear impact: the SB correlation in MAGIC-I has a larger σ than in MAGIC-II.
Calibration pulses are more useful to study shape of the correlation signal because they include both the effect of the digitizer board and PMT. According to the result for calibration pulses the correlation signals for LB channel pairs should have a constant pulse width. The SB correlation signal of MAGIC-I is expected to have a ~ 17 % smaller pulse width than the SB signal of MAGIC-II .

5.2. Comparison of channel pairs

In the previous section, the shape of the correlation signal was compared for different channel pairs using raw data from injected and calibration pulses. In this section, I will continue to study and compare the performance of the channel pairs. The focus is hereby on LB channel pairs. The correlation of SB channel pairs will be discussed in Section 5.5.

5.2.1. Signal shape

In Section 5.1.2 the expected signal width for each channel pair was determined by analyzing raw data of calibration pulses. The result can be compared to the width of the correlation signal from observations of stars. I extracted the signal using a Gaussian fit to the correlation signal of different stars and channel pairs (see Section 3.6 and Figure 3.13 for the signal extraction). In Figure 5.5 the distribution of the σ for each channel pair can be seen. In Table 5.3 the weighted average σ (weighted according to the standard error of each σ) of correlation signals from observations are compared to the σ of the correlation signal of the average shape of calibration pulses. The average σ of correlation signals from observations is very similar for all LB channel pairs as expected from the results of Section 5.1.2. However, the average measured σ from observations of $\sim$ 2.3 ns is slightly higher than the σ determined from calibration pulses. This could be due to the impact of the NSB. In addition, the temperature and PMT have an impact on the time jitter of the pixel which in turn affects the width of the correlation signal.

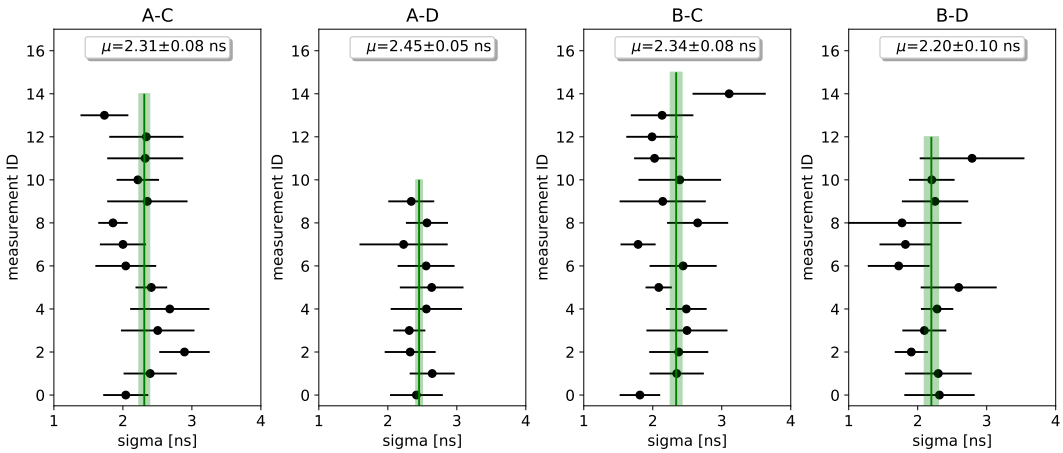

Figure 5.5.: Distribution of the σ of the Gaussian fit to the correlation signal obtained from different stars for all LB channel pairs. The average correlation signal has a width of $\sim$ 2.3 ns.

channel pair	σ from observations [ns]	calibration pulses σ [ns]
A-C	2.3 ± 0.3	2.1 ± 0.1
A-D	2.5 ± 0.2	2.1 ± 0.1
B-C	2.2 ± 0.3	2.1 ± 0.1
B-D	2.2 ± 0.3	2.1 ± 0.1

Table 5.3.: Average of the σ of the Gaussian fit to the correlation signal obtained from different stars for all LB channel pairs. The average was weighted according to the standard error of each σ. The average σ from observations is compared to the σ from the correlation signal of calibration pulses (see Section 5.1).

5.2.2. Calibration of the visibility fit

The performance of the channel pairs can be compared with data of the star ϵ CMa (Adhara). ϵ CMa is a bright star and hence it is possible to obtain a significant correlation signal with only a few minutes of observations. MAGIC-SII recorded ϵ CMa data in a large range of baselines and with different mirror configurations. This star was observed by the Narrabi Stellar Telescope with which they measured a diameter of 0.77 ± 0.05 milliarcsec (mas) [84].

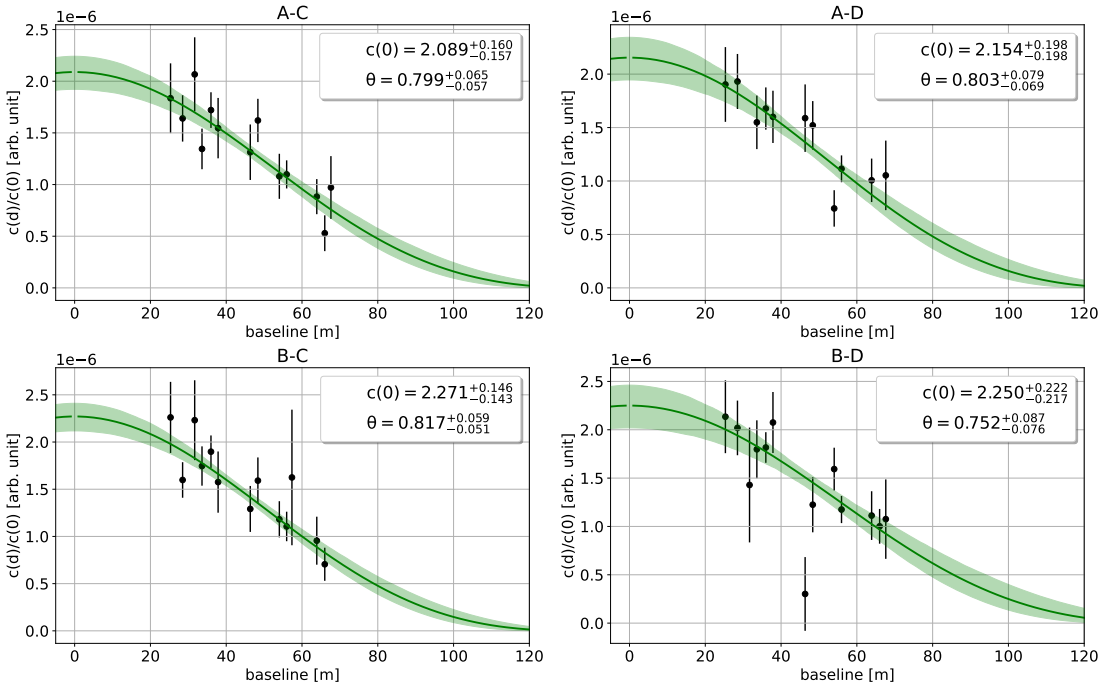

Figure 5.6.: Correlation as a function of the baseline for different channel pairs for the star ϵ CMa. With the visibility fit the diameter θ and the correlation at zero baseline $c(0)$ is extracted. The data were taken in Chessboard mode.

Figure 5.6 shows the visibility fit for ϵ CMa obtained by looking at the correlation of LB channel pairs of data taken in Chessboard mode. For each channel pair ~ 250 minutes of data were taken. The diameter θ and $c(0)$ obtained with the visibility fit are consistent between different channel pairs. The visibility fits obtained with different channel pairs were also compared using data taken in Full-mirror mode (see Figure 5.7). These observations were performed with the channel pairs $A-C$ and $B-D$. The values of θ and $c(0)$ obtained from the visibility fits are compatible within the error to the results obtained in Chessboard mode. When comparing the result of the channel pairs $A-C$ and $B-D$ with each other, two things have to be considered: (1) observations in Full-mirror mode cannot be performed simultaneously for the channel pairs $A-C$ and $B-D$, thus the data were taken with different observational conditions and different baselines; (2) with $A-C$ ~ 150 minutes of data were measured, with $B-D$ only ~ 45 minutes (in contrast to the ~ 250 minutes of data taken with each channel pair in Chessboard mode). As a consequence, Full-mirror data were available only at a few baselines and the fit of $B-D$ has a large uncertainty.
Since the results obtained with different channel pairs are compatible it should be possible to combine the data from all the pairs (thus, increasing the sensitivity of the instrument as can be seen in Figure 3.11). Figure 5.8 shows the visibility fit to

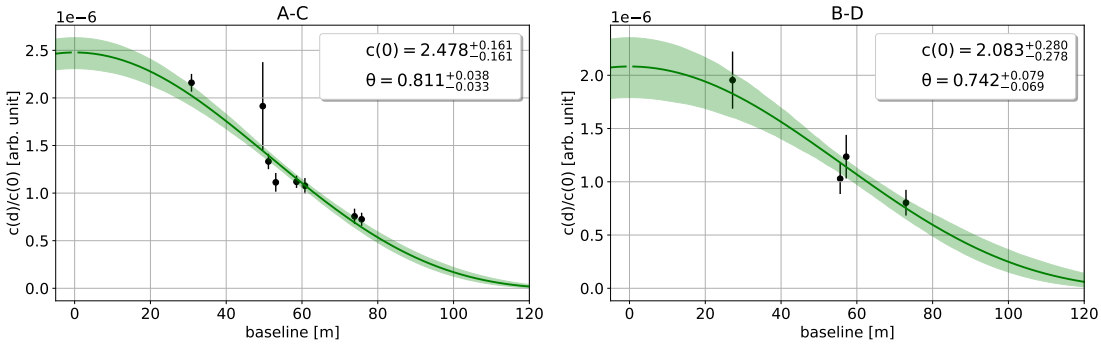

Figure 5.7.: Visibility fits for ϵ CMa and different channel pairs. The data were taken in Full-mirror mode.

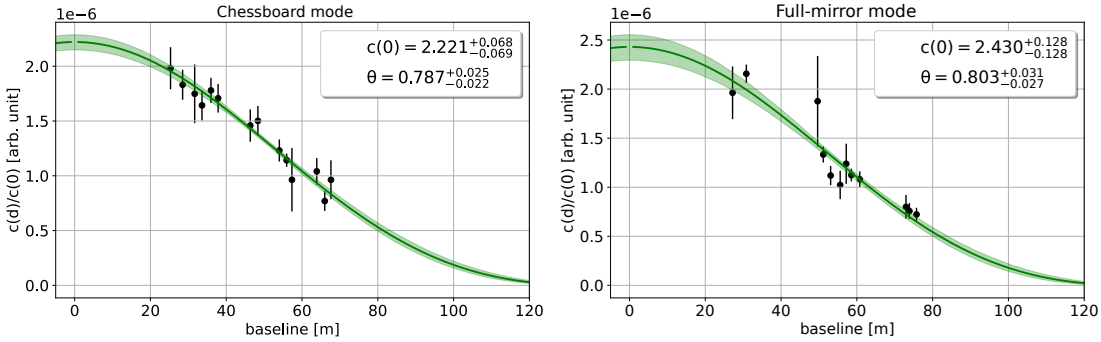

Figure 5.8.: Visibility fits for ϵ CMa for combined data from different channel pairs. The data were taken in Chessboard mode (**left**) or in Full-mirror mode (**right**).

Chessboard mode

channel pair	θ **[mas]**	$\mathbf{c(0)}$
A-C	0.799 ± 0.065	2.089 ± 0.160
A-D	0.803 ± 0.079	2.154 ± 0.198
B-C	0.817 ± 0.059	2.271 ± 0.146
B-D	0.752 ± 0.087	2.250 ± 0.222
All	0.787 ± 0.025	2.221 ± 0.069

Full-mirror mode

channel pair	θ **[mas]**	$\mathbf{c(0)}$
A-C	0.811 ± 0.038	2.478 ± 0.161
B-D	0.742 ± 0.079	2.083 ± 0.280
All	0.803 ± 0.031	2.430 ± 0.128

Table 5.4.: Comparison of $c(0)$ and θ for ϵ CMa. The visibility function was fitted to different data sets, either including only data from one channel pair or combining data from all channel pairs.

combined data from different channel pairs for the star ϵ CMa, in the left panel for data taken in Chessboard mode and in the right panel for data taken in Full-mirror mode. The fit results of the combined channel pair visibility fits in Figure 5.8 are consistent with the single channel pair visibility fits of each mirror configuration. The fit results are summarized in Table 5.4.

5.2.2.1. Combining data from different mirror modes

Data taken in different mirror configurations can be combined if two conditions are fullfilled: (1) a correction factor is applied in the calculation of the correlation to correct for the different mirror surface of the configurations. (2) the angular distribution of the light that hits the pixel is the same in both cases.
A larger mirror surface collects more light which results in a higher DC of the PMT that detects the light. Dividing the numerator of the Pearson's correlation coefficient by the DCs during the calculation of the contrast $c(d)$ (see Equation 2.24) corrects for the available amount of light (and thus for the mirror surface). The second condition is true for the Chessboard mode and Full-mirror mode, therefore data taken in these mirror configurations can be combined. However, between different Submirror configurations the angles of the light hitting the optical filters are expected to be very different. Hence data taken in different Submirror modes cannot be combined.

In Figure 5.9 visibility fits for ϵ CMa for combined data of different channel pairs are shown using two methods: in the left panel Chessboard and Full-Mirror mode data were combined in the same baseline bins (method I); in the right panel the data of each mirror mode was analyzed independently, but the obtained correlation signals were combined in the visibility fit (method II). Method I and method II led to compatible results for θ and $c(0)$ within errors.
For ϵ CMa I found no difference between the results obtained with both methods. This may be different for other stars. To study a potential impact of the mirror combining method on the visibility fit result, I decided to analyze the available data of different stars with both methods.

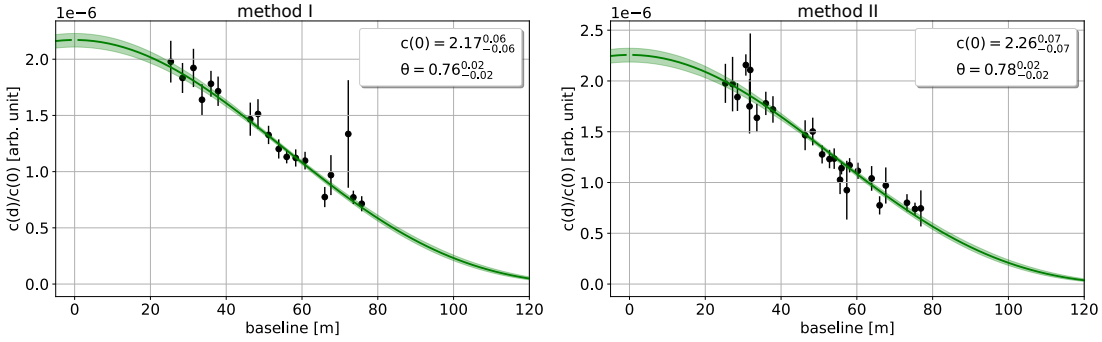

Figure 5.9.: Visibility fits for ϵ CMa for combined data of different channel pairs. The data taken in Chessboard and Full-mirror mode was combined, method I (**left**) or not combined in baseline bins, method II (**right**).

5.3. Reference stars

As explained before, ϵ CMa is a bright star that allows obtaining a clear correlation signal with short observation times. Besides, it is detectable from the MAGIC-SII site at many different baselines. This allowed us to determine its θ and $c(0)$ with relatively low uncertainty. Therefore we have chosen ϵ CMa as the star for calibrating the MAGIC-SII and evaluating its performance.
Next to ϵ CMa, we tried to measure the diameter of other stars. Most of these stars are typically weaker or only observable over a relatively short period of time. In these cases we might only get data in a very narrow baseline range. Still, it is *a priori* possible to estimate the diameter of a star even with a single bin in the visibility plot, as long as we know $c(0)$. And since $c(0)$ is supposed to be a constant of the instrument (see Section 3.7) we can use the value of $c(0)$ found for ϵ CMa to estimate the diameter of other stars (see example in Figure 5.10 for the candidate star ϵ Ori).

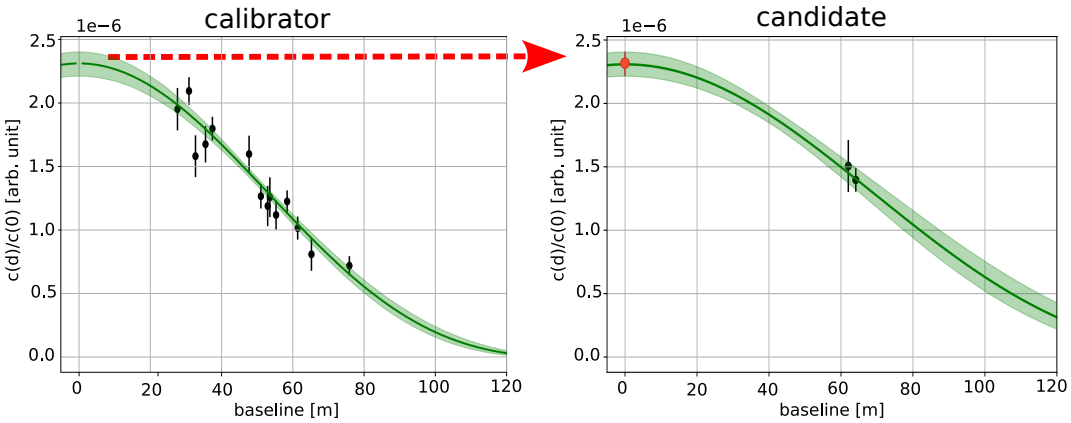

Figure 5.10.: By determining the zero-baseline correlation $c(0)$ from data of a calibrator star with strong correlation signals over a wide range of baseline bins (here the calibrator star is ϵ CMa), it is possible to perform the visibility fit in those stars where data were taken in a limited baseline range (the candidate star is here ϵ Ori).

reference stars

star	HD number	magnitude in B	reference θ [mas]	band	catalog	observing period	baselines [m]	T_{obs} [h]
ϵ CMa	HD52089	1.29 [50]	0.770 ± 0.050 [84]	4430A	II/345/jmdc	02 2022	26.7 - 77.1	2.9
γ Ori	HD35468	1.42 [50]	0.720 ± 0.040 [84]	4430A	II/345/jmdc	08 2022	75.2 - 82.2	1.2
ϵ Ori	HD37128	1.51 [50]	0.631 ± 0.017 [5]	4200A	II/345/jmdc	02 2022	61.7 - 64.8	0.6
β CMa	HD44743	1.73 [50]	0.523 ± 0.017 [5]	4430A	II/345/jmdc	02 2022	52.0 - 75.9	0.8
κ Ori	HD38771	1.88 [50]	0.440 ± 0.030 [84]	4430A	II/345/jmdc	02 2022	51.8 - 53.4	0.3
γ Crv	HD106625	2.47 [50]	0.720 ± 0.060 [84]	4430A	II/345/jmdc	05/06 2021, 02/04/05 2022	40.3 - 67.1	6.9

Table 5.5.: List of reference stars to test the performance of the interferometer. For each star, its HD number and magnitude in the blue wavelength band (450 – 485 nm) is given as well as a reference diameter, the wavelength band in which the reference diameter was measured and the catalog where the reference is listed. The observing period indicates in which months the star was observed, in which baseline range and for how many hours.

MAGIC-SII observed several stars whose diameter had been previously measured by other instruments, even at wavelengths close to the transmission band of the interference filter. We used these stars, hereafter called *reference stars*, to test and validate the MAGIC-SII. To enter in this category stars should not be variable nor spectroscopic binaries. In addition, they need to be bright enough to obtain a significant signal within a few minutes and they should not be very close to other stars in the FOV. In Table 5.5 the reference stars are listed with their name, their HD number and their stellar magnitude in the blue wavelength band (450 – 485 nm). The diameter measured by previous instruments (reference θ) is also given. These reference diameters are either the result of observations of the Narrabri Stellar Telescope [84] or from intensity interferometry observation of the VERITAS Telescopes [5]. The observing period indicates the months in which the stars have been observed (02 2022 corresponds to

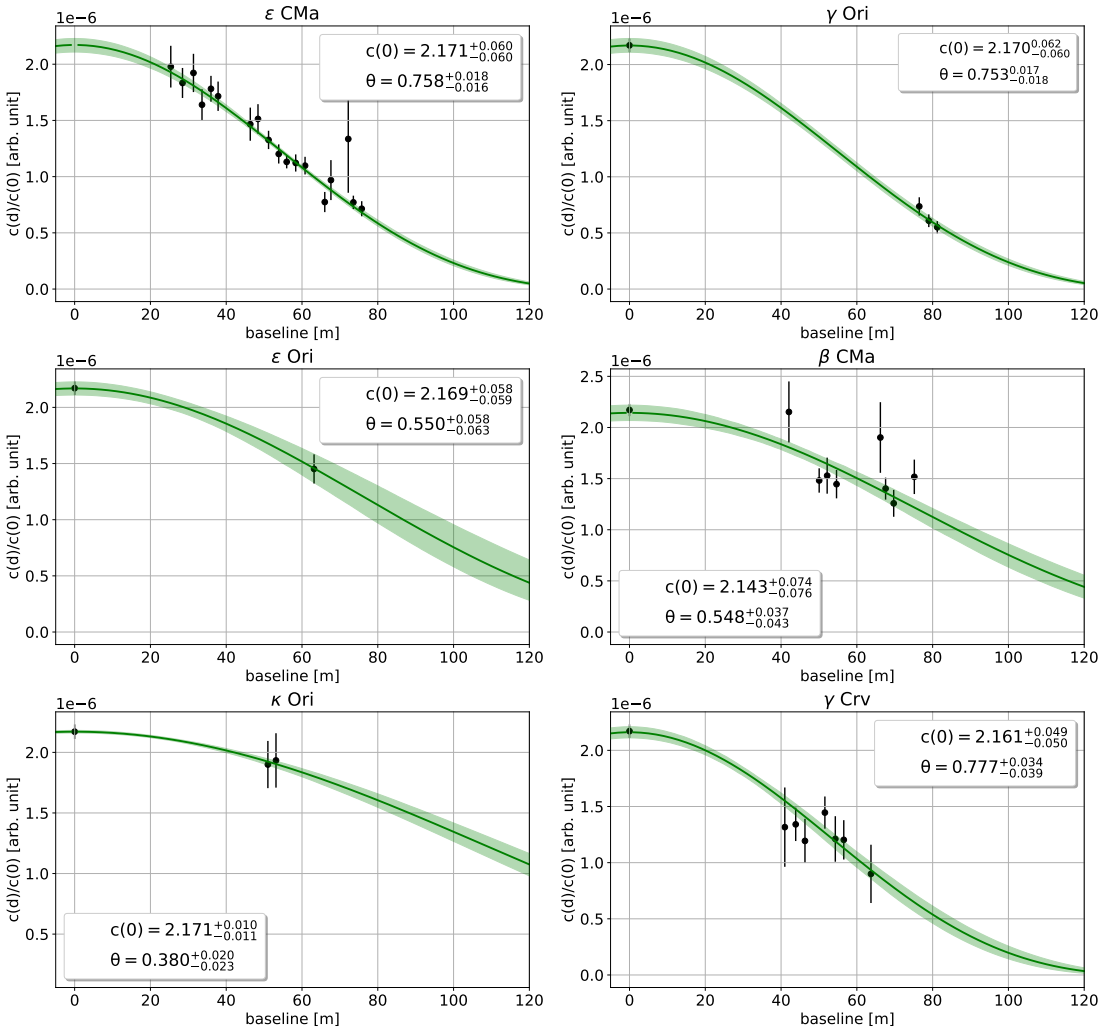

Figure 5.11.: Visibility fits for the reference stars observed with the MAGIC-SII. The signal was extracted with a Gaussian fit and the mirror combining method I was applied. $c(0)$ of ϵ CMa was used as zero-baseline calibration for all other stars.

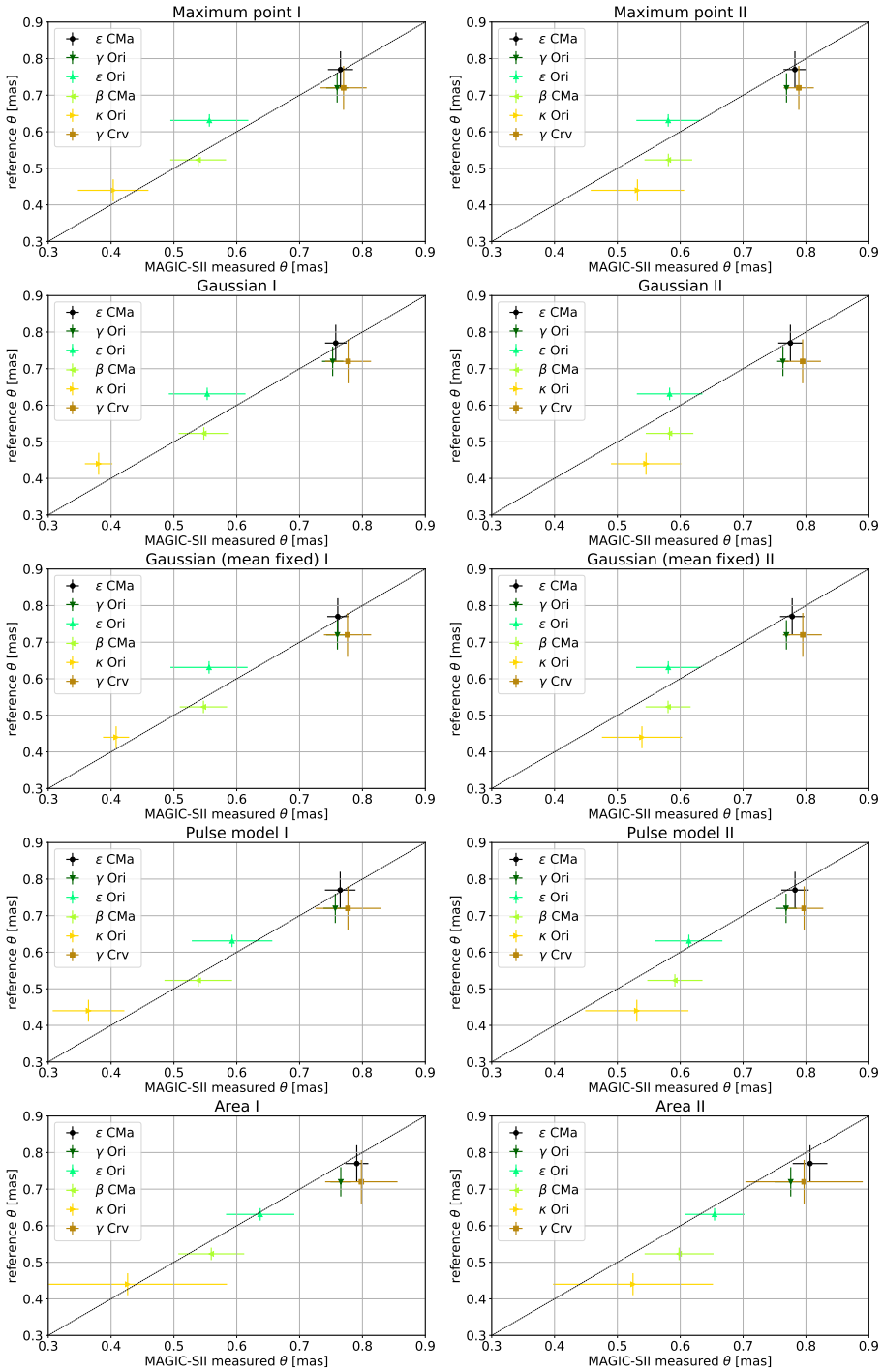

Figure 5.12.: θ measured by MAGIC-SII versus reference θ using different signal extraction methods. The line marks the perfect match between the measured diameter to the reference diameter. Different mirror configurations were either combined, method I, (**left**) or not combined, method II (**right**). For all stars $c(0)$ determined from ϵ CMa data were used as calibration of the zero-baseline correlation.

February 2022). The baseline range that was covered and the observing time T_{obs} of the source are listed as well.

The visibility fits for the reference stars are shown in Figure 5.11. For all stars $c(0)$ determined from ϵ CMa data were used as calibration of the zero-baseline correlation. For the stars ϵ Ori, κ Ori and β CMa less than 1 hour of data were available (see Table 5.5). In the case of β CMa the data were, in addition, spread over a large range of baselines and just a small amount of data were available in each baseline bin. κ Ori was observed only for 20 minutes even if it is one of the dimmest reference stars. Astronomic sources like stars can be observed only within a time window in the year and some stars were observable solely at a limited range of baselines. The observation of 'winter sources' like κ Ori was restricted heavily by the volcano eruption in autumn/winter 2021.
The diameter θ was determined using different signal extraction methods (see Section 3.6) and for both methods of combining data taken in different mirror modes (see Section 5.2.2.1). In order to study the impact of each method, the measured diameter was compared to the reference diameter.
Figure 5.12 compares the stellar diameters of the reference stars measured by MAGIC-SII with the reference values. The black line marks the perfect match of the measured diameter to the reference. The left panels show method I (different mirror configurations were combined), and the right panels method II (different mirror configurations were not combined). In Table 5.6 the error-weighted mean of the residuals between the measured diameter and the reference diameter is listed. The weighted mean of the residuals obtained using different signal extraction methods are consistent within

signal extraction method	combining method	weighted mean residuals [mas]
Maximum point	I	0.039 ± 0.009
Gaussian	I	0.046 ± 0.010
Gaussian (mean fixed)	I	0.043 ± 0.009
Pulse model	I	0.040 ± 0.010
Area	I	0.031 ± 0.010
Maximum point	II	0.059 ± 0.010
Gaussian	II	0.059 ± 0.013
Gaussian (mean fixed)	II	0.060 ± 0.012
Pulse model	II	0.057 ± 0.012
Area	II	0.066 ± 0.009

Table 5.6.: Error-weighted mean of the residuals between the measured and reference θ for different signal extraction methods and the mirror combining methods I and II.

uncertainties. Combing the mirrors seems to provide slightly better results, although larger statistics would be needed to extract more robust conclusions.

The results shown in this section suggest that the signal extraction method has no impact. Hereafter I decided to use a Gaussian for the signal extraction. The diameter measurements for the reference stars were affected partly by low statistics thus no robust conclusion can be drawn about differences in methods I and II in Figure 5.12.

5.4. Candidate stars

MAGIC-SII observed several *candidate stars*. These are stars whose diameter had been measured at different wavelengths of those of the MAGIC-SII or that had not been measured at all. Some of these stars are fast rotators which leds to different diameters results depending on when they are observed (because the orientation in the UV plane is different at any given time). The candidate stars are listed in Table 5.7 with their HD number, their magnitude in the blue wavelength band (450 – 485 nm) and a reference value for the uniform disk diameter. These reference values come either from a measurement at some wavelength (jmdc catalog) or from theoretical estimations (jsdc catalog). The observing period and the baseline range that was covered as well as the total observing time T_{obs} are given also in the Table.

In Figure 5.13, 5.14 and 5.15 the visibility fits for the candidate stars using mirror combining method I are shown. In some stars we could only achieve one bin with a significant correlation signal. In those cases the weighted baseline fit method introduced in Section 3.7 could not estimate a finite uncertainty of the fit. Then the fit was performed using the python `emcee` package (see Section 3.7 for details).
In total, I managed to perform the visibility fit to the data of 19 candidate stars that were observed between 2021 and 2022. The largest measured diameter was for β Cas and was 1.974 ± 0.355 mas. The dimmest star that was successfully observed was τ Her with a magnitude of 3.73 in the blue wavelength band .

candidate

star	HD number	magnitude in B	reference θ [mas]	band	catalog	observing period	baselines [m]	T_{obs} [h]
η UMa	HD 120315	1.67 [50]	0.818 ± 0.060 [65]	H	II/345/jmdc	05 2021, 02/04 - 06 2022	48.9 - 84.8	7.2
η Cen	HD 127972	2.12 [50]	0.570 ± 0.059[33]	B	II/346/jsdc_v2	05/06 2021, 02 2022	30.1 - 66.3	2.5
γ Cas	HD 5394	2.29 [50]	0.545 ± 0.098 [157]	B0V	J/AJ/153/-16/table3	05/06 2021, 05 - 08 2022	22.2 - 65.9	14.6
υ Sco	HD 158408	2.48 [90]	0.483 ± 0.047 [33]	B	II/346/jsdc_v2	07 2022	41.8 - 62.6	1.5
β Lib	HD 135742	2.51 [50]	0.747 ± 0.077 [33]	B	II/346/jsdc_v2	05 2021	26.9 - 47.8	0.7
ζ Oph	HD 149757	2.58 [50]	0.500 ± 0.050 [84]	4430A	II/345/jmdc	05/06 2021, 02 2022	49.3 - 83.9	4.3
γ Peg	HD 886	2.61 [50]	0.364 ± 0.038 [33]	R	II/345/jmdc	07/08 2022	72.5 - 83.6	3.0
β Cas	HD 432	2.61 [50]	2.03 ± 0.015 [171]	550 - 850 nm	II/345/jmdc	07 2022	21.8 - 29.2	1.0
α Cep	HD 203280	2.680 [126]	1.342 ± 0.144 [33]	B	II/346/jsdc_v2	05 2022	28.2 - 42.1	3.1
α02 CVn	HD 112413	2.76 [50]	0.706 ± 0.067 [33]	B	II/346/jsdc_v2	07/08 2022	85.0 - 85.3	2.7
δ Cas	HD 8538	2.810 [126]	1.189± 0.121 [33]	B	II/346/jsdc_v2	05/08 2022	26.9 - 47.8	4.6
γ Gru	HD 207971	2.89 [50]	0.694 ± 0.057 [33]	B	II/346/jsdc_v2	07/08 2022	18.8 - 62.6	9.6
ζ Per	HD 24398	2.97 [50]	0.531 ± 0.007 [39]	734 nm	II/345/jmdc	07/08 2022	45.7 - 74.6	4.2
θ Oph	HD 157056	3.03 [50]	0.4 ± 0.1 [168]			06 2021, 04 - 08 2022	30.4 - 83.6	11.5
ϕ Sgr	HD 173300	3.050 [90]	0.630 ± 0.069 [33]	B	II/346/jsdc_v2	07/08 2022	28.0 - 74.7	8.1
γ Lyr	HD 176437	3.200 [127]	0.712 ± 0.038 [65]	R	II/345/jmdc	05 2022	45.2 - 84.4	9.8
ϵ Cas	HD 11415	3.22 [50]	0.350 ± 0.038 [33]	B	II/346/jsdc_v2	07/08 2022	29.6 - 59.5	7.1
ζ Cas	HD 3360	3.47 [50]	0.274 ± 0.018 [65]	R	II/345/jmdc	07/08 2022	30.9 - 75.7	11.1
τ Her	HD 147394	3.73 [51]	0.354 ± 0.020 [64]	R	II/345/jmdc	05 - 07 2022	46.7 - 85.2	18.6

Table 5.7.: List of candidate stars detected by MAGIC-SII. For each star, its HD number and magnitude in the blue wavelength band (450 – 485 nm) is given as well as a reference diameter, the wavelength band in which the reference diameter was measured and the catalog where the reference is listed. The observing period indicates in which months the star was observed, in which baseline range and for how many hours.

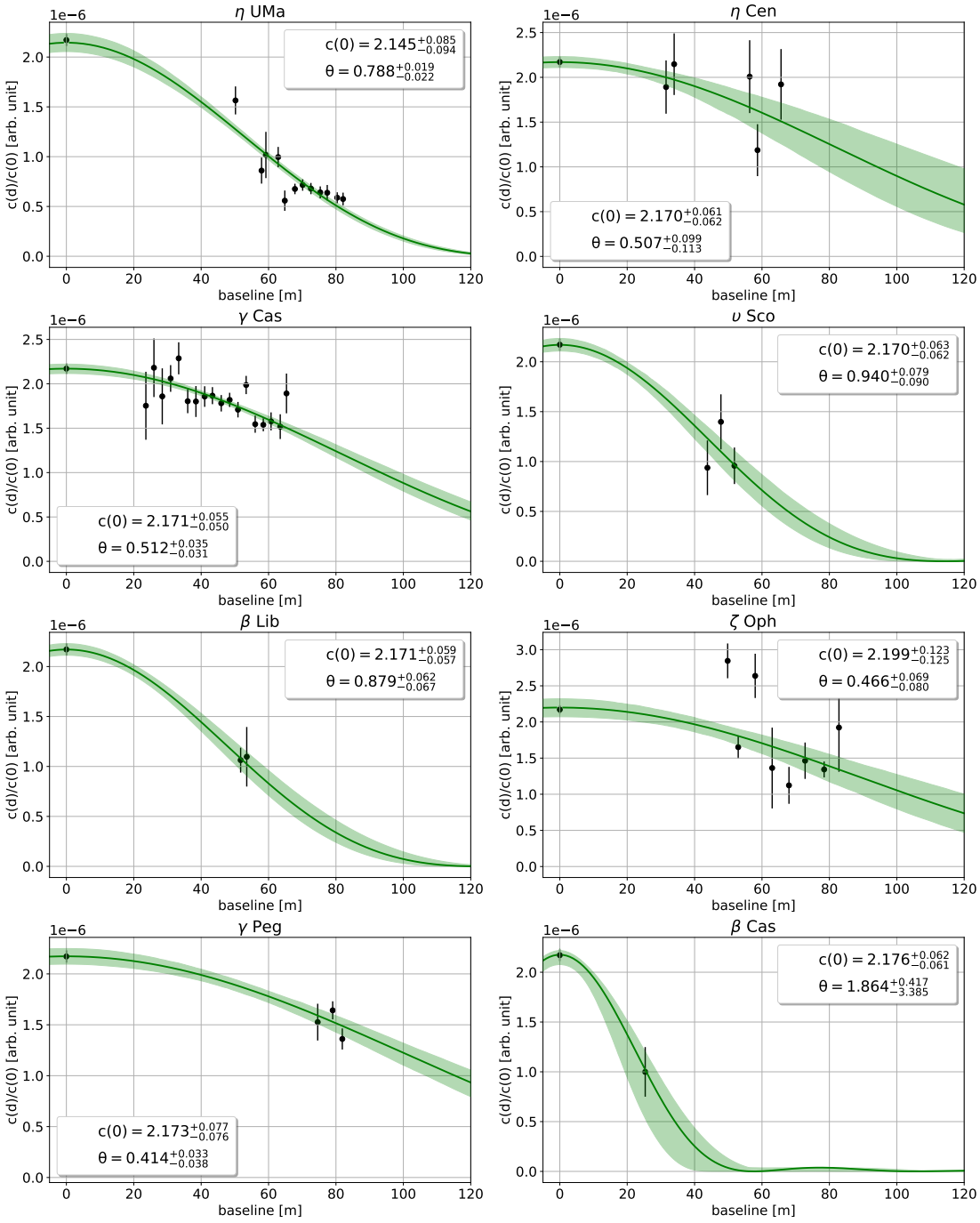

Figure 5.13.: Visibility fits for candidate stars using mirror combing method I. The parameter $c(0)$ of ϵ CMa served as calibration of the zero-baseline correlation.

In Figure 5.16 the measured θ is plotted versus the reference θ. The left panel shows the comparison for mirror combining method I, and the right panel for mirror combining method II. Except for υ Sco, ϵ Cas and, for mirror combining method II, β Lib, all measured diameters are matching well with their references. Since the reference

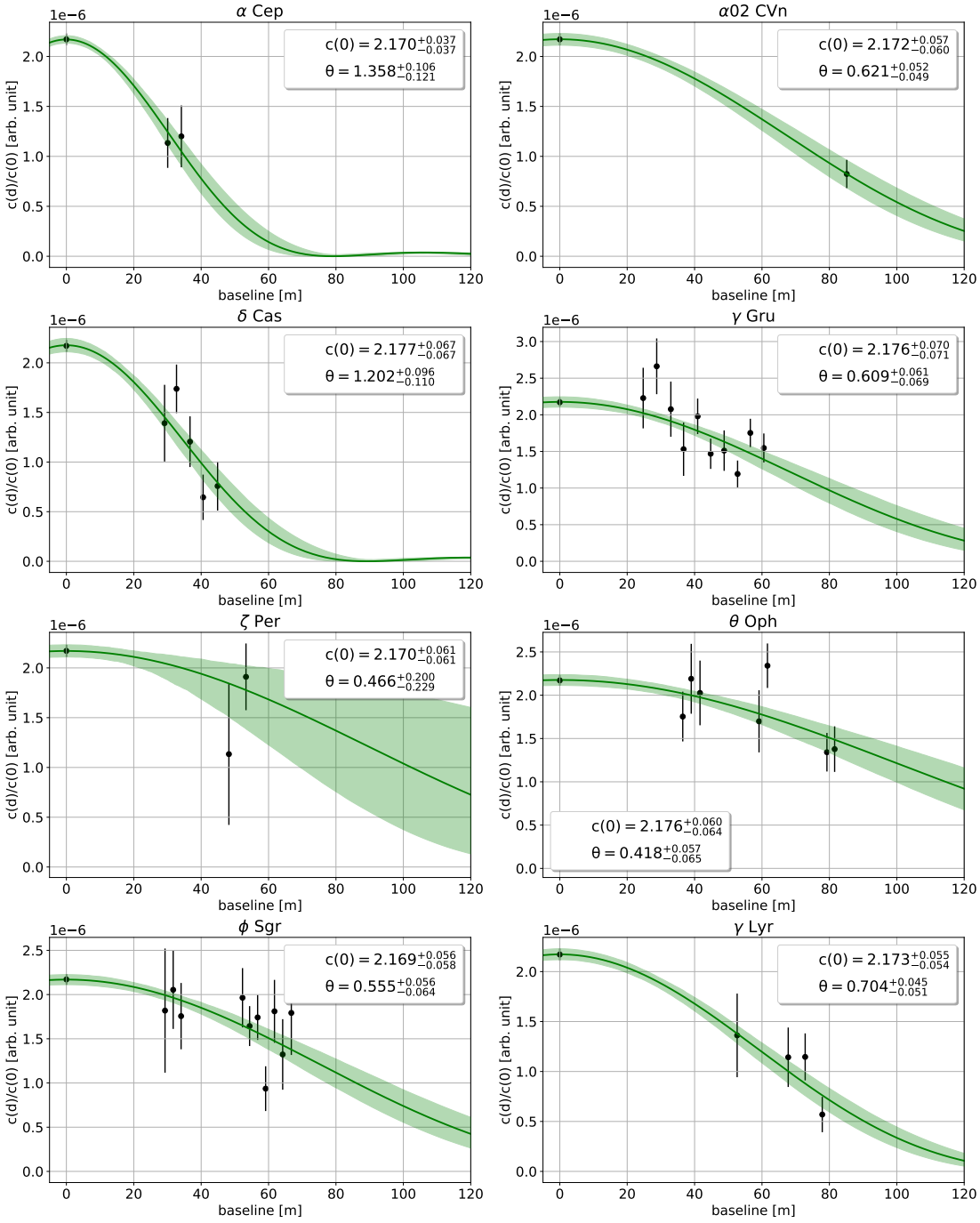

Figure 5.14.: Visibility fits for candidate stars with mirror combing method I. The parameter $c(0)$ of ϵ CMa served as calibration of the zero-baseline correlation.

diameter is either from simulations or from measurements at a different wavelength, the diameter measured by MAGIC-SII should not necessarily match the reference diameter. Especially since some stars are fast rotators with a certain oblateness. It is, however, remarkable that the diameters obtained with MAGIC-SII and the reference diameters

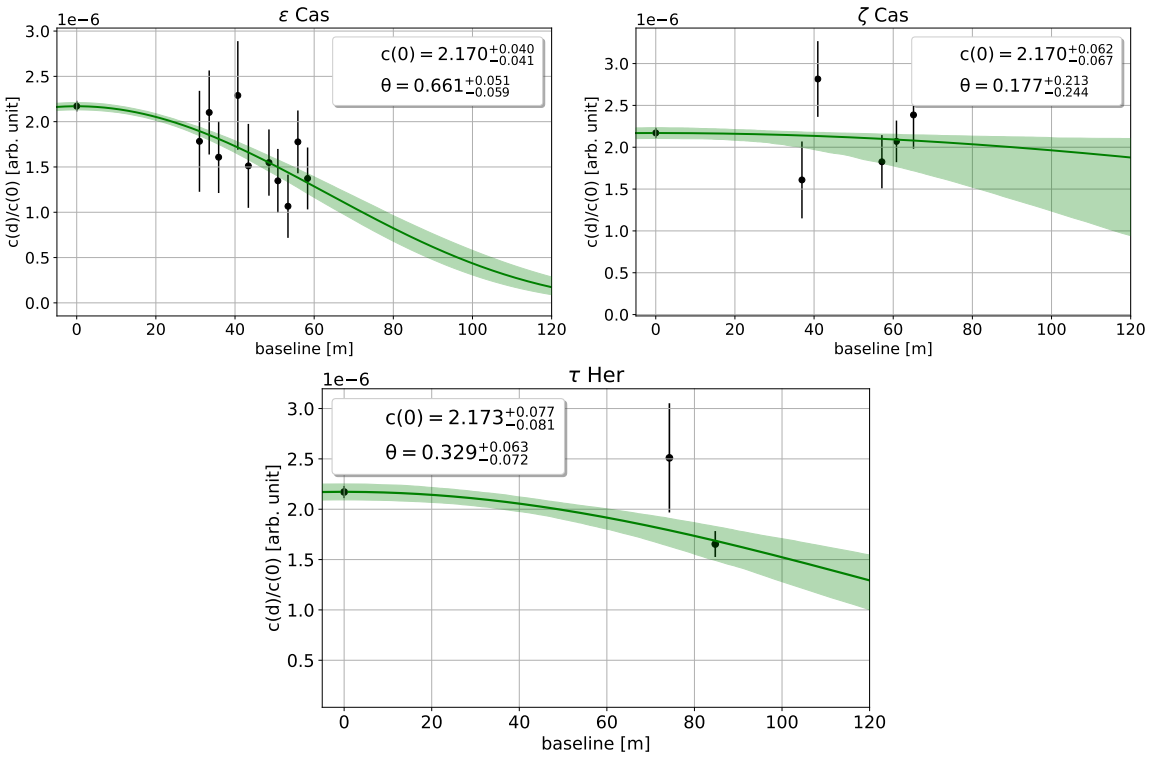

Figure 5.15.: Visibility fits for candidate stars with mirror combing method I. The parameter $c(0)$ of ϵ CMa served as calibration of the zero-baseline correlation.

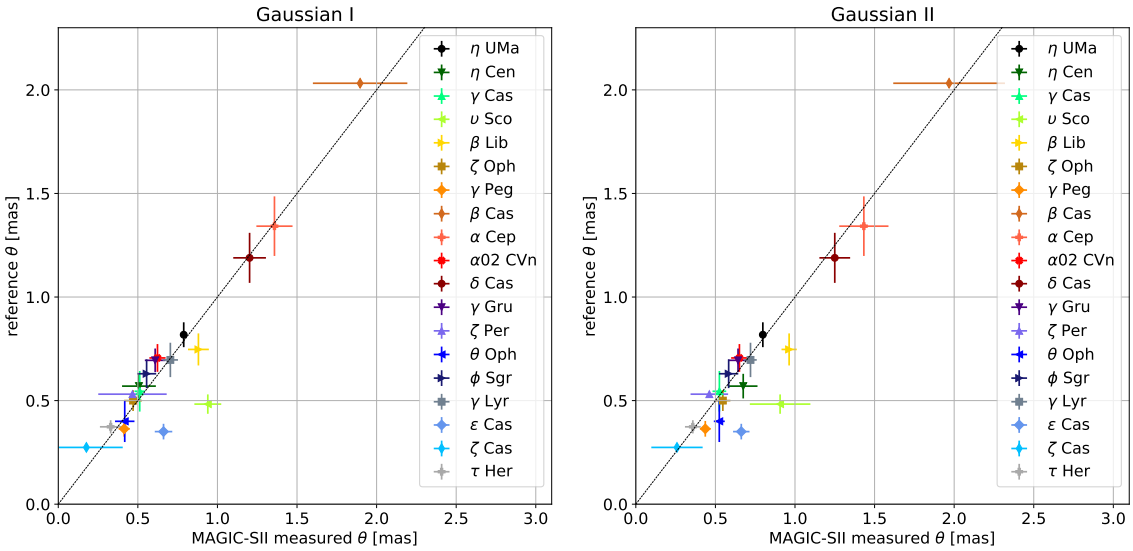

Figure 5.16.: θ measured by MAGIC-SII versus reference θ of candidate stars. The line marks the perfect match of the measured diameter to the reference diameter. The correlation signal was extracted with a Gaussian fit. Either was used mirror combining method I (**left**) or II (**right**).

coincide in most cases.

In Table 5.8 a summary of all MAGIC-SII measured diameters with their corresponding reference values is listed. In addition the table lists the uncertainty of the diameter measurement which is defined as the ratio of the diameter to its error, expressed as a percentage. The majority of the stars have an uncertainty > 5 %, i.e. the diameter measurement is not very precise in most cases. Additional data from observations in the next months may improve the results.

star	**reference θ [mas]**	**θ [mas]**	**uncertainty [%]**
ϵ CMa	0.770 ± 0.050	0.758 ± 0.018	2 %
γ Ori	0.720 ± 0.040	0.753 ± 0.018	2 %
ϵ Ori	0.631 ± 0.017	0.553 ± 0.069	12 %
β CMa	0.523 ± 0.017	0.548 ± 0.043	8 %
κ Ori	0.440 ± 0.030	0.380 ± 0.023	6 %
γ Crv	0.720 ± 0.060	0.777 ± 0.039	5 %
η UMa	0.818 ± 0.060	0.788 ± 0.022	3 %
η Cen	0.570 ± 0.059	0.507 ± 0.113	22 %
γ Cas	0.545 ± 0.098	0.512 ± 0.035	7 %
υ Sco	0.483 ± 0.047	0.940 ± 0.090	10 %
β Lib	0.747 ± 0.077	0.879 ± 0.066	8 %
ζ Oph	0.500 ± 0.050	0.466 ± 0.080	17 %
γ Peg	0.364 ± 0.038	0.414 ± 0.038	9 %
β Cas	2.03 ± 0.015	1.904 ± 0.296	16 %
α Cep	1.342 ± 0.144	1.358 ± 0.121	9 %
α02 CVn	0.706 ± 0.067	0.622 ± 0.054	9 %
δ Cas	1.189± 0.121	1.202 ± 0.110	9 %
γ Gru	0.694 ± 0.057	0.609 ± 0.069	11 %
ζ Per	0.531 ± 0.007	0.466 ± 0.229	50 %
θ Oph	0.4 ± 0.1	0.418 ± 0.065	16 %
ϕ Sgr	0.630 ± 0.069	0.555 ± 0.064	12 %
γ Lyr	0.712 ± 0.038	0.704 ± 0.051	7 %
ϵ Cas	0.350 ± 0.038	0.661 ± 0.059	9 %
ζ Cas	0.274 ± 0.018	0.177 ± 0.244	138 %
τ Her	0.354 ± 0.020	0.329 ± 0.072	22 %

Table 5.8.: List of MAGIC-SII measured θ (using mirror combining method I) with reference θ for all reference and candidate stars. Additionally the uncertainty is given defined as the ratio of the measured diameter to is error. The majority of the MAGIC-SII diameters have an uncertainty > 5 %.

In Section 5.2 I demonstrated that the visibility fit is consistent between different channel pairs and mirror configurations. This proved that MAGIC-SII is now a stable and working interferometer. Section 5.3 showed that MAGIC-SII is able to measure diameters and is a reliable instrument. The diameters of the reference stars are, within uncertainties, compatible with reference values from catalogs.
This section was focused on the new achievements of MAGIC-SII: we were able to detect many candidate stars and measure their diameters. For the majority of these stars this is the first diameter measurement in the blue visible light band.

5.5. Short Baseline Correlation

Correlation data of SB channel pairs is taken either in Submirror or in Chessboard mode (see Section 3.1). In Submirror mode the correlation at baselines < 17 m can be studied. This allows measuring the diameter of very large stars, for example, α CMa (Sirius). Correlation data taken in Chessboard mode of SB channel pairs have baselines close to zero. The baselines are not zero because of the extension of the reflectors. Light from all parts of the reflector is focused on pixels 251 and 260 and the baselines between different parts of the reflector are significantly larger than 0. The available baseline range can be estimated by simulating various points on the mirror surface (see Section 3.7). The average baseline of correlation data taken in Chessboard mode for SB channel pairs is ~ 7.7 m. For stars of diameters < 1 mas $c(d)$ is almost equal to $c(0)$ at such a short baseline. Therefore the correlation signal in Chessboard mode for SB channel pairs can be assumed as equivalent to the zero-baseline correlation: $c(0) \simeq c(7.7\text{m})$.
The input channels are affected by correlated noise, i.e. a noise component in the signal which is equivalent in the input channels. Correlated noise has only an impact on the correlation data of SB channel pairs because the noise of MAGIC-I and MAGIC-II is not correlated and cannot affect correlations of channels from different telescopes. The correlated noise contains a low and a high-frequency component. The low-frequency component can be removed with a simple high-pass filter because the low-frequency noise is < 12 MHz, whereas the correlation signal from the starlight has a frequency of ~ 100 MHz. In the left panel of Figure 5.17 the correlation signal of data taken in Chessboard mode of channel pair $A - B$ for ϵ CMa is shown. The region where the correlation signal is located is marked with a red ellipse. The data is dominated by low-frequency noise. In the right panel of Figure 5.17 a 12 MHz high-pass filter was applied.

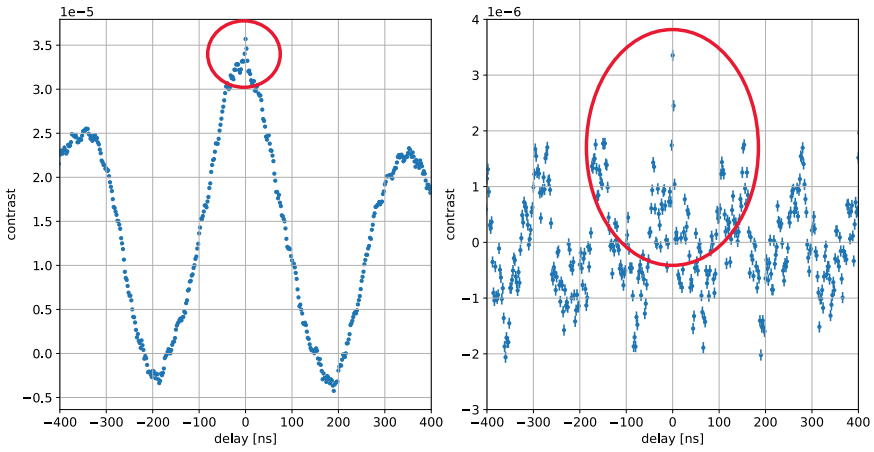

Figure 5.17.: Correlation data of SB channel pair $A - B$ for ϵ CMa, without applying the high-pass filter (**left**) and with high-pass filter (**right**). The region where the correlation signal is located is marked with a red ellipse.

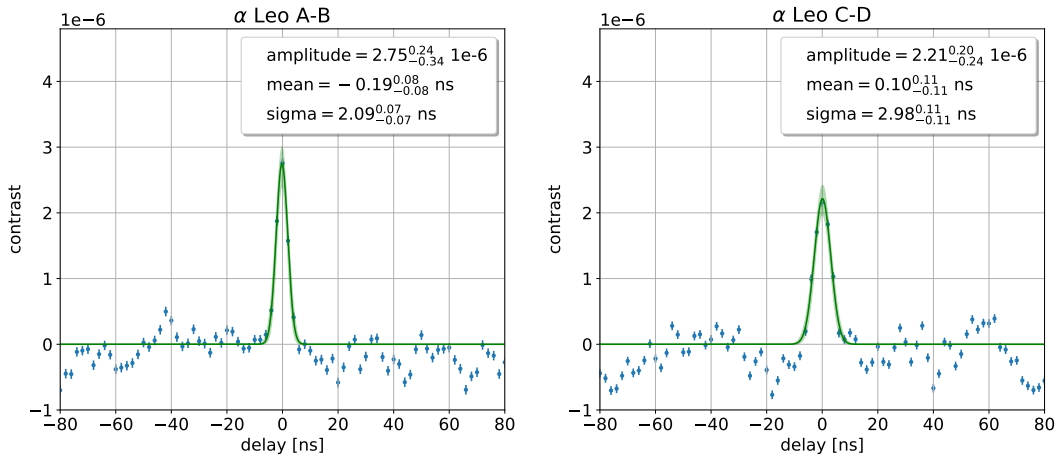

Figure 5.18.: Correlation signal of 55 minutes of SB correlation data taken in Chessboard mode for α Leo.

After the low-frequency cut still a high-frequency component of the noise is present in the data. Therefore the error bars of the data points are not representative of the actual spread of correlation. The frequency of this noise component is too close to the one of the starlight signal, therefore it cannot be removed with a simple band-pass filter.
The SB channel pairs are differently affected by the correlated high-frequency noise, as can be seen in Figure 5.18. This figures shows the correlation signal obtained from data taken in Chessboard mode for α Leo with the channel pairs $A-B$ and $C-D$. The correlation data of $A-B$ and $C-D$ are not compatible with each other. The correlation signals have a different amplitude. In addition, the signal of $A-B$ is narrower than that of $C-D$. It was expected to find a difference of ~ 17 % for the signal width between channel pairs $A-B$ and $C-D$ according to the results of the analysis of raw data (see Section 5.1.2), but the difference of the signal width in Figure is of ~ 30 %. Since the signals in Figure 5.18 are affected by the high-frequency component of the noise, it is difficult to say whether the difference in signal amplitude and signal width of the correlation data of channel pair $A-B$ and $C-D$ is due to differences in the PMT and digitizer bandwidth of MAGIC-I and MAGIC-II or due to the correlated noise.

During my shift in La Palma I measured correlation data in Submirror mode as shown in Figure 5.19 for α CMa using channel pair $A-B$. The upper configuration has an average baseline of ~ 10.4 m, the center configuration of ~ 8.7 m and the lower configuration of ~ 6.0 m.
Until the submission of this thesis, neither the source of the correlated noise nor a reliable and stable method to remove its high-frequency component has been found. Even if clear signals are visible in Figure 5.19, the amplitude of those signals is affected by the high-frequency component of the correlated noise and is not reliable. Correlation data of SB channel pairs could not be used so far to determine the diameter of stars or the zero-baseline correlation.

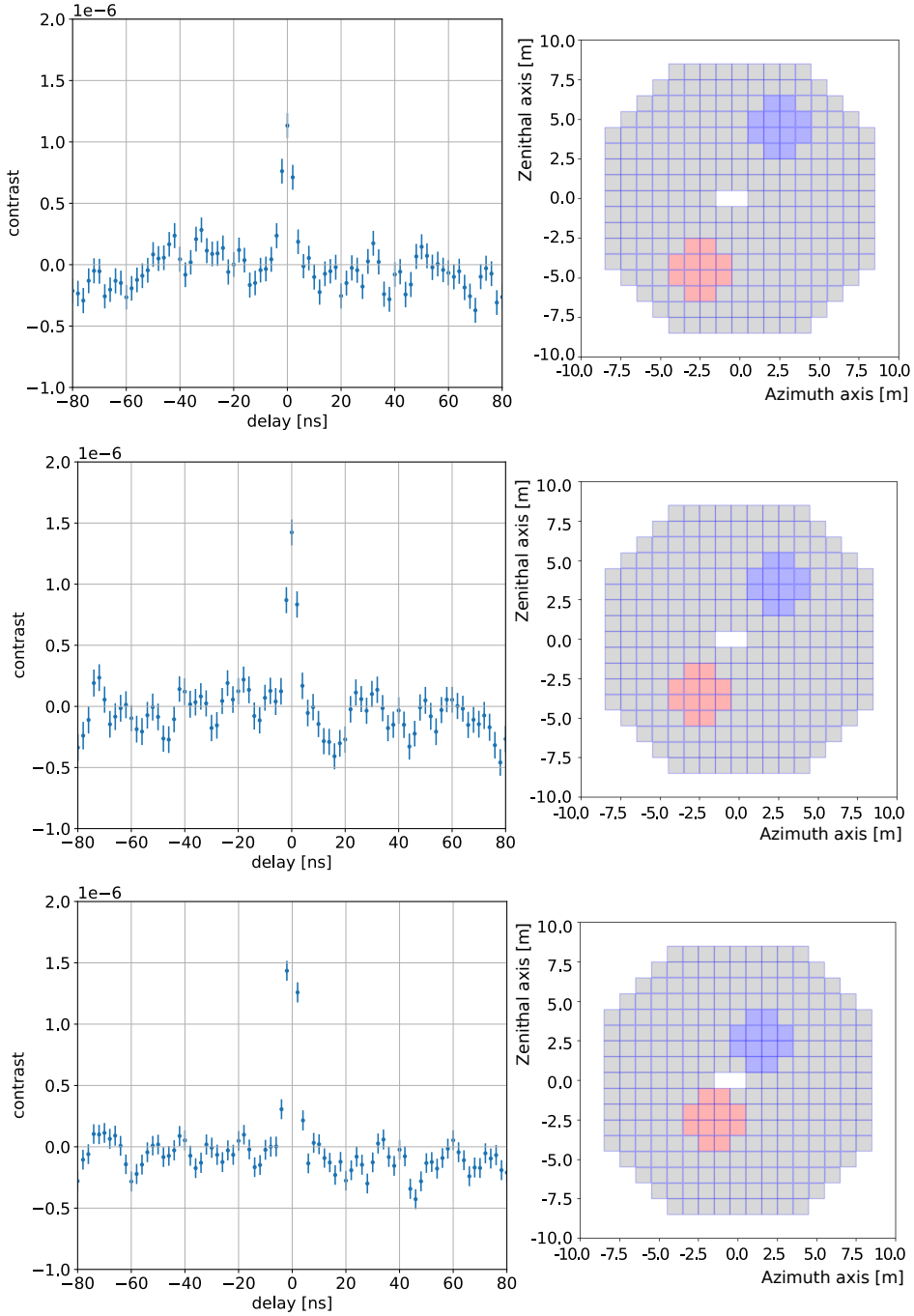

Figure 5.19.: Correlation signal of 65 minutes of data recorded in different $A-B$ Submirror configurations for α CMa. The Submirror configurations have an average baseline of ~ 10.4 m (**up**), ~ 8.7 m (**center**) and ~ 6.0 m (**down**).

5.6. SiPMs in intensity interferometry

In Chapter 1 I introduced fast photodetectors and presented the working principle of PMTs and SiPMs. As was mentioned before, SiPMs have many advantages compared to PMTs as a higher PDE and a better time resolution.As introduced in Section 4.1.5, a modular SiPM detector cluster was developed for the MAGIC-I camera (see [76, 77]) which uses large SiPM pixels similar to the LASiP concept presented in Section 4.1. The goal of this SiPM cluster was to study the feasibility of constructing and controlling SiPM modules in large-size IACTs. Intensity Interferometry could possibly benefit from the use of SiPMs in large-size IACTs. The performance of an intensity interferometer depends significantly on the time resolution and the PDE of its photodetectors. SiPMs with a SPTR better than 200 ps (FWHM) have been reported [73], whereas the MAGIC PMTs have a SPTR of ~ 2 ns (FWHM). SiPMs have also a different pulse shape with a very fast rise time (from 30 ps [144] to a few hundred ps [35]) and an exponential decay of ~ 1-100 of ns [144]. In addition, SiPMs typically feature a higher PDE in the red wavelength band compared to PMTs. This would allow observing sources at longer wavelengths.

As I was working during my PhD studies both in the intensity interferometry group of MAGIC and with large pixels made of SiPMs (see Chapter 4), naturally the question came up about the possible benefit of using SiPMs instead of PMTs for intensity interferometry observations. The question was hereby focused on the impact of the the pulse shape (i.e. the rise time, the pulse width and the decay time of the signal) and time resolution on the interferometer performance. To understand better this impact on the correlation signal, I performed a simple simulation with `root`. I did not simulate a full interferometer, but just two detectors collecting photons. Those photons could be correlated (and hence were detected simultaneously in both detectors) or not. I extracted a correlation signal in a similar way as it is done in the MAGIC-SII and compare the results for different pulse shapes.

5.6.1. Structure of the simulation

In Figure 5.20 a scheme with the structure of the simulation is shown. The data were simulated in two windows of 2600 ns, representing the simultaneous observation with two telescopes. The windows are named hereafter waveform 1 for the first telescope and waveform 2 for the second one. For each telescope 11000 waveforms were simulated. The pulse shape and the number of photons per second (event rate) were the input parameters of the simulation. I simulated both correlated and uncorrelated events. Correlated events have the same arrival time in both waveforms, while the arrival times of the uncorrelated ones are independent. The mean ratio of correlated to uncorrelated photons was 2 %. Both detectors record the same number of correlated photons. The mean number of uncorrelated events was calculated as the product of the event rate and the window size. The number of uncorrelated events in each waveform was randomly generated following a Poisson distribution. Additional un-

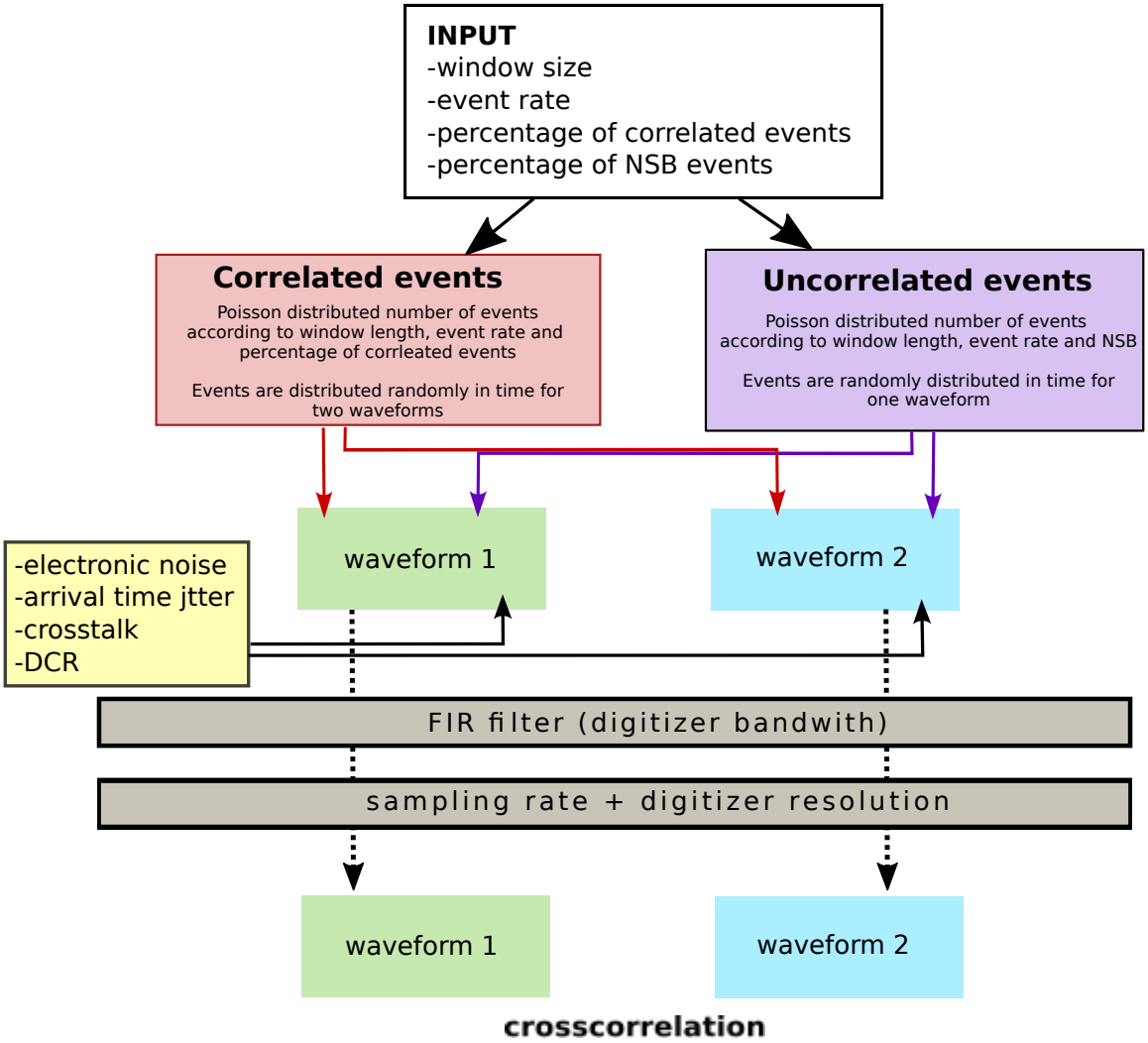

Figure 5.20.: Scheme of the structure of the simulation. Correlated and uncorrelated events were added to waveform 1 and waveform 2 according to several input parameters such as the window size, the event rate, the percentage of correlated events and the NSB. Optional noise could be added to the simulation in form of electronic noise, an arrival time jitter, crosstalk or dark counts. A FIR filter was applied to waveforms 1 and 2 to simulate the digitizer bandwidth. Additionally, the sampling rate and the digitizer resolution of the readout were considered. At the end the correlation between the two waveforms is calculated.

correlated events (15% of the event rate [6]) were included to take the NSB into account.

5.6.1.1. Pulse shape

To represent the pulse of a *simplified* SiPM (hereafter called *SiPM pulse*), I built a simple pulse defined by two exponentials, the rise time r, the decay time d and the arrival time μ of the pulse.

$$f_1(x, r, d, \mu) = \begin{cases} \exp\left(\frac{x-\mu}{r}\right) & \text{if } x \leq \mu \\ \exp\left(\frac{\mu+x}{d}\right) & \text{if } x > \mu \end{cases} \tag{5.1}$$

In addition, a MAGIC PMT-like pulse, hereafter called *PMT pulse*, was used. The pulse shape was extracted from data of a MAGIC PMT by defining a function capable of fitting the real pulses (see Figure 5.21):

$$f_2(x, \mu_1) = \begin{cases} \exp\left(\frac{-(x-\mu_1)^2}{2\sigma_1^2}\right) & \text{if } x \leq \mu_1 \\ \exp\left(\frac{-(x-\mu_1+\mu_2)^2}{2\sigma_2^2}\right) & \text{if } x > \mu_1 \end{cases} \tag{5.2}$$

μ_1 is the arrival time of the pulse, all other parameters have fixed values that are listed in Table 5.9. The pulse shapes of f_1 and f_2 allowed obtaining the correlation signal of waveforms containing either SiPM or PMT pulses. This way it was possible to compare the impact of the pulse shape on the correlation.

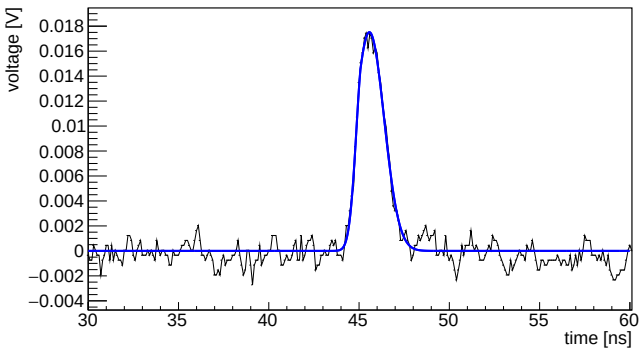

Figure 5.21.: Pulse of a MAGIC PMT recorded with an oscilloscope.

parameter	fixed value
μ_2	-0.31
σ_1	0.40
σ_2	0.81
t	μ_1-0.17

Table 5.9.: Parameters of Equation 5.2.

5.6.1.2. Noise

Noise could also be added to the waveforms.

Electronic noise

Electronic noise was randomly generated following a Gaussian distribution. The σ of that distribution was estimated by looking at the fluctuations of the baseline from real data taken with a MAGIC SiPM pixel. Figure 5.22 shows the amplitude distribution

of that baseline. The distribution was fitted with a Gaussian, which yielded a σ of $\sim$ 0.2 phe.

Arrival time jitter

Arrival time fluctuations were randomly generated following a Gaussian distribution. The σ of this distribution represented the SPTR (given as σ) of the photodetector. I used three different values of sigma: 1 ns, which is the typical jitter of a MAGIC PMT [17], 0.5 ns and 0.1 ns, which represent different SPTR values that could be obtained using SiPMs [73].

Crosstalk

Crosstalk is generated as additional pulses that are correlated in time to their parent pulse. The number of crosstalk events is Poisson distributed according to a typical crosstalk probability of 20 % (see MicroFJ-60035-TSV from SensL [147]). The crosstalk events enter the simulation with an arrival time jitter of 100 ps [139].

DCR

Dark counts can be included as additional uncorrelated events. It is assumed that the SiPM pixel consists of nine SiPMs of 6 × 6 mm ^{2}. I used two different DCRs: 50 kHz/mm^2 and 100 kHz/mm^2.

5.6.1.3. Simulated readout

To simulate the data-taking in an interferometer, the simulated waveforms were 'digitized' in order to take into account the impact of digitizer bandwidth, the sampling rate and the digitizer resolution. The digitizer bandwidth was simulated by using a

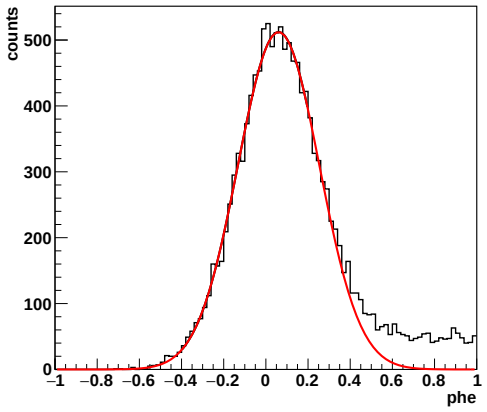

Figure 5.22.: Distribution of the baseline of a MAGIC SiPM pixel far away from the signal region to evaluate the electronic noise.

Finite Impulse Response (FIR) filter [155, 162]. The original signal is stored in an array $X = x[1], ..., x[n]$ and the filtered signal in an array $Y = y[1], ..., y[n]$. The nth component of Y is

$$y[n] = b_0 x[n] + b_1 x[n-1] + ... + b_N x[n-N] = \sum_{i=0}^{N} b_i \cdot x[n-i]. \tag{5.3}$$

N is here the order of the FIR filter and b_i the FIR coefficients. To define $y[n]$ the information of all $N+1$ points of the original signal going from $x[n-N]$ to $x[n]$ is required. Thus, the output of a FIR filter is the sum of past, present and possible future signals. The coefficients depend on the cut-off frequency of the filter, which represents the bandwidth limit of the digitizer.
The number of data points per window is reduced according to the sampling rate. The

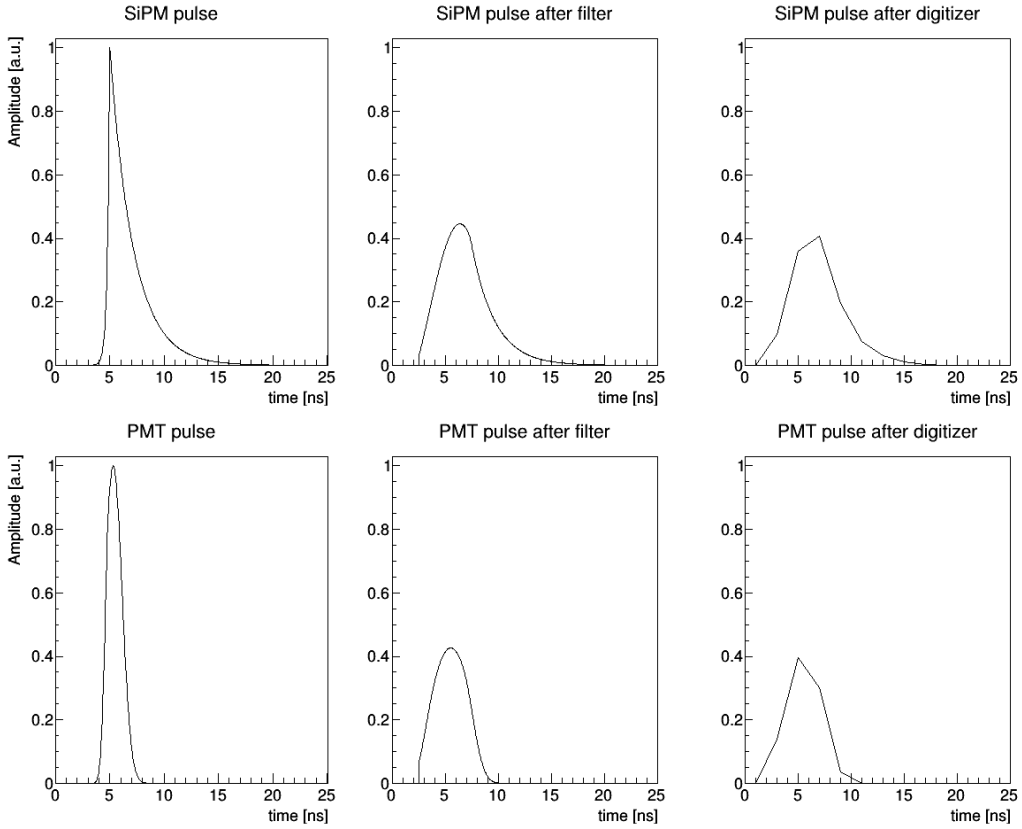

Figure 5.23.: Impact of the FIR filter and digitizer noise/sampling rate: in the left panels the original SiPM pulse with a rise time of 1 ns and a decay time of 10 ns (**upper left**) and the PMT pulse (**lower left**) are shown. In the central panels, the signal after the FIR filter is shown for a bandwidth of 130 MHz (as in MAGIC-SII). In the right panels, digitizer noise was added and the signal was averaged according to the sampling rate of 500 MS/s (as in the MAGIC-SII readout).

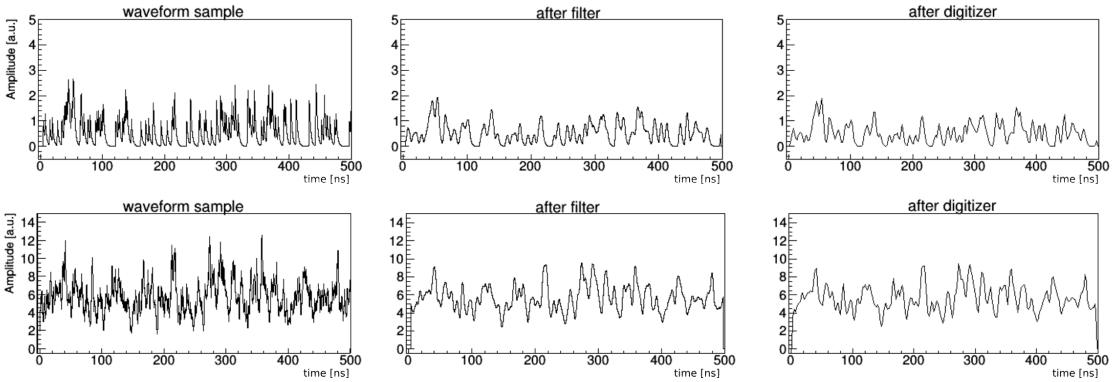

Figure 5.24.: Waveform with 200 MHz event rate (**up**) and 2 GHz event rate (**down**) for SiPM pulses with a rise time of 1 ns and a decay time of 10 ns. The bandwidth was 130 MHz and the sampling rate was 500 MS/s.

digitizer resolution is set to 14 bits. Additional digitizer noise is generated following a Gaussian distribution with a σ of 0.4 phe.
In Figure 5.23 the impact of the bandwidth (central panels) and the sampling rate (right panels) is shown for a SiPM pulse (upper panels) and a PMT pulse (lower panels). The bandwidth was 130 MHz and the sampling rate was 500 MS/s as in the MAGIC-SII readout.

5.6.1.4. Event rates

I used two different event rates: 200 MHz and 2 GHz. The lower rate corresponds to a dim star. In the upper panels of Figure 5.24 an example of a zoom into a waveform with SiPM pulses at an event rate of 200 MHz is shown. The pulses have a rise time of 1 ns and a decay time of 10 ns. The bandwidth was 130 MHz and the sampling rate was 500 MS/s. At this rate, individual pulses can be distinguished in the waveform. In the lower panels of Figure 5.24 a waveform with 2 GHz is shown. The waveform exhibits much more pile up, the event rate is continuous and individual pulses cannot be distinguished. Such a rate is of the order of what MAGIC-SII achieves when observing a bright star (for example a reference star as κ Ori observed at a zenith angle of 63 deg has an estimated rate of 5.5 GHz).

5.6.2. Results of the simulation

The simulation was run for SiPM pulses with different rise and decay times (see Equation 5.1). The rise time was defined as the time it took the pulse signal to get from 1 to 99 % of the pulse maximum amplitude. The decay time was defined as the time after the peak it took to get from 99 to 1 % of the maximum amplitude. In order to evaluate the impact of the pulse shape, noise and digitizer properties on the correlation, I compared the different SNRs I obtained. The correlation signal was extracted using

the Maximum point method introduced in Section 3.6. The SNR was calculated as the extracted signal amplitude divided by the RMS defined in a background region of

$$\text{delay} = \begin{cases} -1500 \text{ ns} < x < -500 \text{ ns} \\ 500 \text{ ns} < x < 1500 \text{ ns} \end{cases} \tag{5.4}$$

If not stated otherwise, the bandwidth of the digitizer was 130 MHz and the sampling rate was 500 MS/s.

5.6.2.1. Pulse shape

The decay time has a strong impact on the correlation signal as can be seen in Figure 5.25 where the correlation signal of SiPM pulses with a rise time of 1 ns and decay times of 10, 30 and 60 ns are shown. With an increasing rise time the correlation signal becomes broader and the SNR decreases.
In the left panel of Figure 5.26 the obtained SNR of the correlation signal for a SiPM pulse with a rise time of 0.5 ns relative to the SNR of the correlation signal for a PMT pulse is plotted as a function of the decay time, for event rates of 2 GHz and 200 MHz. The dependence of the SNR on the rise time is similar for 2 GHz and 200 MHz. In the right image the obtained SNR of the correlation signal for a SiPM pulse with a decay time of 10 ns relative to the SNR of the correlation signal for the SiPM pulse with the fastest rise time of 0.05 ns is shown. The correlation signal hardly changes for different

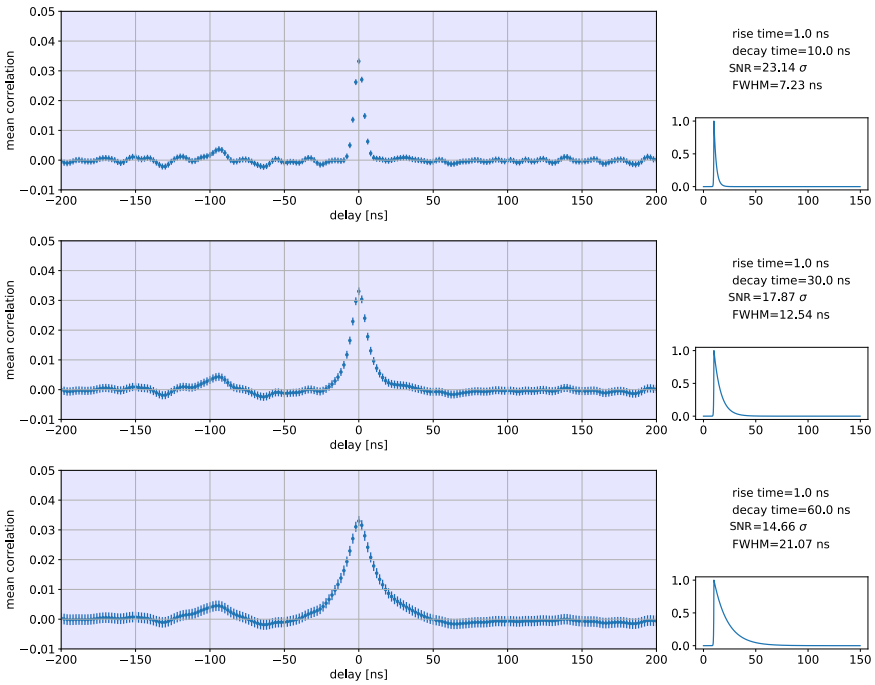

Figure 5.25.: Correlation signal for SiPM pulses with a rise time of 1 ns and decay times of 10, 30 and 60 ns. The event rate is here 2 GHz.

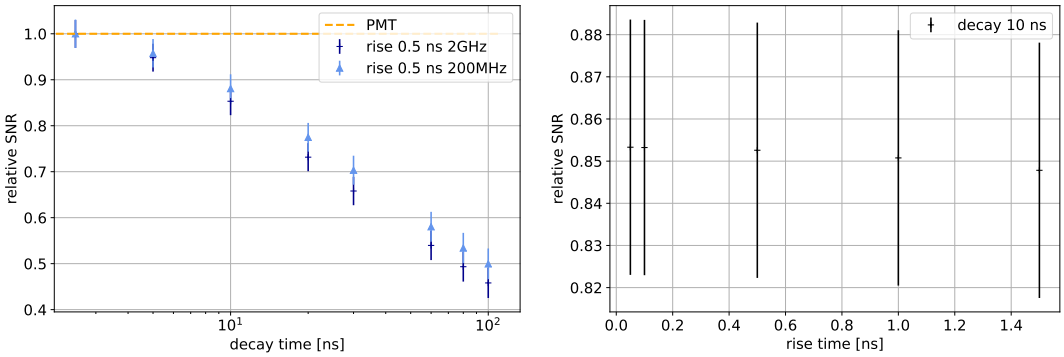

Figure 5.26.: SNR of the correlation signal for SiPM pulses relative to SNR of the correlation signal for a PMT pulse as a function of the decay time. The SiPM pulses have a rise time of 0.5 ns. The SNR is compared for two different rates. (**left**). SNR for a SiPM pulse with a decay time of 10 ns relative to the SNR for the SiPM pulse with the fastest rise time of 0.05 ns (**right**).

rise times. The SNR is dominated by the decay time because $d \gg r$ for a typical SiPM pulse.

5.6.2.2. Noise

Electronic noise

In Figure 5.27 the impact of electronic noise on the correlation signal is shown, in the left panel for an event rate of 2 GHz and in the right panel for 200 MHz. The SNR of the correlation signal for a SiPM pulse with a rise time of 0.5 ns and different decay times is given relative to the SNR of the correlation signal for a PMT pulse without electronic noise. In the case of a 2 GHz rate, the electronic noise has no impact. For a

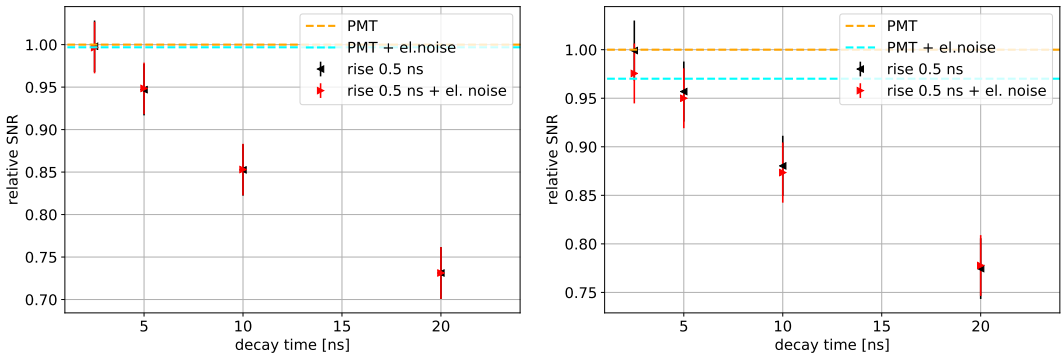

Figure 5.27.: Impact of the electronic noise on the correlation signal: SNR of the correlation signal for a SiPM pulse relative to the SNR of the correlation signal for a PMT pulse without electronic noise, for an event rate of 2 GHz (**left**) and 200 MHz (**right**).

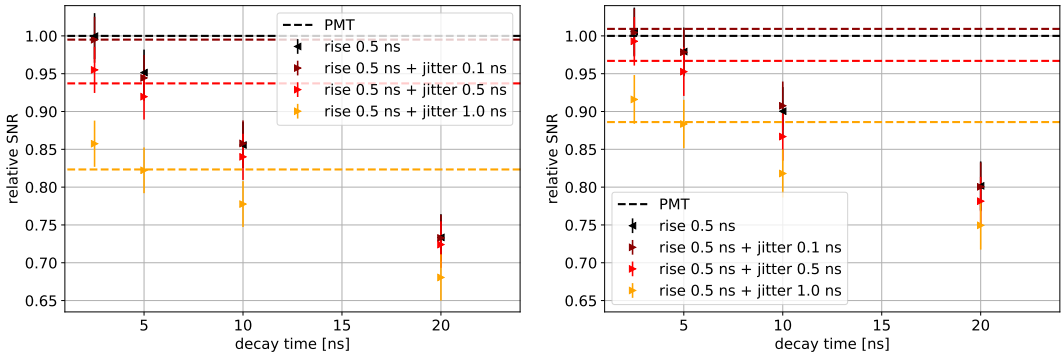

Figure 5.28.: Effect of the arrival time jitter on the correlation signal: SNR of the correlation signal for a SiPM pulse relative to the SNR of the correlation signal for a PMT pulse without arrival time jitter, for an event rate of 2 GHz (**left**) and 200 MHz (**right**).

200 MHz rate the electronic noise has a small effect of ~ 2 % on pulses with a rise time of 0.05 ns. For such a fast rise time and an event rate of 200 MHz the waveform did not show a continuous signal and I could distinguish individual pulses. In this case fluctuations of the baseline seem to affect the correlation signal.

Arrival time jitter

Figure 5.28 shows the effect of arrival time variations on the correlation signal, in the left panel for an event rate of 2 GHz and in the right panel for 200 MHz. The SNR of the correlation signal for a SiPM pulse with a rise time of 0.5 ns and different decay times is given relative to the SNR of the correlation signal for a PMT pulse without arrival time jitter. A small arrival time jitter of 0.1 ns has nearly no effect on the SNR, while a larger arrival time jitter of 0.5 ns or 1 ns reduced the SNR by ~ 5-15%. The arrival time jitter has a stronger impact on fast signals and for high rates.

Crosstalk

Figure 5.29 shows the impact of optical crosstalk on the correlation signal, in the left panel for an event rate of 2 GHz and in the right panel for 200 MHz. The SNR is given relative to the SNR of the correlation signal for the fastest SiPM pulse with a decay time of 2.5 ns without crosstalk. Crosstalk reduced the SNR by ~ 10-12 %.

DCR

In Figure 5.30 the effect of dark counts on the correlation signal is shown, in the left panel for an event rate of 2 GHz and in the right panel for an event rate of 200 MHz. The SNR is given relative to the SNR of the correlation signal for the fastest SiPM pulse with a decay time of 2.5 ns without DCR. Dark counts are uncorrelated events and have exactly the same effect than uncorrelated photons from the star or from

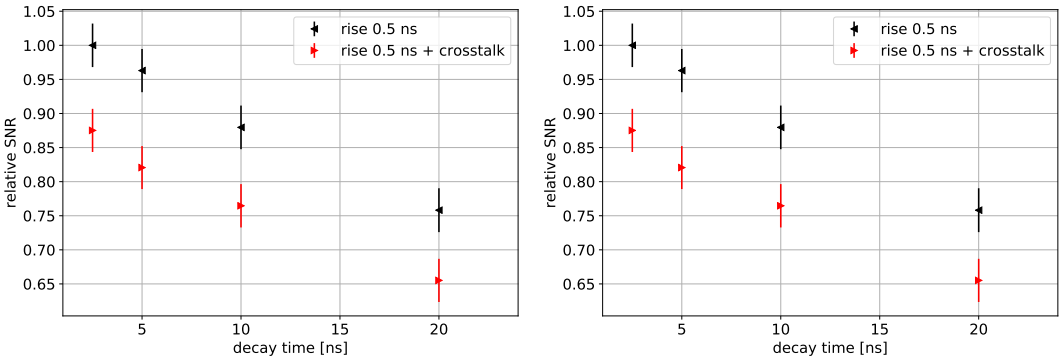

Figure 5.29.: Impact of crosstalk on the correlation signal: SNR of the correlation signal for a SiPM pulse relative to the correlation signal for the fastest SiPM pulse with a decay time of 2.5 ns without crosstalk, for an event rate of 2 GHz (**left**) and 200 MHz (**right**).

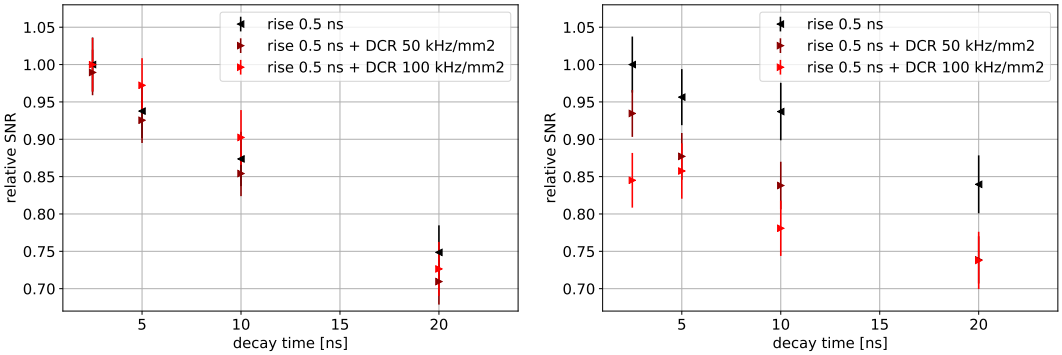

Figure 5.30.: Effect of the DCR on the correlation: SNR of the correlation signal for a SiPM pulse relative to the SNR of the correlation signal for the fastest SiPM pulse with a decay time of 2.5 ns without DCR, for an event rate of 2 GHz (**left**) and 200 MHz (**right**).

the NSB. They have no impact on the SNR for an event rate of 2 GHz since they increased the number of uncorrelated events just by 1.6 %. For an event rate of 200 MHz, additional dark counts increased the number of uncorrelated events by 16.2 %. In this case a DCR of 50 kHz/mm^2 reduced the SNR by ~ 7-10 %, while a DCR of 100 kHz/mm^2 by ~ 10-15%.

5.6.2.3. Digitizer

In Figure 5.31 the impact of digitizer bandwidth and the sampling rate on the correlation signal is shown. In the left panel the obtained SNR relative to a bandwidth of 130 MHz is plotted as a function of the bandwidth. The sampling rate was fixed at 4 GS/s. A larger bandwidth increased the SNR. The effect was stronger for a decay time of 2.5 ns, i.e. fast SiPM pulses. A bandwidth of 600-800 MHz can double the SNR for

fast SiPM pulses. However, for a decay time of 30 ns the improvement due to a larger bandwidth is limited to ~ 25 %.
In the right panel the obtained SNR relative to a sampling rate of 500 MS/s is plotted as a function of the sampling rate. The bandwidth is set to a fixed value of 1 GHz. A larger sampling rate increased the SNR. Similar to an increased bandwidth, this effect was stronger for signals with a small decay time. For a decay time of 2.5 ns, a sampling rate of 1 GHz increased the SNR by ~ 30 %.

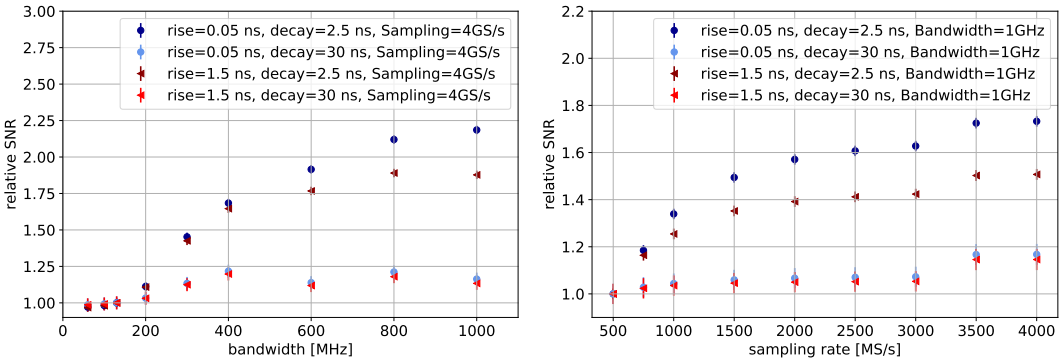

Figure 5.31.: SNR of correlation signal for SiPM pulses as a function of the bandwidth (**left**) or as a function of the sampling rate (**right**). The SNR is given relative to the SNR for a bandwidth of 130 MHz (**left**) or a sampling rate of 500 MS/s (**right**).

5.6.3. Conclusions

Due to the simplicity of the simulations, no strict constraints should be derived from the results, but several basic conclusions can be drawn:

1. If SiPMs are used instead of PMTs in intensity interferometry, the decay time of the SiPMs has a significant impact on the correlation signal.

2. Electronic noise is not expected to have a significant impact, if kept at reasonable levels.

3. The arrival time jitter has a strong effect. The SNR of the correlation signal could benefit from a detector with a reduced arrival time jitter. In this case SiPMs could outperform PMTs.

4. Optical crosstalk reduces the SNR of the correlation signal.

5. DCR has only an effect for low event rate, i.e. for dim stars.

6. Increasing digitizer bandwidth and the sampling rate could significantly increase the SNR.

5.7. Future prospects

One of the main targets of future upgrades of the MAGIC-SII is the increase of its SNR. The SNR of the correlation signal for a pair of equal telescopes for unpolarized light is given by Equation 5.17 in [85]

$$\mathrm{SNR} = A \cdot \alpha(\lambda_0) \cdot q(\lambda_0) \cdot n(\lambda_0) \cdot |V|^2(\lambda_0, d) \cdot \sqrt{b_\nu} \cdot F^{-1} \cdot \sqrt{T/2} \cdot \sigma. \tag{5.5}$$

A is the mirror area, $\alpha(\lambda_0)$ is the quantum efficiency (QE) of the photodetector for a central filter wavelength λ_0, $q(\lambda_0)$ is the QE of the remaining optics and $n(\lambda_0)$ is the differential photon flux of the star. b_ν is the effective crosscorrelation electrical bandwidth, F is the excess noise factor of the detector and T is the observation time. σ is the normalized spectral distribution of the light as defined in Equation 5.6 in [85]. If we had an ideal filter with rising and falling edges $\to 0$, σ would be one. In a filter like the one shown in Figure 3.4 we have $\sigma \simeq 0.86$ [43]. The SNR in Equation 5.5 does not depend on the width of the spectral range ('optical passband'). Hence it is possible to split the light into several spectral channels N_{spectral} with smaller optical passbands. Each of these channels would feature the same SNR, but the total SNR of the combination of these channels would rise by a factor $\sqrt{N_{spectral}}$ [43]. Moreover, the SNR depends on the number of telescopes: with an array of N_t telescopes the SNR increases with the square root of the telescope pairs $\sqrt{N_t(N_t-1)/2} \sim N_t$ [43].

The sensitivity of MAGIC-SII could be improved, for instance, by increasing the following parameters: (1) the number of telescopes N_t and spectral channels $N_{spectral}$, (2) the QE of the photodetectors and (3) the bandwidth of the readout and the time resolution of the photodetectors [43].

New correlator architecture

With an increasing number of spectral channels and telescopes, the correlator must have an appropriate dimension. What is particularly challenging is that the required computation power grows quadratically with N_t, since the correlation of each individual telescope pair needs to be calculated. The approach of the MAGIC-SII group to tackle this problem is to develop a new correlator architecture that is able to scale up to large N_t because the computation power increases linearly with N_t. The approach is based on ideas developed for radio astronomy (see [141]).
In Figure 5.32 the correlation between all possible 2-channels pairs is illustrated. The difference with the correlator that is currently implemented in MAGIC-SII (see Section 3.4) is that in this case the computation of the correlation is separated in several computers. The correlator is structured as follows: first the signal from N camera pixels (channels) ch1, ..., chN is digitized. Then a FFT is performed over a defined time interval (frame) and the FFT is encoded as a Hartely transform to reduce the amount of information saved in the buffer. This part of the computation is called *F-Machine*. The N encoded FFT is transferred to the *X-Machine* to be decoded. For each of

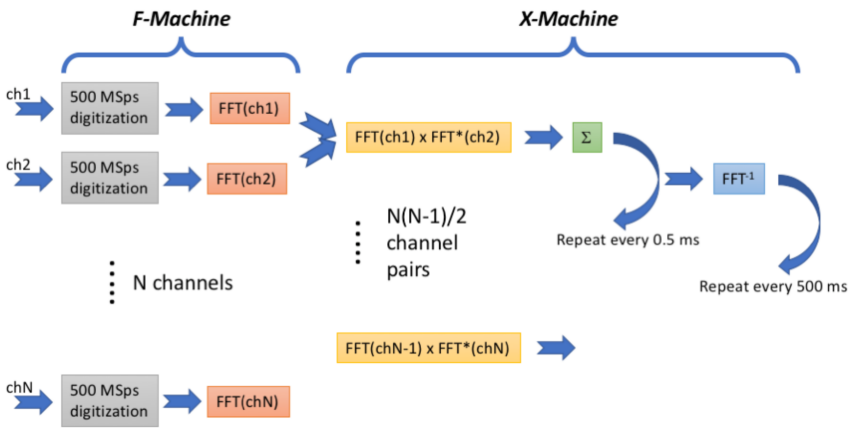

Figure 5.32.: Structure of a scalable correlator with N independent channels. The computation is seperated to several computers. Image from [43].

the $N(N-1)/2$ channel pairs ch_{ij} $\mathrm{FFT}(\mathrm{ch}_i)$ is multiplied with the complex conjugate $\mathrm{FFT}^*(\mathrm{ch}_j)$. The result is summed in a buffer, where the summation of previous time frames is collected. This process is repeated over 1000 frames before an inverse FFT is applied to the sum. From there it is possible to calculate the array of correlation coefficients as a function of the time delay.
In this correlator architecture, the F-Machine defines the need for computation power which scales approximately linearly with N as long as N is smaller than the number of frames over which the result is summed. Details of the hardware implementation and a test correlator are presented in [43].

Extending the interferometer

A new generation of IACT arrays is under construction, the Cherenkov Telescope Array (CTA). It will be the largest ground-based gamma-ray detection observatory in the world [44]. The Cherenkov Telescope Array Observatory (CTAO) will be constructed in two sites: in the northern hemisphere on the island La Palma, next to the MAGIC telescopes, and in the southern hemisphere near Paranal, Chile. The CTAO will consist of telescopes of different sizes: Small-Sized Telescopes (SST), Medium-Sized Telescopes (MST) and Large-Sized Telescopes (LST). The LST reflector has a diameter of 23 m (roughly 400 m^2). Since 2018 a full-size LST (LST-1) is in operation in the ORM, at a distance of around 100 m from one of the MAGIC telescopes (see Figure 2.10). Another three LSTs shall be installed during the next 2 years at the ORM [43]. The direct neighborhood of the future CTAO to MAGIC-SII offers a huge potential for a possible synergy between them. Due to its large number of telescopes (and hence of possible baselines that can be achieved) the CTAO has the potential to provide a huge increase in the performance of IACTs as intensity interferometers.

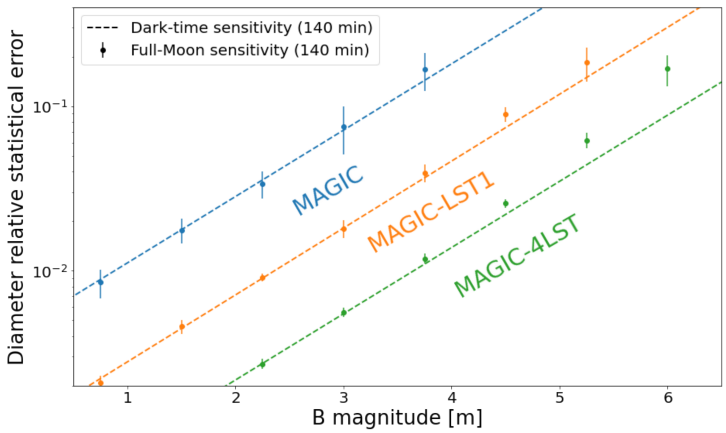

Figure 5.33.: Expected uncertainty of the measurement of the diameter of a star similar to γ Crv as a function of its magnitude B, estimated for three different interferometers: in blue the current MAGIC-SII, in orange MAGIC-SII in combination with the already existing LST-1 and in green MAGIC-SII with four LSTs. The simulated total observing time across a single night is 140 minutes. The error bars are the σ of 100 simulated iterations, while the dashed lines show the linear trend of the relative uncertainty under dark-sky conditions. Image from [43].

The MAGIC-SII group performed a simulation to examine the performance of three different interferometer setups: the current MAGIC-SII, MAGIC-SII in combination with LST-1 or MAGIC-SII combined with all four LSTs of the La Palma site of CTA. In Figure 5.33 the expected diameter uncertainty of a star like γ Crv (diameter 0.72 mas and -17.5° declination) is shown as a function of the stellar magnitude in the blue wavelength band. γ Crv is used as a reference because its diameter and declination are well adapted to the baseline range and latitude of MAGIC [43]. The dashed lines in Figure 5.33 correspond to an ideal case where the NSB can be neglected. The points show a more realistic estimation that includes the NSB background at Full Moon. When LST-1 is combined with MAGIC, the magnitude limit increases by 2.8 mag. The combination of MAGIC+4 LST could even measure a diameter of a B=6.2^m star with an uncertainty of 10% within 2 hours (in the case in which NSB can be neglected). In addition, such a setup would feature 15 different telescope pair combinations which would allow covering baselines in a range of ~ 20 - 250 m. Details about a possible implementation of a combined MAGIC-LST interferometer are discussed in [43].

Bandwidth limit

As demonstrated in Section 5.6 a higher bandwidth and sampling rate can heavily improve the sensitivity of an interferometer. A faster readout would allow exploiting the capabilities of faster photodetectors. In the current MAGIC-SII setup, the limited bandwidth of the digitizer (130 MHz) and the arrival time jitter of the PMTs (~ 1 ns [17]) set a clear limit to the sensitivity.

In modern Field Programmable Gate Arrays (FPGAs) high-speed acquisition of up to 4 GHz is possible. The advent of 5G telephony has pushed forward such developments. Industry has created complete Systems On a Chip (SOC) with monolithic integration of ADCs within a large FPGA fabric[43]. This could possibly eliminate the bottleneck of transporting data from the Application Delivery Controllers (ADCs) to the processing system. In 2022 a new digitizer card (HTG-ZRF8 from HiTech Global) using this technology was tested in the MAGIC interferometer. It is now fully integrated into regular observations. Details of the new digitizer card system can be found in [43].
With higher digitizer bandwidth and sampling rate, the interferometer may benefit from the use of SiPMs with high time resolution and high PDE. Since already a SiPM pixel cluster is installed in the MAGIC camera, this could be a starting point for testing the feasibility of using SiPMs in intensity interferometry. The SPTR of the SiPM pixel cluster is with ~ 1 ns (see Section 4.1.5) better than the time resolution of the MAGIC PMTs. An upgraded SiPM pixel cluster with even faster SiPMs and electronics (i.e. large SiPM pixels designed for this application) would allow to exploit SiPM capabilities in the context of optical intensity interferometry.

Conclusions

At the beginning of this thesis I gave an introduction to fast photodetectors with the ability to resolve single photons (time resolution of at least a few ns and high intrinsic gain). I presented PMTs, which are still the photodetector of choice in many applications, and SiPMs which challenge the dominant position of PMTs in fields like medical physics or astrophysics. SiPMs are advantageous whenever an excellent SPTR and a high PDE are required. This would be the case, for instance, in intensity interferometry.

After decades intensity interferometry is again used to measure stellar diameters. This was possible thanks to the existence of telescopes with large collection areas equipped with fast PMTs. I introduced the theory of intensity interferometry and I explained how existing IACT arrays could be used as intensity interferometers. I showed how the correlation of the intensity of the incoming photon flux can be obtained in MAGIC, which are the potential targets that could be observed with the MAGIC-SII and what kind of physics we could learn with these observations.

A few years ago MAGIC-SII was implemented by applying adjustments to the existing MAGIC IACT array. Since then the interferometer was upgraded several times and is now able to routinely perform observations. MAGIC-SII is ten times more sensitive than the Narrabri Stellar Telescope. MAGIC-SII can provide data that allows us to gain knowledge about stellar structure and evolution. I participated actively in the first development of an analysis chain for MAGIC-SII data.

Since the MAGIC-SII is a new and evolving instrument, there are continuous discussions ongoing on how to upgrade it and improve its sensitivity. One of the key parts of the instrument are the photodetectors. Improved photodetector properties as a higher PDE or a better SPTR could increase the sensitivity of the interferometer. This could be achieved if the PMTs were replaced by SiPMs. Probably the main drawback of SiPMs is their limited area. This is problematic when needing to equip a large camera like that of IACTs. I worked on two approaches that aimed at overcoming this limitation: LASiP and Photo-Trap. The first one sums the current of several SiPMs into a single output. We built and characterized a LASiP prototype that used an ASIC called MUSIC to sum the output of 8 SiPMs of 6 mm × 6 mm. I was able to equalize its gain and studied how the SNR degraded as the number of summed SiPMs increased. I also explored the feasibility of using LASiPs in SPECT, which is another application in which one needs to cover a large area (50 × 40 cm^2) with a limited amount of readout channels (typically ~ 100). I showed that it was possible to reconstruct simple images with a performance that is comparable to that of standard

SPECT cameras: an energy resolution of ~ 11.6 % and an intrinsic spatial resolution of ~ 2 mm (see details in Appendix A and B). This application could be particularly suitable for LASiPs because timing is not critical, but with a high PDE the energy resolution could be improved. Especially, using SiPMs, which are much more compact than PMTs, would allow reducing by at least 50 % the volume of a SPECT camera. This enables to lower significantly the amount of lead needed to shield the camera. As a result, we would have a much more compact and lighter camera which would also soften the requirements for building a scanner (and then its cost).
Since a few LASiPs were also present in one of the MAGIC cameras [78], I studied the time resolution of one of them. In a pixel holding 9 SiPMs of 6 × 6 mm^2 I found a SPTR of 0.9 ± 0.2 ns FWHM, which is clearly better than the time resolution of the MAGIC PMTs (~ 2 ns FWHM). Besides, the shape of this pixel resembles that of a PMT: it has basically the same rise time, pulse width and decay time. This pixel could then be a good starting point for testing the feasibility of using SiPMs in intensity interferometry.
I presented a dedicated simulation that studied the impact of pulse shape, digitizer bandwidth and sampling rate on the SNR of the correlation signal. The results of this study demonstrated that the time resolution and the pulse shape are key factors. Especially thanks to their excellent SPTR, SiPMs could then provide a boost in the performance of intensity interferometers. However, the SiPM itself and its readout should be designed in order to minimize the decay time. The problem of the decay time might be minimized in the future with digital SiPMs. Or alternatively, with the combination of analog SiPMs and ASICs that digitizes the signal. The FastIC, for instance, encodes the information about the arrival time and amplitude of a pulse in two consecutive binary pulses that can be easily digitized, for instance with an FPGA [63]. With this ASIC, and an HPK S13360-3050CS SiPM a SPTR of 140 ps FWHM was obtained.
As it was mentioned before, a LASiP cannot be easily scaled to very large sizes because the SNR degrades as the total LASiP area increases. In a LASiP the electronic noise of all the SiPMs is summed and the capacitance and DCR also increase with the area. Of course, the cost of a LASiP still increases linearly with the area. Photo-Trap provides a different solution to build large SiPM pixels, combining a WLS plastic and a dichroic filter with a commercial SiPM. We built four prototypes using WLS plastics of 20 × 20 mm^2 or 40 × 40 mm^2 and SiPMs of 3 × 3 mm^2 or 3 × 12 mm^2. One of those prototypes is, as far as I know, the largest existing SiPM pixel with single-phe resolution at room temperature. One of the main advantages of Photo-Trap is that it is easily scalable to larger sizes. And this can be done without increasing the DCR, the capacitance, the power consumption or the cost of the pixel. Indeed it is possible to have a pixel with the noise of a small commercial SiPM with a collection area that can be ~ 100 times larger. The prototypes achieved a trapping efficiency of ~ 10 – 50% (which corresponds to a peak PDE of ~ 5 – 25%) with a time resolution of ~ 2 – 5 ns (FWHM). The time resolution of Photo-Trap is comparable to that of the MAGIC PMTs (~ 2 ns FWHM [17]) or the larger IceCube PMTs (~ 4 ns FWHM IceCube [165]). These prototypes are probably not suitable for the MAGIC-SII, since their performance

in terms of time resolution and PDE is worse than that of the PMTs that are installed in MAGIC. Photo-Trap would be more suitable in those applications in which the lower PDE can be compensated with a much larger collection area, like in large water Cherenkov detectors [69].

My main contribution to the MAGIC-SII was the development of the analysis chain which was used to analyze the data of multiple calibration campaigns. The calibration results of the MAGIC-SII showed that the correlation signals of different output channel pairs are consistent with each other. This result validated that the current MAGIC-SII is a working and reliable instrument. Based on these results, I used the constant $c(0)$, derived from the visibility fit of a calibrator star, to perform the visibility fit of candidate stars.
MAGIC-SII has so far measured the diameter of over 25 stars. The diameters of several of them were measured for the first time by MAGIC-SII, at least in its wavelength band (412-438 nm). Since some of them are variable stars, they appear as interesting targets to study their oblateness and might be candidates for asteroseismology studies. Observations of these types of targets may contribute to improving our knowledge of stellar structure and evolution.
As commented before, fast SiPMs with short decay times combined with fast amplifiers and digitizers could play a key role in a future upgrade of MAGIC-SII. A huge upgrade for the interferometer would be to have more telescopes, as it may happen if MAGIC-SII is combined with the future telescopes of CTA. With more telescopes it would be possible to improve the sensitivity by orders of magnitudes and to increase the baseline range during observations. This would allow observing dimmer stars but also increasing the accuracy of the diameter measurement, which is essential for instance in asteroseismology.

A. The proof-of-concept micro-camera

In Section 4.1 I introduced the LASiP and presented the prototype we have developed at INFN in Pisa. This prototype was designed for an application in SPECT. In order to test the feasibility of using LASiPs in SPECT we built a proof-of-concept micro-camera that consisted of 4 LASiPs coupled to a $40 \times 40 \times 8$ mm^3 NaI(Tl) crystal. Four pixels was the minimum number of pixels needed to build a camera with which we could evaluate the energy resolution, test if we could reconstruct simple images with a reasonable spatial resolution and validate Monte Carlo (MC) simulations of the system. In this chapter, I introduce the micro-camera, discuss the results of its characterization and compare it with simulations. This chapter is based on the results that were published in [72].

A.1. Structure of the micro-camera

The figures A.1 and A.2 show an overview of the components of the micro-camera. The camera consisted of 4 SCT matrices and 4 eMUSIC MiniBoards (one for each LASiP) as shown in the left panel of Figure A.1 (see Section 4.1.2 for details). An interface board held the 4 LASiPs together. The eMUSIC board distributed the power supply to all SiPMs using a bias voltage of 33 V (chosen as a balance between PDE, DCR and single-phe resolution). The bias voltage offsets were adjusted to minimize the gain difference between the SiPMs, as described in Section 4.1.3. A NaI(Tl) crystal from OST Photonics [2] (see the central panel of Figure A.1) was coupled to the 4 LASiPs with SS-988 optical gel (refractive index 1.47, above 99% transmission at 300-600 nm) from Silicone Solutions [3]. According to the manufacturer, the crystal, which is sealed in an aluminum housing, is surrounded by a MgO diffuse reflector and has a 3 mm thick fused silica glass exit window. The crystal, the LASiPs and the electronic readout boards were mounted on a 3-D printed holder which was designed to be connected to different lead collimators (see right panel of Figure A.1):

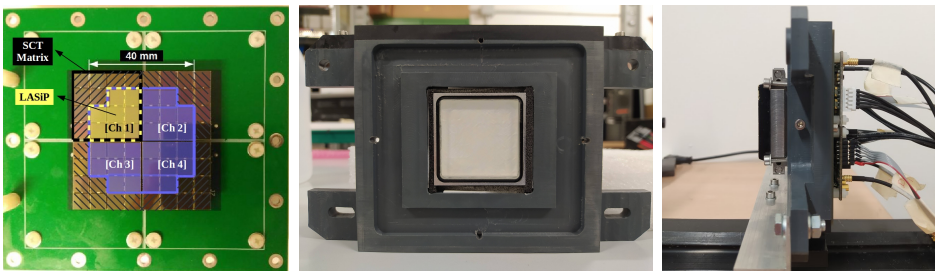

Figure A.1.: Main components of the proof-of-concept micro-camera: top-view of the 4 LASiPs mounted in the readout board (**left**), the NaI(Tl) crystal placed in a custom-designed holder (**center**), side-view of the fully-assembled micro-camera, including a lead collimator (**right**).

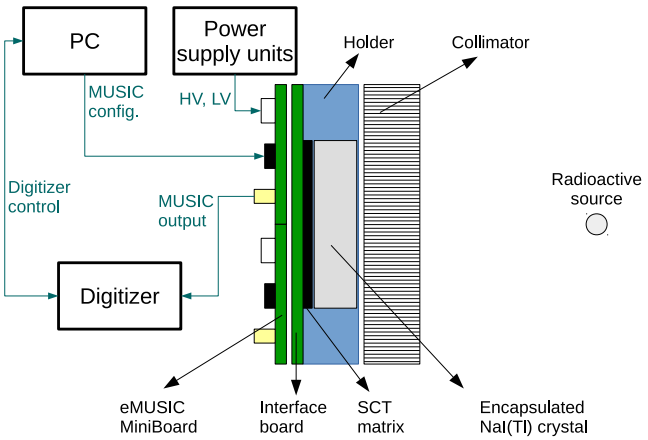

Figure A.2.: Scheme showing the different components of the micro-camera and the setup employed.

- collimator 1: hole diameter $d \sim 0.5$ mm and thickness $a \sim 2$ cm
- collimator 2: clinical LEUHR collimator with $d \sim 1.2$ mm and $a \sim 3$ cm

The holder and collimator were mounted on a positioning platform that allowed movements with sub-millimeter precision in the detector plane.

We used a CAEN DT5720 digitizer for the data acquisition (250 MS/s). Individual discriminator thresholds were set to each channel, optimized to minimize the triggering by dark count events. For each event, a 2 μs waveform was acquired on each channel.

A.2. Characterization of the micro-camera

Two radioactive sources were imaged with the micro-camera: a sealed ^{241}Am source that was assumed to be point-like and a liquid radioactive solution of ^{99m}Tc (total activity of ~ 50 μC) filling a glass capillary of 0.5 mm inner diameter and 100 mm length. The ^{241}Am source emits gamma-rays at ~ 60 keV and the ^{99m}Tc sources at 140 keV.

A.2.1. Energy resolution

The energy resolution of the micro-camera was evaluated using the ^{99m}Tc source in two different setups. The first setup was with the fully-filled capillary near the micro-camera using collimator 2 and the second setup was with the partly-filled capillary far from the micro-camera without collimator to obtain a flat field irradiation (FFI) of the detector.

For each LASiP i and each event, the charge q_i was integrated within a fixed time window (see left panel of Figure A.3). The total charge Q collected in an event is defined as the sum of the charges collected by the four LASiPs q_i.

$$Q = \sum_{i=1}^{4} q_i \tag{A.1}$$

It was possible to build a histogram with Q of all events in a measurement. The maximum of the charge distribution, the so-called *photopeak*, corresponds to the energy of the gamma rays emitted by the radioactive source.

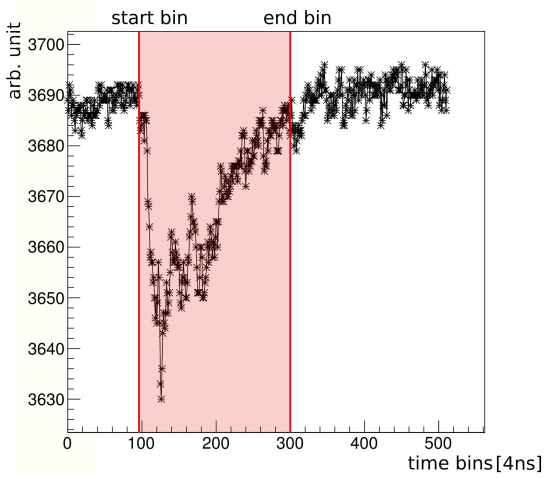

Figure A.3.: Scintillation event recorded by a LASiP of the micro-camera: the charge of each event is integrated within a fixed time window defined between the start bin and the end bin

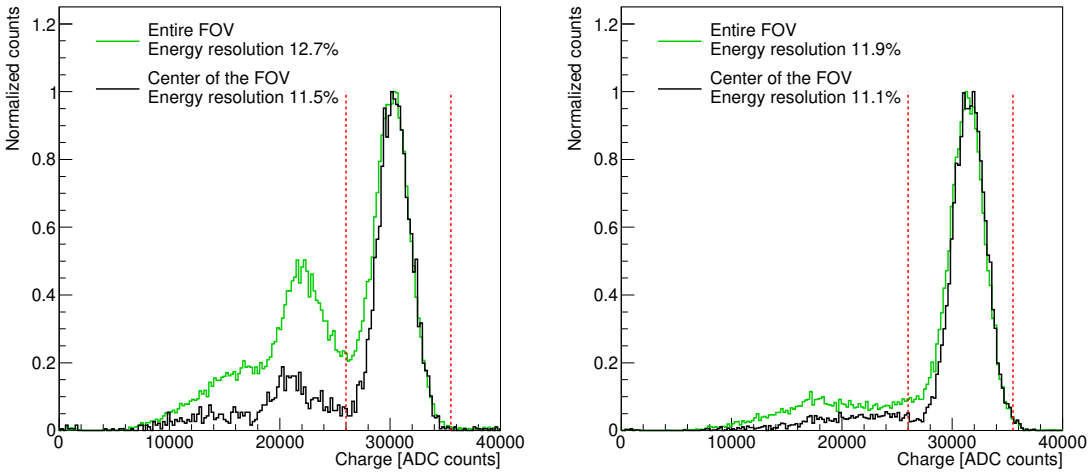

Figure A.4.: Charge histograms obtained during a FFI with ^{99m}Tc (**left**) and during the imaging of the capillary fully-filled with ^{99m}Tc at a distance of 20 cm from collimator 2 (**right**). The green histograms contain all the events in the FOV, and the black histograms only those reconstructed in a 6 × 6 mm^2 region around the camera center. The photopeak corresponds to 140 keV. The dashed vertical lines show the limit of the acceptance window for the event position reconstruction.

The left panel of Figure A.4 shows the charge histograms obtained during a FFI with ^{99m}Tc and the right panel of Figure A.4 the charge histograms obtained when imaging the capillary using collimator 2. The green histograms contain all the events reconstructed inside a 13×13 mm^2 region around the camera center (i.e., the full FOV excluding 1 mm at the edges). The black histograms include only those events that were reconstructed in a 6×6 mm^2 region around the camera center. The green histograms exhibit wider peaks, which was expected since they are more sensitive to a non-uniform charge collection across the crystal area, especially close to the crystal corners where light is not detected. In fact, as it will be shown in Section A.3, simulations suggest that the LASiP dead corners could degrade significantly the energy resolution and be the main responsible for the second peak at 22000 ADC counts that appears in the left panel of Figure A.4. The non-uniform light collection across the whole crystal area also explains why the photopeaks are broader in the left panel of Figure A.4 than in the right panel of Figure A.4. While in the first case, all parts of the FOV equally contribute to the charge histogram, in the second one most of the histogram counts come from the specific region in which the capillary was imaged, which was close to the camera center and far from the corners. For the same reason the mean of the photopeak in the right panel of Figure A.4 is slightly higher than in the left panel of Figure A.4. As it will be shown in Section A.3, the dead corner does not only impact the width of the photopeak but also the mean collected charge.

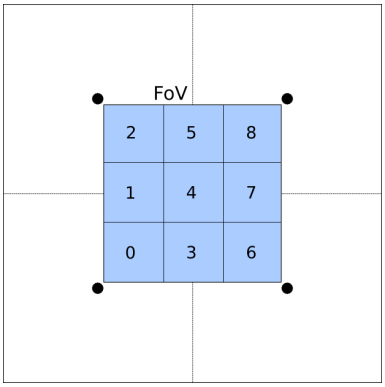

Figure A.5.: The FOV of the micro-camera is limited by the central coordinates of the 4 LASiPs (black points). It was divided into 9 subregions.

subregion	relative peak position	energy resolution [%]
0	1.02 ± 0.05	11.1 ± 0.5
1	1.01 ± 0.05	11.7 ± 0.4
2	0.98 ± 0.05	12.2 ± 0.5
3	1.00 ± 0.05	11.5 ± 0.5
4	1.00 ± 0.05	11.3 ± 0.4
5	0.97 ± 0.05	11.6 ± 0.4
6	0.99 ± 0.05	11.5 ± 0.5
7	0.99 ± 0.05	10.9 ± 0.5
8	0.98 ± 0.05	12.7 ± 0.7

Table A.1.: Relative photopeak position for each subregion (according to central subregion) with energy resolution for FFI of ^{99m}Tc at 140 keV.

The measured energy resolution depends on the position in the FOV. To study its impact, the FOV of the micro-camera was divided into nine subregions as shown in Figure A.5. In Table A.1 the position of the photopeak and the energy resolution of the micro-camera (the total charge of all four LASiPs) for an FFI of ^{99m}Tc at 140 keV is listed for each subregion. The variation of the photopeak position is around 5%. The average energy resolution is 11.6 %, with a minimum value of 10.9 % and a maximum value of 12.7 %.

The integration window for the charge integration was optimized to achieve the lowest possible energy resolution. In Figure A.6 the FWHM in keV of the photopeak is plotted as a function of the start bin and the end bin of the integration window. The corresponding waveforms were obtained using the ^{241}Am source. Since this source emits gamma rays at ~ 60 keV, the energy resolution that can be achieved is lower than when using the ^{99m}Tc source. A larger integration signal would collect more photons, but also more noise (dark counts in particular). I found that an integration window of about ~ 600 ns was the optimal one.

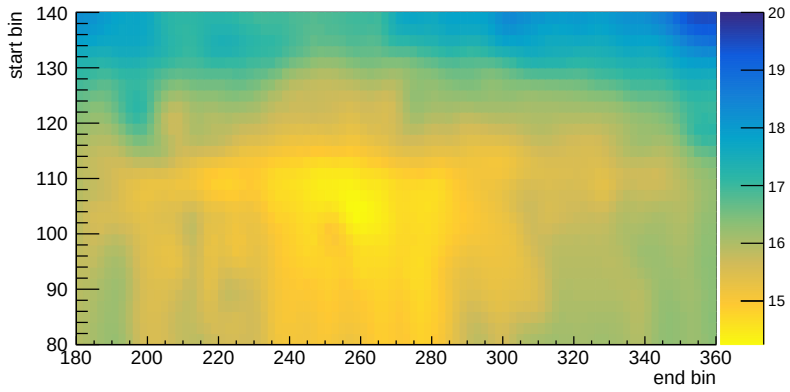

Figure A.6.: The FWHM of the photopeak is plotted in keV as a function of the start time bin and the end time bin of the integration window with a binning of 2 in the x- and y-axis. Each time bin corresponds to a time interval of 4 ns. The charge histogram of a single LASiP was calibrated according to the known position of the photopeak at ~ 60 keV of the ^{241}Am source.

A.2.2. Intrinsic spatial resolution

A.2.2.1. Event position reconstruction

The spatial resolution of the micro-camera was examined by imaging both the ^{241}Am and the ^{99m}Tc sources. Only events with energy within ±15% of the photopeak position were used for the image reconstruction. The coordinates x_c, y_c of an event were reconstructed with the Centroid Method [72]

$$x_c = \frac{\sum_{i=1}^{4} x_i q_i}{\sum_{i=1}^{4} q_i}, \qquad y_c = \frac{\sum_{i=1}^{4} y_i q_i}{\sum_{i=1}^{4} q_i}, \tag{A.2}$$

where x_i and y_i are the coordinates of the pixel center of the ith LASiP. The Centroid Method is fast and robust but has several limitations. Events cannot be reconstructed outside the region defined by the (x_i, y_i) coordinates of the four pixels. This is true even in the ideal case in which the crystal surfaces are perfectly polished and all scintillation photons are carrying information about their initial direction. In a more realistic scenario, events contain also a diffuse component. For instance, due to diffuse reflections in the crystal walls, as in our case. As a result, with the centroid method events are reconstructed within an area that is much smaller than the one delimited by the center of the four pixels.
To improve the image quality spatial and uniformity corrections were applied after the event position reconstruction. The spatial linearity was recovered using a similar method as described in [140]. A radioactive point source was positioned near the micro-camera. With the translation stage, the camera was moved along a 2D grid. At each coordinate of the grid, an image of the source was recorded. From these measurements, it was possible to extract a map of the mean reconstructed position with the

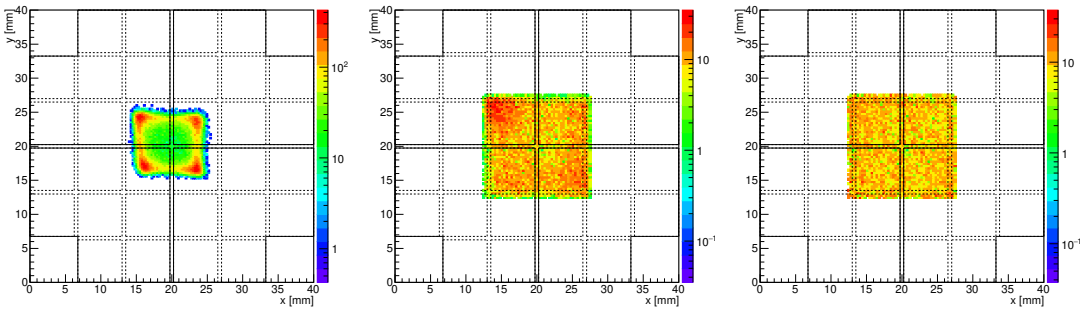

Figure A.7.: Reconstructed image of FFI obtained in the laboratory with the micro-camera before (raw-reconstructed with Centroid method) (**left**), after spatial linearity correction (**center**) and after additional uniformity corrections (**right**). The black solid lines show the borders of LASiPs and the dashed lines show the borders of the SiPMs that are part of those LASiPs.

Centroid method compared with the known true position of the source coordinates. An interpolation of this map was used to correct the reconstructed images to recover the spatial linearity.
The uniformity correction was executed using the data set of a long-exposure FFI image. The FFI image was obtained by placing a radioactive point source far from the micro-camera (> 50 cm). The image was reconstructed with the Centroid method and corrected with the spatial linearity correction. The resulting image was inverted and used as a uniformity correction map. All images were multiplied by this map.

In the left panel of Figure A.7 the FFI image is shown after the event position reconstruction, in the central image after spatial linearity correction and in the right panel after uniformity correction. The raw images reconstructed with the centroid method appear 'collapsed' in the center of the FOV (left panel of Figure A.7). The response of the real micro-camera is not uniform all across the FOV, probably caused by a combination of several factors including a non-homogeneous crystal response due to the presence of impurities, a non-uniform crystal-LASiP coupling or a non-perfect SiPM gain equalization. The bulk of this effect is corrected after spatial linearity and uniformity corrections, as can be seen in the central and right panels of Figure A.7. After corrections, the FOV is also enlarged.

A.2.2.2. Intrinsic spatial resolution

To evaluate the intrinsic spatial resolution, the ^{241}Am source was imaged at a distance h of ~ 15 mm from the micro-camera using collimator 1. The reconstructed image was fitted with a 2D-Gaussian. The FWHM of the fit gave the extension R of the source. The fully filled ^{99m}Tc capillary was imaged at h ~ 20 mm from the micro-camera using collimator 2. R was here defined as the FWHM of the projection of the reconstructed image in the axis perpendicular to the capillary orientation.

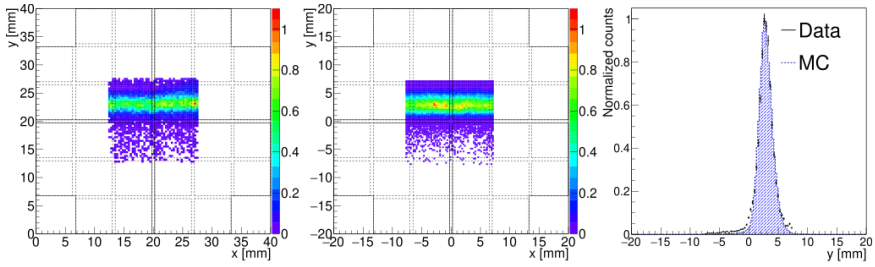

Figure A.8.: Image of ^{99m}Tc capillary of 0.5 mm diameter taken with the micro-camera, at a distance of 20 mm using a LEUHR collimator (3 cm thickness, 1.2 mm hole diameter) (**left**). MC image obtained when the same experimental conditions were simulated (**center**). The black solid lines show the borders of LASiPs and the dashed lines show the borders of the SiPMs that are part of those LASiPs. The left and center images were projected in the y-axis (**right**).

The measured R is a function of the source diameter R_s (negligible for the point-like source), the collimator resolution R_c and the intrinsic resolution of the detector R_d [72]:

$$R = \sqrt{R_d^2 + R_c^2 + R_s^2} \tag{A.3}$$

with R_c defined as

$$R_c(h) = d\frac{a_{\text{eff}} + h}{a_{\text{eff}}}, \tag{A.4}$$

where $a_{\text{eff}} = a - 2/\mu$, with a the collimator thickness and μ the linear attenuation coefficient (μ^{-1}=0.37 mm at 140 keV in lead).
Figure A.8 compares the reconstruction of an image of the ^{99m}Tc capillary from laboratory measurements and simulations. To obtain the MC images we simulated the same conditions of the experiments (see Section 4.2.3.2 for details about the simulation): same orientation of the capillary, geometrical characteristics of the collimator and the capillary, and source-to-detector distance. As a reference, the projection in one of the main axis of the detector plane is also shown. We consider that the agreement between data and simulations is good enough to use the simulations as a test probe to study with more detail the impact of the LASiP characteristics in the system performance (see Section 4.2.3.2).
The capillary was imaged at different positions in horizontal and vertical orientations. The mean width of the capillary measured in the experiments was $R_{cap} = (2.8 \pm 0.2)$ mm. Removing the source diameter and the collimator resolution we obtained $R_d = (1.9 \pm 0.4)$ mm. From the measurements of the ^{241}Am point-like source an intrinsic spatial resolution of R_d=(2.2±0.2) mm has been found (see [72] for details).

A.2.3. Uncorrelated noise

The uncorrelated noise in the micro-camera was studied by recording events in a dark measurement, i.e. in absence of visible light and radioactive radiation, with all eight channels enabled and acquiring random triggers. The resulting charge histogram was fitted with a Gaussian function of variance σ^2_{UN}. Figure A.9 shows the charge distribution of the dark measurement with random trigger and all 8 SiPM enabled in the LASiPs. The Gaussian fit resulted in σ_{UN}=186 ADC counts which corresponded to ~ 0.6% of the mean position of the photopeak.

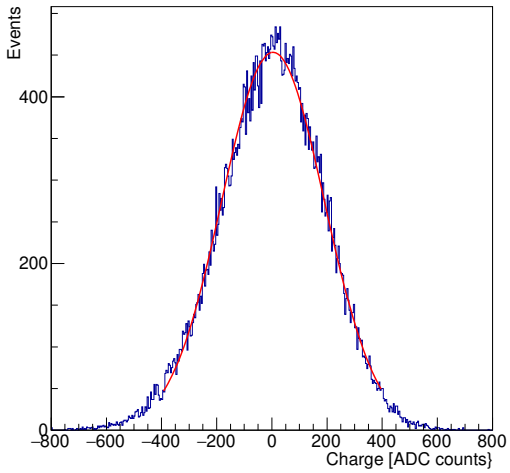

Figure A.9.: Charge distribution from dark measurement with random trigger and all 8 SiPMs enabled. The red line marks the Gaussian fit.

A.3. Simulations of the micro-camera

In order to better understand the performance of the micro-camera, a simulation of the system was performed in Geant4. The aim was not to perfectly match the micro-camera response but to create a model with which it was possible to study the effect of the LASiP noise and the dead pixel corner of the prototype on the performance. The details of the simulation are described in the corresponding paper [72].
The simulation featured a camera made of a 40 × 40 × 8 mm^3 NaI(Tl) crystal which was coupled to 36 SiPMs of 6 × 6 mm^2. Lead collimators with the same characteristics as collimators 1 and 2 could be set in front of the camera. A capillary source with a diameter of 0.5 mm and 40 mm length at 140 keV was simulated as well. Scintillation inside the crystal created optical photons that were tracked until they were either absorbed, escaped or detected by one of the SiPMs. The SiPMs in the simulation were arranged in the same way as in the micro-camera. The number of detected scintillation events was recorded individually for each SiPM. The SiPMs could be grouped in *pixels* of 8 SiPMs or 9 SiPMs (without dead corners) by summing the events of the individual SiPMs. Given N scintillation photons hitting a SiPM, the noise was injected in three steps:

1. Crosstalk: ΔN artificial counts were added which are randomly generated following a Poisson distribution with mean $\mu(N, p_{XT})$ and p_{XT} the crosstalk probability. After that $N' = N + \Delta N$ events were present.

2. Detector resolution: this accounts for the single-phe resolution of the LASiP and for the resolution of the digitizer used for the acquisition. N' was blurred with a Gaussian distribution G with expected value N' and variance $\sigma_t(\sigma_0, \sigma_1, N')$, let N'' be the result of applying this correction to N'.

3. Uncorrelated noise: the impact of dark counts was included by generating a random number $\Delta N''$ from a Gaussian distribution of variance σ^2_{UN}. The final noise-corrected charge recorded by the sensor was $N''' = N'' + \Delta N''$.

The noise input parameters in the simulation are $p_{XT}, \sigma_0, \sigma_1$ and σ_{UN}. The reference values for these parameters (see Table A.2) were obtained from the measurements of the LASiP noise presented in Section 4.1.3 and in Section A.2.3.

Table A.3 summarizes the impact of the different input noise parameters on the detector energy resolution measured in the center of the FOV (6×6 mm^2 region around the

p_{XT} [%]	σ_0 [phe]	σ_1 [phe]	σ_{UN} [Q]
25	0.53	0.07	$6 \cdot 10^{-3}$

Table A.2.: Input noise parameters of the simulation obtained from measurements of LASiP noise. σ_{UN} is noted in units of the total charge Q.

Nr	p_{XT} [%]	σ_0 [×]	σ_1 [×]	σ_{UN} [×]	ϵ (8-SiPM LASiP) [%]	ϵ (9-SiPM LASiP) [%]
1	-	-	-	-	9.7	9.1
2	5	-	-	-	9.8	9.1
3	10	-	-	-	10.0	9.3
4	25	-	-	-	10.1	9.4
5	40	-	-	-	10.4	9.7
6	-	1	1	-	9.8	9.1
7	-	10	5	-	10.2	9.5
8	-	1	1	-	10.2	9.5
9	-	-	-	1	10.1	9.4
10	-	-	-	2	11.6	10.8
11	-	-	-	5	19.5	18.6
12	25	1	1	1	10.7	9.9

Table A.3.: Simulation of the micro-camera system performed with Geant4 to study the impact of LASiP noise in the micro-camera energy resolution. $p_{XT}, \sigma_0, \sigma_1$ and σ_{UN} were introduced in Section 4.1.3 and Section A.2.3 and their reference values (n.r.v) were listed in Table A.2. The energy resolution ϵ was calculated assuming LASiPs built by summing 8 SiPMs (as the LASiP prototype) or 9 SiPM (without dead corners).

camera center) for a FFI. The input noise parameters are given in units of the noise reference values (n.r.v) of Table A.2 except for p_{XT}. The obtained energy resolution is shown both for the case in which all 36 SiPMs are enabled (each pixel summing 9 SiPMs) and for the case in which each LASiP sums 8 SiPMs, as in the laboratory measurements. The first row in the table shows the energy resolution when no noise is simulated. Row nr. 12 represents the closest situation to our laboratory measurements (when the input noise parameters are exactly those of Table A.2). Even if the energy resolution that was obtained with the 8-SiPM LASiPs is slightly better compared to what was found in Section A.2.1 (expected due to the simplification of the simulations), we considered it to be close enough to the values measured with the micro-camera, at least for the scope of studying how energy resolution changes when we modify the input noise parameters.

The LASiP dead corners affect significantly the detector performance, as can be seen in all entries of Table A.3. This suggests that we expect to achieve a significantly better energy resolution in a camera in which LASiPs are built without dead corners, fully covering the crystal surface. The effect of the dead corner can also be seen in Figure A.4, which shows the obtained charge spectra for the case of row nr. 12. The green histograms contain all the events reconstructed inside a 13×13 mm^2 region around the camera center. The black histograms include only those events that were reconstructed in the center of the FOV. In the left panel, Figure A.4 a second peak left to the main peak can be seen that does not appear in the right panel Figure A.4. It is

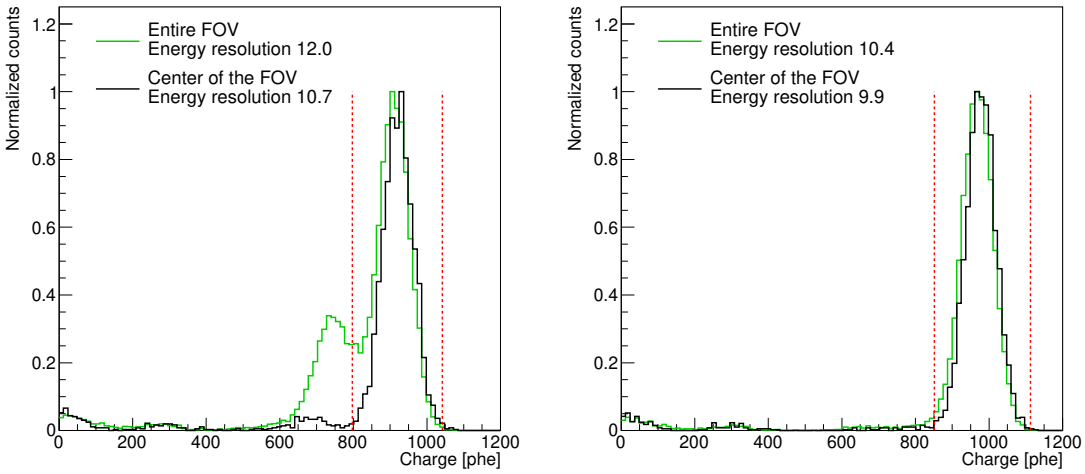

Figure A.10.: Charge histograms obtained with Monte Carlo simulations (row nr. 12 in Table A.3) during a FFI with ^{99m}Tc when: the SiPMs in the corners are switched-off (each LASiP is the sum of 8 SiPMs, as in the micro-camera) (**left**); all 36 SiPMs are enabled (each LASiP is the sum of 9 SiPMs) (**right**).

more pronounced in the green histogram that includes events that were reconstructed closer to the camera corners. The dead corner impacts both the mean position and width of the photopeak.

Optical crosstalk seems to have a minor impact on the energy resolution of the system (rows nr. 2–5 in Table A.3), although not very critical: the results suggest that reducing p_{XT} to ~ 10% (typically achievable at the expense of a lower PDE) would not provide a significant improvement. The parameters σ_0 and σ_1 that describe the finite single-phe resolution of the SiPMs must be increased by a factor 5 or 10 with respect to their reference measured values to give a non-negligible contribution (rows nr. 6–8). The energy resolution seems to be much more sensitive to an increase in uncorrelated noise, likely dominated by dark counts (rows nr. 9–11). The noise level measured in the micro-camera LASiPs (relative to their mean signals) seems to be adequate if we compare entries 9 and 1. However, an increase in σ_{UN} by a factor 2 (which is not so unlikely, for instance, if using noisier SiPMs) already degrades significantly the energy resolution (row nr. 10). This must be taken into account when designing a large camera with several and larger LASiPs.

Regarding spatial resolution, it was 10% worse in the images of the capillary simulated with the n.r.v. than in the case in which no noise was added. This difference would not be very significant in the context of full-body SPECT, where the collimator contribution typically dominates spatial resolution. However, I note that the impact of noise on the detector spatial resolution should be studied in cameras holding more pixels, where the relative weight of noise will be high in pixels showing low (or no) signal (see Chapter B).

A.4. Comparison with standard SPECT cameras

We were able to reconstruct simple images with a simple system like the proof-of-concept micro-camera, which supports the idea that LASiPs can be used in SPECT.

The measured energy resolution of the micro-camera was ~ 11.6% at 140 keV. This value is similar to typical values from standard full-body SPECT cameras based on PMTs (~ 10 % at 140 keV [4, 72]). The simulations suggest that the performance could be significantly improved if we could completely cover the area of the scintillator using pixels without dead corners. The energy resolution is affected by all the detector components: scintillation crystal, reflective surface surrounding the crystal, photodetectors, and coupling between crystal and photodetectors. From the LASiP side, the energy resolution could be improved by using SiPMs with higher PDE, reducing the pixel noise and increasing the photodetector active area. A better performance should be achieved using modern SiPMs with peak sensitivity at the 420 nm where NaI(Tl) scintillation light peaks. Some of them provide a PDE higher than 50%, with crosstalk probability of ~ 10% and a DCR of ~70 kHz (half the DCR of the SiPMs used in the micro-camera) [74]. The photodetector active area could be increased if reducing the dead space between the SiPMs that build the LASiP.
Our simulations showed that DCR is the dominant noise component affecting energy resolution. In [124] it was shown that a relatively high dark count rate (400 kHz/mm^2 at 20°) could significantly degrade the energy resolution of a camera using SiPMs with a ~ 30% PDE in the wavelength of interest. In fact, the detector module that was under study (later developed in [92]) was cooled down to ~ 0°C to reduce the DCR. For the same reason, a cooling system was also employed in the camera of [32], which was equipped with digital photon counters. With the micro-camera, we were able to reconstruct images and achieve a reasonable energy resolution operating the LASiPs at room temperature. However, it should be noted that in the micro-camera all four pixels always exhibit a relatively large signal and hence achieve a high SNR ratio. In a larger camera, the situation could be different (see Chapter B).
Even if we had only four pixels we were able to reconstruct the images produced by a ^{99}Tc capillary and by a ^{241}Am point-like source. This supports the idea that LASiP pixels could be an alternative to PMTs in SPECT. The measured intrinsic spatial resolution close to the micro-camera center was ~ 2 mm. Standard full-body SPECT cameras based on PMTs achieve a typical intrinsic spatial resolution of 5 mm [4]. The experiment with the capillary source was also simulated with Geant4. We were able to obtain a reasonable agreement between experiments and simulations in terms of spatial resolution and image reconstruction.

With the current LASiP prototype (area ~ 2.9 cm^2) ~ 500 readout channels would be needed to cover a Full-Body SPECT camera (~ 40 × 50 cm^2). This is still high compared to a standard SPECT camera with 50-100 PMTs. Larger LASiPs would be needed if we wanted to keep reducing the number of channels. The challenge of using LASiPs in large cameras is discussed in Appendix B.

B. A large LASiP camera for SPECT

A full-body SPECT camera consists of a lead collimator followed by a large scintillating crystal (~ 50 × 40 × 1 cm^3) [20] and an array of 50-100 PMTs (4-8 cm diameter) (see Section 4.1.4). If one wanted to equip a full-body SPECT camera with LASiPs of the size of the LASiP prototype in Section 4.1, more than 500 readout channels would be needed. The LASiP concept of summing SiPMs allows us to build larger pixels, but with more SiPMs collecting the charge, also more noise (especially dark counts) will be included. This can potentially degrade the camera performance. Therefore the trigger settings for the charge collection of the camera need to be optimized to maximize the SNR. I performed a deep study of the impact of the pixel size, geometry and noise on performance of a large camera.

B.1. Simulation of a large camera

In Section A.3 a Geant4 simulation of a proof-of-concept micro-camera with four LASiP prototypes was introduced. In order to study the feasibility of using larger LASiPs in a full-body SPECT camera, this simulation was extended to a large camera of 500 × 400 mm × 9 mm^3 equipped with 6 × 6 mm^2 SiPMs. A 0.25 mm gap was left between neighboring SiPMs. In this case, there was no collimator. Instead, the simulated gamma rays hit the camera at normal incidence. The simulation was performed only in a region of ~ 225 × 225 mm around the center of the camera to reduce computing time. In this part, a grid of 1296 SiPMs was simulated. In Figure B.1 the collected charge, relative to the total charge, as a function of the number of SiPMs used to collect the charge is shown . The total charge of a scintillation event is distributed over ~ 500 SiPM. This demonstrates that the part of the camera that was simulated is large enough to obtain some key parameters of the performance like the energy resolution.

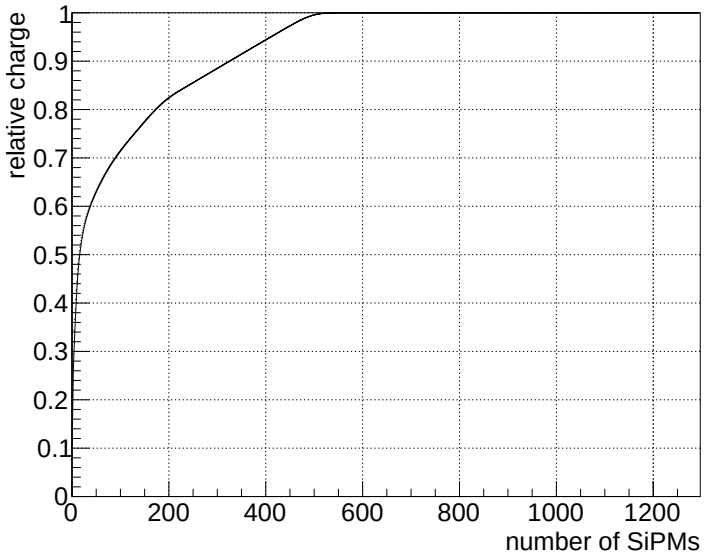

Figure B.1.: Collected charge (relative to the total number of collected photons) as a function of the number of SiPMs used to collect the charge.

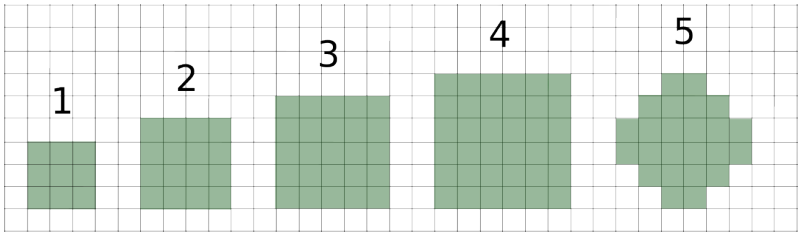

Figure B.2.: Scheme showing the different LASiP configurations.

model	Nr of SiPMs per LASiP	pixel area [mm^2]	shape
1	9	324	square
2	16	576	square
3	25	900	square
4	36	1296	square
5	24	864	flower

Table B.1.: The simulated SiPM grid could be grouped into a grid of LASiPs of different sizes and shapes.

The simulated grid of SiPMs allowed forming LASiPs of different sizes and geometry. This was done by grouping the SiPMs and summing their signals. Five different LASiPs were studied: square-shaped LASiPs of 9, 16, 25 and 36 SiPMs and a 'flower-shaped' LASiP of 24 SiPMs. Their shape is shown in Figure B.2 and their properties in Table B.1. LASiP 1 is similar to the LASiP prototype presented in Section 4.1
LASiP noise was added to the simulation following the same procedure as in the proof-of-concept micro-camera simulation in Section A.3. In [72] it was shown that the mean impact of LASiP noise on the performance of a gamma camera is due to dark counts, whereas correlated noise such as Crosstalk has a minor impact. To study the effect of LASiP noise on the performance of a large camera with large pixels, three dark count rate (DCR) levels were simulated:

- 'cooled-SiPM' noise: DCR = 0.015 MHz/ mm^2
- 'room-SiPM' noise: DCR = 0.050 MHz/ mm^2
- 'hot-SiPM' noise: DCR = 0.150 MHz/ mm^2

The simulated optical crosstalk probability was 25 %.

B.2. Image Reconstruction in Gamma cameras

The light of a scintillation event is collected by the photodetectors in a gamma camera. A positioning algorithm is used to estimate the coordinates x and y of the scintillation event. In Section A.2 the Centroid Method for image reconstruction was introduced. The Centroid method has been used in the first gamma camera by Anger in 1957 [20]. This method estimates the position of the scintillation event as the weighted average of the pixel coordinates (centroid) [152]. The Centroid Method is simple and robust but it has several drawbacks. As explained in Section A.2.2.1, the FOV is limited by the coordinates of the outermost pixels. Moreover, a diffuse light component in the setup can distort the image: each pixel measures some amount of this diffuse light. As a result, even for an event close to the camera edge, the central pixels will detect light. Therefore the reconstructed position is biased in the direction of the camera center. The reconstructed image is shrunk compared to the actual camera area.

As an alternative approach, the position of the scintillation event can be reconstructed with statistical reconstruction techniques (examples in [23], [41], [67], [117]). The statistical approach has several advantages compared to the Centroid Method as potentially smaller distortions and a large useful FOV as well as a better filtering of noise events (see [23] and [67]). In this work, the images were reconstructed with a statistical reconstruction method based on a Maximum Likelihood Estimation as in [117, 124, 152].
The challenge of statistical reconstruction is that detailed knowledge of the spatial response of the detector is required [117] which is a not trivial task to perform. The key is to obtain the signal amplitude of each pixel as a function of the scintillation event position, hereafter called Light Response Function (LRF).

B.2.1. Light Response Function

The LRF can be estimated either via direct access (using measurements as in [32] or simulations as in [122]) or with an iterative approach (as in [118] and [152]). In my implementation of a statistical reconstruction technique, I accessed the LRF directly using a simulated calibration grid. I tested also an iterative estimation approach for the LRF estimation.

B.2.1.1. Direct assessment

The LRF can be estimated by experimentally scanning the scintillation crystal as in [23, 114]. The scintillator surface is scanned with a collimated radiation beam which is moved by a robotic mechanism. The beam hits the scintillation crystal in different (x, y) coordinates. In doing so, the average light response of the crystal is obtained for every beam position. I used instead a simulated 2D grid of N point sources which was achieved by firing the simulated beam at normal incidence towards the camera at several (x_{cal}, y_{cal}) positions. For scintillation events that are related to the calibration

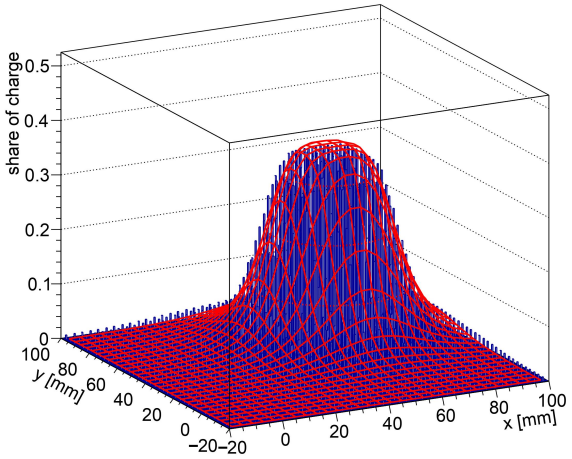

Figure B.3.: Histogram h_i filled with normalized charge distribution q_{ij}/Q_j. The histogram was interpolated and fitted with Equation B.2. The resulting fit function was an estimate of the Light response function (LRF) $\hat{f}_i$ of the pixel i.

point source j with the coordinates $x_{cal,j}$ and $y_{cal,j}$ I obtained the charge q_{ij} collected by the pixel i. For a camera with M pixels, the total charge of all pixels collected for scintillation events of the point source j was Q_j.

$$Q_j = \sum_{i}^{M} q_{ij} \tag{B.1}$$

The normalized charge distribution q_{ij}/Q_j was calculated and filled in a histogram h_i according to the coordinates $x_{cal,j}$ and $y_{cal,j}$. The histogram h_i was interpolated and then fitted with a generalized bell-shaped membership function [159].

$$f(x, y, a, b, c, d, e) = \frac{a}{1 + \sqrt{\left(\frac{x-d}{b}\right)^2 + \left(\frac{x-e}{b}\right)^2}^{2c}} \tag{B.2}$$

I tried different bell-shaped functions to fit h_i, including a 2D Gaussian. In my case, Equation B.2 proved to be the best function to describe the shape of the distribution of h_i. The resulting fit function was an estimate of the LRF $\hat{f}_i(x, y)$ of the pixel i. An example of h_i and the corresponding estimated LRF $\hat{f}_i(x, y)$ can be seen in Figure B.3. In a simulation, it is easy to create a 2D-calibration grid of point sources for direct access to the LRF function. To obtain, however, such a calibration grid with direct measurements a very precise setup would be needed (including robotics control) and it would be very time-consuming which is hardly feasible in clinical SPECT scanners. The advantage of the direct access is its reliability since the LRF is estimated on basis of experimental data including complex and non-linear effects of the light collection or a possible non-uniformity in the photodetector array [124].

Another way to directly access the LRF of the camera pixels would be with numerical simulations of the light response (and simulations of a calibration grid as I did). However, the accuracy of such a simulation depends on knowledge of many optical parameters [117].

B.2.1.2. Iterative approach

The LRF can also be estimated with an iterative technique requiring only the measurement of a FFI which is easy to obtain in the laboratory. This method was proposed in [116], [117] and [152]. As a first step, the N events of a FFI image that was acquired with a camera of M pixels are reconstructed with the Centroid method in order to estimate the interaction coordinates $(x_{est,j},y_{est,j})$ of an event j. The normalized charge distribution q_{ij}/Q_j is filled in a histogram h_i according to the estimated event position $x_{est,j}$ and $y_{est,j}$. The histogram h_i is fitted with an appropriate function to have a first estimate of the LRF $\hat{f}_{i,0}$ of pixel i. In the next step, the image is reconstructed using $\hat{f}_{i,0}$. The result is a new reconstructed FFI image, which is the basis of a second estimation of the LRF $\hat{f}_{i,1}$. The previous step is iteratively repeated with a new LRF estimate $\hat{f}_{i,k}$ in every iteration k. The process continues until the parameters of the LRF estimates reached stable values. The iterative technique is explained in detail in [118] and [124].
I also tested one of these iterative techniques. Figure B.4 shows the result of this test. The reconstructed FFI image after iteration 0 corresponds to the first estimate with the Centroid Method. The image is heavily biased to the center of the camera with a reduced FOV (as has been observed for laboratory measurements with the micro-camera in Section A.2). Iteration 1 uses for the first time the estimated LRF to reconstruct the image. With every iteration, the FOV of the reconstructed image increases and shows smaller distortions. After 17 iterations the calculation of the LRF converged. The resulting image covers now nearly the complete area of the simulated camera and is for most parts of the FOV flat as expected for a FFI.

Since I worked only with simulations, I could easily obtain the LRF via a simulated calibration grid. This was the easiest way to find the best possible estimate of the LRF. As Figure B.4 proves, the iterative approach of my implementation worked as well which could be beneficial for the reconstruction of laboratory measurements in the future.

B.2.2. Maximum Likelihood Estimation

The statistical reconstruction method presented here is based on the assumption that the probability P_i for a pixel i to collect n_i photons in a scintillator camera can be described by a Poisson distribution [23]:

$$P_i(n_i) = \frac{\mu_i^{n_i} e^{-\mu_i}}{n_i!}. \tag{B.3}$$

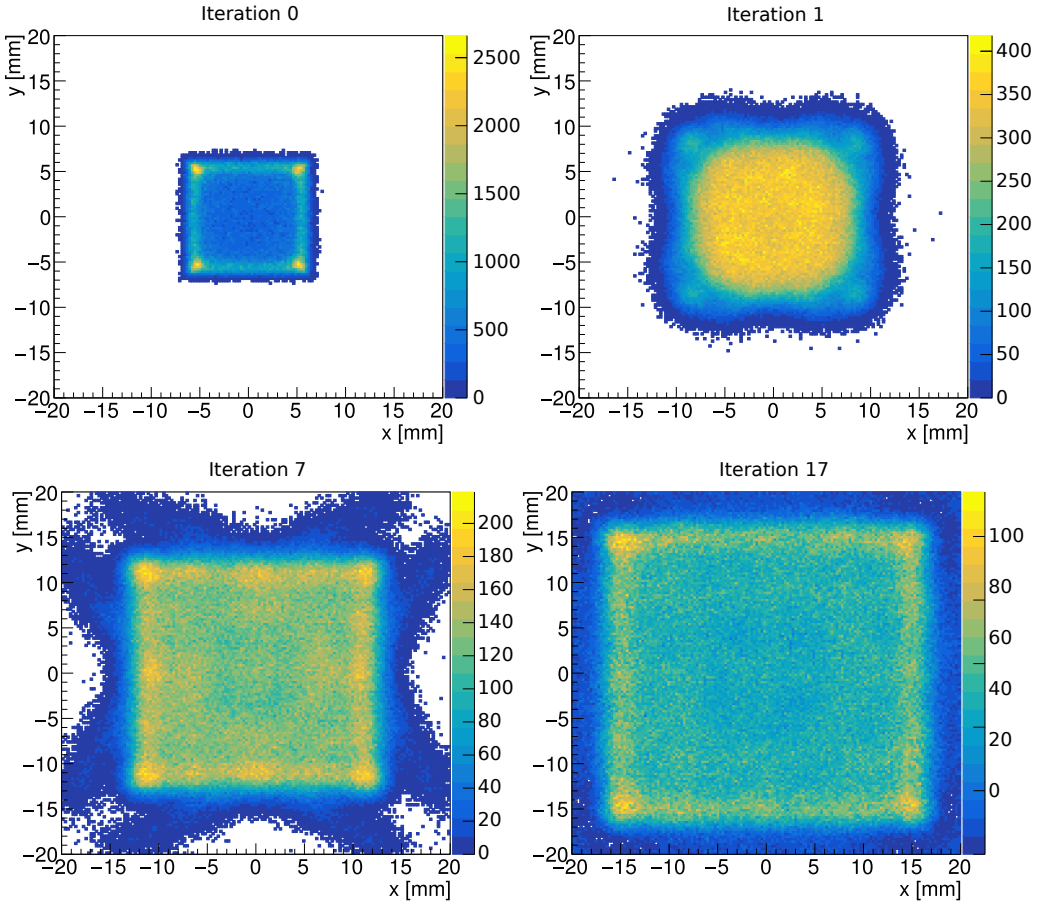

Figure B.4.: Iterative approach to estimate the LRF of the camera pixels: in the first iteration a FFI image is reconstructed with the Centroid. From this reconstruction, a first estimate of the LRF is extracted (iteration 0). The first estimate is used to reconstruct the image again, this time using the LRF with a statistical image reconstruction method (iteration 1). This is repeated until the LRF reaches a stable value. With every iteration the reconstruction result improves, i.e. in the case of a FFI the reconstructed image becomes flatter and covers a larger FOV (see iterations 7 and 17).

The expected value μ_i is defined as $N \cdot f_i(x, y)$ with N the number of incoming photons on the pixel. $f_i(x, y)$ is the LRF of the pixel i, i.e. the fraction of photons that were emitted in a scintillation event in a position (x, y) and detected with pixel i.
The statistical reconstruction is based on a Maximum Likelihood Estimation (MLE). The reconstruction problem of finding the position of a scintillation event (x, y) is rephrased to find a set of parameters $(\hat{x}, \hat{y}, \hat{N})$ that maximize the likelihood to get the experimentally measured result. $\hat{x}$ and $\hat{y}$ are the estimates of the scintillation event coordinates and $\hat{N}$ is the estimate of the signal of the event.
The likelihood function is built from the joint density function $P(n_i|\mu_i)$. It represents

the probability to register a signal of n_i photons (that corresponds to a charge q_i) of a pixel i with an average number of detected photons μ_i:

$$L = \prod_i^M P(n_i|\mu_i) \tag{B.4}$$

The total number of pixels is M. The average number of detected photons μ_i is expressed as the product of the estimated signal and the LRF for an estimated scintillation event position $\mu_i = \hat{N} f_i(\hat{x}, \hat{y})$. Equation B.4 is valid if n_i are independent for each pixel i and identically distributed over the camera. The likelihood function in Equation B.4 can be simplified to the Log-Likelihood function $\ln(L)$ of the system:

$$\ln(L) = \sum_i^M P(n_i|\mu_i) = \sum_i^M (n_i \ln(\mu_i) - \mu_i) - \sum_i^M (n_i!) \tag{B.5}$$

The second sum in Equation B.5 is a constant and can be neglected in the maximization. Using $\mu_i = f_i(\hat{x}, \hat{y}) \cdot \hat{N}$, Equation B.5 can be rewritten as:

$$\ln(L(\hat{x}, \hat{y}, \hat{N})) = \sum_i^N \left(n_i \cdot \ln\left(f_i(\hat{x}, \hat{y}) \cdot \hat{N} \right) - f_i(\hat{x}, \hat{y}) \cdot \hat{N} \right) + Const \tag{B.6}$$

$\hat{N}$ is a function of the scintillation event position:

$$\hat{N}(\hat{x}, \hat{y}) = \frac{\sum_i^M n_i}{\sum_i^M f_i(\hat{x}, \hat{y})} \tag{B.7}$$

$\hat{N}$ in Equation B.6 can be expressed with $\hat{N}(\hat{x}, \hat{y})$ of Equation B.7. Now the Likelihood function depends only on the estimated event position $\hat{x}$ and $\hat{y}$.

$$\ln(L(\hat{x}, \hat{y})) = \sum_i^N \left(n_i \cdot \ln\left(f_i(\hat{x}, \hat{y}) \cdot \frac{\sum_i^N n_i}{\sum_i^N f_i(\hat{x}, \hat{y})} \right) - f_i(\hat{x}, \hat{y}) \cdot \frac{\sum_i^N n_i}{\sum_i^N f_i(\hat{x}, \hat{y})} \right) + Const \tag{B.8}$$

The reconstruction of the event position is achieved by maximizing the Equation B.8 to find the best estimate of the coordinates x and y of an event as in [117, 124, 152].

B.2.2.1. Implementation of the reconstruction method

In order to implement the reconstruction, Equation B.8 was rewritten as:

$$-\ln(L(\hat{x}, \hat{y})) = -\sum_i^N \left(q_i \cdot \ln\left(f_i(\hat{x}, \hat{y}) \cdot \frac{\sum_i^N q_i}{\sum_i^N f_i(\hat{x}, \hat{y})} \right) - f_i(\hat{x}, \hat{y}) \cdot \frac{\sum_i^N q_i}{\sum_i^N f_i(\hat{x}, \hat{y})} \right) \tag{B.9}$$

The signal n (number of phes) of an event is here expressed with the charge q. In addition, the Equation was multiplied with a negative sign so that the problem could

be solved by finding the minimum. The minimization of Equation B.9 was realized in the C++-based language `root` using the `Minuit2Minimizer` class. The total data of a simulated image was divided into files of 20000 events each. Thereby it was possible to reconstruct the files in parallel which saved a lot of time. The reconstructed events were combined afterwards to obtain the complete image of the source. The reconstruction was run on the main computing facility of INFN, Tier-1 at CNAF [30]. The input for the reconstruction of an event position was q_i for every pixel i and the central coordinates x_i and y_i of the pixels as well as the estimates of the LRF. The total charge Q of an event was calculated. In the left panel of Figure B.5 the charge distribution generated by a simulated point source after 20000 events is shown.
If Q is outside of a preset energy window (in Figure B.5 1700 phe < q_i < 2100 phe), the event is rejected. As the first estimation of x and y, I used the central coordinates of the pixel which detected the maximum charge, x_{max} and y_{max}. During the Likelihood minimisation only estimates of x and y within a certain diameter r_{rec} around (x_{max}, y_{max}) were accepted. This assured that no local minima far away from the approximate location of the signal distort the reconstruction. In addition, the number of pixels used to reconstruct the event is limited to the pixel with the maximum charge and its nearest neighbors, in total M_{rec} pixels. This is done to maximize the summed signal but minimize the included noise as well. In the right panel of Figure B.5 the collected charge, relative to the total charge, as a function of the number of SiPMs used to collect the charge is shown. This Figure shows the case of room-SiPM noise. The SiPMs were sorted according to the amount of signal they detected. The Figure shows that there is a point in which if we kept adding SiPMs we would add more noise than signal, which degrades the energy resolution.
The optimal value for r_{rec} and M_{rec} depends on the position of the source with respect to the camera and the noise settings. The impact of r_{rec} is minor. A minimization radius of 40 mm around the starting coordinates proved to give reliable results. I

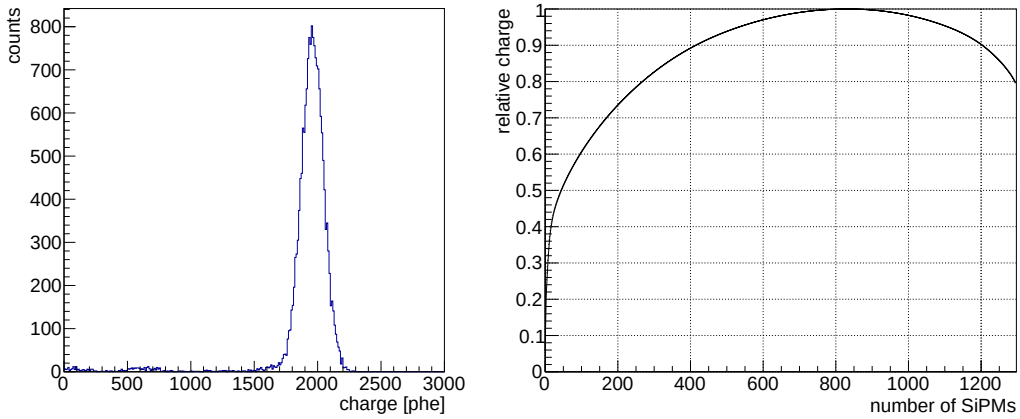

Figure B.5.: Charge distribution of 20000 events for a simulated point source (**left**). The collected charge, relative to the total charge, as a function of the number of SiPMs used to collect the charge at room-SiPM noise (**right**).

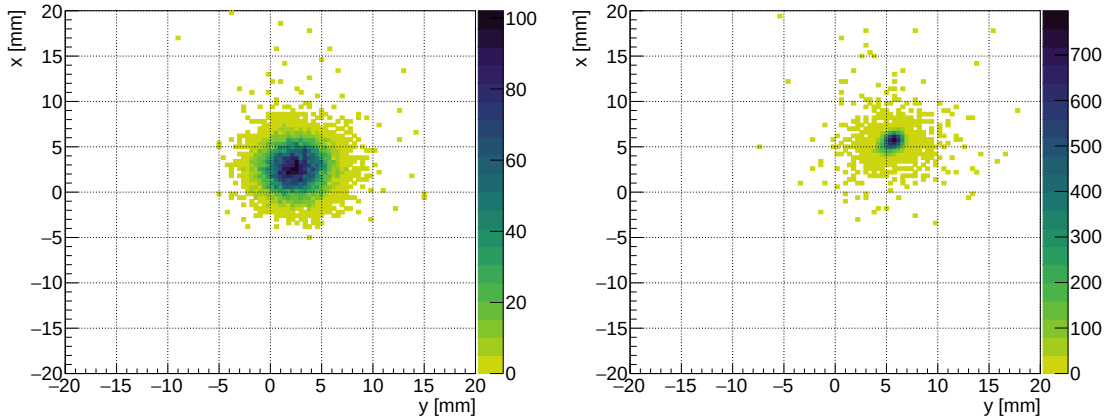

Figure B.6.: Image of a simulated point source at room-SiPM noise with LASiP 3 situated at x=6.25 mm and y=6.25 mm reconstructed with the Centroid method (**left**) and the statistical method presented in this thesis (**right**). The statistical method did clearly better reconstruct the position of the source and provided a higher spatial resolution.

tried different M_{rec} to reconstruct images of sources in several positions. A larger M_{rec} of 21 lead to a higher spatial resolution (~ 10-15 % better) compared to M_{rec}=9. For the following results I used M_{rec}=21, which was a trade-off between maximizing the intrinsic spatial resolution, the summed signal and the reconstruction speed and minimizing the included noise.
After the estimated distance to the minimum of Equation B.9 is $< 10^{-6}$, the achieved $\hat{x}$ and $\hat{y}$ of an event together with q_i is saved. In Figure B.6 the reconstruction of a simulated image at room-SiPM noise of a point source at (6.25, 6.25) mm with LASiP 3 is compared for the Centroid method (left panel) and the statistical method (right panel). The reconstruction with the statistical method provides a much better spatial resolution and is less affected by non-linearities.

B.2.3. Spatial linearity and uniformity corrections

Two corrections were applied to the raw reconstruction that was obtained by minimizing the reconstruction algorithm in Equation B.9: a spatial linearity correction and a uniformity correction. This was done in a similar way as during the reconstruction process of the LASiP micro-camera presented in A.2.

In the left panel of Figure B.7 a grid of reconstructed point sources at room-SiPM noise with LASiP 3 is shown. The grid has a lattice space of 6.25 mm, which corresponds to the size of a SiPM of 6 mm and the gap between the SiPMs of 0.25 mm. The dashed lines mark the edges of the LASiPs. The plot shows that the reconstruction result is non-linear, i.e. it depends on the position of the point sources with respect to the pixel center.

The spatial linearity correction was based on [140]. For this, the already mentioned 2D calibration grid of point-like sources, from which I derived the LRF, was used (see Section B.2.1.1). The events of all simulated point sources in a small part of the camera far away from the camera edges that contained at least one entire pixel were reconstructed. The mean of the reconstructed coordinates $x_{rec,j}$ and $y_{rec,j}$ of a point source j was compared to its known real position $x_{cal,j}$ and $y_{cal,j}$. This allowed us to build a correction map of the x- and y-component of the event position. The correction map was then repeated to cover the full SPECT camera as shown in the right panel of Figure B.7 for the x-component. The repetition worked by adding the multiples of the length of the pixel to the x- and y-component. It was possible to derive the correction map from a small part of the camera because in the simulation the camera response of all pixels was assumed to be uniform. Hence it was even possible to use the repetition of one LRF estimate for the reconstruction of the full camera. After the preparation of the correction map, the position of each event was corrected by interpolation.
The uniformity correction method was applied as in [72]. For this method, a FFI was reconstructed as can be seen in the left panel of Figure B.8. A small part of the camera that contained at least one entire pixel was repeated to create a large FFI with good statistical coverage (see right panel of Figure B.8). The large, repeated FFI was corrected with the spatial linearity correction map. Then it was inverted and used as a uniformity correction map.

In Figure B.9 the effect of applying spatial linearity and uniformity corrections is demonstrated with the example of a simulated capillary source with a negligible diameter at x=0 mm, at room-SiPM noise and using LASiP 3. In the left panel,

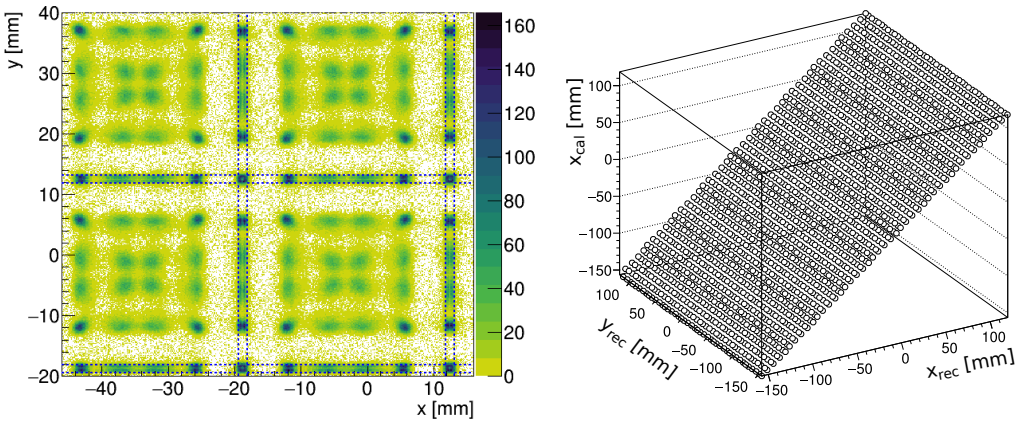

Figure B.7.: Reconstructed grid of simulated point sources with a lattice space of 6.25 mm at room-SiPM noise and using LASiP 3. The reconstructed source position depends on the pixel geometry. The dashed lines mark the edges of the pixel (**left**). Correction grid that compares the reconstructed position of a point source x_{rec} and y_{rec} to the know x-position of the simulated source x_{cal}. The event position is corrected by interpolation.

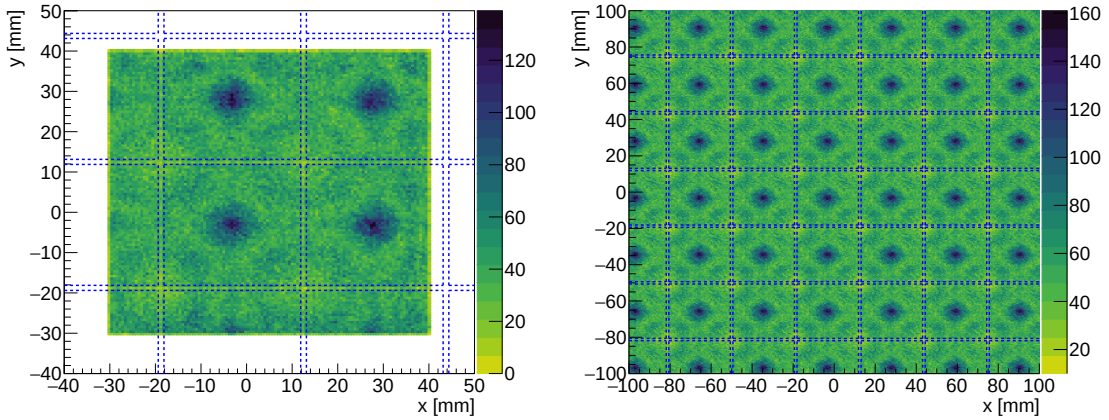

Figure B.8.: Raw reconstruction of a simulated FFI with room-SiPM noise and using LASiP 3 (**left**) and repeated FFI using a small part of the camera in the center (**right**).

the raw reconstruction is shown after minimizing Equation B.9 for each event. The capillary is not centered at x=0 mm and many events were reconstructed close to the pixel center. In the central panel, the reconstructed image was linearity corrected. Now it is centered at x=0 mm as expected. In the right panel, a uniformity correction was applied. The events are now smoothly distributed in the source region. This is the final reconstruction result.

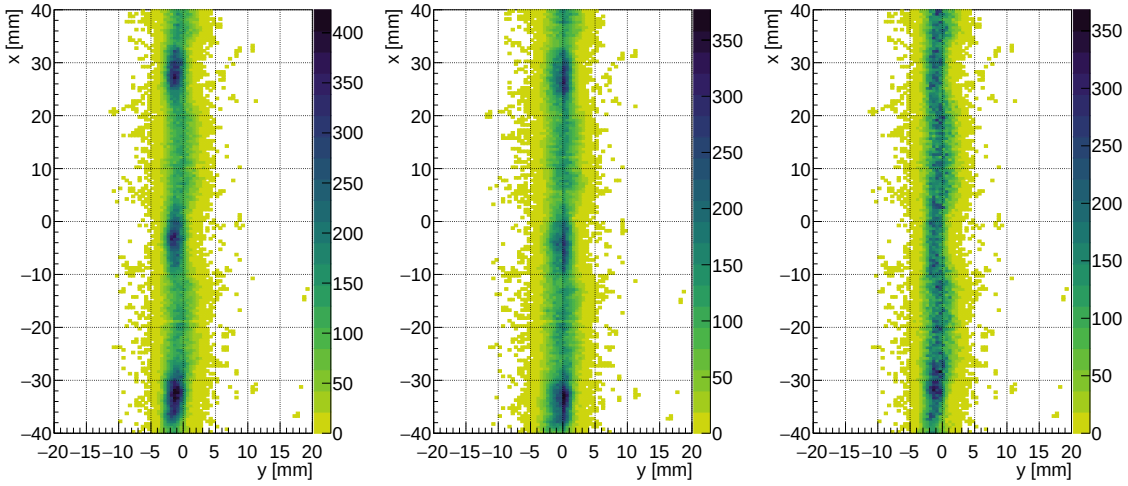

Figure B.9.: A simulated capillary source with negligible diameter positioned at x=0 mm at room-SiPM noise and using LASiP 3: raw reconstruction (**left**), after spatial linearity correction (**center**) and after uniformity correction (**right**).

B.3. Impact of geometry and pixel size

By means of the simulation, I could study the impact of pixel size and geometry as well as the effect of LASiP noise on the performance of a large LASiP camera. The performance was evaluated by examining the intrinsic spatial resolution and the energy resolution of different camera settings.
Several simulated sources were available for this study: point sources at different positions, capillary sources with a negligible diameter at different x-positions (-12, -10, -8, 0, 2, 5, 10, 20, 30 mm) and a phantom source consisting of circles of increasing diameters (1, 2, 3, 4, 6 and 8 mm).

B.3.1. Pixel size

Intrinsic spatial resolution

In Figure B.10 the reconstructed images of capillary sources at different x-positions (-12, 0, 10 mm) and at room-SiPM noise are shown. Both the LASiP configuration and the x-position (relative to the pixel center) of the capillary have an impact on the intrinsic spatial resolution.
The spatial resolution was studied using the FWHM of projections of the capillary in the x-direction as in Section A.2. The histogram of the reconstructed image was projected within a 4 mm window in different y-positions. The y-range that was covered corresponded to a multiple of the pixel size in order to consider all parts of the pixel equally. The resulting projection was evaluated using a Cubic Spline interpolation. The interpolation was performed in `root` using the `TSpline3` class. From the interpolation result the FWHM was extracted and used as an indicator for the intrinsic spatial resolution.
In Figure B.11 examples of projections of the images in Figure B.10 of LASiP 2 at -4 mm $\leq y \leq$ 0 mm and 12 mm $\leq y \leq$ 16 mm are shown. The first projection is close to the pixel center and the second projection is close to the pixel edge. In the left panel, the capillary is located at x=−12 mm, i.e. exactly between two pixels. Both projections give a FWHM of 1.1 mm and match perfectly. In the right panel, a similar situation is found: here the capillary is located at x=10 mm which is very close to the pixel edge. the FWHM is between 1.0-1.1 mm, but the projections have a slightly different shape. In the central panel, the capillary is positioned at x=0 mm at the pixel center. The FWHM is significantly larger with 1.9-2.2 mm and has a vertical dependency. This dependency is even larger if the capillary is not located at x=0 mm, i.e. directly at the pixel center, but close to the pixel center at x=5 mm as demonstrated in Figure B.12. In the left panel, the reconstructed image of the capillary with LASiP 2 is shown, in the right panel the projections at -4 mm $\leq y \leq$ 0 mm and 12 mm $\leq y \leq$ 16 mm with the Cubic Spline interpolation and the FWHM. The FWHM is very different depending on which part of the reconstructed capillary is projected: close to the pixel center it is larger (FWHM=2.7 mm), at the pixel edges it is smaller (FWHM=1.5 mm).

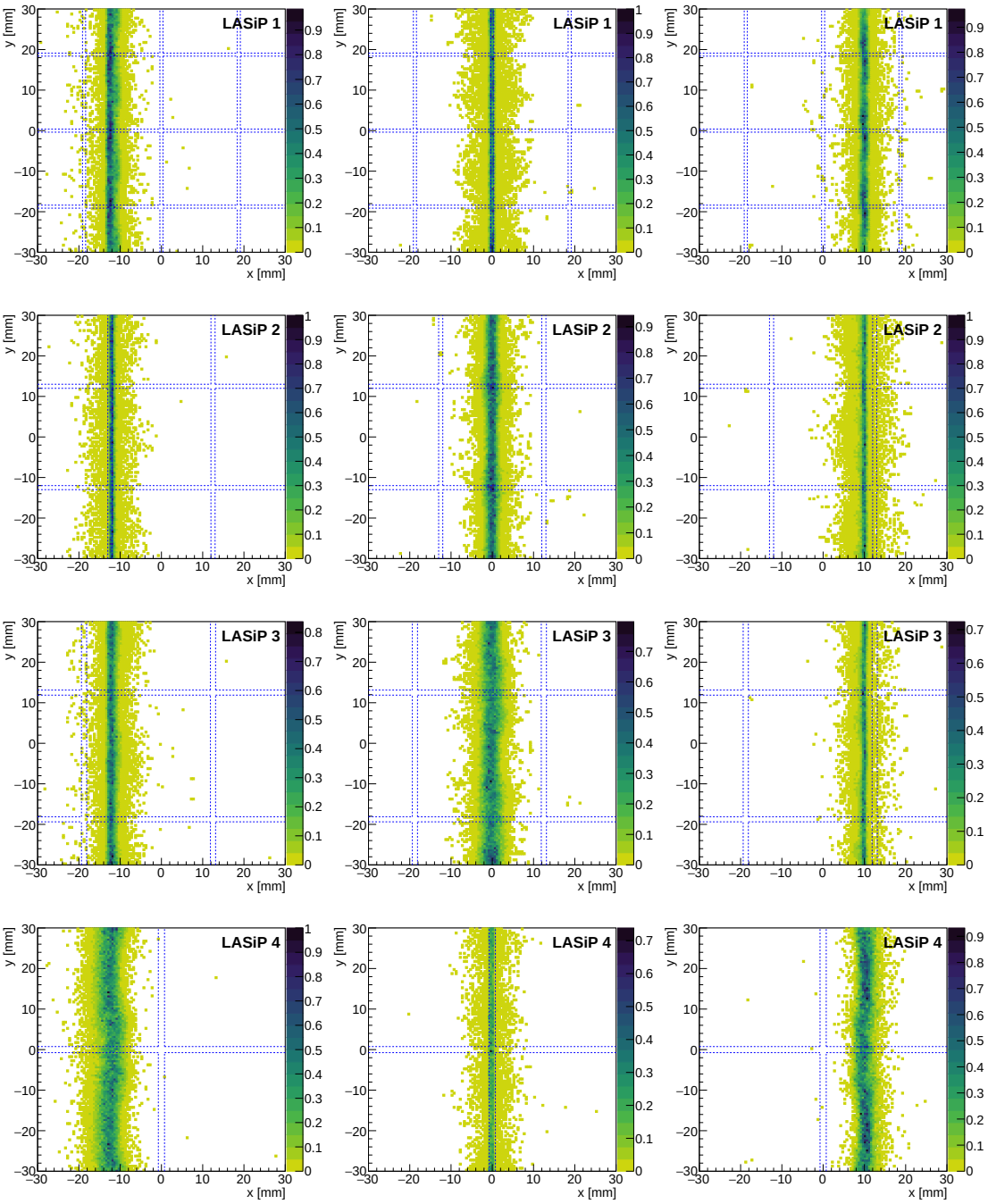

Figure B.10.: Reconstructed image of a capillary source at x=-12,0,10 mm for LASiP 1 to 4 at room-SiPM noise. The dashed lines mark the position of the LASiPs.

Figure B.13 gives a summary of the average FWHM of reconstructed images of capillaries at different x-positions with all LASiP configurations. The x-position was expressed as the distance to the closest pixel center in units of the pixel size. Small LASiPs have a clearly better resolution than large LASiPs. The difference is especially strong

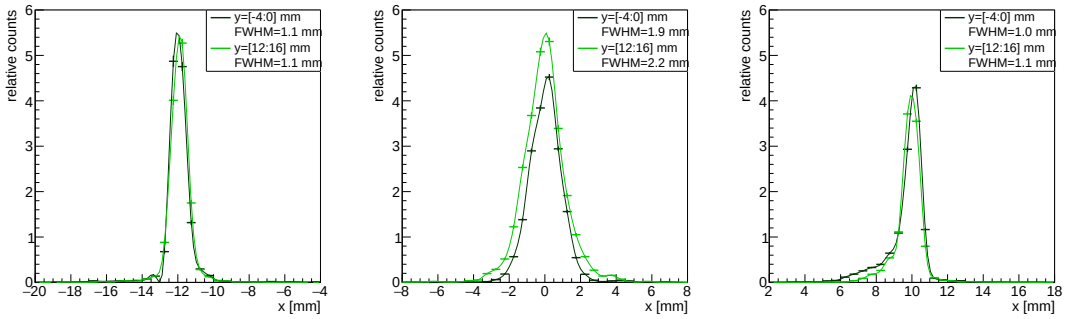

Figure B.11.: Projections of capillaries shown in Figure B.10 of LASiP 2 at room-SiPM noise at -4 mm $\leq y \leq$ 0 mm and 12 mm $\leq y \leq$ 16 mm. Capillary located at x=-12 mm (**left**), at x=0 mm (**center**) and x=10mm (**right**). The FWHM of the projections was evaluated with a Cubic Spline.

between LASiP 3 and LASiP 4 which is the largest one. In addition, the FWHM decreases close to the edges of the pixel and increases near the pixel center. The effect is less prominent for LASiP 1 which gives nearly the same FWHM independently of the position of the source. The larger the LASiP, the stronger the position dependency of the resolution. Close but not directly at the pixel center the FWHM is very variable in y (see Figure B.12). As a result, the error bars of the FWHM of capillary images in this x-position are larger compared to that at the pixel center. This effect was observed only for LASiP 1 and 2. Large LASiPs show a larger FWHM and higher variability of the FWHM in general.

The results can be explained by taking a closer look at the reconstruction mechanism. The achievable intrinsic spatial resolution is a result of the positional information

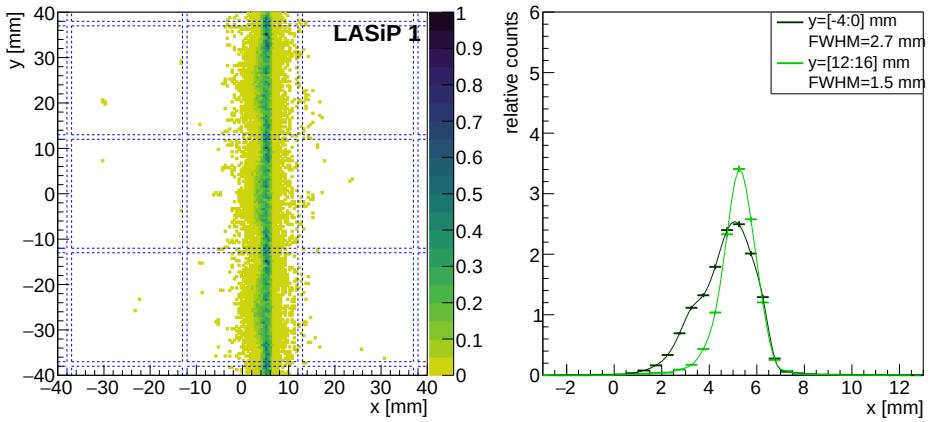

Figure B.12.: Capillary at room-SiPM noise at x=5mm reconstructed with LASiP 2 (**left**) and projection at at -4 mm $\leq y \leq$ 0 mm and 12 mm $\leq y \leq$ 16 mm (**right**). The FWHM of the projections was evaluated with a Cubic Spline.

provided to the reconstruction algorithm. The position of an event is determined by exploiting the information about the central coordinates of the pixels that detected a significant amount of light. The more pixels collect a significant percentage of the photons of an event, the more input information is available for the reconstruction algorithm. If an event is recorded close to the pixel center, a single pixel will detect most of the photons (especially when the pixels are large). In this case, the reconstruction is less precise. In addition, the algorithm tends to reconstruct events that fall around but not at the pixel center closer to the pixel center, because the proportion of charge seen by the maximum pixel will be dominating over all other pixels. The position dependency of the spatial resolution is weakened by the corrections that were applied to the raw reconstruction however the corrections are not able to compensate for all position-dependent effects, especially in the case of large LASiPs.

In Figure B.14 the reconstructed phantom image with LASiPs 1 to 4 at room-SiPM noise is shown. The largest pixel, LASiP 4, provides the worst spatial resolution. Only points ≥ 6 mm are resolved. LASiP 2 and 3 resolve points ≥ 3 mm and LASiP 1 points ≥ 2 mm.

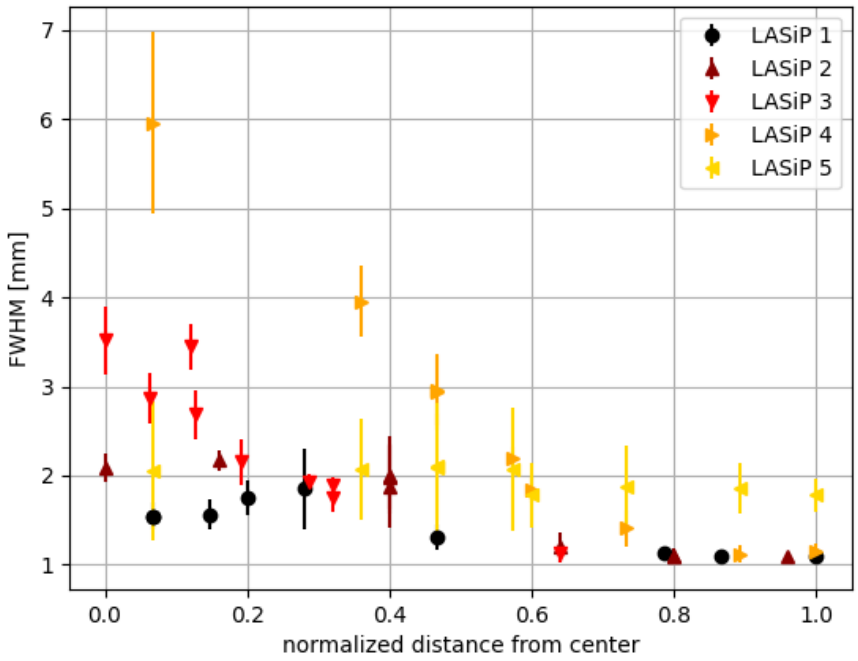

Figure B.13.: Average FWHM as a function of the distance of the capillary to the closest pixel center normalized to the pixel size of LASiP 1-5. The FWHM was smaller far away from the pixel center and larger close to the pixel center.

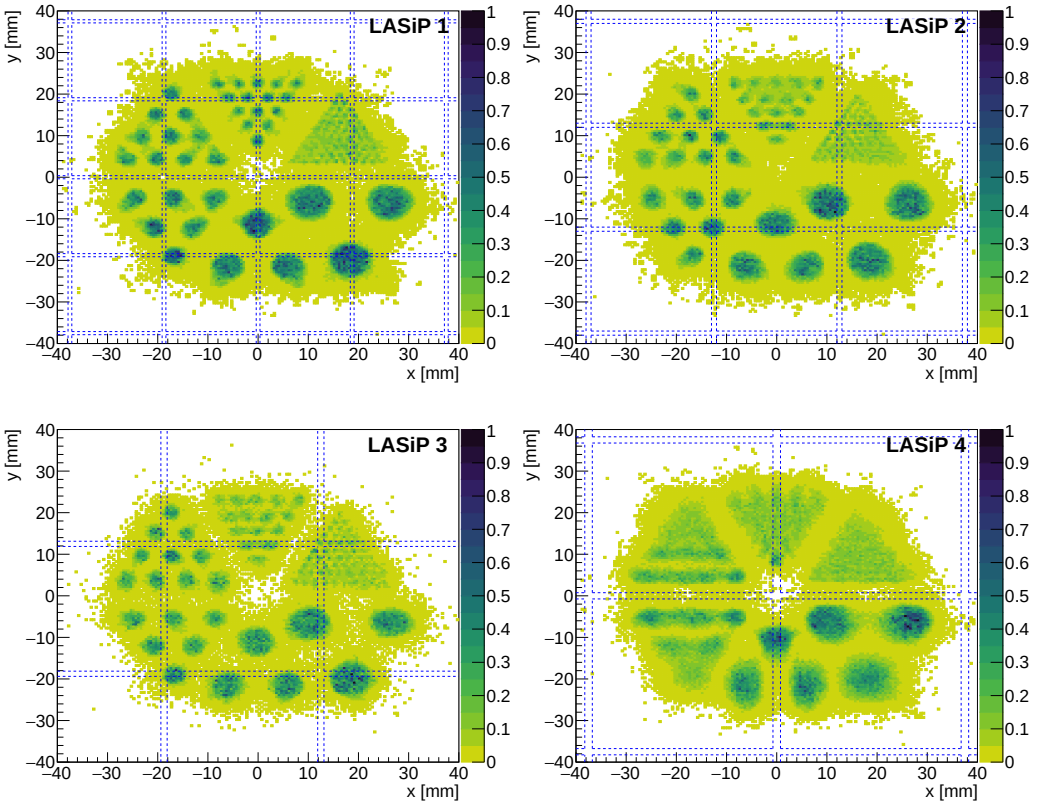

Figure B.14.: Reconstructed image of a simulated phantom source consisting of circles of increasing diameters (1, 2, 3, 4, 6 and 8 mm) and at room-SiPM noise with square-shaped LASiPs of different sizes. The dashed lines mark the position of the LASiPs.

Energy resolution

The energy resolution was calculated as the ratio of the FWHM of the peak of the charge distribution (see the left panel of Figure B.5) to the position of that peak. Both variables were obtained by applying a Gaussian fit to the distribution. The charge distribution was studied as a function of the number of pixels used to collect the charge. In doing so, the pixels were sorted by their collected charge.

In Figure B.15 the energy resolution as a function of the number of pixels used to collect the charge for LASiP 1 to 4 is shown. In addition, the number of corresponding SiPMs of the pixels used is given in the second axis. The energy resolution decreases with an increasing number of pixels used to collect the charge and reaches a stable minimum. The minimum is reached when the total charge of an event is summed and is ~ 8 % for LASiP 1 to 4. According to Figure B.1 the total charge is distributed over ~ 500 SiPMs. In Figure B.15 the charge as a function of pixels used to collect the charge is given. In this case, the number of corresponding SiPMs (as a component

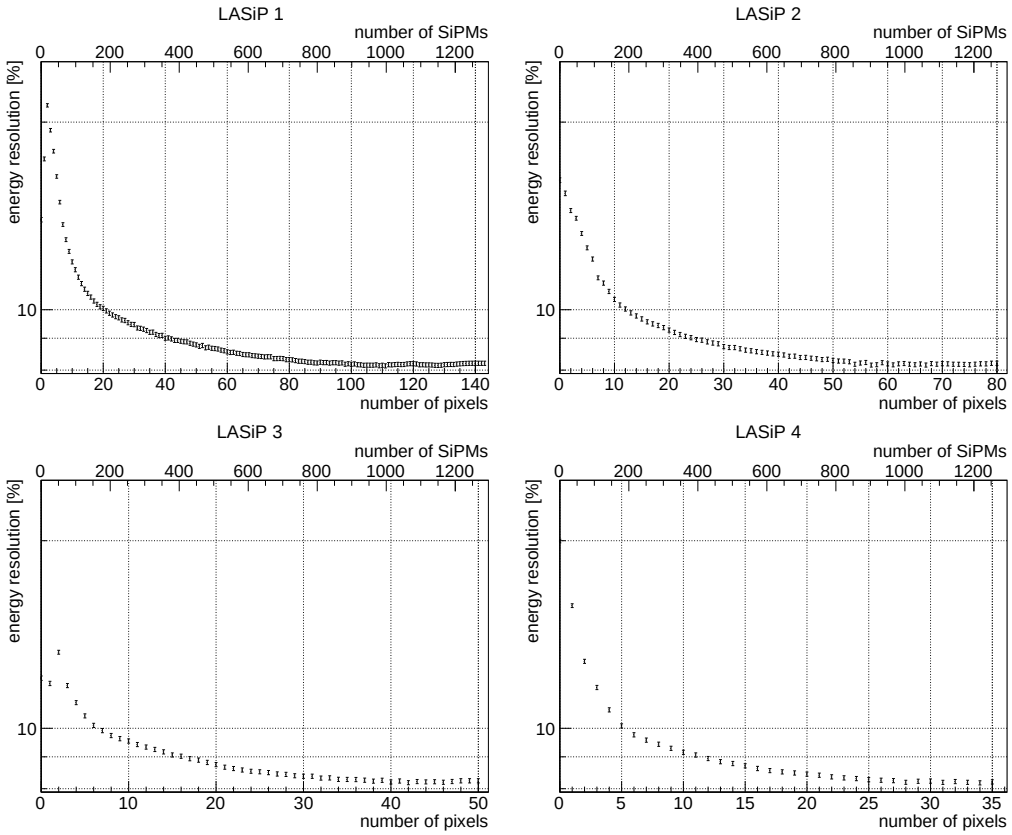

Figure B.15.: Energy resolution as a function of the number of pixels used to collect the charge for LASiP 1 to 4 with an additional axis showing the corresponding number of SiPMs in the pixels. The best resolution is achieved if all pixels are taken into account and is the same for LASiP 1 to 4.

of pixels used) required to collect the total charge of a scintillation event is larger (> 1000) as if the charge of individual SiPMs is collected.

In Figure B.16 the energy resolution as a function of the number of pixels used to collect the charge for LASiP 1 to 4 at room-SiPM noise is shown. Additionally, the number of SiPMs in the pixels used is plotted as the second axis. The energy resolution exhibits a minimum. The more pixels are used, the more signal as well as noise are included. At some point, sufficient pixels are used to collect the total charge of an event. Additional pixels are only contributing noise which reduces the mean of the charge distribution as can be seen in the left panel of Figure B.17 for LASiP 1 at room-SiPM noise. The FWHM of the charge distribution grows however constantly for an increasing number of pixels as shown in the right panel of Figure B.17.
The energy resolution in Figure B.16 degrades slightly for larger pixels. The best energy resolution is found for LASiP 1 with 9.0 ± 0.1 %. The worst energy resolution for LASiP 4 with 9.6 ± 0.1 %. The difference in the energy resolution between LASiP

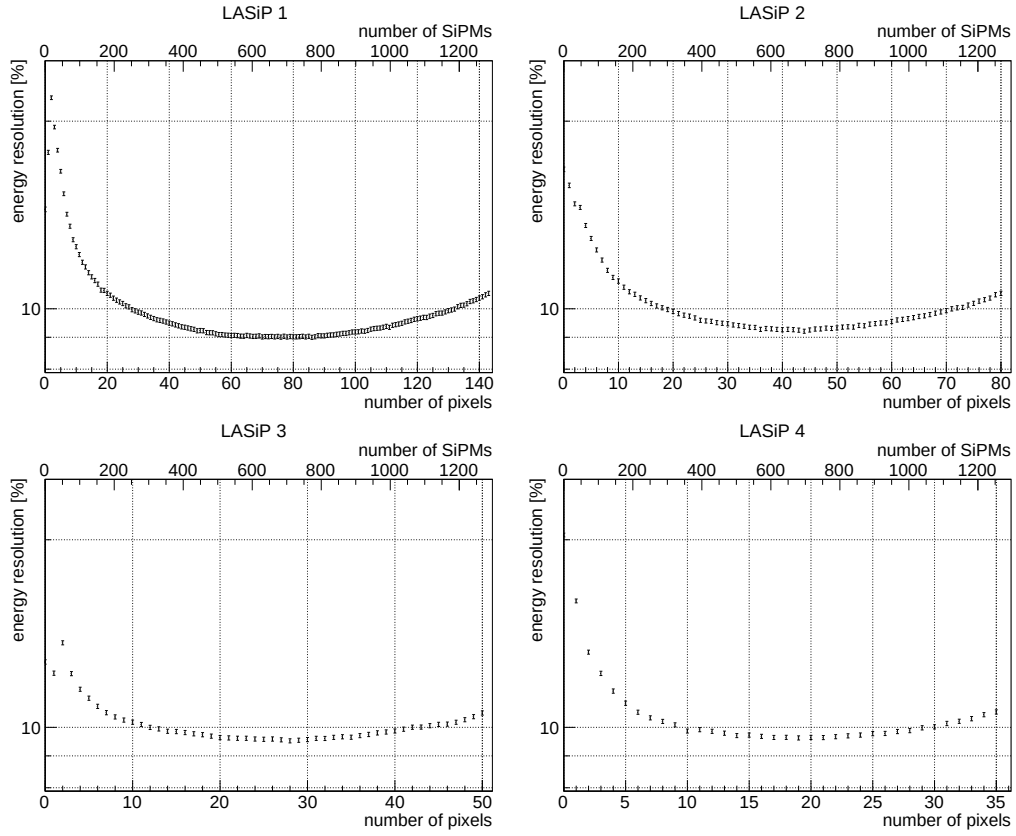

Figure B.16.: Energy resolution as a function of the number of SiPMs used to collect the charge for LASiP 1 to 4 at room-SiPM noise with an additional axis showing the corresponding number of SiPMs in the pixels. The value of the energy resolution exhibits a minimum.

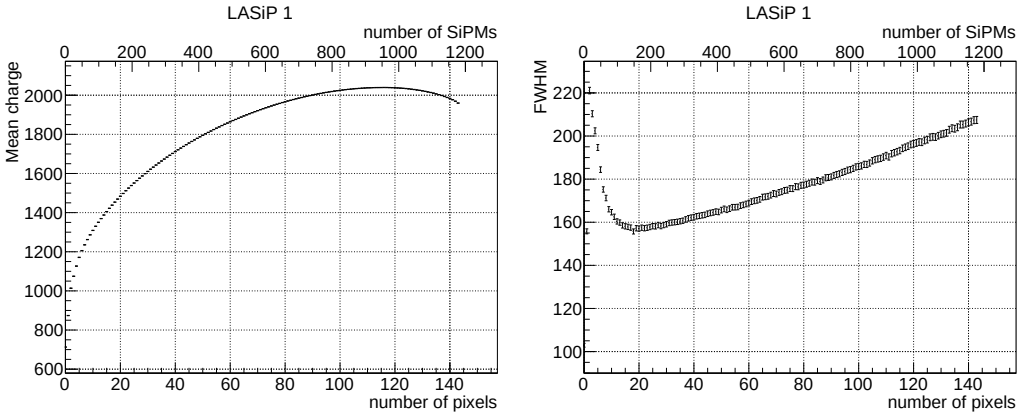

Figure B.17.: Mean (**left**) and FWHM (**right**) of the charge distribution as a function of the number of pixels used to collect the charge of LASiP 1 at room-SiPM noise with additional axis showing the corresponding SiPM number in the pixels.

1 to 4 is 6 %. Thus, the impact of the pixel size on the energy resolution can be considered minor.

B.3.2. Pixel geometry

The impact of the geometry can be studied by comparing the performance obtained with LASiP 3 and 5, which have almost the same area (see Figure B.2).

Intrinsic spatial resolution

In Figure B.18 the reconstruction of a capillary close to the pixel center is compared for LASiP 3 and LASiP 5 by means of projections at -18 mm ≤ y ≤ -14 mm and -6 mm ≤ y ≤ -2 mm. The reconstruction with LASiP 5 provides a smaller FWHM than with LASiP 3. However, the FWHM of the reconstruction with LASiP 5 exhibits a stronger variability. In the region of the corners of LASiP 5 (for instance ~ x=-12, ~ y=-4) a better spatial resolution is achieved, close to the pixel center (~ x=-12, ~ y=-16) the

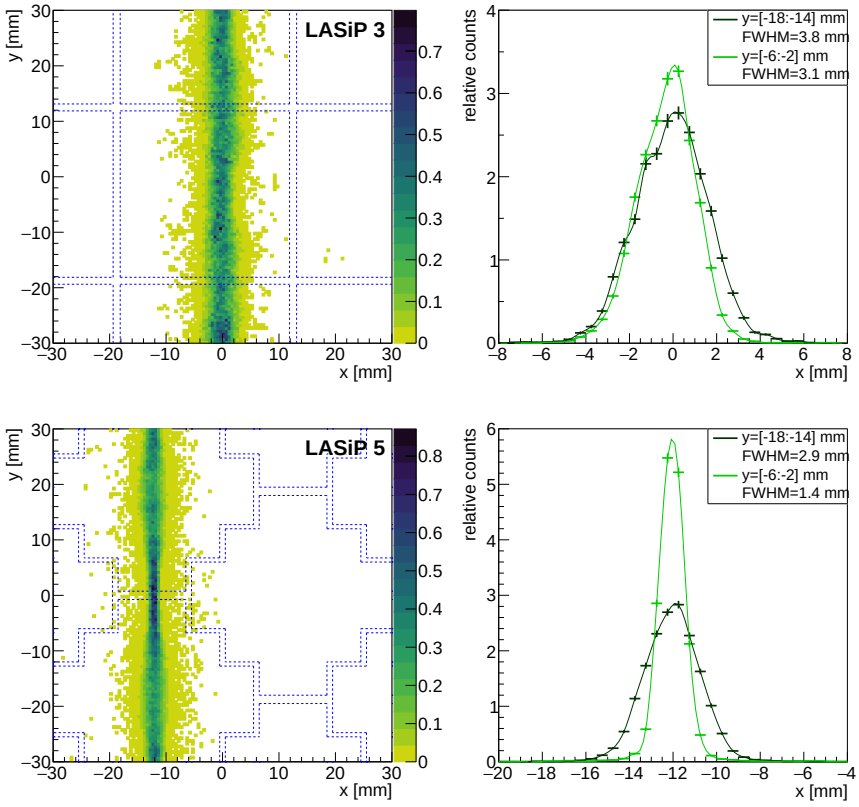

Figure B.18.: Reconstructed image of a capillary source close to the pixel center with LASiP 3 and LASiP 5 at room-SiPM noise. The dashed lines mark the position of the LASiPs. (**left**). Projections of capillary image at -18 mm ≤ y ≤ -14 mm and -6 mm ≤ y ≤ -2 mm with Cubic Spline interpolation and FWHM (**right**).

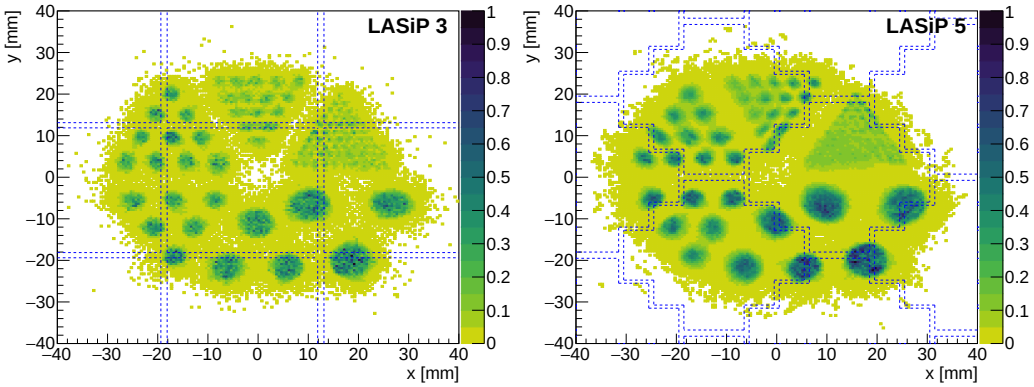

Figure B.19.: Reconstructed image of a simulated phantom source consisting of circles of increasing diameters (1, 2, 3, 4, 6 and 8 mm) and at room-SiPM noise with LASiP 3 and 5. The dashed lines mark the position of the LASiPs.

resolution is worse. LASiP 3 shows a similar spatial resolution for both projections. In Figure B.19 the reconstructed phantom with LASiP 3 in the left panel and LASiP 5 in the right panel is shown. With LASiP 5 even a part of the points ≥ 2 mm are resolved. The reconstruction with LASiP 5 proved that the geometry has indeed an effect on the performance. A simulated camera equipped with LASiP 5 provided a higher spatial resolution. I assume that this is because the shape of LASiP 5 is closer to the one of a circle. A camera equipped with LASiP 5 has fewer regions with a low spatial resolution compared to a camera with square pixels.

Energy resolution

In Figure B.20 the energy resolution as a function of the number of pixels used to collect the charge is shown for LASiP 3 and 5 at room-SiPM noise. An additional axis is plotted with the corresponding number of SiPMs in the pixels. LASiP 5 provides a worse energy resolution than LASiP3 if only a few pixels are used to collect the charge. If a larger number of pixels is considered, the energy resolution curve of LASiP 3 and LASiP 5 is similar with a minimum at ~ 9.5 %. According to this result, the geometry has no impact on the energy resolution.

B.3.3. Pixel noise

Intrinsic spatial resolution

In Figure B.21 the reconstructed image of a simulated phantom source consisting of circles of increasing diameters (1, 2, 3, 4, 6 and 8 mm) at different noise levels using LASiP 3 is shown. Hot-SiPM noise does clearly degrade the spatial resolution compared to the ideal case of no noise. However, there is no apparent difference between no noise and cooled-SiPM noise. For room-SiPM noise, all points with a diameter ≥ 3 mm could be resolved.

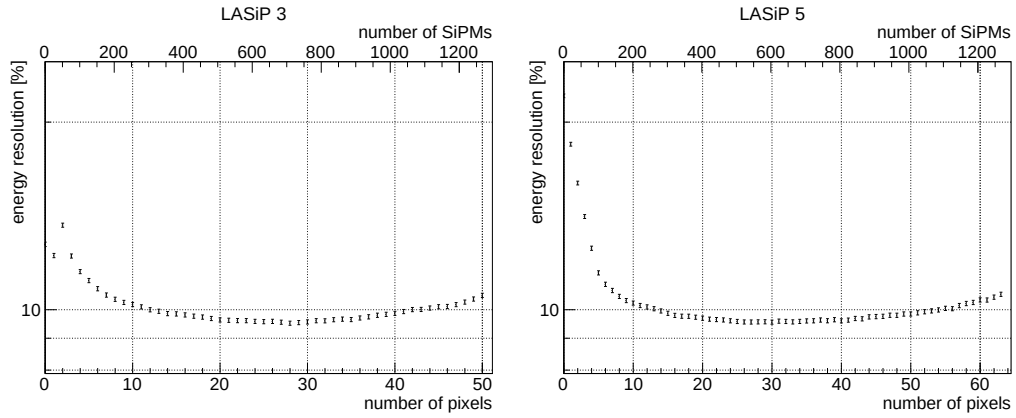

Figure B.20.: Energy resolution as a function of the number of pixels for LASiP 3 and 5 at room-SiPM noise with an additional axis showing the corresponding number of SiPMs.

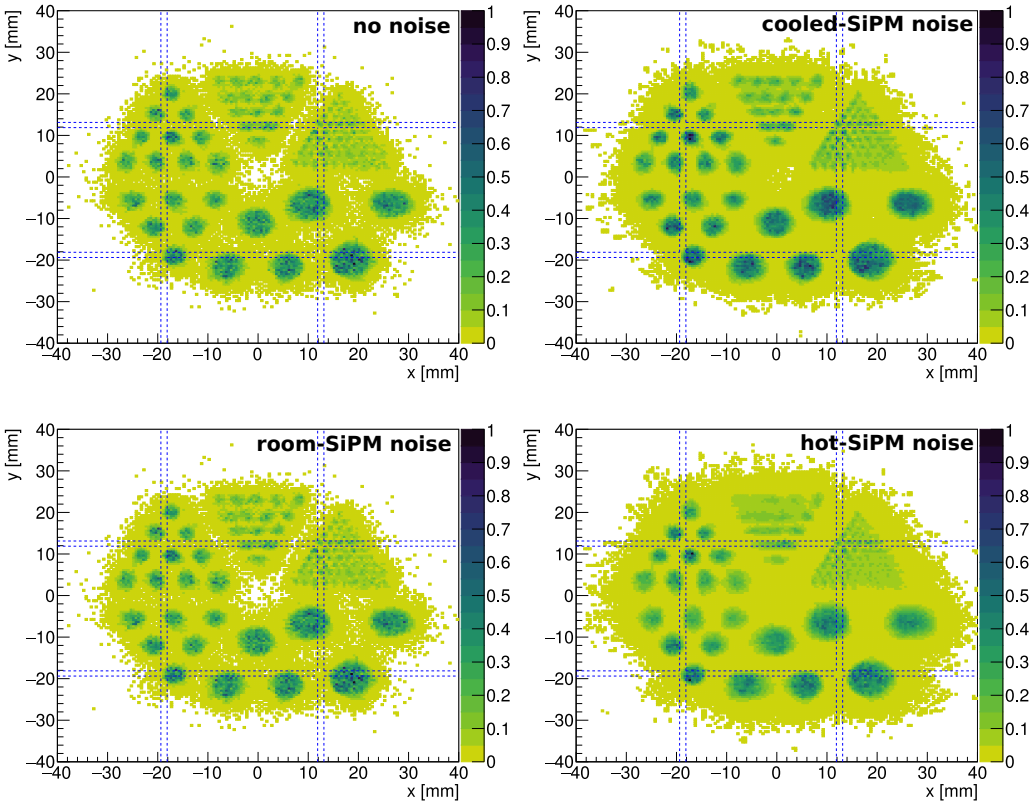

Figure B.21.: Reconstructed image of a simulated phantom source consisting of circles of increasing diameters (1, 2, 3, 4, 6 and 8 mm) at different noise levels using LASiP 3. The dashed lines mark the position of the LASiPs.

In Table B.2 the mean intrinsic spatial resolution for LASiPs with different sizes, shapes and noise levels are listed. The mean intrinsic spatial resolution was extracted

model	mean intrinsic spatial resolution [mm]			
	no noise	cooled-SiPM noise	room-SiPM noise	hot-SiPM noise
1	1.4 ± 0.3	1.4 ± 0.2	1.6 ± 0.2	1.6 ± 0.1
2	1.7 ± 0.4	1.9 ± 0.3	2.0 ± 0.4	2.2 ± 0.2
3	2.5 ± 0.3	2.6 ± 0.3	3.5 ± 0.4	4.0 ± 0.2
4	4.0 ± 1.2	4.8 ± 1.2	6.0 ± 1.0	8.4 ± 1.5
5	1.5 ± 0.4	1.6 ± 0.4	2.1 ± 0.6	2.5 ± 0.9

Table B.2.: Mean intrinsic spatial resolution for a simulated capillary of negligible diameter with LASiPs of different sizes and shapes.

from reconstructions of a capillary source with a negligible diameter as introduced in Section B.3.1. Due to the position dependency of the spatial resolution, the FWHM is significantly higher close to the pixel center. The FWHM listed in Table B.2 was extracted for capillaries located close to the pixel center, thus they present an upper limit of the average FWHM to be expected.
The intrinsic spatial resolution degrades with noise. The effect is minor for small LASiPs but has a large impact on LASiP 3 to 5. The uncertainty of the FWHM decreases with noise for LASiP 1 to 3. As was explained in Section B.3.1 the FWHM exhibits a strong variation close to the pixel center. This effect is most significant in the case with no noise. Additional noise, i.e. dark counts, acts as a blurring to the image. As a result, the variation of the FWHM decreases. This phenomenon is only apparent for small and medium-sized pixels. LASiP 4 shows a larger FWHM and uncertainty in general and LASiP 5 features a much more variable intrinsic spatial resolution due to its different geometry as was discussed in Section B.3.2.

Energy resolution

In Figure B.22 the energy resolution is plotted as a function of the number of pixels for LASiP 3 at different noise levels with an additional axis showing the corresponding number of SiPMs in the pixels. If noise is added to the simulation, the minimum energy resolution is achieved if not all pixels are used to collect the charge. The position of the minimum with respect to the number of pixels depends on the noise level: the more noise is added, the more is the minimum shifted to a smaller pixel number. At cooled-SiPM noise, the best resolution is achieved if summing the charge of ~ 35 pixels, at hot-SiPM noise the minimum is at ~ 20 pixels.
The energy resolution depends on the noise as demonstrated in Table B.3. Here the minimum energy resolution for LASiP 1 to 5 at all simulated noise levels is listed. With increasing noise level, the energy resolution degrades by ~ 20 %. The degradation effect is stronger for larger pixels: the energy resolution of LASiP 1 is reduced by 16 % from the ideal case of no noise to hot-SiPM noise; for LASiP 4 by 21 %. However, cooling the LASiPs could significantly improve the energy resolution by 10 %.

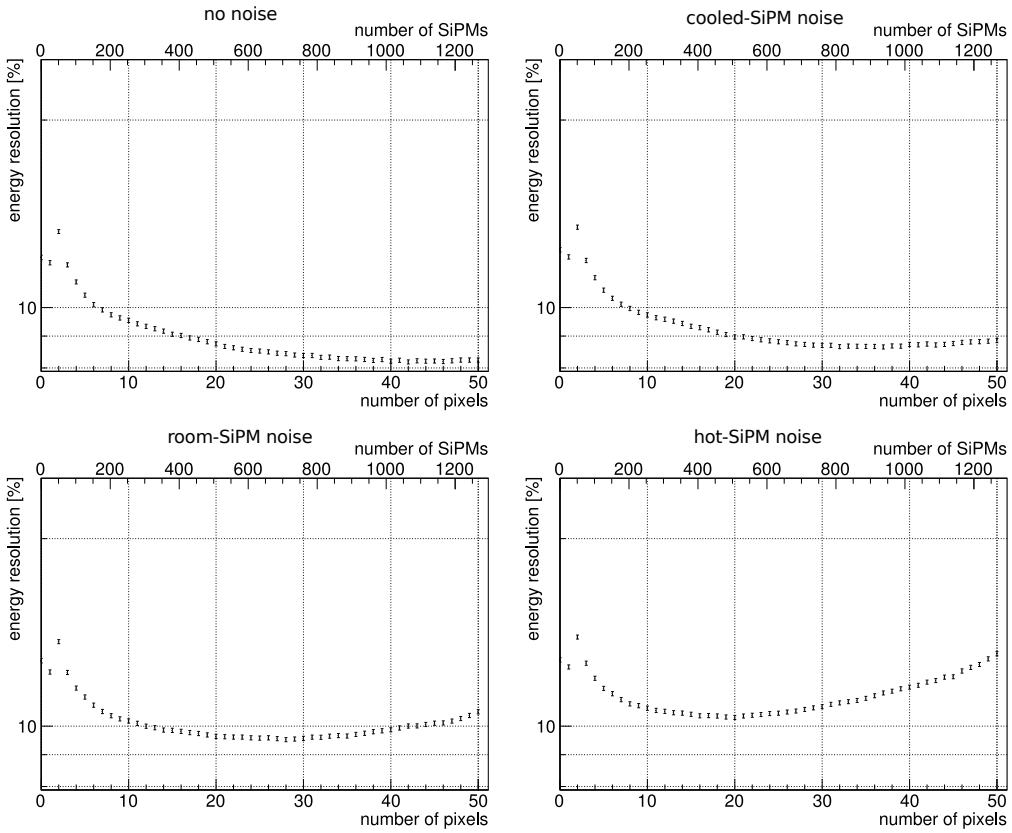

Figure B.22.: Energy resolution as a function of the number of pixels for LASiP 3 at different noise levels with an additional axis showing the corresponding number of SiPMs in the pixels.

	energy resolution [%]			
model	**no noise**	**cooled-SiPM noise**	**room-SiPM noise**	**hot-SiPM noise**
1	8.1 ± 0.1	8.4 ± 0.1	9.0 ± 0.1	9.4 ± 0.1
2	8.2 ± 0.1	8.5 ± 0.1	9.2 ± 0.1	9.9 ± 0.1
3	8.2 ± 0.1	8.6 ± 0.1	9.5 ± 0.1	10.3 ± 0.1
4	8.2 ± 0.1	8.7 ± 0.1	9.6 ± 0.1	10.6 ± 0.1
5	8.2 ± 0.1	8.6 ± 0.1	9.6 ± 0.1	10.4 ± 0.1

Table B.3.: Energy resolution for a simulated capillary of negligible diameter with LASiPs of different sizes and shapes.

B.4. Conclusions

For a standard full-body SPECT, an intrinsic spatial resolution better than 5 mm and an energy resolution of ~ 10 % at 140 keV is typically obtained [4]. In the simulation with LASiP 3 at room-SiPM noise a mean intrinsic spatial resolution of 3.5 ± 0.4 mm and an energy resolution of 9.5 ± 0.1 % were achieved. LASiP 3 was the largest LASiP (active area ~ 9 cm^2, total area ~ 9.8 cm^2) with a performance better than a standard full-body SPECT camera. By reducing the DCR the intrinsic spatial resolution of LASiP 3 could be improved by ~ 25 % and the energy resolution by ~ 10 %. Of nearly similar size but different geometry was LASiP 5 (active area ~ 8.6 cm^2, total area ~ 9.4 cm^2) which achieved at room-SiPM noise an even better resolution of 2.1 ± 0.6 mm and an energy resolution of 9.6 ± 0.1 %. It should be noted that with the achieved intrinsic spatial resolution during most SPECT scans the overall spatial resolution will be dominated by the collimator.

The results of this study of the impact of the pixel size, geometry and noise on the performance suggest that LASiP 3 or LASiP 5 would be the best configurations for building a large SPECT camera using LASiPs. The intrinsic spatial resolution could be improved by cooling the LASiPs (reduced DCR). The use of LASiP 3 or LASiP 5 would reduce the number of readout channels to ~ 200. This number is still higher than the typical 50-100 PMTs in a standard SPECT camera but starts to be affordable. Besides, the increase in cost could be compensated with simpler mechanics and electronics.

My results showed the huge impact that LASiP size and noise have in the performance of a SPECT camera. In addition, the results obtained with LASiP 5 suggest that a better performance might be achieved when using non-square pixels. These results could provide valuable information if aiming to design a SPECT camera based on SiPMs.

Bibliography

[1] URL: https://www.scientifica.es/products/emusic-miniboard (visited on 01/14/2023).

[2] URL: https://www.ost-photonics.com/product-category/scintillation-crysta%20l-2/naitl-scintillator (visited on 01/14/2023).

[3] URL: https://siliconesolutions.com/ss-988.html (visited on 01/14/2023).

[4] 2021. URL: https://www.siemens-healthineers.com.

[5] Abeysekara, A. U. et al. "Demonstration of stellar intensity interferometry with the four VERITAS telescopes". In: *Nature Astronomy* 4.12 (2020), pp. 1164–1169. DOI: 10.1038/s41550-020-1143-y.

[6] Acciari, V. A. et al. "Optical intensity interferometry observations using the MAGIC imaging atmospheric Cherenkov telescopes". In: *Monthly Notices of the Royal Astronomical Society* (2019). DOI: 10.1093/mnras/stz3171.

[7] Acerbi, F. et al. "High Efficiency, Ultra-High-Density Silicon Photomultipliers". In: *IEEE Journal of Selected Topics in Quantum Electronics* PP (2017), pp. 1–1. DOI: 10.1109/JSTQE.2017.2748927.

[8] Acerbi, F. et al. "Silicon photomultipliers and single-photon avalanche diodes with enhanced NIR detection efficiency at FBK". In: *Nuclear Instruments and Methods in Physics Research Section A: Accelerators, Spectrometers, Detectors and Associated Equipment* 912 (2018), pp. 309–314. DOI: https://doi.org/10.1016/j.nima.2017.11.098.

[9] Acerbi, F. et al. "Understanding and simulating SiPMs". In: *Nuclear Instruments and Methods in Physics Research Section A: Accelerators, Spectrometers, Detectors and Associated Equipment* 926 (2019), pp. 16–35. DOI: https://doi.org/10.1016/j.nima.2018.11.118.

[10] Adams, C. et al. "Characterization and assembly of near-ultraviolet SiPMs for the Schwarzschild-Couder medium-size telescope proposed for the CTA Observatory". In: *Proc. SPIE Hard X-Ray, Gamma-Ray, and Neutron Detector Physics XXI*. Vol. 11114. SPIE, 2019, pp. 52–60. DOI: https://doi.org/10.1117/12.2530617.

[11] Agostinelli, S. et al. “Geant4—a simulation toolkit”. In: *Nuclear Instruments and Methods in Physics Research Section A: Accelerators, Spectrometers, Detectors and Associated Equipment* 506.3 (2003), pp. 250–303. DOI: https://doi.org/10.1016/S0168-9002(03)01368-8.

[12] Agostini, D. et al. “Performance of cardiac cadmium-zinc-telluride gamma camera imaging in coronary artery disease: a review from the cardiovascular committee of the European Association of Nuclear Medicine (EANM)”. In: 43 (2016). DOI: https://doi.org/10.1007/s00259-016-3467-5.

[13] Aharonian, F. et al. “Measurement of the radial distribution of Cherenkov light generated by TeV -ray air showers”. In: *Astroparticle Physics* 10.1 (1999), pp. 21–29. DOI: 10.1016/s0927-6505(98)00039-5.

[14] Aharonian, F. et al. “Observations of the Crab nebula with HESS”. In: *A&A* 457.3 (2006), pp. 899–915. DOI: 10.1051/0004-6361:20065351.

[15] Ahnen, M. et al. “Performance of the MAGIC telescopes under moonlight”. In: *Astroparticle Physics* 94 (2017), pp. 29–41. DOI: 10.1016/j.astropartphys.2017.08.001.

[16] Aleksić, J. et al. “Performance of the MAGIC stereo system obtained with Crab Nebula data”. In: *Astroparticle Physics* 35.7 (2012), pp. 435–448. DOI: https://doi.org/10.1016/j.astropartphys.2011.11.007.

[17] Aleksić, J. et al. “The major upgrade of the MAGIC telescopes, Part I: The hardware improvements and the commissioning of the system”. In: *Astroparticle Physics* 72 (2016), pp. 61–75. DOI: https://doi.org/10.1016/j.astropartphys.2015.04.004.

[18] Alfaro, R. et al. “All-particle cosmic ray energy spectrum measured by the HAWC experiment from 10 to 500 TeV”. In: *Physical Review D* 96.12 (2017). DOI: 10.1103/physrevd.96.122001.

[19] Anderhub, H. et al. “Design and operation of FACT – the first G-APD Cherenkov telescope”. In: *Journal of Instrumentation* 8.06 (2013), P06008–P06008. DOI: 10.1088/1748-0221/8/06/p06008.

[20] Anger, H.O. “Scintillation camera”. In: *Rev Sci Instrum* 29 (1958), p. 27.

[21] Austin, L. et al. “Ueber die Reflexion der Kathodenstrahlen und eine damit verbundene neue Erscheinung secundärer Emission”. In: *Annalen der Physik* 314.10 (1902), pp. 271–292. DOI: https://doi.org/10.1002/andp.19023141003. eprint: https://onlinelibrary.wiley.com/doi/pdf/10.1002/andp.19023141003.

[22] Balona, L.A. “The Be Phenomenon”. In: *International Astronomical Union Colloquium* 175 (2000), pp. 1–12. DOI: 10.1017/S0252921100055524.

[23] Barrett, H. et al. “Maximum-Likelihood Methods for Processing Signals From Gamma-Ray Detectors”. In: *IEEE Transactions on Nuclear Science* 56.3 (2009), pp. 725–735. DOI: 10.1109/TNS.2009.2015308.

[24] Baym, G. “The Physics of Hanbury Brown-Twiss intensity interferometry: From stars to nuclear collisions”. In: *Acta Phys. Polon. B* 29 (1998). Ed. by A. Bialas, pp. 1839–1884. arXiv: nucl-th/9804026.

[25] Benaglia, A. et al. “Detection of high energy muons with sub-20ps timing resolution using L(Y)SO crystals and SiPM readout”. In: *Nuclear Instruments and Methods in Physics Research Section A: Accelerators, Spectrometers, Detectors and Associated Equipment* 830 (2016), pp. 30–35. DOI: https://doi.org/10.1016/j.nima.2016.05.030.

[26] Benn, C. R. et al. “Brightness of the night sky over La Palma”. In: *New Astronomy Reviews* 42.6 (1998), pp. 503–507. DOI: https://doi.org/10.1016/S1387-6473(98)00062-1.

[27] Bernlöhr, K. “Simulation of imaging atmospheric Cherenkov telescopes with CORSIKA and sim_telarray”. In: *Astroparticle Physics* 30.3 (2008), pp. 149–158. DOI: 10.1016/j.astropartphys.2008.07.009.

[28] Biland, A. et al. “The Active Mirror Control of the MAGIC Telescope”. In: (2007). DOI: 10.48550/ARXIV.0709.1574.

[29] Bisogni, M. G. et al. “Medical applications of silicon photomultipliers”. In: *Nuclear Instruments and Methods in Physics Research Section A: Accelerators, Spectrometers, Detectors and Associated Equipment* 926 (2019), pp. 118–128. DOI: https://doi.org/10.1016/j.nima.2018.10.175.

[30] Boccali, T. et al. “Extending the farm on external sites: the INFN Tier-1 experience”. In: *Journal of Physics: Conference Series* 898.8 (2017), p. 082018. DOI: 10.1088/1742-6596/898/8/082018.

[31] Bonesini, M. et al. “Study on SiPM breakdown voltage, dark current and gain from room down to liquid nitrogen temperature”. In: *Nuclear Instruments and Methods in Physics Research Section A: Accelerators, Spectrometers, Detectors and Associated Equipment* 936 (2019), pp. 192–194. DOI: https://doi.org/10.1016/j.nima.2018.08.111.

[32] Bouckaert, C. et al. “Evaluation of a compact, high-resolution SPECT detector based on digital silicon photomultipliers”. In: *Phys. Med. Biol.* 59 (2014), pp. 7521–39. DOI: https://doi.org/10.1088/0031-9155/59/23/7521.

[33] Bourges, L. et al. “VizieR Online Data Catalog: JMMC Stellar Diameters Catalogue - JSDC. Version 2 (Bourges+, 2017)”. In: *VizieR Online Data Catalog*, II/346 (2017), pp. II/346.

[34] Bretz, T. et al. “Design constraints on Cherenkov telescopes with Davies–Cotton reflectors”. In: *Astroparticle Physics* 45 (2013), pp. 44–55. DOI: https://doi.org/10.1016/j.astropartphys.2013.03.004.

[35] Broadcom. “AFBR-S4NxxC013-44P163 - Brief Introduction to Silicon Photomultipliers”. In: (2020). URL: https://docs.broadcom.com/doc/Introduction-to-Silicon-Photomultipliers (visited on 01/14/2023).

[36] Brummelaar, T. A. et al. “First Results from the CHARA Array. II. A Description of the Instrument”. In: *The Astrophysical Journal* 628.1 (2005), p. 453. DOI: 10.1086/430729.

[37] Calice Collaboration. URL: https://twiki.cern.ch/twiki/bin/view/CALICE/WebHome (visited on 01/14/2023).

[38] Carminati, M. et al. “Challenges for Microelectronics in Non-Invasive Medical Diagnostics”. In: *Sensors* 20 (2020), p. 3636. DOI: 10.3390/s20133636.

[39] Challouf, M. et al. “Improving the surface-brightness color relation for early-type stars using optical interferometry”. In: *Astronomy Astrophysics* 570 (2014). DOI: 10.1051/0004-6361/201423772.

[40] Classen, L. et al. “The multi-PMT optical module for the IceCube-Upgrade”. In: *EPJ Web Conf.* 207 (2019), p. 06004. DOI: 10.1051/epjconf/201920706004.

[41] Clinthorne, N. H. et al. “A Hybrid Maximum Likelihood Position Computer for Scintillation Cameras”. In: *IEEE Transactions on Nuclear Science* 34.1 (1987), pp. 97–101. DOI: 10.1109/TNS.1987.4337309.

[42] Conti, M. “State of the art and challenges of time-of-flight PET”. In: *Physica Medica* 25.1 (2009), pp. 1–11. DOI: https://doi.org/10.1016/j.ejmp.2008.10.001.

[43] Cortina, J. et al. “First measurements and upgrade plans of the MAGIC intensity interferometer”. In: *SPIE proceeding* (2022).

[44] CTA Consortium. *Science with the Cherenkov Telescope Array*. WORLD SCIENTIFIC, 2018. DOI: 10.1142/10986.

[45] Cunha, M. S. et al. “Asteroseismology and interferometry”. In: *The Astronomy and Astrophysics Review* 14.3-4 (2007), pp. 217–360. DOI: 10.1007/s00159-007-0007-0.

[46] Currie, M. J. et al. “High-Efficiency Organic Solar Concentrators for Photovoltaics”. In: *Science* 321.5886 (2008), pp. 226–228. DOI: 10.1126/science.1158342. eprint: https://science.sciencemag.org/content/321/5886/226.full.pdf.

[47] Davies, J. M. et al. “Design of the quartermaster solar furnace”. In: *Solar Energy* 1.2-3 (1957), pp. 16–22. DOI: 10.1016/0038-092X(57)90116-0.

[48] Dragojević, A. et al. “RDMA Reads: To Use or Not to Use?” In: IEEE Computer Society Technical Committee on Data Engineering, 2017. URL: https://www.cs.utah.edu/~stutsman/cs6450/public/papers/rdma.pdf.

[49] Dravins, D. et al. “Optical intensity interferometry with the Cherenkov Telescope Array”. In: *Astroparticle Physics* 43 (2013), pp. 331–347. DOI: https://doi.org/10.1016/j.astropartphys.2012.04.017.

[50] Ducati, J. "Catalogue of Stellar Photometry in Johnson's 11-color system". In: *VizieR Online Data Catalog* (2002).

[51] Fabricius, C. et al. "The Tycho double star catalogue". In: *Astronomy and Astrophysics* 384 (2002), p. 180. DOI: 10.1051/0004-6361:20011822.

[52] FACT Collaboration. *The First G-APD Cherenkov Telescope*. URL: https://www.isdc.unige.ch/fact/ (visited on 01/14/2023).

[53] Fernández-Tenllado, J.M. et al. "Optimal design of single-photon sensor front-end electronics for fast-timing applications". In: *2019 IEEE Nuclear Science Symposium and Medical Imaging Conference (NSS/MIC)*. 2019, pp. 1–5. DOI: 10.1109/NSS/MIC42101.2019.9059805.

[54] Fink, D. *MAGIC Hardware School - An introduction to MAGIC Telescope Cameras*. 2018.

[55] Fink, D. et al. "SiPM Based Focal Plane Instrumentation Prototype for the MAGIC Atmospheric Cherenkov Telescope". In: 2016, p. 006. DOI: 10.22323/1.252.0006.

[56] First sensor. *Red, Green, Blue (RGB) SiPMs*. URL: https://elearning.unimib.it/pluginfile.php/521118/mod_folder/content/0/SiPM.pdf?forcedownload=1 (visited on 01/14/2023).

[57] First sensor. "Introduction to silicon photomultipliers (SiPMs)". In: (2019). URL: https://www.first-sensor.com/cms/upload/appnotes/AN_SiPM_Introduction_E.pdf.

[58] Foellmi, C. "Intensity interferometry and the second-order correlation function $g^{(2)}$ in astrophysics". In: *A&A* 507.3 (2009), pp. 1719–1727. DOI: 10.1051/0004-6361/200911739.

[59] Foreman-Mackey, D. *emcee*. URL: https://emcee.readthedocs.io/en/stable/ (visited on 01/14/2023).

[60] Frémat, Y. et al. "Effects of gravitational darkening on the determination of fundamental parameters in fast-rotating B-type stars". In: *A&A* 440.1 (2005), pp. 305–320. DOI: 10.1051/0004-6361:20042229.

[61] SPECTRUM Instrumentation GmbH. *M4i.4450-x8*. 2022. URL: https://spectrum-instrumentation.com/products/details/M4i4450-x8.php (visited on 01/14/2023).

[62] Gómez, S. et al. "Multiple Use SiPM Integrated Circuit (MUSIC) for Large Area and High Performance Sensors". In: *Electronics* 10.8 (2021). DOI: 10.3390/electronics10080961.

[63] Gómez, S. et al. "FastIC: a fast integrated circuit for the readout of high performance detectors". In: *Journal of Instrumentation* 17.05 (2022), p. C05027. DOI: 10.1088/1748-0221/17/05/C05027.

[64] Gordon, K. D. et al. “Angular Sizes and Effective Temperatures of O-type Stars from Optical Interferometry with the CHARA Array”. In: *The Astrophysical Journal* 869.1 (2018), p. 37. DOI: 10.3847/1538-4357/aaec04.

[65] Gordon, K. D. et al. “Angular Sizes, Radii, and Effective Temperatures of B-type Stars from Optical Interferometry with the CHARA Array”. In: *The Astrophysical Journal* 873.1 (2019), p. 91. DOI: 10.3847/1538-4357/ab04b2.

[66] Gori, P. et al. “I3T: Intensity Interferometry Imaging Telescope”. In: *Monthly Notices of the Royal Astronomical Society* 505.2 (2021), pp. 2328–2335. DOI: 10.1093/mnras/stab1424.

[67] Gray, R. M. and others. “Maximum a Posteriori Estimation of Position in Scintillation Cameras”. In: *IEEE Transactions on Nuclear Science* 23.1 (1976), pp. 849–852. DOI: 10.1109/TNS.1976.4328354.

[68] Grindlay, J. E. et al. “Evidence for the detection of gamma rays from Centaurus A at $E_{gamma} \geq 3\times10^{11}$eV.” In: 197 (1975), pp. L9–L12. DOI: 10.1086/181764.

[69] Grusovin, S. et al. “A prototype tank for the SWGO detector”. In: (2023). DOI: 10.48550/ARXIV.2301.02449.

[70] Guberman, D. “MAGIC observations with bright Moon and their application to measuring the VHE gamma-ray spectral cut-off of the PeVatron candidate Cassiopeia A”. PhD thesis. Universitat Autònoma de Barcelona, 2018.

[71] Guberman, D. et al. “The Light-Trap: A novel concept for a large SiPM-based pixel for Very High Energy gamma-ray astronomy and beyond”. In: *Nuclear Instruments and Methods in Physics Research Section A: Accelerators, Spectrometers, Detectors and Associated Equipment* 923 (2019), pp. 19–25. DOI: https://doi.org/10.1016/j.nima.2019.01.052.

[72] Guberman, D. et al. “Large-Area SiPM Pixels (LASiPs): A cost-effective solution towards compact large SPECT cameras”. In: *Physica Medica* 82 (2021), pp. 171–184. DOI: http://dx.doi.org/10.1016/j.ejmp.2021.01.066.

[73] Gundacker, S. et al. “SiPM time resolution: From single photon to saturation”. In: *Nuclear Instruments and Methods in Physics Research A* 718 (2013). DOI: 10.1016/j.nima.2013.01.047.

[74] Gundacker, S. et al. “Experimental time resolution limits of modern SiPMs and TOF-PET detectors exploring different scintillators and Cherenkov emission”. In: *Physics in Medicine &amp Biology* 65.2 (2020), p. 025001. DOI: 10.1088/1361-6560/ab63b4.

[75] Haas, H. et al. “Optical wireless communication”. In: *Philosophical Transactions of the Royal Society A: Mathematical, Physical and Engineering Sciences* 378.2169 (2020), p. 20200051. DOI: 10.1098/rsta.2020.0051. eprint: https://royalsocietypublishing.org/doi/pdf/10.1098/rsta.2020.0051.

[76] Hahn, A. et al. “Development of a composite large-size SiPM (assembled matrix) based modular detector cluster for MAGIC”. In: *NIM-A* 845 (2017), pp. 89–92. DOI: https://doi.org/10.1016/j.nima.2016.06.102.

[77] Hahn, A. et al. “Development of three silicon photomultiplier detector modules for the MAGIC telescopes for a performance comparison to PMTs”. In: *NIM-A* 912 (2018), pp. 259–63. DOI: https://doi.org/10.1016/j.nima.2017.11.071.

[78] Hahn, A. et al. “Performance evaluation of three silicon photomultiplier detector modules within the MAGIC telescopes PMT-based camera”. In: *Nuclear Instruments and Methods in Physics Research Section A: Accelerators, Spectrometers, Detectors and Associated Equipment* 1046 (2023), p. 167686. DOI: 10.1016/j.nima.2022.167686.

[79] HAMAMATSU PHOTONICS K.K. *MPPC S13360 series*. URL: https://www.hamamatsu.com/content/dam/hamamatsu-photonics/sites/documents/99_SALES_LIBRARY/ssd/s13360_series_kapd1052e.pdf (visited on 01/14/2023).

[80] Hanbury Brown, R. et al. “LXXIV. A new type of interferometer for use in radio astronomy”. In: *The London, Edinburgh, and Dublin Philosophical Magazine and Journal of Science* 45.366 (1954), pp. 663–682. DOI: 10.1080/14786440708520475. eprint: https://doi.org/10.1080/14786440708520475.

[81] Hanbury Brown, R. et al. “A Test of a New Type of Stellar Interferometer on Sirius”. In: *Nature* 178 (1956). DOI: https://doi.org/10.1038/1781046a0.

[82] Hanbury Brown, R. et al. “Correlation between photons in two coherent beams of light”. In: *Nature* 177 (1956). DOI: https://doi.org/10.1038/177027a0.

[83] Hanbury Brown, R. et al. “The stellar interferometer at Narrabri Observatory-II. The angular diameters of 15 stars”. In: 137 (1967), p. 393. DOI: 10.1093/mnras/137.4.393.

[84] Hanbury Brown, R. et al. “The Angular Diameters of 32 Stars”. In: 167 (1974), pp. 121–136. DOI: 10.1093/mnras/167.1.121.

[85] Hanbury Brown, R. et al. “The Intensity Interferometer: Its Application to Astronomy”. In: (1974).

[86] Handler, G. “Asteroseismology”. In: (2013), pp. 207–241. DOI: 10.1007/978-94-007-5615-1_4.

[87] Haniff, C. “An introduction to the theory of interferometry”. In: *New Astronomy Reviews* 51.8 (2007), pp. 565–575. DOI: https://doi.org/10.1016/j.newar.2007.06.002.

[88] Heath, R. M. et al. “On the orbital evolution of binaries with circumbinary discs”. In: *A&A* 641 (2020), A64. DOI: 10.1051/0004-6361/202038548.

[89] Hertz, H. “Ueber einen Einfluss des ultravioletten Lichtes auf die electrische Entladung”. In: *Annalen der Physik* 267.8 (1887), pp. 983–1000. DOI: https://doi.org/10.1002/andp.18872670827. eprint: https://onlinelibrary.wiley.com/doi/pdf/10.1002/andp.18872670827.

[90] Høg, E. et al. “The Tycho-2 Catalogue of the 2.5 million brightest stars”. In: *Astronomy and Astrophysics* 355 (2000), pp. L27–L30.

[91] Holder, J. et al. “Status of the VERITAS Observatory”. In: *AIP Conf. Proc.* 1085.1 (2009). Ed. by Felix A. Aharonian, Werner Hofmann, and Frank Rieger, pp. 657–660. DOI: 10.1063/1.3076760. arXiv: 0810.0474 [astro-ph].

[92] Hutton, B. F. et al. “Development of clinical simultaneous SPECT/MRI”. In: *Br J Radiol* 91 (2018), p. 1081. DOI: https://doi.org/10.1259/bjr.20160690.

[93] Iams, H. et al. “The Secondary Emission Phototube”. In: *Proceedings of the Institute of Radio Engineers* 23.1 (1935), pp. 55–64. DOI: 10.1109/JRPROC.1935.227243.

[94] Semrock Inc. *425/26 nm BrightLine single-band bandpass filter*. 2021. URL: https://www.semrock.com/FilterDetails.aspx?id=FF01-425/26-25 (visited on 01/14/2023).

[95] Julius, E. et al. *Ueber die Entladung negativ electrischer Körper durch das Sonnen- und Tageslicht*. 1889. DOI: 10.1002/andp.18892741202.

[96] Hamamatsu Photonics K. K. “Photomultiplier Tubes - Basics and Applications”. In: 4 (2017). URL: https://www.hamamatsu.com/content/dam/hamamatsu-photonics/sites/documents/99_SALES_LIBRARY/etd/PMT_handbook_v4E.pdf.

[97] Knoetig, M. L. et al. “SiPM Avalanche Size and Crosstalk Measurements with Light Emission Microscopy”. In: *IEEE Transactions on Nuclear Science* 61.3 (2014), pp. 1488–1492. DOI: 10.1109/TNS.2014.2322957.

[98] Korpar, S. et al. “Silicon photomultiplier based photon detector module as a detector of Cherenkov photons”. In: *Nuclear Instruments and Methods in Physics Research Section A: Accelerators, Spectrometers, Detectors and Associated Equipment* 623.1 (2010), pp. 333–335. DOI: https://doi.org/10.1016/j.nima.2010.02.239.

[99] Le Bohec, S. et al. “Optical Intensity Interferometry with Atmospheric Cerenkov Telescope Arrays”. In: *The Astrophysical Journal* 649.1 (2006), pp. 399–405. DOI: 10.1086/506379.

[100] Lecoq, P. et al. “SiPM applications in positron emission tomography: toward ultimate PET time-of-flight resolution”. In: *The European Physical Journal Plus* 136.292 (2021). DOI: 10.1140/epjp/s13360-021-01183-8.

[101] Leo, W. R. *Photomultipliers*. Springer Berlin Heidelberg, 1994, pp. 177–198. ISBN: 978-3-642-57920-2. DOI: 10.1007/978-3-642-57920-2_8.

[102] Loudon, R. *The Quantum Theory of Light*. OUP Oxford, 2000. ISBN: 9780191589782.

[103] Lutz, Benjamin et al. "Upgrade of the CMS Hadron Outer Calorimeter with SiPM sensors". In: *Journal of Physics: Conference Series* 404 (2012), p. 012018. DOI: 10.1088/1742-6596/404/1/012018.

[104] Machadom, A. A. et al. "ARAPUCA a new device for liquid argon scintillation light detection". In: *Journal of Instrumentation* 11.02 (2016), pp. C02004–C02004. DOI: 10.1088/1748-0221/11/02/c02004.

[105] Madsen, M. T. "Recent Advances in SPECT Imaging". In: *Journal of Nuclear Medicine* 48.4 (2007), pp. 661–673. DOI: 10.2967/jnumed.106.032680. eprint: https://jnm.snmjournals.org/content/48/4/661.full.pdf.

[106] MAGIC collaboration. *The MAGIC Telescopes*. URL: https://magic.mpp.mpg.de/ (visited on 01/14/2023).

[107] Mallamaci, M. et al. "Design of a SiPM-based cluster for the Large-Sized Telescope camera of the Cherenkov Telescope Array". In: *NIM-A* 936 (2019), pp. 231–2. DOI: https://doi.org/10.1016/j.nima.2018.09.141. arXiv: 1807.06281 [astro-ph.IM].

[108] Marano, D. et al. "Silicon Photomultipliers Electrical Model Extensive Analytical Analysis". In: *IEEE Transactions on Nuclear Science* 61.1 (2014), pp. 23–34. DOI: 10.1109/TNS.2013.2283231.

[109] Maravelias, G. et al. "Resolving the kinematics of the discs around Galactic B[e] supergiants". In: *Monthly Notices of the Royal Astronomical Society* 480.1 (2018), pp. 320–344. DOI: 10.1093/mnras/sty1747. eprint: https://academic.oup.com/mnras/article-pdf/480/1/320/25244380/sty1747.pdf.

[110] Matsubayashi, E. et al. "Correction for PMT temperature dependence of the LHCf calorimeters". In: *Journal of Physics: Conference Series* 587 (2015), p. 012023. DOI: 10.1088/1742-6596/587/1/012023.

[111] McClain, R. L. et al. "Description of the Role of Shot Noise in Spectroscopic Absorption and Emission Measurements with Photodiode and Photomultiplier Tube Detectors: Information for an Instrumental Analysis Course". In: *Journal of Chemical Education* 91.9 (2014), pp. 1455–1457. DOI: 10.1021/ed4005112. eprint: https://doi.org/10.1021/ed4005112.

[112] Miroshnichenko, A. S. et al. "VizieR Online Data Catalog: Properties of Galactic Be Supergiants. VI. (Miroshnichenko+, 2020)". In: *VizieR Online Data Catalog*, J/ApJ/897/48 (2021), J/ApJ/897/48.

[113] Mirzoyan, R. et al. “Evaluation of novel PMTs of worldwide best parameters for the CTA project”. In: *Nuclear Instruments and Methods in Physics Research Section A: Accelerators, Spectrometers, Detectors and Associated Equipment* 845 (2017), pp. 603–606. DOI: https://doi.org/10.1016/j.nima.2016.06.080.

[114] Miyaoka, R. S. et al. “Resolution Properties of a Prototype Continuous Miniature Crystal Element (cMiCE) Scanner”. In: *IEEE Transactions on Nuclear Science* 58.5 (2011), pp. 2244–2249. DOI: 10.1109/TNS.2011.2165296.

[115] Monnier, J. D. “Optical interferometry in astronomy”. In: *Reports on Progress in Physics* 66.5 (2003), pp. 789–857. DOI: 10.1088/0034-4885/66/5/203.

[116] Morozov, A. et al. “Adaptive algorithms of position and energy reconstruction in Anger-camera type detectors: experimental data processing in ANTS”. In: *Journal of Instrumentation* 8.05 (2013), P05002. DOI: 10.1088/1748-0221/8/05/P05002.

[117] Morozov, A. et al. “Iterative reconstruction of detector response of an Anger gamma camera”. In: *Physics in Medicine Biology* 60.10 (2015), p. 4169. DOI: 10.1088/0031-9155/60/10/4169.

[118] Morozov, A. et al. “Iterative reconstruction of SiPM light response functions in a square-shaped compact gamma camera”. In: *Physics in Medicine Biology* 62.9 (2017), p. 3619. DOI: 10.1088/1361-6560/aa6029.

[119] Musienko, Y. “Advances in multipixel Geiger-mode avalanche photodiodes (silicon photomultiplies)”. English. In: *Nuclear Inst. and Methods in Physics Research, A* 598.1 (2009), pp. 213–216. DOI: 10.1016/j.nima.2008.08.031.

[120] Nagai, A. et al. “Characterization of a large area silicon photomultiplier”. In: *NIM-A* 948, 162796 (2019), p. 162796. DOI: https://doi.org/10.1016/j.nima.2019.162796. arXiv: 1810.02275 [physics.ins-det].

[121] Nemallapudi, M.V. et al. “Single photon time resolution of state of the art SiPMs”. In: *Journal of Instrumentation* 11 (2016), P10016–P10016. DOI: 10.1088/1748-0221/11/10/P10016.

[122] Neves, F. et al. “Position reconstruction in a liquid xenon scintillation chamber for low-energy nuclear recoils and -rays”. In: *Nuclear Instruments and Methods in Physics Research Section A: Accelerators, Spectrometers, Detectors and Associated Equipment* 573.1 (2007), pp. 48–52. DOI: https://doi.org/10.1016/j.nima.2006.10.390.

[123] Nudi, F. et al. “Diagnostic Accuracy of Myocardial Perfusion Imaging With CZT Technology: Systemic Review and Meta-Analysis of Comparison With Invasive Coronary Angiography”. In: *JACC: Cardiovascular Imaging* 10.7 (2017), pp. 787–94. DOI: https://doi.org/10.1016/j.jcmg.2016.10.023.

[124] Occhipinti, M. “Development of a gamma-ray detection module for multimodal SPECT/MR imaging”. PhD thesis. Politecnico di Milano, 2015. URL: http://hdl.handle.net/10589/114190.

[125] Ofir, A. et al. “Offline, multidetector intensity interferometers – I. Theory”. In: *Monthly Notices of the Royal Astronomical Society* 368.4 (2006), pp. 1646–1651. DOI: 10.1111/j.1365-2966.2006.09966.x. eprint: https://academic.oup.com/mnras/article-pdf/368/4/1646/3966194/mnras0368-1646.pdf.

[126] Oja, T. “UBV photometry of stars whose positions are accurately known. VI.” In: 89 (1991), p. 415.

[127] Oja, T. “UBV photometry of stars whose positions are accurately known. VII.” In: 100 (1993), pp. 591–592.

[128] Oldham, W.G. et al. “Triggering phenomena in avalanche diodes”. In: *IEEE Transactions on Electron Devices* 19.9 (1972), pp. 1056–1060. DOI: 10.1109/T-ED.1972.17544.

[129] Oppenheim, A.V. et al. *Discrete-time Signal Processing*. Prentice Hall international editions. Prentice Hall, 1999. ISBN: 9780137549207.

[130] Pagano, R. others. “Dark current in SiPM pixels: data and model”. In: *IEEE Transactions on Electron Devices* 59 (2012), p. 2410.

[131] Otono, H. et al. “Study of the internal mechanisms of Pixelized Photon Detectors operated in Geiger-mode”. In: *Submitted to: Nucl. Instrum. Meth.* (2008). arXiv: 0808.2541 [physics.ins-det].

[132] Otte, A.N. et al. “Silicon photomultiplier integration in the camera of the mid-size Schwarzschild-Couder Cherenkov telescope for CTA”. In: *Nuclear Instruments and Methods in Physics Research Section A Accelerators Spectrometers Detectors and Associated Equipment* 787 (2015), pp. 85–88. DOI: 10.1016/j.nima.2014.11.026.

[133] Otte, A.N. et al. “Characterization of three high efficiency and blue sensitive silicon photomultipliers”. In: *Nuclear Instruments and Methods in Physics Research Section A: Accelerators, Spectrometers, Detectors and Associated Equipment* 846 (2017), pp. 106–125. DOI: https://doi.org/10.1016/j.nima.2016.09.053.

[134] Pablo, H. et al. “The most massive heartbeat: an in-depth analysis of Orionis”. In: *Monthly Notices of the Royal Astronomical Society* 467.2 (2017), pp. 2494–2503. DOI: 10.1093/mnras/stx207.

[135] Pearson, K. “Notes on the History of Correlation”. In: *Biometrika* 13.1 (1920), pp. 25–45. (Visited on 09/01/2022).

[136] Physclips, UNSW.edu.au. *Interference beats and Tartini tones*. 2016. URL: https://www.animations.physics.unsw.edu.au/jw/beats.htm (visited on 01/14/2023).

[137] Piatek, S. *How does temperature affect the gain of an SiPM?* 2011. URL: https://hub.hamamatsu.com/us/en/technical-notes/mppc-sipms/how-does-temperature-affect-the-gain-of-an-SiPM.html (visited on 01/14/2023).

[138] Piemonte, C. et al. "Development of an automatic procedure for the characterization of silicon photomultipliers". In: *2012 IEEE Nuclear Science Symposium and Medical Imaging Conference Record (NSS/MIC)*. 2012, pp. 428–432. DOI: 10.1109/NSSMIC.2012.6551141.

[139] Piemonte, C. et al. "Overview on the main parameters and technology of modern Silicon Photomultipliers". In: *Nuclear Instruments and Methods in Physics Research Section A: Accelerators, Spectrometers, Detectors and Associated Equipment* 926 (2019), pp. 2–15. DOI: https://doi.org/10.1016/j.nima.2018.11.119.

[140] Popovic, K. et al. "Development and Characterization of a Round Hand-Held Silicon Photomultiplier Based Gamma Camera for Intraoperative Imaging". In: *IEEE Transactions on Nuclear Science* 61.3 (2014), pp. 1084–1091. DOI: https://doi.org/10.1109/TNS.2014.2308284.

[141] Danny C. Price. "Real-time stream processing in radio astronomy". In: *Big Data in Astronomy*. Elsevier, 2020, pp. 83–112. DOI: 10.1016/b978-0-12-819084-5.00013-4.

[142] Rando, R. et al. "Silicon Photomultiplier Research and Development Studies for the Large Size Telescope of the Cherenkov Telescope Array ". In: *Proc of The 34th International Cosmic Ray Conference — PoS(ICRC2015)*. Vol. 236. 2016, p. 940. DOI: https://doi.org/10.22323/1.236.0940.

[143] Rivet, J. et al. "Optical long baseline intensity interferometry: prospects for stellar physics". In: *Experimental Astronomy* 46.3 (2018), pp. 531–542. DOI: 10.1007/s10686-018-9595-0.

[144] Saveliev, V. "Silicon Photomultiplier - New Era of Photon Detection". In: (2010). Ed. by Ki Young Kim. DOI: 10.5772/7150.

[145] Schoorlemmer, H. "A next-generation ground-based wide field-of-view gamma-ray observatory in the southern hemisphere". In: *36th International Cosmic Ray Conference (ICRC2019)*. Vol. 36. International Cosmic Ray Conference. 2019, p. 785. arXiv: 1908.08858 [astro-ph.HE].

[146] Schottky, W. "Über spontane Stromschwankungen in verschiedenen Elektrizitätsleitern". In: *Annalen der Physik* 362.23 (1918), pp. 541–567. DOI: https://doi.org/10.1002/andp.19183622304. eprint: https://onlinelibrary.wiley.com/doi/pdf/10.1002/andp.19183622304.

[147] Semiconductor Components Industries. *J-Series SiPM Sensors*. URL: https://www.onsemi.com/pdf/datasheet/microj-series-d.pdf (visited on 01/14/2023).

[148] SensL. *Introduction to SiPM TECHNICAL NOTE*. URL: https://www.first-sensor.com/cms/upload/datasheets/SiPM-RGB_5000080-5000083.pdf (visited on 01/14/2023).

[149] Shi, F. et al. "Comparative studies of silicon photomultipliers and traditional vacuum photomultiplier tubes". In: *Chinese Physics C* 35.1 (2011), pp. 50–55. DOI: 10.1088/1674-1137/35/1/011.

[150] Silva, B. et al. "The colored Hanbury Brown–Twiss effect". In: *Scientific Reports* 6.1 (2016). DOI: 10.1038/srep37980.

[151] Simon, F. "Silicon photomultipliers in particle and nuclear physics". In: *Nuclear Instruments and Methods in Physics Research Section A: Accelerators, Spectrometers, Detectors and Associated Equipment* 926 (2019), pp. 85–100. DOI: 10.1016/j.nima.2018.11.042.

[152] Solovov, V. N. et al. "Position Reconstruction in a Dual Phase Xenon Scintillation Detector". In: *IEEE Transactions on Nuclear Science* 59.6 (2012), pp. 3286–3293. DOI: 10.1109/tns.2012.2221742.

[153] Son, S. et al. "Imaging analysis of Parkinson's disease patients using SPECT and tractography". In: *Scientific Reports* 6 (2016), p. 38070. DOI: 10.1038/srep38070.

[154] Stockhoff, M. et al. "Advanced optical simulation of scintillation detectors in GATE V8.0: first implementation of a reflectance model based on measured data". In: 62.12 (2017), pp. L1–L8. DOI: https://doi.org/10.1088\%2F1361-6560\%2Faa7007.

[155] Subhabrata, R. et al. "A Survey of FIR Filter Design Techniques: Low-complexity, Narrow Transition-band and Variable Bandwidth". In: *Integration* 77 (2021), pp. 193–204. DOI: https://doi.org/10.1016/j.vlsi.2020.12.001.

[156] Sun, Y. et al. "SiPMs characterization and selection for the DUNE far detector photon detection system". In: *Journal of Instrumentation* 11.01 (2016), pp. C01078–C01078. DOI: 10.1088/1748-0221/11/01/c01078.

[157] Swihart, S. J. et al. "A CATALOG OF CALIBRATOR STARS FOR NEXT-GENERATION OPTICAL INTERFEROMETERS". In: *The Astronomical Journal* 153.1 (2016), p. 16. DOI: 10.3847/1538-3881/153/1/16.

[158] T2K Collaboration. URL: https://t2k-experiment.org/ (visited on 01/14/2023).

[159] Talpur, N. et al. "An investigation of membership functions on performance of ANFIS for solving classification problems". In: *IOP Conference Series: Materials Science and Engineering* 226.1 (2017), p. 012103. DOI: 10.1088/1757-899X/226/1/012103.

[160] Tohline, J. E. "The Origin of Binary Stars". In: 40 (2002), pp. 349–385. DOI: 10.1146/annurev.astro.40.060401.093810.

[161] Tridon, D. B. et al. *Performance of the Camera of the MAGIC II Telescope*. 2009. DOI: 10.48550/ARXIV.0906.5448.

[162] Trimale, M. B. et al. "A review: FIR filter implementation". In: *2017 2nd IEEE International Conference on Recent Trends in Electronics, Information Communication Technology (RTEICT)*. 2017, pp. 137–141. DOI: 10.1109/RTEICT.2017.8256573.

[163] Valotassiou, V. et al. "SPECT and PET imaging in Alzheimer's disease". In: *Annals of Nuclear Medicine* 32 (2018), pp. 1–11. DOI: 10.1007/s12149-018-1292-6.

[164] van Belle, G. "Interferometric observations of rapidly rotating stars". In: *The Astronomy and Astrophysics Review* 20.1 (2012). DOI: 10.1007/s00159-012-0051-2.

[165] van Eijk, D. et al. "Characterisation of Two PMT Models for the IceCube Upgrade mDOM". In: *36th International Cosmic Ray Conference (ICRC2019)*. Vol. 36. International Cosmic Ray Conference. 2019, p. 1022. arXiv: 1908.08446 [astro-ph.IM].

[166] Wagadarikar, A. A. et al. "Performance of Low Afterpulsing Probability Multi-Pixel Photon Counters for Time-of-Flight Positron Emission Tomography". In: *2013 IEEE Nuclear Science Symposium and Medical Imaging Conference (2013 NSS/MIC)*. 2013, pp. 1–5. DOI: 10.1109/NSSMIC.2013.6829595.

[167] Walczak, P. et al. "Seismic modelling of early B-type pulsators observed by BRITE – I. Ophiuchi". In: *Monthly Notices of the Royal Astronomical Society* 485.3 (2019), pp. 3544–3557. DOI: 10.1093/mnras/stz639. eprint: https://academic.oup.com/mnras/article-pdf/485/3/3544/28168808/stz639.pdf.

[168] Walter, R. personal communication. Nov. 3, 2022.

[169] Wehrens, R. et al. "The bootstrap: a tutorial". In: *Chemometrics and Intelligent Laboratory Systems* 54.1 (2000), pp. 35–52. DOI: https://doi.org/10.1016/S0169-7439(00)00102-7.

[170] Weiss, W. W. et al. "BRITE-Constellation: Nanosatellites for Precision Photometry of Bright Stars". In: *Publications of the Astronomical Society of the Pacific* 126.940 (2014), p. 573. DOI: 10.1086/677236.

[171] Wittkowski, M. et al. "Multi-epoch VLTI-PIONIER imaging of the supergiant V766 Cen - Image of the close companion in front of the primary". In: *A&A* 606 (2017), p. L1. DOI: 10.1051/0004-6361/201731569.

[172] Zhao, M. et al. "IMAGING AND MODELING RAPIDLY ROTATING STARS: CEPHEI AND OPHIUCHI". In: *The Astrophysical Journal* 701.1 (2009), p. 209. DOI: 10.1088/0004-637X/701/1/209.